Spring 2020

Structurally and electronically diverse polyanion-based cathode materials for alkali-ion batteries

Prashanth Sandineni

Department: Chemistry

STRUCTURALLY AND ELECTRONICALLY DIVERSE POLYANION-BASED CATHODE MATERIALS FOR ALKALI-ION BATTERIES

by

PRASHANTH SANDINENI

A DISSERTATION

Presented to the Graduate Faculty of the

MISSOURI UNIVERSITY OF SCIENCE AND TECHNOLOGY

In Partial Fulfillment of the Requirements for the Degree

DOCTOR OF PHILOSOPHY

in

CHEMISTRY

2020

Approved by:

Amitava Choudhury, Advisor
Philip Whitefield
Manashi Nath
Jay A. Switzer
Xinhua Liang

PUBLICATION DISSERTATION OPTION

This dissertation consists of the following four articles, formatted in the style used by the Missouri University of Science and Technology:

Paper I, found on pages 23-61, has been published in *Journal of Solid State Chemistry*.

Paper II, found on pages 62–128, has been published in *Inorganic Chemistry.*

Paper III, found on pages 129–170, has been published in *Journal of the Electrochemical Society.*

Paper IV, found on pages 171–203, has been submitted to *ACS Applied Energy Materials.*

Paper V, found on pages 204–226, is under preparation.

The associated supporting information (SI) for each publication is provided along with the respective papers.

ABSTRACT

Through this investigation polyanion-based cathode materials including sulfates, phosphates, and phosphites of transition metal have been synthesized for lithium and sodium-ion batteries and their electrochemical performances were evaluated. The emphasis was on soft chemical routes to discover metastable phases which are often missed in high temperature synthesis. Iron-based compounds were the main focus of this investigation, however, concurrently a few vanadium-analogues of iron compounds were investigated to evaluate the effect of multi-electron process on achievable voltage and capacity.

This investigation resulted in the discovery of several compounds with unique crystal structures, namely $AFe_3(SO_4)_2(OH)_6$ (A = Na/NH_4), $NaFe(HPO_4)_2$, $Li_2Fe(H_{0.5}PO_4)_2$, $Li_3Fe(PO_4)_2$, $Fe_3(PO_4)_2(OH)_2$, $LiV(HPO_3)_2$ and $Na_3(VO)_2(PO_4)_2F$. Single-crystal and synchrotron powder X-ray diffraction techniques have been used to determine the crystal structures. Partial fluoro-substitution in $NaFe_3(SO_4)_2(OH)_6$ improved Li-ion insertion voltage and achievable capacity owing to a synergistic effect of smaller particle size and inductive effect. A new composition, $NaFe(HPO_4)_2$, was synthesized through a hydrothermal route. Subsequent partial and full ion-exchange produced two new electroactive compounds, $Li_2Fe(H_{0.5}PO_4)_2$ and $Li_3Fe(PO_4)_2$, respectively. A mineral, barbosalite, $Fe_3(PO_4)_2(OH)_2$, has been evaluated as a cathode for Li-ion battery and exhibited capacity enhancement on cycling. $LiV(HPO_3)_2$ and $Na_3(VO)_2(PO_4)_2F$ exhibited facile electrochemistry with an average voltage of 4.0 and 3.8 V in Li- and Na–ion batteries, respectively. Both of these compounds showed two electron processes with capacities exceeding 125 and 150 $mAh.g^{-1}$, respectively.

ACKNOWLEDGMENTS

I would like to express my sincere gratitude to my advisor Dr. Amitava Choudhury for his continued support during my Ph.D. study and research. His guidance helped me in understanding the basics of crystallography and solid state chemistry.

Besides my advisor, I would like to thank the rest of my thesis committee members, Dr. Philip Whitefield, Dr. Manashi Nath, Dr. Jay A. Switzer, and Dr. Xinhua Liang for their time and effort in reading the dissertation, and providing valuable suggestions.

I would like to acknowledge the department of chemistry for their financial support during my course of Ph.D. in the form of graduate teaching assistantship.

I sincerely thank all my past and present lab-mates, Hooman, Srikanth and Santhosh for creating a congenial atmosphere in the laboratory. I am especially grateful to Dr. Hooman Yaghoobnejad Asl, for teaching me the basics of lithium-ion battery fabrication.

I would also like to thank administrative and technical staff members of chemistry department for their continued support and help. I am also grateful to Dr. Eric Bohannan of MRC for his assistance in analyzing samples with his expertise in X-ray diffraction.

Finally, I would like to thank all my friends and family members for their love and encouragements in all these years. I am especially thankful to my parents who have provided me with moral and emotional support in my life without which I could not have accomplished my goal.

TABLE OF CONTENTS

Page

PAPER

LIST OF ILLUSTRATIONS

SECTION Page

PAPER II

PAPER III

PAPER IV

PAPER V

LIST OF TABLES

1. INTRODUCTION

1.1. PERSPECTIVE AND BROADER IMPACT

The dependence on fossil fuels which has finite supply and unequal global distribution has two severe consequences for our civilization: 1. Development of a nation becomes severely dependent on fossil fuel imports, and 2. Release of excessive amount of CO_2 through their combustion causing global warming and acidifying water bodies. Therefore, development of renewable and clean energy sources is the most sought-after goal around the world. This has led to a sharp increase in the demand for efficient energy storage systems with high safety features and affordable cost.

There are lot of alternative and clean energy options such as solar panels, wind mills and ocean waves that are intermittent and scattered in different locations. Energy storage is the only solution to ensure continuous supply of energy from these intermittent sources. Batteries have the ability to store energy in the form of chemical energy and deliver this energy back to electrical energy without much loss and most importantly without producing any harmful gases. Battery is portable whereas other alternative energy sources are stationary, which allows battery to be the most favored candidate for power supply for electric vehicles. Therefore, to be sustainable batteries need to be low-cost, safe, and rechargeable (secondary) with high energy density and rate capability.[1,2]

Electrochemical energy storage was known from the beginning of nineteenth century in the form of voltaic pile. Later, due to the rise of auto-mobile industry lead-acid batteries became reliable source of energy for engine ignition. Though inexpensive and reliable, lead acid batteries lack the gravimetric and volumetric energy density required for

many applications. Later Ni-MH emerged as a high power density relatively light-weight battery and became quite popular for power tools and some hand-held devices[1].

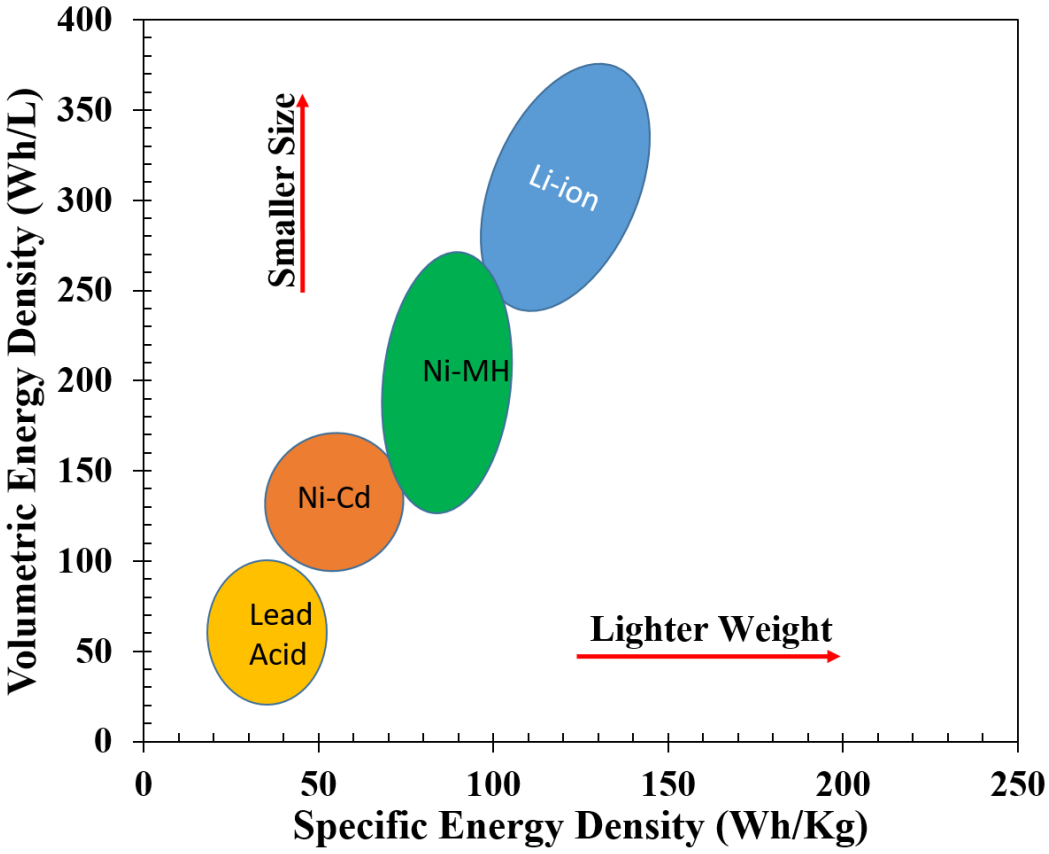

Figure 1.1. Comparison of mass-based and volume-based energy densities for different batteries[1].

The lithium-based batteries though in theory had the best power densities but suffered set-backs due to high price and inability to design a safe, reliable and functional cell. The energy densities of few most-used battery systems are given in Figure 1.1. However, things changed when market for portable electronic devices, for example, digital camera, laptop etc. started booming, the need for a lithium-ion battery became inevitable. Driven by this need finally a successful Li-ion battery (LIB) with a working cell chemistry

was commercially unveiled by Sony corporation in 1991.[1-4] Since then LIBs have become omnipotent from use in smart phones, laptops to electric and hybrid vehicles. Such an increased usage in electronic devices and expanding into cleaner technology for auto-mobile industry due to revolution of Li-ion batteries have finally earned the pioneers, John Goodenough, Stanley Whittingham and Akira Yoshino, a most coveted award in science, a Nobel Prize in chemistry in 2019.

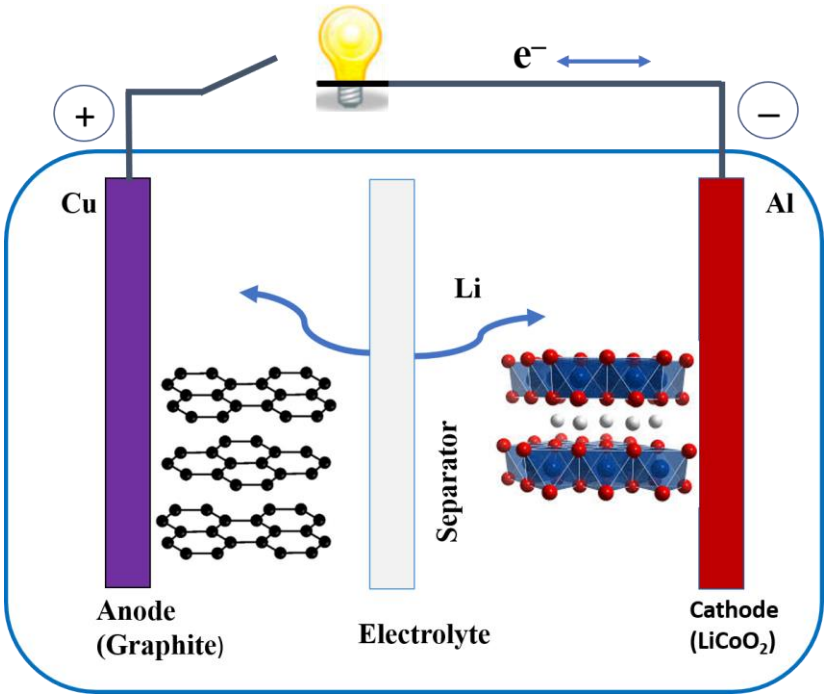

Figure 1.2. Schematic representation of a Li-ion battery (LIB).[4]

Batteries convert chemical energy to electrical energy and vice-versa and are classified as primary and secondary. Primary batteries are disposed after single usage, whereas secondary batteries are recharged multiple times. In a battery, reduction and oxidation reactions are separated by an insulating separator, forcing the electrons to travel

through an external circuit where they power up an electric device. There are three main components in a battery: an anode (negative electrode-reductant), a cathode (positive electrode-oxidant) and an electrolyte which acts as an ionic contact between the two electrodes by permitting ion transport. During normal operation, which is a discharge, the ions travel from anode to cathode and the direction is reversed during charging (recharging the battery). The separator provides a physical barrier to prevent direct contact between the anode and cathode and thus preventing the short-circuiting in a battery. The separator should be permeable to ions to allow ionic conduction between the electrodes. The electrode materials are nicely pasted as a thin film on metal current collectors to ensure electronic connection to the external circuit. Figure.1.2 shows the basic schematic representation of LIB.[4]

1.2. ELECTRODE MATERIALS

1.2.1. Cathode Materials. The cathode accepts lithium ions during discharge that comes from the anode, and the ionic movement occurs through the electrolyte. Thus, the cathode acts as a host for lithium ions and this process needs to be reversible for rechargeable batteries meaning the host should be able to release the lithium ions during the opposite process called charging. Materials that can accommodate lithium ions in the inter-layer space or in the channels and tunnels in the structure without much change in the overall structure is called intercalation material and generally work good as cathodes. The opposite of intercalation, called de-intercalation can be achieved with the application of reverse voltage of same magnitude at which intercalation occurred.

Sony used lithium cobalt oxide ($LiCoO_2$, LCO) as the cathode material in their first commercialized battery, which exhibited reasonably good performance. However, high cost and toxicity of cobalt (Co) along with the safety issues due to O_2 evolution at over-charging forced further research to discover new cathode materials.[4] Substitution of Co by manganese, nickel and aluminum was successfully utilized to create subfamilies of LCO, to form mixed metal oxides such as lithium nickel manganese cobalt oxide (NMC) or lithium nickel cobalt aluminum oxide (NCA) with improved thermal stability and have become potential replacement for LCO. Recently, layered Li-rich oxides, $xLi_2MnO_3\cdot(1-x)LiMO_2$ ($0 < x < 1$, M = $Ni_{0.5}Mn_{0.5}$, $Mn_{x'}Ni_{y'}Co_{1-x'-y'}$, $0 < x', y' < 1$) have attracted lot of attention due to their high specific capacities and low-cost, but the challenges still remain related to capacity fading and safety hazards before they can be used commercially in LIBs.[5–9] These compositions reduces the amount of Co but fails to eliminate it completely. Therefore, efforts are still on to find non-cobalt-based materials as cathode for LIBs.

Concurrently a non-layered oxide namely spinel lithium manganese oxide ($LiMn_2O_4$, LMO) was extensively explored as a potential non-cobalt-based cathode but suffered from manganese dissolution issues. Turns out manganese with an average oxidation state of +3.5 is unstable and disproportionate into the +2 and +4 oxidation states ($Mn^{+3} \rightarrow Mn^{+2} + Mn^{+4}$) thus causing dissolution. Nickel substitution in LMO to create $LiMn_{1.5}Ni_{0.5}O_2$, LMNO, not only reduces Mn dissolution but also increases the intercalation voltage from ~4 V to ~4.7 V in comparison to LMO material, making LMNO as one of the high voltage cathode materials. Unfortunately, currently electrolytes compatible with such high voltage stability window is still unavailable.

To bring down the cost and address the concerns related to toxicity an iron-based compound as cathode would be more desirable. However, oxides of iron do not show reasonable voltage to be used as cathode. During the investigation Goodenough reported that lithium iron phosphate ($LiFePO_4$, LFP)[10] can satisfy the required voltage and fulfill requirements of cost and sustainability. Soon LFP became one of the most sought after materials for commercial LIBs and also opened up possibilities of finding new cathode materials based on polyanion moiety (discussed later in detail).

1.2.2. Anode Materials. Initially pure lithium metal was used as anode in LIBs, but proved to be very hazardous. Repeated charging led to dendrite formation and eventually it grew enough to pass through separator and reached cathode shorting the battery. This could potentially cause battery to set thermal runaway followed by fire or explosion. To avoid this safety hazard, alternative materials with different chemistry were investigated, among them intercalation, conversion and alloying materials are noteworthy.[1] Graphite as an intercalation anode was extensively used in all commercial LIBs thus alleviating safety hazards.

1.3. ELECTROLYTE

The electrolyte enables lithium ion conduction between the two electrodes. Electrolyte should be ionically conducting but electronically insulating and compatible to the components of the battery. Liquid electrolytes are extensively used in commercial LIBs because of high ion conductivity required to meet the performance. The operating potential of LIBs extends to several volts and the electrochemical stability window (ESW) of the liquid should be within the operating potentials. Therefore, water with ESW of ~1.2 V is

far too narrow to sustain as LIB electrolyte solvent. Generally organic solvents with high ESW are used to dissolve lithium salt to form the electrolyte solution. Besides wide ESW, the solvent should also have a high dielectric constant, low viscosity, and melting and boiling points within reasonable limits of operation. Therefore, to cover all the properties often chosen electrolyte is a mixture of solvents. Ethylene carbonate (EC) and dimethyl carbonate (DMC) in a 1:1 ratio is the most commonly used combination today. The reduction of EC at the anode surface cause decomposition and formation of a thin film that passivates the graphite anode. EC also provides a higher dielectric constant facilitating easy dissociation of the lithium salt required for high ion conductivity[11]. High viscosity and low melting point (~36 °C) of EC pose some disadvantage but can be mitigated by the addition of small amount of diethyl carbonate (DEC). Lithium hexafluorophosphate ($LiPF_6$) is the most commercially used lithium salt in LIBs. Though it has issues with respect to thermal stability and sensitivity towards moisture, but helps in protecting the aluminum current collector at the back of cathode from corrosion by creating a corrosion resistance layer of aluminum (oxy) fluoride. Derivatives of $LiPF_6$, some imide- and borate-based salts of lithium are currently under investigation for improved stability but most of them suffer from lower ionic conductivities.

1.4. THE ELECTRODE/ ELECTROLYTE INTERPHASE

The usefulness of electrolyte solvent is determined by the electrochemical stability window (ESW) of the solvent within the entire operating voltage range of the battery. The gap between the HOMO and the LUMO states of the solvent molecule is therefore a determining factor. The ESW of the electrolyte must be higher than the operating potential

limits of the electrode, otherwise electron transfer will take place between the electrode and the electrolyte as shown in Figure 1.3a. In the most used graphite/LCO cell, LCO lies within the ESW of commonly used electrolytes but graphite does not.

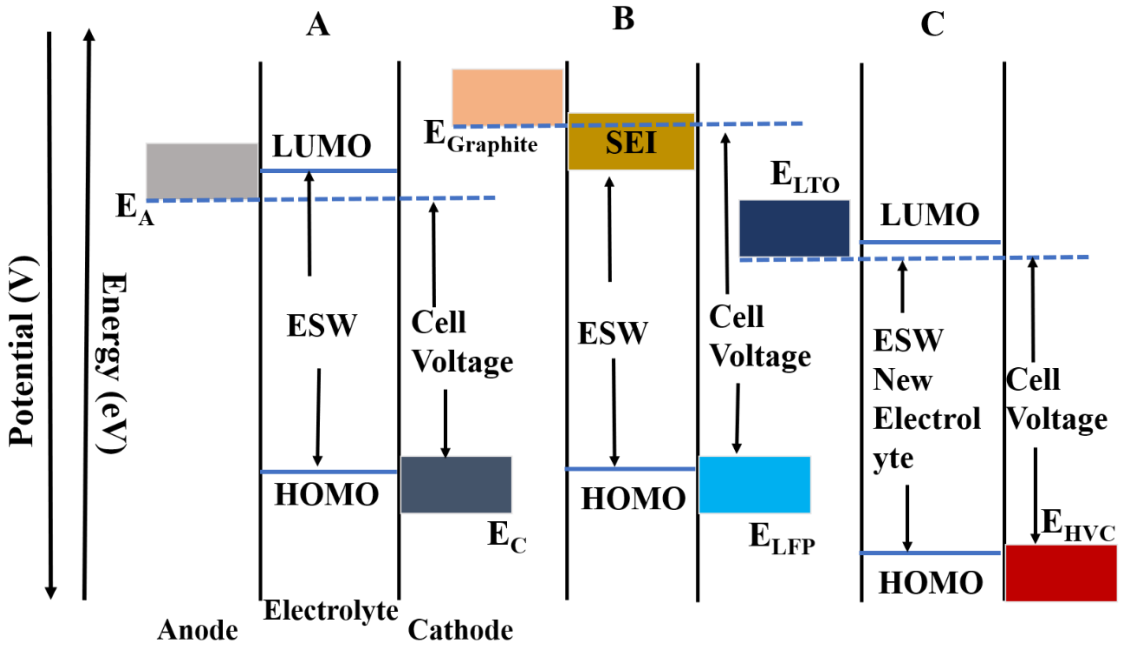

Figure 1.3. A schematic illustration of potentials leading to SEI formation in batteries.[11]

The reduction of common electrolytes occurs on graphite surface around 0.8 – 1V. This reduction and subsequent decomposition of electrolyte solvent accumulates on the surface of graphite and creates a Solid Electrolyte Interphase (SEI) layer.[11,12] This SEI layer makes it possible the widespread implementation of graphite anode in LIBs because the SEI is ionically conducting but electronically passivating. SEI layer subsequently stops electrons from the graphite anode to react further with the electrolyte, while at the same time letting ions to travel through the SEI layer enabling battery operation. This is known as passivation of the graphite surface by SEI layer which eventually prevents further decomposition of solvent by preventing electron transfer as shown in Figure 1.3b. SEI layer

is also believed to stop exfoliation of graphite layers during successive (de)-intercalation of lithium ions in graphite. However, SEI also causes increased internal resistance and loss of lithium-ions which can harm the batteries by depleting some amount of electrolyte leading to eventual failure of battery due to high internal resistance. To mitigate this problem often vinylene carbonate (VC) or fluorinated ethylene carbonate (FEC) are used to modify the chemistry of SEI and generate a smooth continuous film which passivates the graphite surface but does not increase internal resistance. Another way to bypass the SEI formation is to choose an anode with slightly higher voltage > 1 V such as lithium titanium oxide, $Li_4Ti_5O_{12}$ (LTO) and avoid SEI formation since the potential of 1.55 V of LTO is well within the electrolyte's ESW, as shown in Figure. 1.3c.

1.5. BEGINNING OF SODIUM ION BATTERIES

Due to massively growing demand arising from energy storage systems, sodium ion batteries (SIBs) are being recognized as the most attractive alternative to the current commercialized lithium ion batteries (LIBs) owing to the wide availability and accessibility of sodium.[13,14] Unfortunately, the low energy density, inferior power density and poor cycle life are still the main issues for SIBs in the current drive to push the entire technology forward to meet the benchmark requirements for commercialization. Over the past few years, tremendous efforts have been devoted to improving the performance of SIBs, in terms of higher energy density and longer cycling lifespans, by optimizing the electrode structure or the electrolyte composition. Unfortunately, graphite is not a good intercalation anode for Na-ion batteries. Therefore, among the established anode systems, those materials, such as metals/alloys, phosphorus/phosphides, and metal

oxides/sulfides/selenides, that typically deliver high theoretical sodium-storage capacities have received growing interest and achieved significant progress.

1.6. POLYANION BASED CATHODE MATERIALS

Polyanion compounds belong to a family of materials in which a tetrahedral polyanion moiety $(XO_4)^{n-}$ or their derivatives $(X_mO_{3m+1})^{n-}$ (X = P, S, As, Mo, or W) with strong covalent bonding combine with metal polyhedral unit, MO_x (*M* = transition metal, x = 4 - 6) to yield two- and three-dimensional structures. Polyanion cathode materials are often thermally more stable than conventionally used layered or spinel-based transition-metal oxides due to the presence of strong covalent bond between the oxygen atoms and central element of the polyanion. By virtue of this added safety polyanion-based cathodes are considered suitable for large-scale Li-ion battery applications as in electric vehicles. Polyanion-based cathode attracted lot of attention since the first report on the electrochemical performance of $LiFePO_4$ by Goodenough group.[10]

Figure 1.4 shows the energy density of different cathode materials for LIB. Even though the energy density of oxides is more than polyanion-based cathodes, there are several advantages of using polyanion-based cathodes over oxides. Figure 1.5 shows the general representation of a polyanion, where X can be P, S, B, or Si etc. as in Phosphates, Sulfates, Borates and Silicates respectively. M represents the transition metal in the polyanion based electrode material.

Considering the achievable capacity, often full capacity cannot be achieved in oxides, as removal of more than 50 % Li from $LiCoO_2$ collapses the structure, because the electrons are then removed from the oxide band leading to O_2 evolution. Within the

polyanion, X – O bond has a high degree of covalency due to either non-metal oxygen electronegativity difference or high order bond formation between metals in high oxidation states and oxygen. This ensures that the oxygen atoms are tightly bound to the material, compared to the pure transition metal oxides. On the other hand, the M – O bond becomes more ionic in nature due to the ample electronegativity differences in the X – O bond, a phenomena known as inductive effect, which helps to improve the redox potential of the active material upon change of oxidation state on the metal center. Unlike the oxide chemistry where the structures are formed by the limited number of anion array close packing schemes, various 2D, 3D and open framework structures can be formed by mixing different polyanions and transitional metal centers. Table 1.1 lists some important polyanion compounds along with their theoretical/ achievable capacities.[10, 16-45]

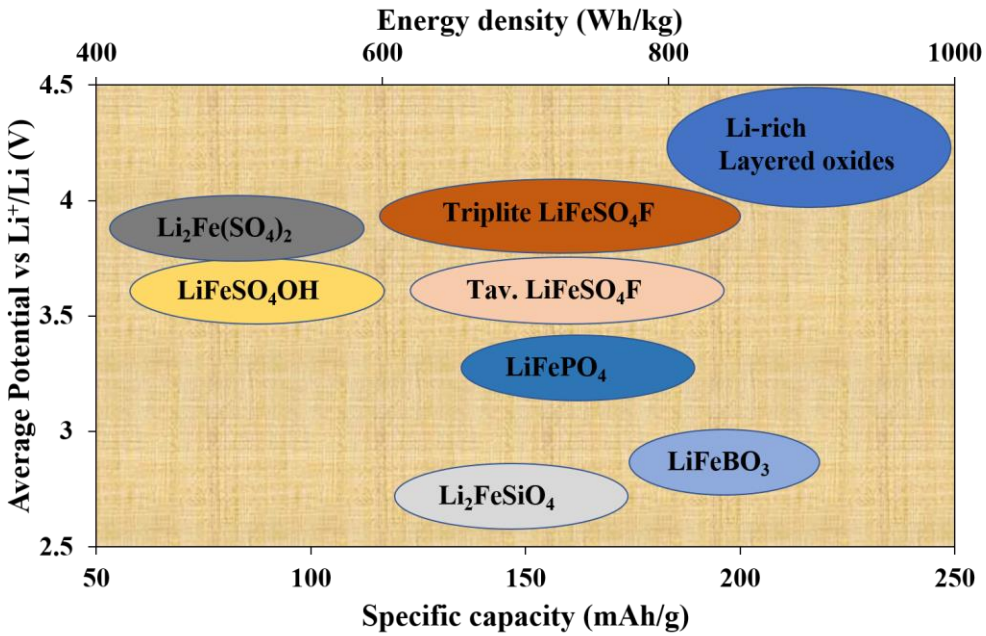

Figure 1.4. Performances in terms of operating voltage, specific capacity and energy density of different positive electrode compounds for LIB.[15]

Table 1.1. Summary of some polyanion compounds with their voltage and capacity

Compound	**Voltage (vs Li)**	**Theoretical/ Achievable capacity ($mAh.g^{-1}$)**
$LiFePO_4$	3.5	170/ 160 [10,16]
$LiMnPO_4$	4.1	171/160 [17-19]
Li_2FeSiO_4	2.8	332/ 200 [20-23]
Li_2MnSiO_4	4.1	333/ 250 [24-26]
Li_2CoSiO_4	4.2	325/ 100 [27-29]
$Li(Na)VPO_4F$	4.2	156/ 155 [30-33]
$Na_3V_2(PO_4)_2F_3$	4.1	192/ 120 [34,35]
$Li_5V(PO_4)_2F_2$	4.1	170/ 70 [36,37]
$Li(Na)_2FePO_4F$	3.5	292/ 135 [38-40]
$LiFeSO_4F$	3.6	151/ 135 [41-43]
$LiFeBO_3$	3.0	220/ 200 [44,45]

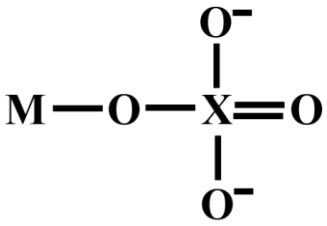

Figure 1.5. General representation of polyanion.

A very intuitive demonstration of the capability of the polyanion chemistry can be visualized by substituting the active metal center with other metals of the first-row

transition metals in the olivine Li*M*PO_4. As the redox potential of the M(II)/M(III) couple increases in the first row of transition metals, so does the cell potential. Apart from the already discussed phosphates, other compounds based on SO_4, SiO_4, BO_3 were also reported. The effect of the electronegativity of the central atom of polyanion on the iono-covalency nature of the metal-ligand bond and their effect on the cell voltage has been demonstrated. (Figure 1.6)

Figure 1.6. Clearly demonstrates the effect of electron withdrawing power of the central atom in the polyanion on the redox potential of different transition metal centers, indicating the numerous compositional combinations which may be used for tuning the cell potential. Moreover, addition of a secondary anion to the primary polyanion adds new structural and chemical dimensions to the polyanion based compounds of transition metals. In this regard mixed oxide-phosphate, fluoride-phosphate and carbonate-phosphate in $LiVOPO_4$, $LiVPO_4F$, $LiFeSO_4F$ and $Li_3FePO_4CO_3$ demonstrate the immense possibilities to discover new opportunities in this field.

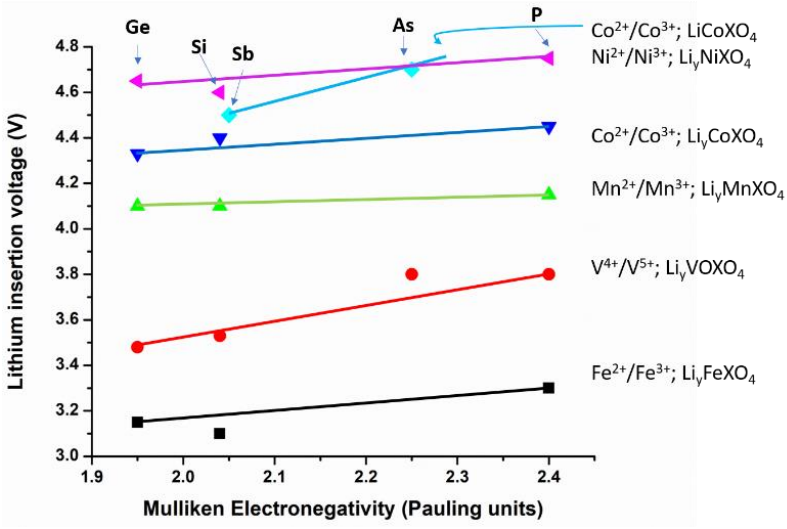

Figure 1.6. Calculated (solid symbols) and experimental (+ symbol) cell voltage for a fixed composition Li_xMXO_4 as a function of the Mulliken electronegativity.[21]

Considering the commercial availability and results for Li-ion battery, oxides have been the primary choices over polyanions, but coming to Na-ion batteries, polyanions outperformed oxides with respect to the operating voltage and structural stability. Recent investigations showed that vanadium-based polyanions, $Na_3V_2(PO_4)_3$ and $Na_3V_2(PO_4)_2F_3$, are better candidates for Na-ion batteries owing to their high energy density and high operating voltages greater than 4.0 V.[46]

1.7. SYNTHESIS PROTOCOLS FOR TRANSITION METAL POLYANIONIC COMPOUNDS

As one may expect, synthetic chemistry contributed a huge role to the ever-growing area of transition metal-polyanion compounds. This is mainly due to the numerous available polyanionic moieties and transition metals, which gives rise to several possible combinations. Moreover, solid-state chemists may use different synthetic strategies to form polymorphs of the same compositions, which are not necessarily identical from an electrochemical point of view; $LiFeSO_4F$ is probably one of the best examples in this regard. Pure $LiFeSO_4F$ crystallizes in two different phases, tavorite (triclinic, space group *P*1) and triplite (monoclinic, space group C*2/c*) through different synthesis methods. The difference in the crystal structure (through same composition) leads to surprising results in lithiation voltages, 3.9 V and 3.6 V for triplite and tavorite, respectively.[15] The lithiation voltage of triplite currently holds the record as the highest observed redox potential of Fe^{2+}/Fe^{3+} couple among all solid-sate materials. The change in crystal structure created by different ordering and connectivity of polyhedral units not only affects the cell voltage through thermodynamic stability factors, but also greatly affects the power rating of the

active material via altering the diffusion path geometry and kinetics of Li^+ ion mass transfer during the cell performance.

With the above argument forming a platform to emphasize the importance of synthetic methods to make solid-state inorganic materials, the following discussion briefly list the mostly used synthetic methods for the synthesis of battery active materials. Different methods have been sorted according to the normally used temperature regime.[47]

Solid-state and ceramic reactions. The direct solid-state methods have been used traditionally for making oxides and other materials with high thermal stability. The methods work based on simple enhanced ionic diffusion at high temperatures through intimate contact between the starting materials. Typically, the reagents are first milled extensively for an extended period of time to achieve uniformity and small particle size, followed by pressing into a pellet and subsequent heating at 600-900°C for a few hours to several days.[10, 20, 44] The reaction environments are generally controlled by passing reactive or inert gasses to tune the desired oxidation state of the transition metal center. For a given set of conditions, normally the most thermodynamically stable phase forms as a result of high activation energy given as thermal energy. This limits the solid-state and ceramic methods to effectively study the polymorphism and also exclude the synthesis of more thermally labile compounds. Moreover, the appearance of impurity phases due to intrinsic inhomogeneity path lengths are very common in these synthetic methods.[48, 49]

Sol-gel processes. The solid-gel process is a multi-step synthetic method which offers better homogeneity and smaller particle sizes compared to the solid-state synthesis case. In this method the reagents are first dissolved and mixed into a solvent, which is then evaporated yielding fine particles of solid residue to be pyrolyzed at high temperatures,

similar to the ceramic methods.[50,51] Since the mixing is performed on an atomic scale, the products present higher degree of pureness. Moreover, conductive carbon layers can be formed on the product particles if carbon-based precursors are used during the synthesis.[52]

Precipitation processes. The precipitation methods can be used for making those materials which form as a precipitate as a result of low solubility constants. The method involves mixing the reagents in a solvent and forming the precipitate by adjusting the pH. The precipitate is normally heated at high temperatures (400 – 700 °C, providing thermally stable) to remove the solvent and possible crystalline disorders.[53-56]

Polyol processes. High boiling point polyols play the role of solvent and reaction medium in polyol based synthesis. The reaction is conducted at the boiling point of the solvent and under isobaric conditions over a hot oil bath, hence eliminating the need to sophisticated reactors. The commonly used polyols are tetraethylene glycol (T_b=314°C), triethylene glycol (T_b=285°C) and diethylene glycol (T_b=245°C).[57-60]

Hydrothermal and Solvothermal processes. These encompass the widest range of synthesis due to the low cost of solvents used, relatively low temperatures required and the high degree of control on the reaction conditions. In a typical reaction the solvent (water in the case of hydrothermal reactions) is loaded along with reagents into a Teflon cup, which is then sealed into an autoclave steel jacket in an oven at a temperature higher than the boiling point of solvent (normally < 250 °C). The combination of high temperature and autogenous pressure leads to the formation of high purity products with good yields.[61-63]

Ionothermal processes. These methods are based on the dissolution of reagents in the ionic solvents with very low vapor pressure. These methods can be classified into two subgroups: 1) the organic ionic liquids which are generally expensive, especially for large-

scale applications though eliminates the need of elaborate reactors, it imposes recycling of the ionic liquid. 2) Inorganic fluxes and eutectic salt mixtures which are generally much cheaper and can have melting points, covering the temperature range required for making transition metal polyanion compounds.[64, 65]

Among the above methods, the hydrothermal and flux-based methods have been used extensively in our work. This is mainly due to the low-cost and scalability requirements of battery manufacturing process. Moreover, due to the low to moderate temperatures involved in hydrothermal and flux-based reactions, they unlock access to a vast area of metastable compounds with interesting structural and performance features, which cannot be formed by other methods. This is more promising in the case of inorganic fluxes, where the flux acts not only as a medium to dissolve the precursors, but also takes a part as reagent, affecting the final compositions of the material. Given the vast studies done so far on the role of the polyanion chemistry for designing cathode materials for LIB application, the innovation has finally reached a plateau. The aim of the work was to focus more on the unexplored areas of the polyanion chemistry and to inspect the possibility of discovering new combinations which may be technologically important for energy storage applications.

Applying the discussed methods, we synthesized our compounds and checked their electrochemical activity in both Lithium and Sodium ion batteries in our work. As mentioned, a small change in the stoichiometry of reactants bring major changes in the product formation. As an example, we synthesized $NaFe_3(SO_4)_2(OH)_6$, sodium jarosite in two different conditions just varying the stoichiometry, which produced the same compound but with different particle size. The compound with smaller particle size

exhibited better capacity achievement and retention when compared with the other. Similarly, we synthesized ammonium jarosite and studied the electrochemical activity, which was poor compared with the sodium, which explains that the bigger size of NH_4^+ was probably causing a barrier during the intercalation. This proves the influence of size of cations and the particle sizes of material on the achievable capacity. A small fluoro substitution in the sodium jarosite, increased the average voltage of the battery and showed better performance, which proves the concept of inductive effect again.

In other work, we employed Ion-exchange to produce different products. We synthesized a new compound, $NaFe(HPO_4)_2$ hydrothermally and used ion-exchange in aqueous medium to replace the Na with Li, to enhance the battery performance which lead to the formation of $Li_2Fe(H_{0.5}PO_4)_2$. We employed solid-state ion exchange of $Li_2Fe(H_{0.5}PO_4)_2$ to replace the proton attached to the phosphate, and succeeded to form $Li_3Fe(PO_4)_2$, a metastable compound, which exhibited better battery performance compared to others. Other works include synthesis of a mineral barbosalite, $Fe_3(PO_4)_2(OH)_2$ with Fe in +2 and +3 oxidation states. We were successful in incorporating Na and Li into the structure and studied their electrochemical properties for the first time.

Most of our work was limited to Fe as transition metal, but we extended it to other metals such as V, in order to achieve higher average voltage for the battery, and increased theoretical capacity owing to the possibility of V^{2+}/V^{3+} and V^{3+}/V^{4+} couple, which couldn't be achieved for the Fe, as Fe^{2+}/Fe^{3+} is only possible in the ESW of the commercially available electrolytes, and Fe^{3+}/Fe^{4+} couple was beyond the ESW. During this process, we successfully synthesized $LiV(HPO_3)_2$ with the flux-based reaction using phosphorous acid as a solvent, which has a low melting point of 94°C. This compound not only doubled the

theoretical capacity for a LIB, but also stood as one of the best sodium ion battery with an average voltage close to 4.0 V. In addition to this, we synthesized another vanadium based compound, $Na_3V_2O_{2-x}(PO_4)_2F_{1+x}$ and studied the electrochemistry with respect to Li- and Na-ion batteries. This compound showed very stable cycle life in LIB when a hybrid cell was fabricated with the Na-containing compound as cathode.

1.8. EXPERIMENTAL

The target of this research was to discover new polyanionic compounds based on iron which can be used as cathode materials in LIBs. The idea here was to incorporate desirable feature of iron i.e. high abundance and low cost, with economical synthesis approaches to design cost effective solutions for energy storage at a stationary level. Unlike the mobile applications where a high-power density battery system is crucial for successful realization of the technology, stationary state applications demand lower battery costs and durability as the primary criteria of interest.

Various exploratory synthesis techniques mainly based on solvent free or low melting point fluxes have been used along with low cost starting substances. After heating the reaction mixture at various temperatures and times, the reaction products were retrieved from the mixture and subjected to the post-synthesis analysis by comprehensive characterization techniques.

As these solid-state products are all crystalline, crystallography plays the primary role in materials characterization. For products formed as large and high-quality crystals, single-crystal X-ray diffraction (SC-XRD) was used to collect the diffraction data and solve the crystal structure, while powder X-ray diffraction (PXRD) was used for sample

purity assessment. On the contrary where the new product obtained only as powder (i.e. micro crystallites), high resolution synchrotron X-ray diffraction data was used for solving the crystal structure.

The solved crystal structure is often the starting point for many complementary chemical analysis techniques to expand our understanding of the material properties under study. These include the Mössbauer spectroscopy for assessing the oxidation state of iron and its coordination sphere. Mossbauer spectroscopy was also used as a quantitative tool for quantification of the proportions of Fe(II) and Fe(III) in cases where a mixing of oxidation states occurred, either through synthesis or as a result of electrochemical treatment. DC magnetization measurements were used for characterization of magnetic interactions and magnetic phase transitions in samples and also to confirm the oxidation state assignments. Thermogravimetric analysis (TGA) and Differential Scanning Calorimetry (DSC) were used for thermal stability determination and also to follow thermally induced structural changes. Fourier-transformed infrared spectroscopy (FTIR) was used as a general tool for functional group characterization, while SEM/EDS analysis utilized for morphological and elemental analysis studies. UV-visible spectroscopy equipped with diffuse reflectance spectroscopy (DRS) was used to check for metal *d-d* and metal-ligand transitions.

Followed by comprehensive material characterization the material was processed for loading as composite cathodes in the test cells. The processing normally comprises milling with conductive carbon to reduce the active materials' particle size and increase the inter-particle electrical conductivity. Furthermore, polyvinylidene fluoride (PVDF) dissolved in N-methyl-2-pyrrolidone (NMP) was added to the active material/carbon

mixture and the resulting slurry was dispersed on the surface of carbon-coated aluminum current collector. Upon evaporation of NMP, PVDF acts as a binder for sticking the cathode mix to the current collector. Followed by the preparation of the composite cathode, a disk of appropriate diameter was cut and assembled in a coin cell versus metallic lithium or sodium as anode, as depicted in Figure 1.7.

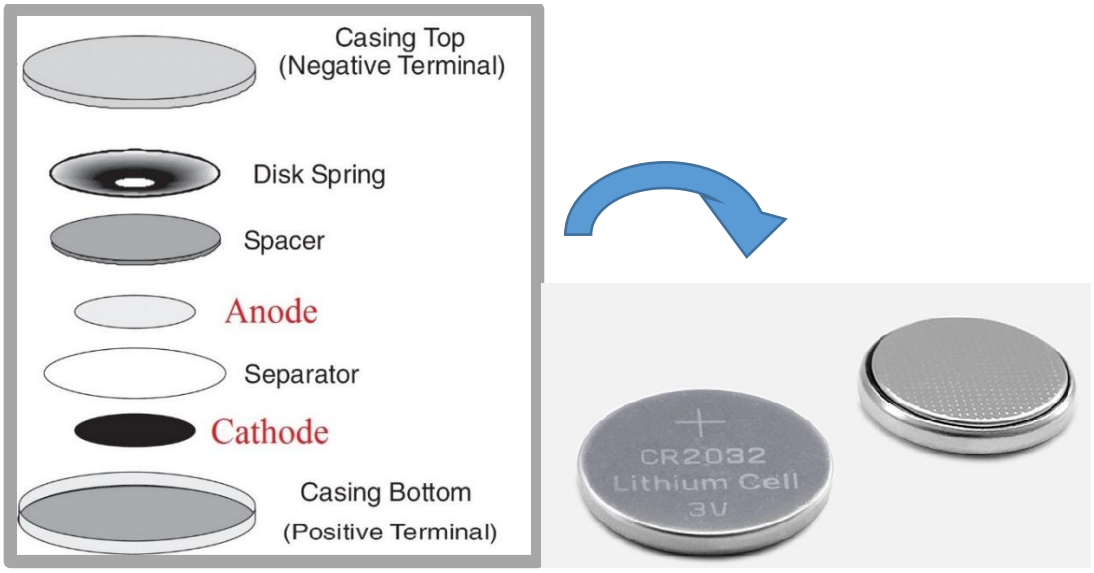

Figure 1.7. Coin cell structure.

Finally, for Li-ion cells, few droplets of electrolyte (A 1M solution of $LiPF_6$ in 1:1 mixture of ethylene carbonate (EC) and dimethyl carbonate (DMC)) was added to the cell and the cell was crimped to seal. The procedure for fabricating Na-ion cells is similar to the Li-ion ones, with the exception that fresh cuts of Na layer was placed as anode and a 1M solution of $NaClO_4$ in DMC/EC has been used as the electrolyte. Later, the cells were aged for few hours for stabilization and the anode SEI formation, as discussed previously.

The cells were then subjected to various electrochemical tests to study the details of the battery performance. Cyclic voltammetry (CV) was employed as a preliminary screening technique to evaluate the electrochemical activity of the as-prepared cathode material, to determine its redox potentials and the reversibility of the charge-discharge process.

Galvanostatic charge-discharge tests were used as a quantitative technique for obtaining the voltage-composition profiles during the cell operation, as well as measurement of the practical specific capacity. The galvanostatic tests were initially started as slow charge-discharge current rates (C-rate), denoted as C/n where n is the time required for complete oxidation/reduction of the active material in hours. Following the slow charge-discharge tests, the C-rate was increased stepwise to evaluate the cell performance and capacity retention at higher charge and discharge rates.

As battery is a complicated multicomponent system, obtaining specific information on individual components is very difficult. Electro-impedance spectroscopy (EIS) was used as a technique of choice for studying the responses of various components of a cell separately. This is done by applying a variable frequency alternating current (AC) voltage input and recording the AC current output; provided that different components of the cell have different time-constant, their current response can be separated in frequency domain.

PAPER

I. KAGOMÉ LATTICES AS CATHODE: EFFECT OF PARTICLE SIZE AND FLUORIDE SUBSTITUTION ON ELECTROCHEMICAL LITHIUM INSERTION IN SODIUM- AND AMMONIUM JAROSITES

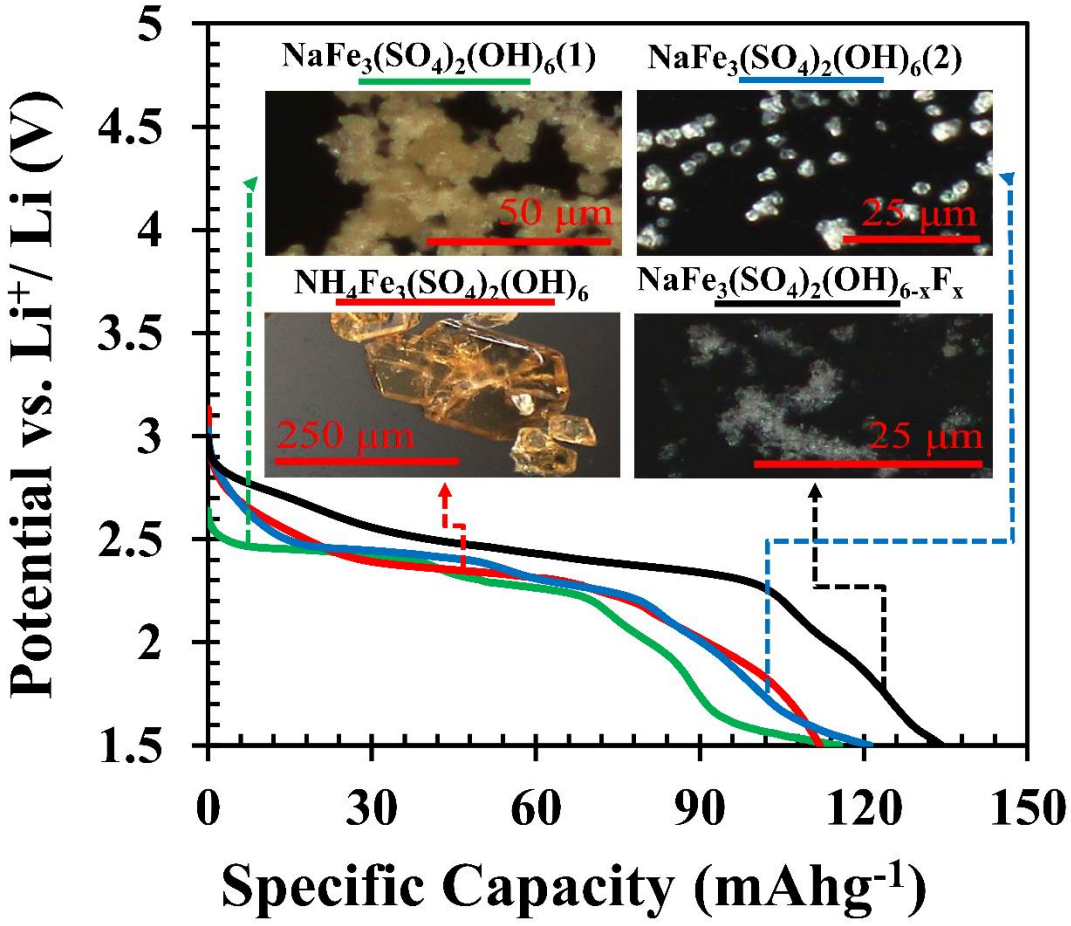

Prashanth Sandineni, Hooman Yaghoobnejad Asl and Amitava Choudhury*

Department of Chemistry, Missouri University of Science and Technology, Rolla, Missouri 65409-0010, United States

ABSTRACT

Highly crystalline sodium and ammonium Jarosites, $NaFe_3(SO_4)_2(OH)_6$ and $NH_4Fe_3(SO_4)_2(OH)_6$, have been synthesized employing hydrothermal synthesis routes. The structures consist of anionic layers of vertex-sharing FeO_6 octahedra and SO_4 tetrahedral units with interlayer space occupied by Na and ammonium ions, respectively. The corner-sharing FeO_6 octahedral units form six and three rings similar to hexagonal tungsten bronze sheets also known as kagomé lattice. These sodium and ammonium Jarosites are thermally stable up to 400 °C and undergo facile electrochemical lithium insertion through the reduction of Fe^{3+} to Fe^{2+}. Galvanostatic charge-discharge indicates that up to 2.25 and 2 lithium ions per formula unit can be inserted at an average voltage of 2.49 and 2.26 V to the sodium and the ammonium Jarosites, respectively, under slow discharge rate of C/50. The cycle-life and experimental achievable capacity show strong dependence on particle sizes and synthesis conditions. A small amount of fluoride substitution improves both achievable capacity and average voltage.

Keywords

Jarosites; Hydrothermal synthesis; Li-ion battery; Cathodes; Mössbauer spectroscopy; Electrochemistry

1. INTRODUCTION

Polyanionic compounds of the transition metals are attractive host for lithium and sodium-ion battery electrode because of a variety of reasons ranging from voltage

tunability of the redox couple to safer electrodes [1]. In 1998, it was shown by the Goodenough group how Fe^{3+}/Fe^{2+} redox potential can be attenuated with respect to Li^{+}/Li in an isostructural compound through the substitution of one PO_4^{3-} polyanion for SO_4^{2-} in NASICON structure, $Fe_2(SO_4)_3$ [2]. Subsequently, tuning of redox potential of the transition metal couple by changing the iono-covalency of metal – ligand bond in polyanion compounds through the inductive effect of $M - O - X$ linkage (M = transition metal; X = central atom of polyanion) became an important strategy for the design of polyanion cathode [1, 3, 4]. Theoretical studies also showed direct correlation between the electronegativity of the central atom of polyanion to the lithium intercalation voltage, displaying a linear relationship in a particular structure type [5]. This voltage range (2. 5 – 3.9 V) in the case of polyanion-based iron compounds is within the safe limit of the electrolyte and with good theoretical capacity materials, it becomes competitive for stationary use as in the electrical grid, where a safer, low-cost cathode with high cycle life gets precedence over high energy density [6, 7]. Thus a large number of polyanion compounds of iron [1], for example, phosphates [2, 8 – 12], pyrophosphates [13 – 15], phosphites [16, 17], sulfates [18], borates [19, 20], silicates [21, 22], as well as mixed polyanions such as carbono-phosphates [23, 24], phosphate-pyrophosphates [25, 26] etc. are currently being investigated as cathode for Li- and Na-ion batteries. Among these polyanions, sulfate is especially attractive due to high electronegativity of S, it often displays high Li-insertion potential. Surprisingly, since the first report of lithium insertion in the NASICON type iron sulfate, $Fe_2(SO_4)_3$ [27] there was a pause in the sulfate electrode research until the report of another iron sulfate, $Fe(OH)SO_4$, appeared in 2009 as a cathode for Li-ion battery [28]. Since then there was a renewed interest and a huge surge in the

sulfate-based cathode especially due to Tarascon group and other groups, who successfully used ball-milling and other innovative techniques to synthesize a variety of known and new iron sulfates [18, 29 – 32]. Some of these recently explored sulfate cathodes especially fluoro-derivatized Tavorite [33] and Triplite [34] show high voltages and good experimental capacities, thus emerging as an alternative to the most famous polyanion cathode, olivine $LiFePO_4$ [8]. Recently, natrojarosite, $NaFe_3(SO_4)_2(OH)_6$, with kagome lattice well known for its frustrated magnetic properties, has been shown to be active for Li-insertion with a potential close to 3 V and has a high theoretical capacity [35, 36]. Jarosites are minerals formed in acidic environments and also precipitated from the acid leached industrial discharge [37, 38], thus with the ease of availability and low cost, attracting lot of attention. In this article, we report new hydrothermal synthesis routes for natro- and ammonium jarosites, along with their characterization by single-crystal and powder X-ray diffraction techniques. We report here for the first time the electrochemical activities with regard to Li-ion insertion for ammonium jarosites and its comparison with the natrojarosites. Moreover, the partially fluoride substituted natrojarosite, $NaFe_3(SO_4)_2(OH)_{6-x}F_x$ has been prepared for the first time and its superior electrochemistry is demonstrated.

2. EXPERIMENTAL

2.1. MATERIALS

All the chemicals used in the synthesis were as purchased and without further purification. $Fe(NH_4)_2(SO_4)_2 \cdot 6H_2O$ (Reagent grade), H_2SO_4 (Trace metal grade, 95-98%

purity), Na_2CO_3 (Reagent grade), $NaNO_3$ (Reagent grade), NaF (Reagent grade), $Fe_2(SO_4)_3 \cdot 5H_2O$ (Reagent grade) and H_3BO_3 (Reagent grade) were purchased from Fischer Scientific. $FeCl_3 \cdot 6H_2O$ (Reagent grade, 97-102% assay), Na_2SO_4 (Reagent grade, 99% purity), and LiCl (Reagent grade, 99% purity) were purchased from MCB, Sigma-Aldrich, and Alfa Aesar, respectively.

2.2. SYNTHESIS

$NaFe_3(SO_4)_2(OH)_6$ has been synthesized by mixing 1.3515 g of $FeCl_3.6H_2O$ (5 mmol), 1.4204 g Na_2SO_4 (10 mmol) in 5 ml of H_2O in a 23 ml capacity Teflon-lined stainless steel Paar acid digestion bomb. The reactants were first dissolved in 5 ml of water with constant stirring in a Teflon beaker, the beaker with the lid was then placed in the steel autoclave, sealed tightly, and placed in an oven at a temperature 200°C for 3 days, followed by cooling down naturally to room temperature. The product of the reaction was composed of millimeter size crystals of mustard yellow color and the product was washed with the hot water and filtered (yield = 65%). The sample was labeled as $NaFe_3(SO_4)_2(OH)_6$(1).

$NH_4Fe_3(SO_4)_2(OH)_6$ has been synthesized by mixing 1.9606 g of $Fe(NH_4)_2(SO_4)_2.6H_2O$ (5 mmol), 0.3092 g H_3BO_3(5 mmol), 0.26 ml of H_2SO_4 (5 mmol), and 0.212 g of LiCl (5 mmol) in 5 ml of water in a 23 ml capacity Teflon-lined stainless steel digestion bomb. The reactants were first mixed in a Teflon beaker along with water, a homogeneous solution was attained with constant stirring and the beaker along with the lid was then transferred to a steel autoclave, sealed tightly, and placed in an oven at a temperature 200 °C for 3 days, followed by cooling down naturally to room temperature. The product of the reaction was composed of millimeter size crystals of golden yellow

color and the product was washed with hot water, filtered and allowed to dry naturally (yield 40%).

To further improve the yield and reduce the particle size of the product for the $NaFe_3(SO_4)_2(OH)_6$, we carried out hydrothermal reaction starting with stoichiometric combination (defined with respect to the mole ratio of iron source to the sulfate source as limiting reagents) of $FeCl_3 \cdot 6H_2O$ (4.0545 g, 15 mmol) and Na_2SO_4 (1.4204 g, 10 mmol) under identical condition. The stoichiometric combination yielded fine powder with good yield (~70 %). This sample was labeled as $NaFe_3(SO_4)_2(OH)_6$(2).

$NaFe_3(SO_4)_2(OH)_{6-x}F_x$ has been synthesized following a reported method for fluoro-substituted potassium Jarosite [39]. The synthesis was accomplished by mixing Na_2CO_3 (0.2120 g, 2 mmol), $NaNO_3$ (0.1702 g, 2 mmol), NaF (0.084 g, 2 mmol), $Fe_2(SO_4)_3 \cdot 5H_2O$ (2.7440 g, 5.6 mmol) in 20 ml water in a conical flux. The reaction mixture was then heated on a hot plate at a temperature of 70 °C for 48 hours, a reflux condenser was used to avoid solvent evaporation to dryness. The reaction was allowed to cool down to room temperature naturally; the whitish fine precipitate was washed with hot water and filtered.

2.2.1. Fluorine Analysis. For determination of fluorine content in the mixed hydroxo-fluoro natrojarosite, $NaFe_3(SO_4)_2(OH)_{6-x}F_x$, a dry and accurately weighed sample was digested in acid and the fluoride ion concentration was subsequently measured with fluoride ion selective electrode calibrated against different concentrations of a standard (NaF) solutions. The analysis showed 1.32% of fluorine in the product, which yielded a value of *x* in the formula as 0.34, giving, $NaFe_3(SO_4)_2(OH)_{5.66}F_{0.34}$.

2.3. MATERIAL CHARACTERIZATION

2.3.1. Single-crystal X-ray Diffraction. The crystal structure of $NaFe_3(SO_4)_2(OH)_6$ and $NH_4Fe_3(SO_4)_2(OH)_6$ was solved from single-crystal intensity data sets collected on a Bruker Smart Apex diffractometer with monochromated Mo Kα radiation (0.7107 Å). A suitable crystal was selected and mounted on a glass fiber using epoxy based glue. The data were collected using SMART [40] software at room temperature employing a scan of 0.3° in ω with an exposure time of 10 s per frame. The cell refinement and data reduction were carried out with SAINT [41], while the program SADABS [41] was used for the absorption correction. The structures were solved by direct methods using SHELX-97 and difference Fourier syntheses. Full-matrix least-squares refinement against $|F^2|$ was carried out using the SHELXTL-PLUS [42] suite of programs. The structure of $NaFe_3(SO_4)_2(OH)_6$ and $NH_4Fe_3(SO_4)_2(OH)_6$ was solved in trigonal crystal system in a noncentrosymmetric space group, $R\bar{3}m$. The positions of Fe and S atoms were located from the heights of electron density peaks and oxygen atoms were assigned based on their distances from Fe and S along with the size of electron densities in the difference Fourier maps and refined isotropically. Subsequently, electron density for the Na^+ and N of the ammonium ion appeared at a distance of 2.712(2) and 2.90(3) Å from O2, respectively, for $NaFe_3(SO_4)_2(OH)_6$ and $NH_4Fe_3(SO_4)_2(OH)_6$. An anisotropic refinement was performed on the located atoms and one more electron density peak, approximately 1 Å away from the bridging oxygen atom (O2) appeared. The latter was assigned as the hydrogen and subsequently refined isotropically without adding any constrain to fix O−H bond distance. Details of the final refinements and the cell parameters for $NaFe_3(SO_4)_2(OH)_6$ and $NH_4Fe_3(SO_4)_2(OH)_6$ are given in Table 1. The final atomic

coordinates and the isotropic displacement parameters are given in Table 2. The selected bond distances for the two compounds along with the bond valence sum (BVS) of the metal ion are given in Table 3.

Table 1. Crystal data and structure refinement parameters for $NaFe_3(SO_4)_2(OH)_6$ and $NH_4Fe_3(SO_4)_2(OH)_6$.

Emperical formula	$NaFe_3(SO_4)_2(OH)_6$	$NH_4Fe_3(SO_4)_2(OH)_6$
Formula weight	484.71 g mol^{-1}	479.76 g mol^{-1}
Crystal system	Hexagonal	Hexagonal
Space Group	$R\bar{3}m$	$R\bar{3}m$
$a = b$	7.3090(17) Å	7.317(2) Å
C	16.542(4) Å	17.619(5) Å
$\alpha = \beta$	90°	90°
γ	120°	120°
Volume	765.3(3) $Å^3$	817.0(4) $Å^3$
Z	3	3
ρ_{calc}	3.155 g cm^{-3}	2.925 g cm^{-3}
F(000)	717	717
Temperature	220 K	298 K
GOF on F^2	1.291	1.293
R factors [I>2sigma(I)]	R1 = 0.0203, wR2 = 0.0547	R1 = 0.0237, wR2 = 0.0676
R factors [all data]	R1 = 0.0211, wR2 = 0.0551	R1 = 0.0241, wR2 = 0.0686

Table 2. Atomic coordinates and equivalent isotropic displacement parameters ($Å^2$) for $NaFe_3(SO_4)_2(OH)_6$ and $NH_4Fe_3(SO_4)_2(OH)_6$. U(eq) is defined as one third of the trace of the orthogonalized Uij tensor.

$NaFe_3(SO_4)_2(OH)_6$					
Atoms	Wyckoff	*x*	*y*	*z*	U(eq)
S1	6*c*	2/3	1/3	0.14588(7)	0.007(1)
Fe1	9*e*	1/2	1/2	0	0.007(1)
O3	18*h*	0.55645(1)	0.44355(1)	0.11611(1)	0.010(1)
O2	18*h*	0.20783(1)	0.4157(3)	0.03385(1)	0.009(1)
O1	6*c*	2/3	1/3	0.2341(2)	0.009(1)
Na1	3*b*	1/3	2/3	1/6	0.045(1)
H1	18*h*	0.1452(1)	0.290(4)	0.053(2)	0.020(1)
$NH_4Fe_3(SO_4)_2(OH)_6$					
S1	6*c*	2/3	1/3	0.13866(8)	0.006(1)
Fe1	9*e*	1/2	1/2	0	0.006(1)
O3	18*h*	0.5567(2)	0.4433(2)	0.10986(1)	0.010(1)
O2	18*h*	0.2059(2)	0.4118(5)	0.02952(1)	0.009(1)
O1	6*c*	2/3	1/3	0.2212(2)	0.011(1)
N1	3*b*	1/3	2/3	1/6	0.013(2)
H1	18*h*	0.157(4)	0.314(7)	0.049(3)	0.011(2)

Table 3. Selected bond lengths for $NaFe_3(SO_4)_2(OH)_6$ and $NH_4Fe_3(SO_4)_2(OH)_6$.

$NaFe_3(SO_4)_2(OH)_6$		$NH_4Fe_3(SO_4)_2(OH)_6$	
Bonds	Distances (Å)	Bonds	Distances (Å)
S1 – O1	1.460(3)	S1 – O1	1.455(4)
3 x S1 – O3 [a, b]	1.480(2)	3 x S1 – O3[a, b]	1.483(2)
4 x Fe1 – O2[c, d, e]	1.984(9)	4 x Fe1 – O2[c, d, e]	1.982(2)
2 x Fe1– O3[c]	2.049(9)	2 x Fe1 – O3[c]	2.065(2)
O2 – H1	0.851(9)	O2 – H1	0.71(5)
BVS for Fe	3.00	BVS for Fe	3.06

Symmetry transformations used to generate equivalent sites: [a] $-y + 1, x - y, z$; [b] $-x + y + 1, -x + 1, z$; [c] $-x + 1, -y + 1, -z$; [d] $y, -x + y, -z$; [e] $-y + 1, x - y + 1, z$;

2.3.2. Powder X-ray Diffraction (PXRD). Phase purity of $NaFe_3(SO_4)_2(OH)_6$ (1 and 2), $NH_4Fe_3(SO_4)_2(OH)_6$, and $NaFe_3(SO_4)_2(OH)_{5.66}F_{0.34}$ were evaluated by comparison of the PXRD pattern with the simulated pattern generated from the atomic coordinates of single-crystal XRD solutions. The powder pattern was obtained from a PANalytical X'Pert Pro diffractometer equipped with a Cu $K_{\alpha 1,2}$ anode and a linear array PIXcel detector over a 2θ range of 5 to 90° with an average scanning rate of $0.0472°s^{-1}$.

2.3.3. Mössbauer Spectroscopy. ^{57}Fe Mössbauer experiments were performed in transmission geometry at room temperature using a conventional constant acceleration spectrometer. The data were collected using a ^{57}Co (25 mCi) gamma-ray source embedded in a Rh matrix. Velocity calibration and isomer shifts are given with respect to alpha-Fe foil at room temperature. The Mössbauer data were analyzed by Lorentzian line fitting using RECOIL software [43].

2.3.4. Thermogravimetric Analysis (TGA). TGA has been performed on the sample with a TA instrument Q50 TGA from room temperature to 800 °C with a scan rate of 10 °C min^{-1} under nitrogen atmosphere.

2.3.5. IR Spectroscopy. The IR spectrum was collected using Thermo Nicolet Nexus 470 FT-IR spectrometer over 400–4000 cm^{-1} on a sample embedded in KBr pellet.

2.3.6. SEM. The morphology of the powder samples was studied by scanning electron microscopy (Hitachi S-4700 FESEM) at 5 kV operating voltage.

2.3.7. Electrochemical Testing. To test the electrochemical performance of Na and NH_4 Jarosites, cathode film of the active material on an aluminum current collector was made first. The active material was subjected to ball-milling thoroughly with super P conductive carbon in a SPEX 8000 miller for 2 hours to reduce the particle size. Poly-vinylidene fluoride (PVDF) was then added to the active material as the binder and an optimum amount of N-methyl-2-pyrrolidone (NMP) was added to dissolve the PVDF. The resulting slurry was further ball milled for another 20 minutes to obtain a homogeneous viscous mixture. The ratio of the active material, conducting carbon, and the binder in the cathode mix was 75 : 15 : 10. The cathode mix was then spread as a film with uniform thickness onto a flat sheet of aluminum current collector with a glass rod and transferred into a vacuum oven and dried for 12 h at 70 °C.

For electrochemical tests, CR2032 type coin cells were fabricated. The composite cathode film was cut into circular disks (3/8 inch diameter) with 4.5–5.0 mg of active material loading and transferred into an argon filled glove box with an oxygen concentration below 2.0 ppm. The cathode disk and Li anode (0.75 mm thickness Li ribbon cut into circular disk) were assembled in the coin cell casing with a Celgard® 2325 circular

sheet placed between the two electrodes as the separator. The electrolyte, 1 M solution of $LiPF_6$ in DMC–EC (1 : 1) was then added and the cell was sealed with a coin cell crimper. The prepared cells were aged for equilibration for about 12 hours before electrochemical testing.

Voltage composition profiles were obtained using galvanostatic charge/discharge experiments on an Arbin Instruments battery tester, model BT2043, within the cut-off potentials of 1.5 to 4 volt at various C-rates.

The electro-impedance spectra has been obtained using an IviumStat potentiostat-galvanostat-FRA by applying a 5 mV excitation wave on OCP over a frequency range of $0.001 – 10^5$ Hz on freshly fabricated coin cells aged for at least 12 hours.

3. RESULTS

3.1. SYNTHESIS AND STRUCTURE

The methods of synthesis reported here for $NaFe_3(SO_4)_2(OH)_6$ and $NH_4Fe_3(SO_4)_2(OH)_6$ are different from the reported procedure of Dutrizac [44] or Basciano and Peterson [45, 46] for sodium and ammonium Jarosites, respectively. Traditionally alkali jarosites are precipitated around 100 °C from an aqueous solution of $Fe_2(SO_4)_3$ and Na_2SO_4 in acidic medium by adding dilute H_2SO_4 [44]. However, in our synthesis we have not used any additional acid and the hydrothermal reactions were carried out at much higher temperature (200 °C), to form good quality single-crystals of pure Na-jarosites devoid of any hydronium substitution. Low temperature precipitation method often produces Na-jarosites with some amount of hydronium substitution [44]. In the case of

ammonium jarosite we have grown good quality single crystals from an acidic solution. Boric acid and LiCl were used to maintain high acidic pH and high ionic strength enabling crystal growth of pure ammonium jarosite at higher temperature (200 °C) under hydrothermal condition. Also it is to be noted here that most ammonium jarosites are synthesized starting with $Fe_2(SO_4)_3$ and $(NH_4)_2SO_4$ but in our synthesized we have used $Fe(NH_4)_2(SO_4)_2 \cdot 6H_2O$, which is a source of both ammonium and iron. The method of synthesis for $NaFe_3(SO_4)_2(OH)_{6-x}F_x$ is similar to the synthesis of $KFe_3(SO_4)_2(OH)_{6-x}F_x$ reported by Kovacs [39], where $x = 1.6$, but x is about 0.34 in our case as confirmed through fluorine analysis. To increase the amount of fluoride substitution further increase of NaF concentration in the synthesis and optimization of reaction conditions will be required.

The Jarosite crystal structure is composed of laterally corner-shared FeO_6 octahedra connected through the common –OH groups equatorially, and capping sulfates tetrahedra connecting three FeO_6 units *via* the axial positions, alternatively above and below the metal-oxide layer. Such an arrangement forms infinite 2D sheets along the ***a*-*b*** planes of the crystal with a Kagomé-like structure composed of hexagonal and trigonal rings with the hydrogen of the hydroxide group projected towards the hexagonal ring (Figure 1a). The forth oxygen of the sulfate group points toward the interlayer space and the layers are stacked along the ***c***-aixs of the crystal with the monovalent ion filling the interlayer space, as viewed along <100> (Figure 1b).

The experimental powder X-ray diffraction data of the well ground as-synthesized compounds are in good agreement with the simulated patterns derived from the atomic coordinates of single-crystal X-ray structure solution, implying the absence of any crystalline impurity phases (Figure 2).

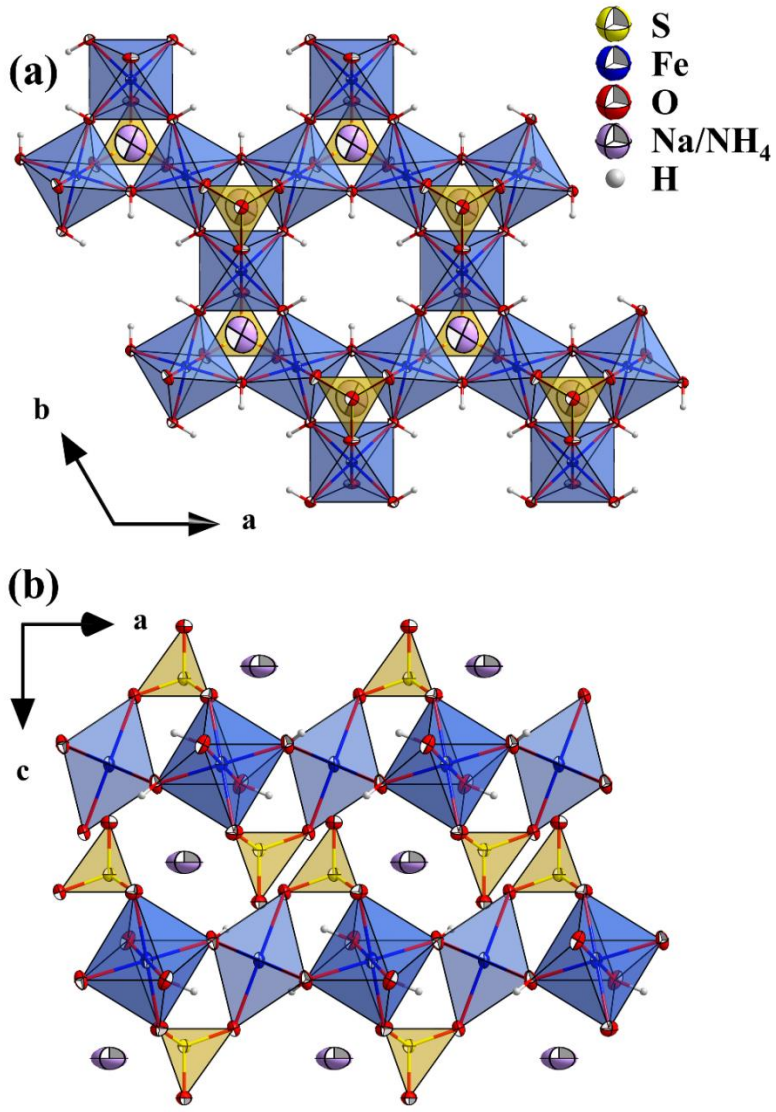

Figure 1. Connectivity pattern and local structure of jarosite as viewed along the **c**-axis (a), and **b**-axis (b).

Comparison of the PXRD patterns of $NaFe_3(SO_4)_2(OH)_6$(1) and $NaFe_3(SO_4)_2(OH)_6$(2) reveals that the two syntheses routes yield high purity natrojarosite. However, the visual inspection of the syntheses products reveals the large crystallite size of the former, which has adverse effects on the electrochemical performance of the cells (*vide infra*). In addition, the PXRD pattern of the as-prepared $NaFe_3(SO_4)_2(OH)_{5.66}F_{0.34}$

matches well with the simulated pattern of $NaFe_3(SO_4)_2(OH)_6$, indicating no major structural changes accompanying the partial substitution of OH with F has occurred akin to that fluoro-substituted potassium jarosite $KFe_3(SO_4)_2(OH)_{1-x}F_x$ [39].

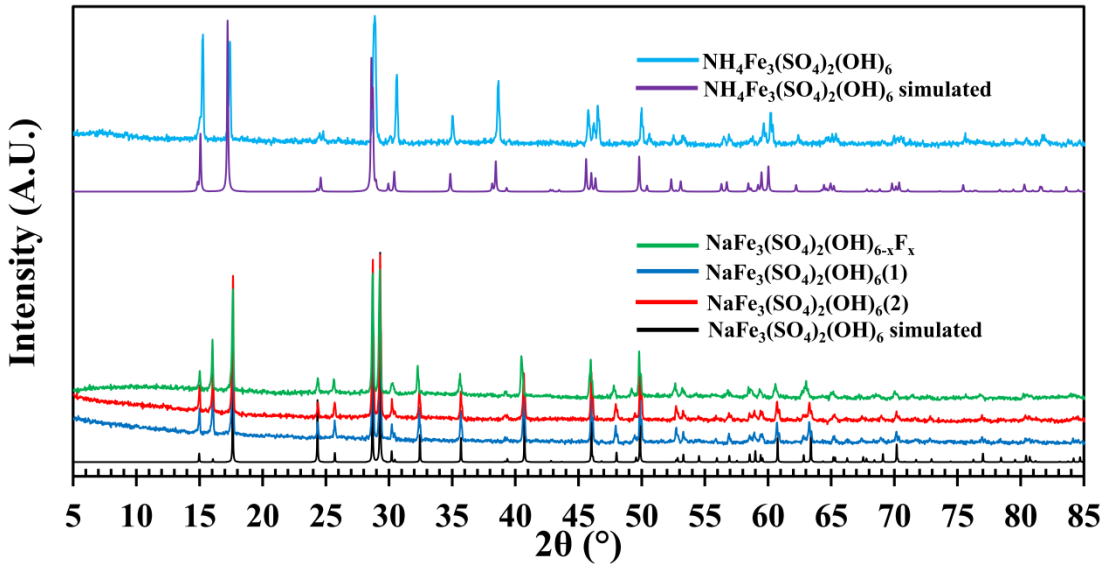

Figure 2. Observed and simulated powder X-ray diffraction patterns of various as-prepared jarosites.

Comparison of the acquired PXRD pattern of $NH_4Fe_3(SO_4)_2(OH)_6$ with its simulated counterpart reveals high sample purity but obvious intensity discrepancy on the acquired pattern may be assigned to the preferred orientation of the crystallites, often observed in layered materials. The preferred orientation of the crystallites was modeled using the fourth order spherical harmonics via Rietveld refinement and the results exhibit sample texture by accumulating the [001] pole, pointing toward the interlayer stacking space (the results for Rietveld refinement and texture analysis are given as supplementary material, Table S1, Figures S1 and S2). The preferred orientation of the crystallites is also

supported by the asymmetry of peaks in the Mössbauer spectrum of $NH_4Fe_3(SO_4)_2(OH)_6$ (*vide infra*). The Rietveld refined lattice parameters match very well with the single-crystal lattice parameters signifying homogeneous ammonium jarosite sample without any hydronium substitution.

3.2. SPECTROSCOPIC AND THERMOGRAVIMETRIC ANALYSIS

To further characterize the chemical nature of the inter-atomic bonding in the as-prepared Jarosite samples, FT-IR spectroscopy has been used (Figure 3). The IR spectra of $NaFe_3(SO_4)_2(OH)_6$(1) and $NaFe_3(SO_4)_2(OH)_6$(2) show no difference, as expected. In each case the spectrum is dominated by the strong absorption bands of O — H and S — O of the hydroxide and sulfate groups, respectively. For $NH_4Fe_3(SO_4)_2(OH)_6$ the stretching and bending mode of N – H bond is also evident at 3410 and 1430 cm^{-1} , respectively, by which it can be differentiated from the sodium version. The collective stretching modes for S — O bonds are visible in the range 1050 - 1200 cm^{-1}, with the strong bending mode of O — H visible at 1000 cm^{-1}, respectively. The IR spectrum of $NaFe_3(SO_4)_2(OH)_{6-x}F_x$ exhibit the associated stretching and bending modes of O — H group, suggesting that a considerable fraction of the hydroxide groups are still present in the material. The IR spectra for all the Jarosites are consistent with those previously reported [47, 48].

TGA has been utilized to evaluate the thermal stability of the Jarosite samples (Figure 4). According to the TGA curves, natro- and ammonium jarosite are stable till 375 °C. The initial weight loss of 11% in the temperature range 375 – 450 °C in the case of $NaFe_3(SO_4)_2(OH)_6$ can be accounted for the loss of three water molecules (theoretical, 11.15%), while for $NH_4Fe_3(SO_4)_2(OH)_6$, the initial loss of 17% in the same temperature

range can be accounted for the loss of 3.5 H_2O and one NH_3 molecules (theoretical, 16.69%).

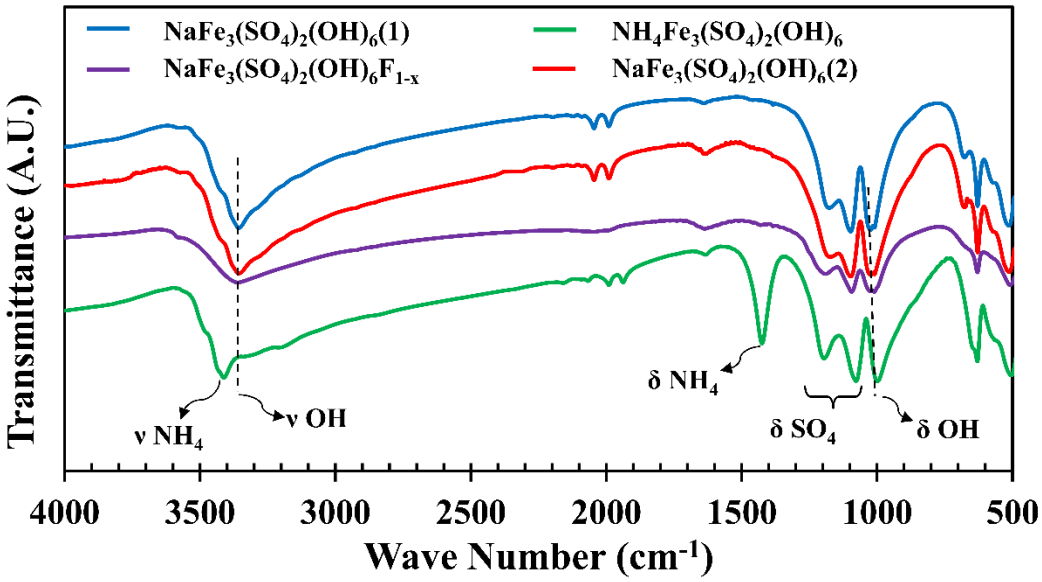

Figure 3. FT-IR spectra of different as-synthesized Jarosites.

Following the loss of volatile molecules, a short plateau in the TGA curves appear which extends from 450 – 600 °C, which then yield to another weight loss step equivalent to the loss of about 21 and 29 % for natro- and ammounium jarosite, respectively. The respective weight losses match well with the decomposition and loss of sulfate as the volatile SO_3. In each case the observed residual mass as well as powder X-ray diffraction analysis on the residues are consistent with the decomposition routes given in equations 1 and 2

$$2\ NaFe_3(SO_4)_2(OH)_6 \rightarrow 6\ H_2O + 3\ SO_3 + 3\ Fe_2O_3 + Na_2SO_4 \quad (1)$$

$$NH_4Fe_3(SO_4)_2(OH)_6 \rightarrow 7/2\ H_2O + NH_3 + 2\ SO_3 + 3/2\ Fe_2O_3 \quad (2)$$

Summaries of the calculated and measured residual weight percentages for the $NaFe_3(SO_4)_2(OH)_6$ and $NH_4Fe_3(SO_4)_2(OH)_6$ are given in Table 4 and the PXRD patterns of the TGA residues are provided as supplementary material, Figure S3.

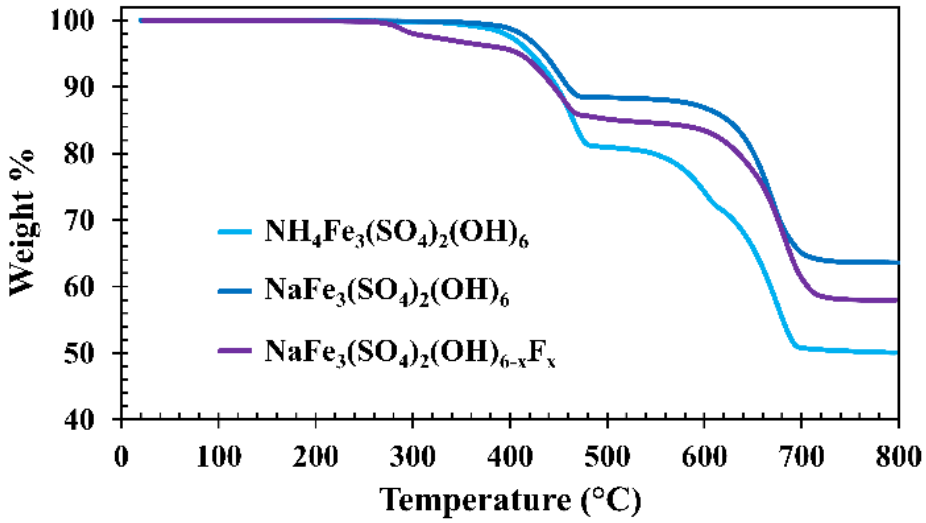

Figure 4. TGA curves of the as-synthesized Jarosite samples.

The TGA of $NaFe_3(SO_4)_2(OH)_{6-x}F_x$ exhibits an initial plateau until 290 °C at which the structure loses some 3.5% of its mass. This mass loss can be attributed to the loss of F^- (as gaseous HF) and H_2O from the structure which implies a lower thermal stability of the mixed hydroxide-fluoride analogue compared to the pure hydroxide jarosites, discussed above. Following the initial mass loss, the mixed anionic sample undergoes the subsequent mass loss steps at 400 and 600 °C similar to $NaFe_3(SO_4)_2(OH)_6$, corresponding to the loss of the remaining hydroxide and sulfate groups (as SO_3), respectively. It is to be noted here that such decrease of thermal stability has been observed in partially fluoro-substituted iron Tavorite, $LiFePO_4(OH)_{1-x}F_x$ as well, which upon full fluoro substitution gains extra

thermal stability compared hydroxy phase [12]. This may be explained by assuming an increase in the ease of proton transfer from hydroxide to fluoride and formation of the volatile HF gas which expedites the degradation of the crystal structure. In contrary, the full hydroxide analogue requires higher thermal energies to initiate expelling the hydroxide as water molecule.

Table 4. Calculated *vs*. experimental weight loss percentages for the $NaFe_3(SO_4)_2(OH)_6$ and $NH_4Fe_3(SO_4)_2(OH)_6$ phases.

Initial formula	1st Step weight loss			2nd step weight loss		
	species	% theo.	% exp.	species	% theo.	% exp.
$NaFe_3(SO_4)_2(OH)_6$	$3H_2O$	88.85	88.29	3/2 SO_3	64.07	63.68
$NH_4Fe_3(SO_4)_2(OH)_6$	7/2 H_2O + NH_3	83.33	81.27	2 SO_3	50.43	50.70

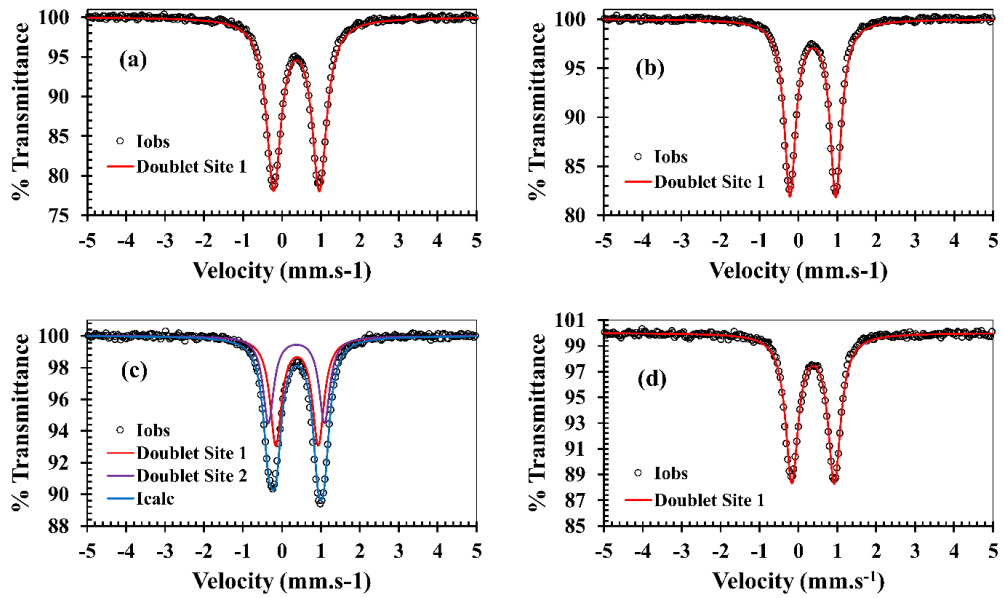

Figure 5. Mössbauer spectra of $NaFe_3(SO_4)_2(OH)_6$(1) (a); $NaFe_3(SO_4)_2(OH)_6$(2) (b); $NH_4Fe_3(SO_4)_2(OH)_6$ (c); and $NaFe_3(SO_4)_2(OH)_{6-x}F_x$ (d)

Table 5. Values of fit parameters for Isomer Shift (IS) and Quadrupole Splitting (QS) for different Jarosite phases.

Compounds	Isomer Shift ($mm.s^{-1}$)	Quadrupole Splitting ($mm.s^{-1}$)
$NaFe_3(SO_4)_2(OH)_6$(1)	0.3767(1)	1.1727(3)
$NaFe_3(SO_4)_2(OH)_6$(2)	0.3740(1)	1.1746(2)
$NH_4Fe_3(SO_4)_2(OH)_6$	0.3816(4)	1.266(2)
$NaFe_3(SO_4)_2(OH)_{6-x}F_x$	0.3802(2)	1.0927(4)

3.2.1. Mössbauer Spectroscopy. The Mössbauer spectra for the as-prepared $NaFe_3(SO_4)_2(OH)_6$(1), $NaFe_3(SO_4)_2(OH)_6$(2), $NH_4Fe_3(SO_4)_2(OH)_6$, and the mixed anionic $NaFe_3(SO_4)_2(OH)_{6-x}F_x$ are shown in Figure 5. In all the cases the spectrum can be fitted using one quadrupole doublet, except for the $NH_4Fe_3(SO_4)_2(OH)_6$. Interestingly ammonium Jarosite phase shows one asymmetric doublet implying the existence of either lattice vibrational anisotropy- Goldanskii-Karyagin effect, known as GKE or preferred orientation of the crystallites, known as texture effect [49]. Since there is no report of asymmetry in the Mössbauer spectrum of finely precipitated $NH_4Fe_3(SO_4)_2(OH)_6$ [50], we eliminated the possibility of GKE and attributed the asymmetry to preferred orientation of crystallites. Therefore, two doublets were necessary for a good fitting of the observed intensity data, however, only average isomer shift (IS) and quadrupole splitting (QS) is reported for $NH_4Fe_3(SO_4)_2(OH)_6$. The values of the IS and QS obtained by Lorentzian fitting (Table 5) are in good agreement with those previously reported and indicate iron species in +3 oxidation state in an octahedral coordination with oxo-ligands [50, 51]. Note

that the value of QS for the $NaFe_3(SO_4)_2(OH)_{6-x}F_x$ sample is slightly smaller than the $NaFe_3(SO_4)_2(OH)_6$ analogue; such a relationship was also observed for the QS values of $KFe_3(SO_4)_2(OH)_{4.4}F_{1.6}$ and $KFe_3(SO_4)_2(OH)_6$ (1.11 vs. 1.13, respectively) [39] and may be taken as another evidence of fluoride incorporation into natro-jarosite structure.

3.3. ELECTROCHEMISTRY

3.3.1. Galvanostatic Charge-Discharge. The charge-discharge experiments were done at various C-rates and the cut-off potentials were set in the range 1.5 – 4.0 V in all the cases (Figure 6). Assuming complete insertion and removal of one lithium ion per Fe atom, 3 lithium ions per formula unit gives a theoretical capacity of 165.54 and 167.60 mAh/g, respectively, for $NaFe_3(SO_4)_2(OH)_6$ and $NH_4Fe_3(SO_4)_2(OH)_6$. The observed capacities are 120 and 110 mAh/g at C/50 rate, which contribute 72 % and 66 % of the theoretical capacity and correspond to the insertion and extraction of 2.2 and 2 lithium ions per formula unit, respectively, for $NaFe_3(SO_4)_2(OH)_6(2)$ and $NH_4Fe_3(SO_4)_2(OH)_6$ in the first discharge cycle (Figure 6 a and b). In the case of sodium Jarosite, the specific capacity decreases with higher C-rates but the experimentally achieved capacity is conserved in all cycles (Fig. 6a). Thus showing 108 mAh/g (65%) in C/20, 83 mAh/g (50%) in C/10, 36 mAh/g (22%) in C/5 and regaining its original capacity when returned to C/50 again. But in the case of ammonium Jarosite, there is an irreversible loss of 11% capacity in the second cycle of discharge at C/50 rate, which further decreases to 30 mAh/g in C/20 and to almost negligible capacity at higher C rates (C/10 and C/5). When the battery is again cycled at C/50 after all the fast C rates, it regains its capacity to a value little lower than the original (82 mAh/g) (Fig. 6b). The capacity loss due to fast C-rate may be limited by the kinetics

of Li-diffusion and electron transfer through the poorly conducting, large size particles of $NH_4Fe_3(SO_4)_2(OH)_6$ and not due to the degradation of cathode. Exactly similar behavior has been observed in the case of $NaFe_3(SO_4)_2(OH)_6$(1) as shown in Figure 6c, where crystallites are relatively bigger and represent inhomogeneous size distribution (discussed later). Importantly, the charge-discharge curves for the fluoro-substituted sodium jarosite exhibit the best cell performance in terms of cycle-life (Figure 6 d). Furthermore a visual inspection of the discharge voltage depicts a slight enhancement of discharge potential compared to $NaFe_3(SO_4)_2(OH)_6$(2). The achievable capacity at high C-rate (more than 60 mAh/g at C/5 rate), long cycle-life and the relatively higher voltage profile observed for $NaFe_3(SO_4)_2(OH)_{6-x}F_x$ may be assigned to the synergistic effects of smaller particle size (discussed later) and incorporation of fluoride in the crystal structure of sodium jarosite yielded by the employed synthesis approach.

In order to achieve a deeper understanding of the fundamental differences between the natro-jarosites synthesized by stoichiometric and non-stoichiometric routes, electro-impedance spectroscopy (EIS) was performed on fresh as well as cycled (after 2 cycles) cells fabricated from respective phases (Figure 7, fitted EIS parameters are supplied as supplementary material, Table S2). In all the cases the cells are in the charged state (Fe in +3 oxidation state, SOC = 1.0) and the EIS spectra have been obtained at the OCV (2.9 — 3.0 V). As EIS spectroscopy is a very sensitive technique toward slight differences between two similar systems, it can provide clues to understand the unusual capacity fade observed in the case of $NaFe_3(SO_4)_2(OH)_6$(1). In all cases the observed impedance spectra can be modeled using one R|C element at medium to high frequencies corresponding to the combined SEI film and iron charge transfer resistances and a low frequency tail describing

the slow Li^+ ions solid-state diffusion inside the cathode active material. The two major features of the impedance curves for the freshly fabricated cells (open circles) are: 1) the considerably larger diffusion resistance for Li^+ ions in $NaFe_3(SO_4)_2(OH)_6$(1) compared to the stoichiometric synthesized natrojarosite, $NaFe_3(SO_4)_2(OH)_6$(2) and; 2) smaller SEI film resistance in case of $NaFe_3(SO_4)_2(OH)_6$(1) which may have implications with different surface properties emanating from a non-stoichiometric synthesis route. By comparing the EIS spectra obtained from cycled cells (open squares) with those before cycling it is evident that the overall features of the curves are conserved, however, the absolute values for charge transfer resistance and Li^+ diffusion has increased, as a result of SEI build up during the cycling process. The increase in Li^+ ionic diffusion for the $NaFe_3(SO_4)_2(OH)_6$(1) is profound after the second cycle, indicating the reason for its rapid capacity decay as observed during the galvanostatic charge-discharge tests. The higher resistance toward ionic diffusion encountered in the case of $NaFe_3(SO_4)_2(OH)_6$(1) was attributed to the larger average particle size as a result of synthesis procedure starting with non-stoichiometric ratio of reactants. This observation was further verified by comparing the SEM micrographs of $NaFe_3(SO_4)_2(OH)_6$(1) and $NaFe_3(SO_4)_2(OH)_6$(2) both milled for 2 hours and taken prior to composite cathode fabrication (Figure 8). Even after two hours of milling it was quite evident that $NaFe_3(SO_4)_2(OH)_6$(1) had particles greater than 2.5 microns while average particle in $NaFe_3(SO_4)_2(OH)_6$(1) was less than 2 microns. The SEM micrographs along with the galvanostatic charge-discharge curves demonstrate the superiority of the stoichiometric synthesis route in terms of cathode active material's particle size and battery performance. The larger diffusion length and larger particle sizes achieved through a non-

stoichiometric synthesis route explains the limited achievable capacity and high decay rate in cycle life for $NaFe_3(SO_4)_2(OH)_6$(1).

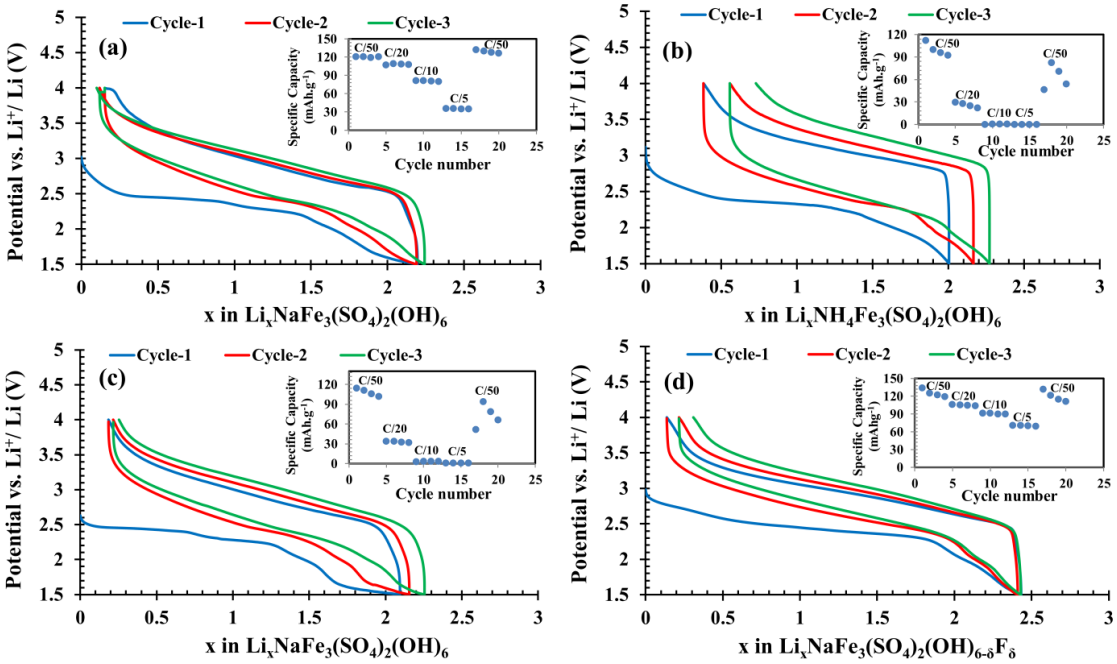

Figure 6. First three galvanostatic charge-discharge curves of $NaFe_3(SO_4)_2(OH)_6$(2) (a); $NH_4Fe_3(SO_4)_2(OH)_6$ (b); $NaFe_3(SO_4)_2(OH)_6$(1) (c), and $NaFe_3(SO_4)_2(OH)_{6-x}F_x$ (d) cathodes in Li-ion cells. Inset shows the cycle-life at various C-rates.

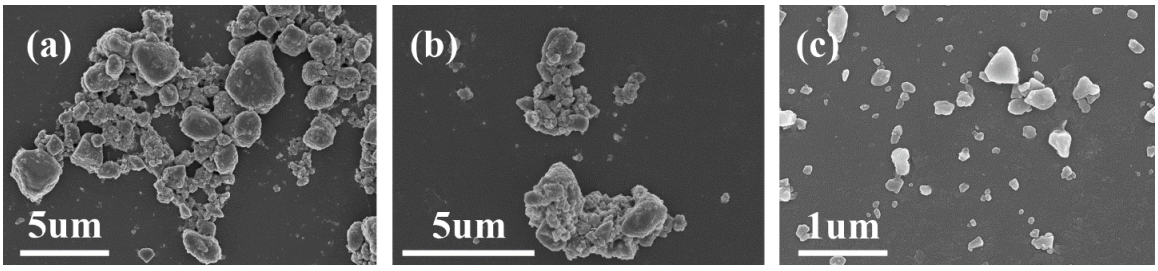

Figure 7. SEM micrographs of $NaFe_3(SO_4)_2(OH)_6$(1), (a); $NaFe_3(SO_4)_2(OH)_6$(2), (b); and Na $NaFe_3(SO_4)_2(OH)_{6-x}F_x$ (c).

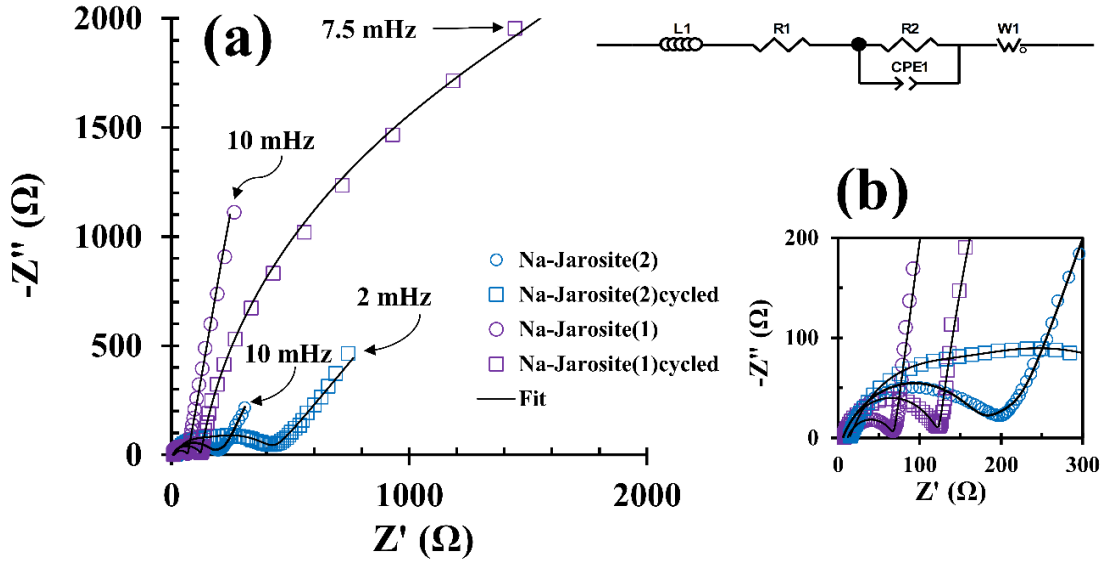

Figure 8. (a) Nyquist plot of freshly fabricated and cycled natro-jarosite cells prepared by stoichiometric and non-stoichiometric syntheses. (b) zoomed area of the mid-high frequency region of the spectra. The typical equivalent circuit used for fitting showed on top.

3.4. EX-SITU CHARACTERIZATION OF DISCHARGE CELLS

To further characterize the local environment of iron and structural changes occurring as a result of chemical/electrochemical reduction of $NaFe_3(SO_4)_2(OH)_6$, Mössbauer spectroscopy and PXRD have been utilized (supplied as supplementary material, Table S3 and Figures S4 and S5). To analyze the reduced phases, the samples have been prepared by extracting the cathodes from the cells discharged to the lower cut-off potential and also on powder samples chemically reduced using $LiAlH_4$. In either case the Mössbauer spectra indicate that the Fe(II) centers in the Jarosite oxidized back to Fe(III) following exposure to air. This air-oxidation phenomenon has also been previously encountered in the case of tavorite, $LiFePO_4OH$ [52], and attributed to the low redox potential of Fe^{3+}/Fe^{2+} couple. The PXRD patterns also exhibited crystallinity in electrochemically and chemically reduced phases. The chemically reduced sample using

$LiAlH_4$, for which the oxidation state of iron have been confirmed to be +3 via Mössbauer spectrum is diffracting and match well with the as-synthesized natrojarosite. Therefore, except for color change (turning dark on reaction with $LiAlH_4$) there is no proof that the chemical oxidation had actually occurred. Similarly the cathode film retrieved from the discharged cell conserves its crystallinity even after exposure to air, with the diffraction pattern of the re-oxidized sample matching fairly well with the as-prepared $NaFe_3(SO_4)_2(OH)_6$, which is a different finding from the reported Na-jarosite electrochemistry [35]. Only in-operando study can be conclusive in determining the oxidation state and nature of crystallinity of the reduced phases.

4. DISCUSSION

In this work alternative methods have been utilized for the synthesis of natro- and ammonium jarosites, a class of materials in which Li can be electrochemically inserted. The optimization of synthesis parameters to get fine particles of Na-jarosite, a requirement for better battery performance has led to a stoichiometric synthesis. In addition ammonium jarosite has been prepared by a new synthesis method, starting from Mohr's salt as a supply of sulfate, iron and ammonium, which yields millimeter size crystals. Moreover a Na-jarosite phase with hydroxide ligand partially substituted with fluoride has been synthesized for the first time by the reflux method. This has been done to study the inductive effect of the electronegative fluoride anion on cell performance. The results of fluorine analysis indicate a minor substitution of fluoride, with the final formula derived as $NaFe_3(SO_4)_2(OH)_{5.66}F_{0.34}$.

The well characterized samples were then studied for their electrochemical intercalation of Li^+ ion in Li-ion cell setups. The results of the galvanostatic charge and discharge curves exhibit intercalation of 2.2 and 2.0 Li ions in sodium and ammonium jarosite, respectively. In each case there is an increase in the voltage profile's slope following the first cycle. Such a change in slope may be assigned to structural changes and formation of solid-solutions in the cathode active material. Comparison of the discharge and charge profiles of $NaFe_3(SO_4)_2(OH)_6$ and $NH_4Fe_3(SO_4)_2(OH)_6$ demonstrates the fact that not only the discharge potential of $NaFe_3(SO_4)_2(OH)_6$ is slightly higher (2.45 vs. 2.35 V), but the polarization (i.e. the separation of charge and discharge potentials) is considerably smaller compared to the $NH_4Fe_3(SO_4)_2(OH)_6$ analogue. More importantly, the first discharge potential of the $NaFe_3(SO_4)_2(OH)_{6-x}F_x$ phase clearly shows a small plateau at the higher potential of 2.75 V, which is an indication of the inductive effect of the higher electronegativity fluoride on the redox potential of Fe^{3+}/Fe^{2+} couple. The onset of the discharge potential also shifts to over 3.0 V, suggesting the persistence effect of fluoride anion on the Li^+ intercalation potential. However, one striking feature of these results is the rapid capacity decay in $NaFe_3(SO_4)_2(OH)_6$(1) and $NH_4Fe_3(SO_4)_2(OH)_6$ as the C-rate increases, while $NaFe_3(SO_4)_2(OH)_6$(2) can match the increase in current more or less. This observation can be explained based on the larger crystallite sizes of the respective phases and indicates the importance of the optimization of synthesis parameters for achieving acceptable cell performance. The larger crystallite sizes will increase the Li^+ ion solid-state diffusion length which is the rate-limiting-step in the kinetics of intercalative electrode materials. This has been further confirmed by comparing the length of the low frequency tail corresponding to the diffusion resistance from EIS spectrum of cathode

materials obtained from stoichiometric and non-stoichiometric syntheses; the larger crystallite size of the $NaFe_3(SO_4)_2(OH)_6$(1) creates an ionic-diffusion resistance which is considerably larger than the $NaFe_3(SO_4)_2(OH)_6$(2). Quite interestingly, $NaFe_3(SO_4)_2(OH)_{6-x}F_x$ exhibits superior results in terms of the discharge potential, achieved capacity, and capacity retention at higher C-rates compared to the rest of the samples examined here. The superiority of the fluoro-substituted phase has been assigned to the inductive effects of fluoride anion on the Fe^{3+}/Fe^{2+} redox potential in the jarosite structure and small crystallite sizes yielded by the synthesis method employed. The SEM micrographs in Figure 8c clearly shows that $NaFe_3(SO_4)_2(OH)_{6-x}F_x$ sample is composed of crystallites ranging from 50 to 500 nm in diameter. The cell performance for the $NaFe_3(SO_4)_2(OH)_{6-x}F_x$ cathode prepared in this work is comparable to the Na-jarosite cathodes reported recently by the Raveau's group [35]. This finding not only supports the initial hypothesis of improving sodium jarosite cathode performance by introducing fluoride ligand, but also opens the path for exploring possible ways to increase the fluoride content in the jarosite host structure.

5. CONCLUSIONS

In this article we have shown that $NaFe_3(SO_4)_2(OH)_6$ and $NH_4Fe_3(SO_4)_2(OH)_6$, synthesized by hydrothermal methods are electrochemically active with respect to Li-ion (de)-insertion and compared their charge-discharge characteristics. The partial fluoro-substitution and precipitation method of synthesis improves the Li-ion insertion voltage and achievable capacity. If full theoretical capacities are achieved then these materials may

become good candidates for cathodes of Li-ion batteries, since these materials are low-cost and synthesis is straightforward. Further improvements in insertion voltage are possible with manganese doping in iron site and fluoride substitution in place of hydroxyl.

ACKNOWLEDGEMENTS

The authors acknowledge the funding from Energy Research and Development Center (Missouri S&T) and University of Missouri Research Board. The authors are also grateful to Professors Nick Leventis and Pericles Stavropoulos for the donation of a potentiostat and a glovebox, respectively.

SUPPLEMENTARY INFORMATION

Table S1. Lattice parameters and weighted residuals after Rietveld refinement (including performing the preferred orientation) on $NH_4Fe_3(SO_4)_2(OH)_6$.

***a* (Å^3)**	7.307(8)
***c* (Å^3)**	17.586(7)
***V* (Å^3)**	813.39(1)
W_R	4.68%

Table S2. Equivalent circuit fit parameters for fresh and cycled natro-jarosite cathodes prepared by non-stoichiometric (1) and stoichiometric (2) synthesis procedure.

					CPE1		CPE2		W		
	L_1 (μH)	R_1 (Ω)	R_2 (Ω)	R_3(Ω)	τ (s)	P	τ (s)	P	R (Ω)	τ (s)	P
Na-Jarosite(1)	2.29E-9	11.57	57.15	N/A	4.44E-5	0.72	N/A	N/A	24231	195	0.89
Na-Jarosite(2)	2.12E-6	4.99	160.9	N/A	2.91E-5	0.72	N/A	N/A	157.2	3.69	0.37
Na-Jarosite(1) Cycled	1.31E-6	6.22	117.7	2514	2.098E-5	0.76	6.091E-3	0.90	N/A	N/A	N/A
Na-Jarosite(2) Cycled	9.1E-7	13.22	79.94	336.2	1.055E-5	0.90	1.821E-4	0.58	N/A	N/A	N/A

Table S3. Details of Lorentzian fitting parameters for the electrochemically and chemically reduced natro-jarosite.

$NaFe_3(SO_4)_2(OH)_6$ discharged to 1.5 V				
	Isomer Shift ($mm.s^{-1}$)	Quadrupole Splitting ($mm.s^{-1}$)	Full width ($mm.s^{-1}$)	% Site
Doublet 1	0.2249(1)	0.8863(9)	0.330(1)	42.6(6)
Doublet 2	0.4820(1)	0.9295(8)	0.378(1)	57.4(6)
$NaFe_3(SO_4)_2(OH)_6$ chemically reduced by $LiAlH_4$				
Doublet 1	0.3763(4)	1.1079(1)	0.516(8)	100

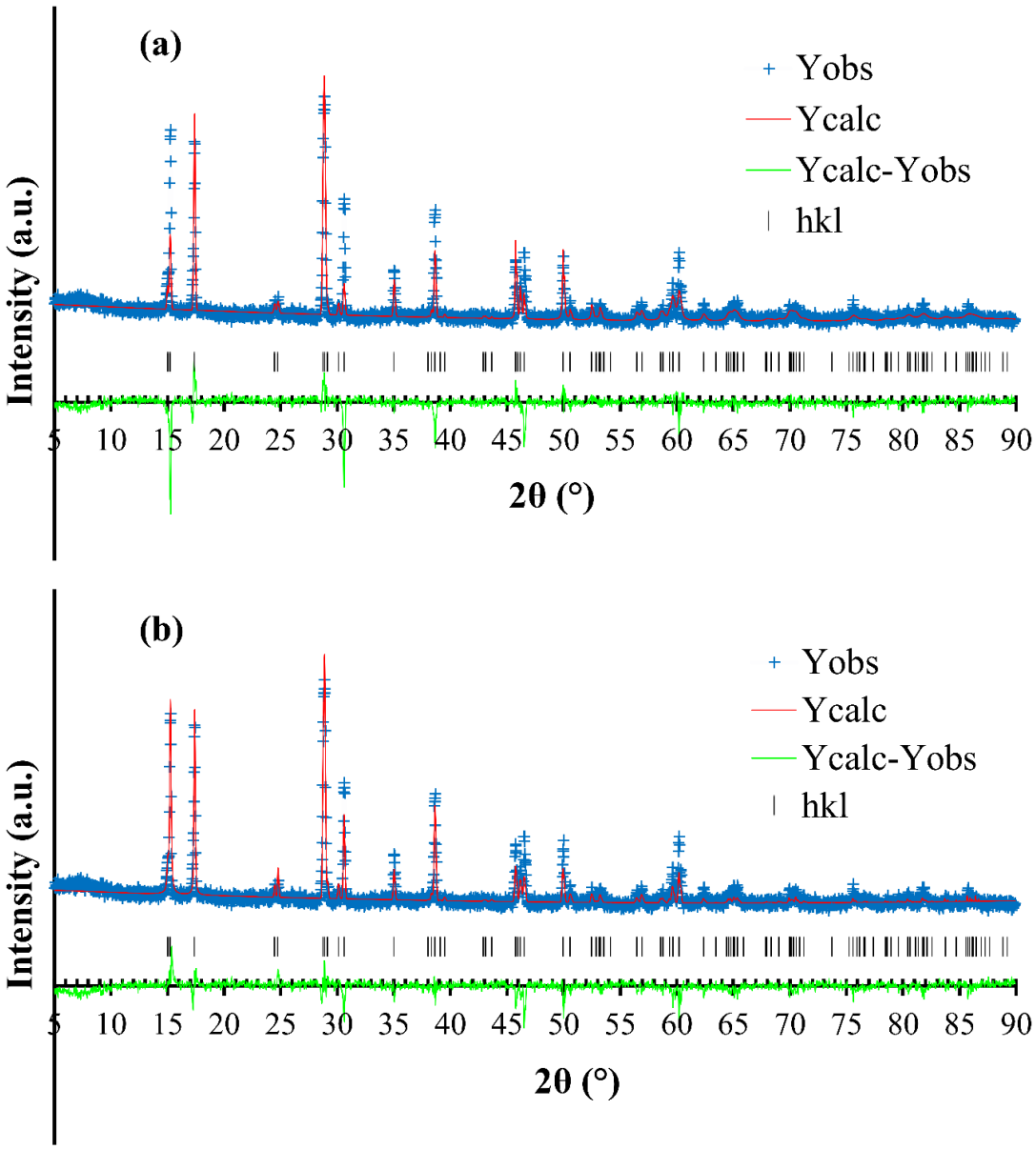

Figure S1. Rietveld refinement on PXRD pattern of $NH_4Fe_3(SO_4)_2(OH)_6$ without (a), and with preferred orientation refinement (b).

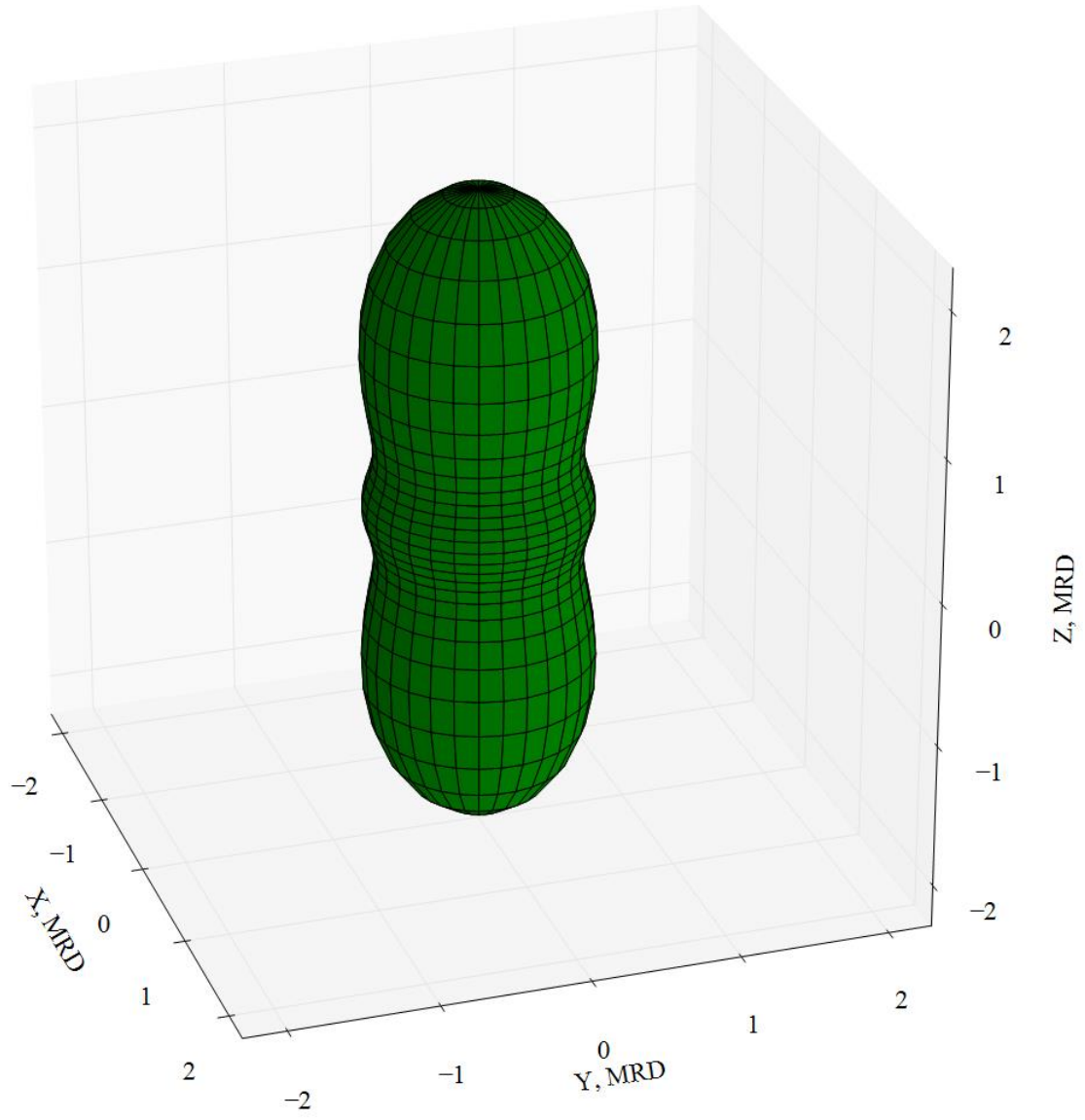

Figure S2. 3D representation of crystallite orientation along the [001] pole for $NH_4Fe_3(SO_4)_2(OH)_6$.

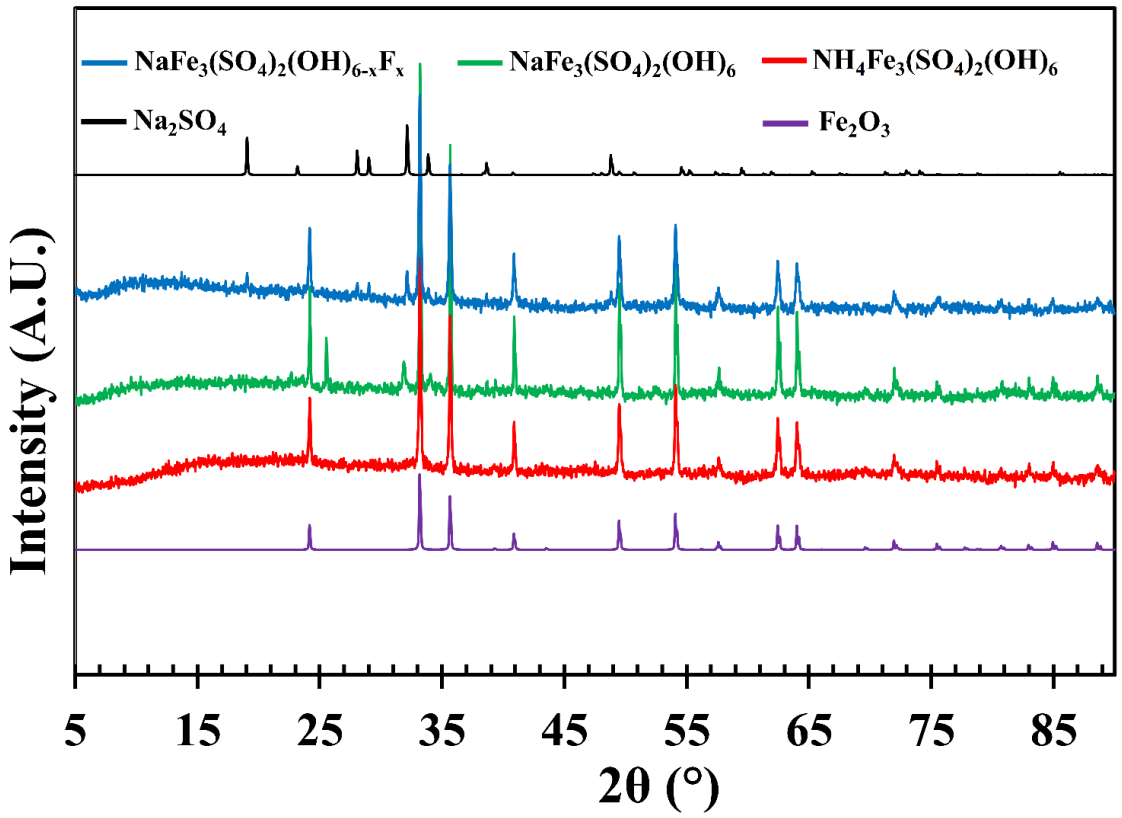

Figure S3. PXRD analysis of the TGA residues various jarosite samples.

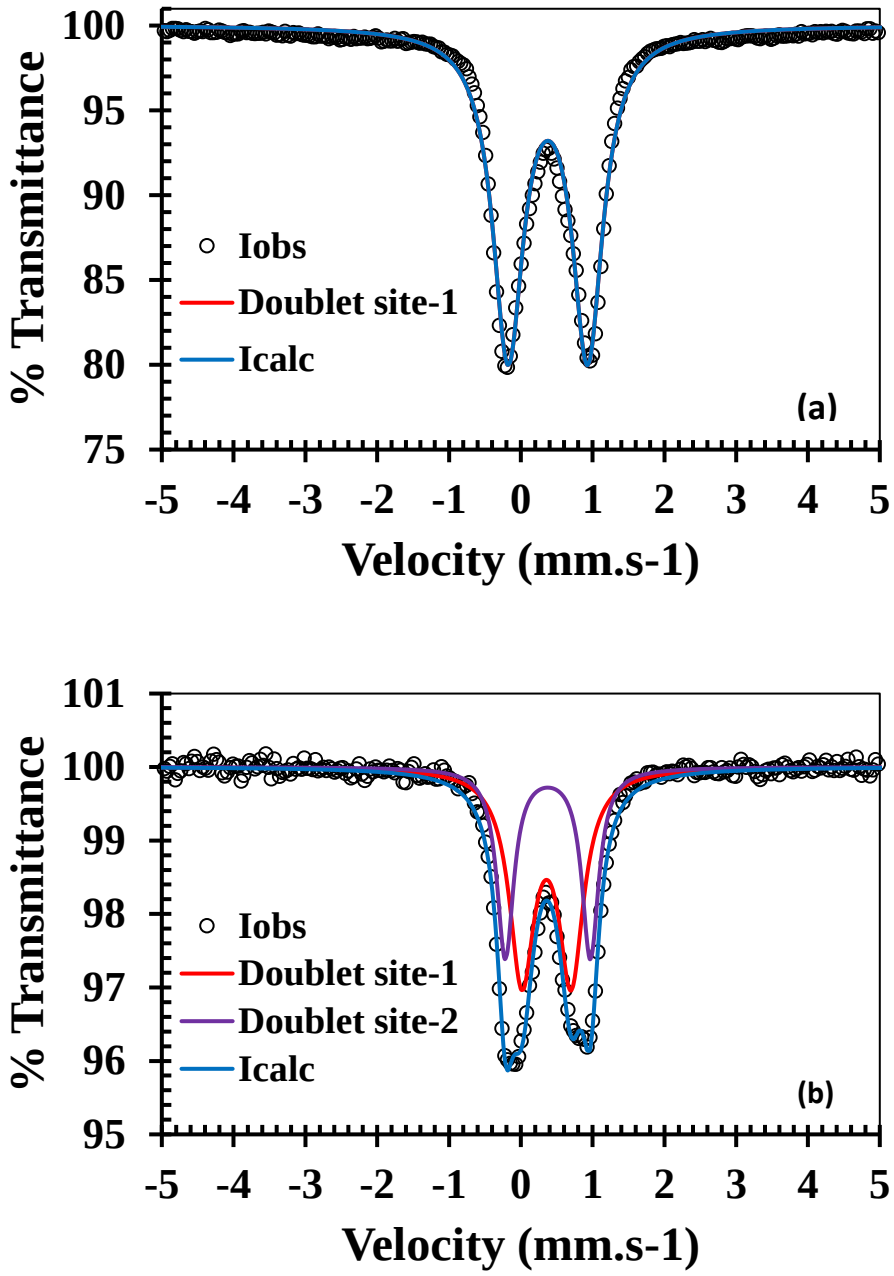

Figure S4. Mössbauer Spectra of Na-Jarosite(1) chemically reduced phase (a) and electrochemically reduced phase (b)

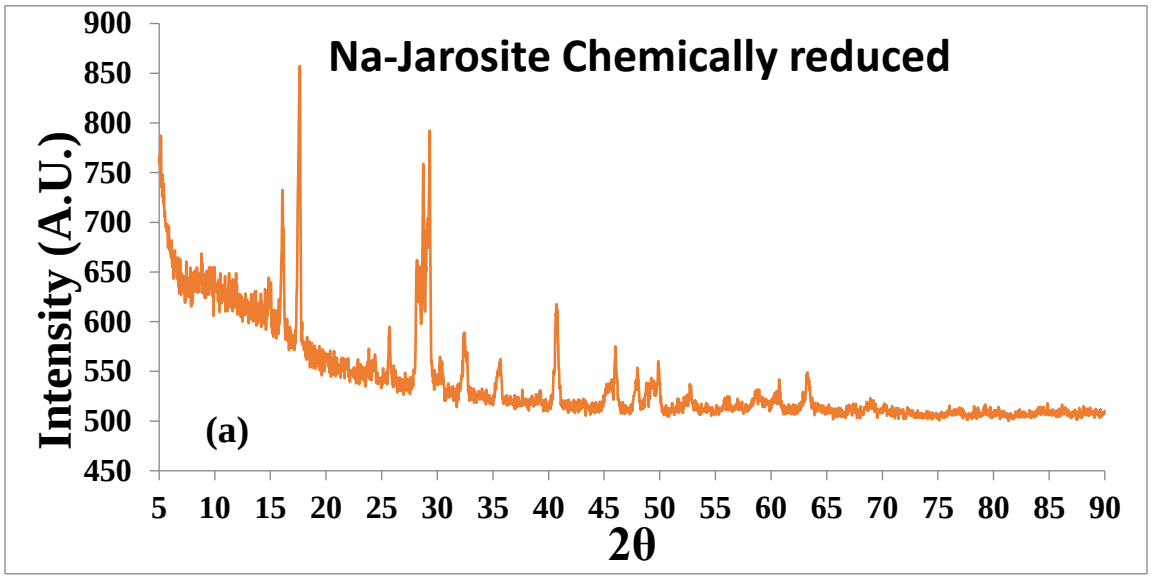

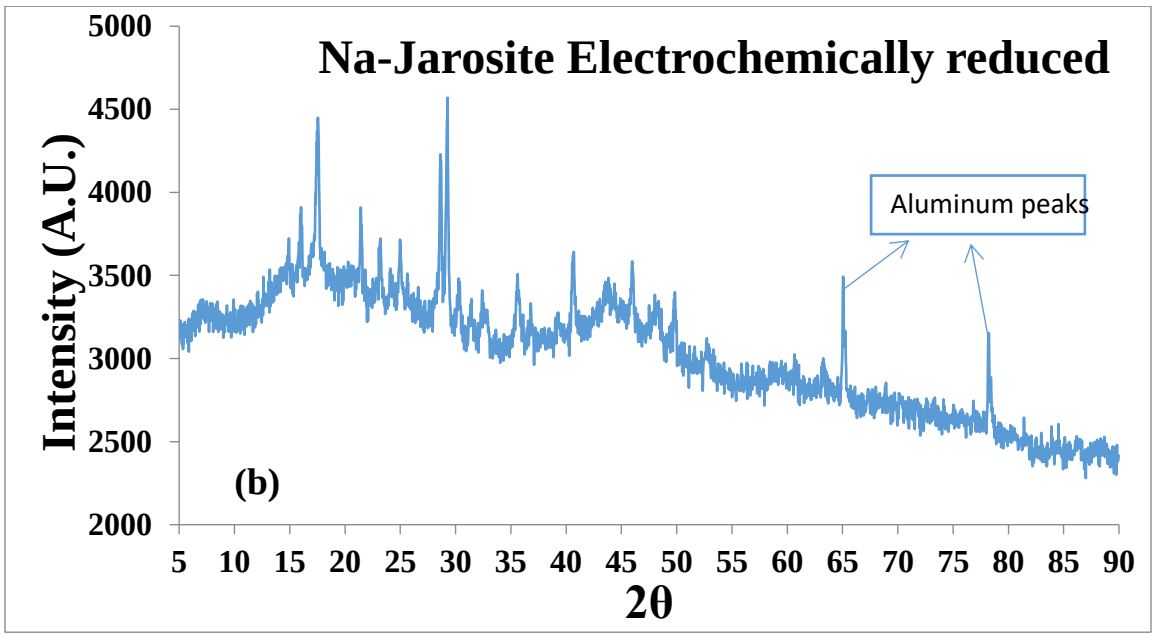

Figure S5. Powder patterns of Na-Jarosite(1) chemically reduced phase (a) and electrochemically reduced phase (b)

REFERENCES

1. M. S. Whittingham, Chem. Rev. 104 (2004) 4271-4302.

2. A. K. Padhi, V. Manivannan, J. B. Goodenough, J. Electrochem. Soc. 145 (1998) 1518-1520.

3. J. B. Goodenough, Y. Kim, Chem. Mater. 22 (2010) 587-603.

4. L. Ellis Brian, Lee Kyu Tae, Linda. F. Nazar, Chem. Mater. 22 (2010) 691-714.

5. M. E. Arroyo-de Dompablo, M. Armand, J. M. Tarascon, U. Amador, Electrochem. Commun. 8 (2006) 1292-1298.

6. J. B. Goodenough, V. Manivannan, Denki Kagaku 66 (1998) 1173-1181.

7. Yang Zhenguo, Zhang Jianlu, C. W. Kintner-Meyer Michael, Lu. Xiaochuan, Choi. Daiwon, J. P. Lemmon, Liu. Jun, Chem. Rev. 111 (2011) 3577-3613.

8. A. K. Padhi, V. Manivannan, J. B. Goodenough, J. Electrochem. Soc. 144 (1997) 1188-1194.

9. D. Larcher, L. Dupont, M. Morcrette, C. Wurm, P. Reale, C. Masquelier, J. Electrochem. Soc. 149 (2002) A1037-A1044.

10. M. Morcrette, C. Wurm, C. Masquelier, Solid State Sci. 4 (2002) 239-246.

11. T. N. Ramesh, K. T. Lee, B. L. Ellis, L. F. Nazar, Electrochem Solid St. 13 (2010) A43-A47.

12. H. Yaghoobnejad Asl, A. Choudhury, RSC Advances, 4 (2014) 37691-37700.

13. S. Nishimura, M. Nakamura, R. Natsui, A. Yamada, J. Am. Chem. Soc. 132 (2010) 13596-13597.

14. P. Barpanda, T. Ye, S. Nishimura, S. Chung, Y. Yamada, M. Okubo, H. Zhou, A. Yamada, Electrochem. Commun. 24 (2012) 116-119.

15. M. Tamaru, S. C. Chung, D. Schimizu, S. I. Nishimura, A. Yamada, Chem. Mater. 25 (2013) 2538-2543.

16. H. Yaghoobnejad Asl, K. Ghosh, M. Vidal Meza, A. Choudhury, J. Mater. Chem. A, 3 (2015) 7488-7497.

17. H. Yaghoobnejad Asl, A. Choudhury, Inorg. Chem., 54 (2015) 6566–6572.

18. G. Rousse, J. M. Tarascon, Chem. Mater. 26 (2014) 394-406.

19. V. Legagneur, Y. An, A. Mosbah, R. Portal, A. Le Gal La Salle, A. Verbaere, D. Guyomard , Y. Piffard, Solid State Ionics, 139 (2001) 37-46.

20. A. Yamada, N. Iwane, Y. Harada, S. Nishimura, Y. Koyama, I. Tanaka, Adv. Mater. 22 (2010) 3583-3587.

21. A. Nytén, A. Abouimrane, M. Armand, T. Gustafsson, J. Thomas, Electrochem. Commun. 7 (2005) 156-160.

22. C. Sirisopanaporn, C. Masquelier, P. Bruce, A. Armstrong, R. Dominko, J. Am. Chem. Soc. 133 (2011) 1263-1265.

23. H. Chen, G. Hautier, G. Ceder, J. Am. Chem. Soc. 134 (2012) 19619-19627.

24. W. Huang, J. Zhou, B. Li, J. Ma, S. Tao, D. Xia, W. Chu, Z. Wu, Scientific Reports, 4 (2014) art. no. 4188.

25. H. Kim, I. Park, D. Seo, S. Lee, S. Kim, W. Kwon, Y. Park, C. Kim, S. Jeon, K. Kang, J. Am. Chem. Soc. 134 (2012) 10369-10372.

26. H. Kim, I. Park, S. Lee, H. Kim, K. Park, Y. Park, H. Kim, J. Kim, H. Lim, W. Yoon, K. Kang, Chem. Mater. 25 (2013) 3614-3622.

27. A. Manthiram, J. B. Goodenough, J. Power Sources 26 (1989) 403-408.

28. M. Anji Reddy, V. Pralong, V. Caignaert, U. V. Varadaraju, B. J. Raveau, Electrochem. Commun. 11 (2009) 1807-1810.

29. L. Lander, M. Reynaud, G. Rousse, M. Sougrati, C. Laberty-Robert, R. Messinger, M. Deschamps, J. M. Tarascon, Chem. Mater. 26 (2014) 4178-4189.

30. P. Barpanda, G. Oyama, C. Ling, A. Yamada, Chem. Mater. 26 (2014) 1297-1299.

31. M. Reynaud, G. Rousse, A. Abakumov, M. Sougrati, G. Tendeloo, J. Chotard, J. M. Tarascon, J. Mater. Chem. A. 2 (2014) 2671-2680.

32. J. Ming, P. Barpanda, S. Nishimura, M. Okubo, A. Yamada, Electrochem. Commun. 51 (2015) 19-22.

33. N. Recham, J, N. Chotard, L. Dupont, C. Delacourt, W. Walker, M. Armand, J. M. Tarascon, Nat. Mater. 9 (2010) 68-74.

34. P. Barpanda, M. Ati, B. C. Melot, G. Rousse, J. N. Chotard, M. L. Doublet, M. T. Sougrati, S. A. Corr, J. C. Jumas, J.M. Tarascon, Nat. Mater.10 (2011) 772-779.

35. Gnanavel, M., Pralong, V., Lebedev, O., Caignaert, V., Bazin, P., Raveau, B. Chem. Mater. 2014, 26, 4521-4527.

36. Y. L. Ding, Y. Wen, P. A. Van Aken, J. Maier, Y. Yu, Chem. Mater. 27 (2015) 3143-3149.

37. C. Drouet, A. Navrotsky, Geochim. Cosmochim. Acta 67 (2003) 2063-2076.

38. J. E. Dutrizac, J.L. Jambor, Jarosites and their application in hydrometallurgy. (2000) Pp. 405-452 in: Sulfate Minerals _ Crystallography, Geochemistry, and Environmental Significance (C.N. Alpers, J.L. Jambor and D.K. Nordstrom, editors). Reviews in Mineralogy and Geochemistry, 40. Mineralogical Society of America,Washington D.C.

39. K. Kovacs, E. Kuzmann, Z. Homonnay, A. Vertes, L. Gunneriusson, A. Sandstrom, Hyperfine Interact. 186 (2008) 69-73.

40. Bruker, SMART, Bruker AXS Inc., Madison, Wisconsin, USA, 2002.

41. Bruker, SAINT and SADABS, Bruker AXS Inc., Madison, Wisconsin, USA, 2008.

42. G. M. Sheldrick, Acta Crystallogr., Sect. A: Found. Crystallogr. 64 (2008) 112–122.

43. K. Lagarec, D.G. Rancourt, Nucl. Instrum. Methods Phys. Res. Sect. B. 129 (1997) 266-280.

44. J. E. Dutrizac, Metal. Trans. B 14 (1983) 531-539.

45. L. C. Basciano, R. C. Peterson, Am. Mineral. 93 (2008) 853-862.

46. L. C. Basciano,, R. C. Peterson, Mineral. Mag. 71 (2007) 427–441.

47. R. Frost, R. Wills, W. Martens, M. Weier, Spectrochim. Acta 62 (2005) 869-874.

48. R. Frost, D. Wain, B. Reddy, W. Martens, J. Martinez-Frias, F. J. Rull, Near Infrared Spectrosc. 14 (2006) 167–178.

49. D. Pfannes, U. Gonser, Appl. Phys. 1 (1973) 93- 102.

50. M. Takano, T. Shinjo, M. Kiyama, T. Takada, J. Phys. Soc. Japan 25 (1968) 902.

51. A. Leclerc, Phys. Chem. Minerals 6 (1980) 327-334.

52. B. L. Ellis, T. N. Ramesh, W. N. Rowan-Weetaluktuk, D. H. Ryan, L. F. Nazar, J. Mater. Chem. 22 (2012) 4759 - 4766.

II. SOFT CHEMICAL ROUTES TO NEW IRON PHOSPHATES AND THEIR ELECTROCHEMICAL PROPERTIES

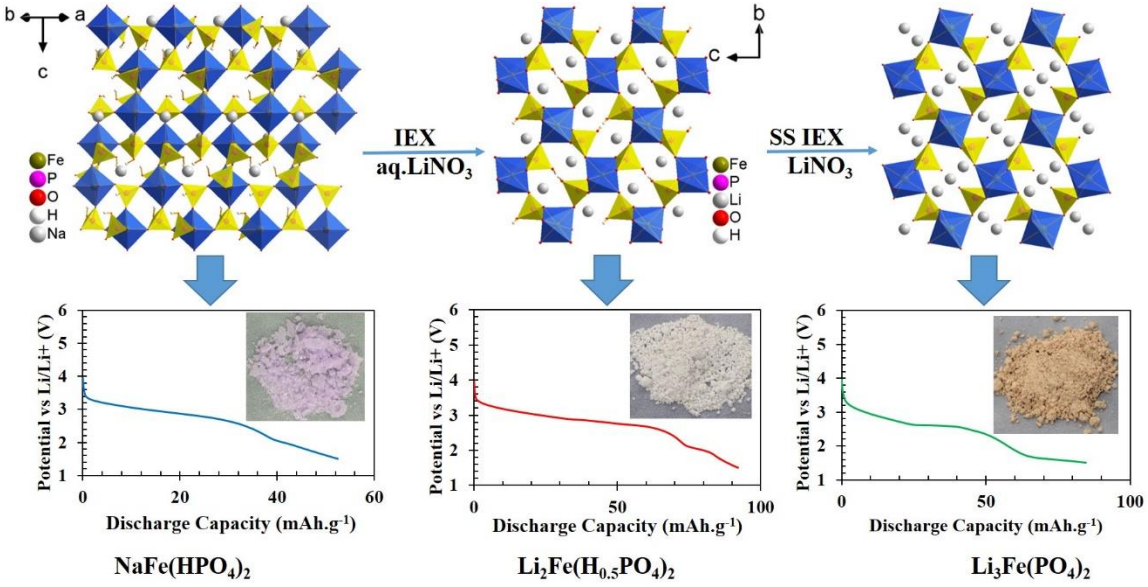

Prashanth Sandineni[a], Hooman Yaghoobnejad Asl[a], Nikolay Gerasimchuk[b], Kartik Ghosh[c], and Amitava Choudhury[a,*]

[a]Department of Chemistry, Missouri University of Science and Technology, Rolla, MO 65409, USA.

[b]Department of Chemistry, Missouri State University, Springfield, MO 65897, USA

[c]Department of Physics, Astronomy and Materials Science and Center for Applied Science and Engineering, Missouri State University, Springfield, Missouri 65897, USA.

ABSTRACT

New iron phosphates with related structures have been synthesized using hydrothermal and ion-exchange routes and their electrochemical properties were investigated. First, $NaFe(HPO_4)_2$ was synthesized employing hydrothermal route and its structure was determined from single-crystal X-ray diffraction data. Subsequent Na^+ and partial proton ion-exchange with Li^+ ion produced a known phase, $Li_2Fe(H_{0.5}PO_4)_2$, and complete deprotonation of $Li_2Fe(H_{0.5}PO_4)_2$ with Li^+ by employing solid-state ion-exchange route produced a new phase $Li_3Fe(PO_4)_2$. The structure of the latter was solved from synchrotron powder X-ray data by employing *ab initio* methods. All these phases are highly crystalline, built up of similar connectivities between FeO_6 octahedra and PO_4 tetrahedral units. Magnetic susceptibility measurements and room temperature ^{57}Fe Mössbauer spectroscopic studies confirm 3+ oxidation state of the compounds and their anti-ferromagnetic ordering with $Li_2Fe(H_{0.5}PO_4)_2$ showing some interesting metamagnetic behavior. The compounds are stable up to 400° C and undergo facile electrochemical lithium/sodium insertion through the reduction of Fe^{3+} to Fe^{2+}. Galvanostatic charge-discharge studies indicate that up to 0.6 lithium ions and 0.5 sodium ions per formula unit can be inserted at an average voltage of 3.0 V and 2.75 V for lithium and sodium ion batteries, respectively, for $NaFe(HPO_4)_2$. The partial Li-ion exchanged compound, $Li_2Fe(H_{0.5}PO_4)_2$, showed better cycle-life and experimental achievable capacities up to 0.9 Li insertion with strong dependence on particle size. The electrochemical Li-insertion in $Li_3Fe(PO_4)_2$ was also investigated. The electrochemistry of these three related phases were compared with each other and correlated with their structures.

1. INTRODUCTION

Since the discovery of olivine $LiFePO_4$ as a viable cathode for lithium ion batteries,[1] iron phosphates are being extensively investigated as electrode materials for lithium- and sodium ion batteries due to their structural diversity and increased operating voltage by virtue of the inductive effect of the phosphate moiety.[2, 3] Phosphate tetrahedra and FeO_n (n = 4, 5, and 6) polyhedra can connect in numerous ways resulting in stable frameworks capable of hosting guest molecules. These guest molecules are often charge-balancing cations, organo-ammonium or alkali ions, and can also be used as a template to further direct the structure of iron-phosphate frameworks.[4-7] In the case of alkali-ion-templated structures, it may create amenable pathways such as channels or interlayer space for facile movement of ions as in classic NASICON-type structures.[8] Besides structural diversity, high abundance, low-cost, low toxicity of iron also make it very lucrative for developing iron phosphates as cathodes for Li- and Na-ion batteries. Most of the known structures of iron phosphates have been tested as electrodes for Li- or Na-ion batteries. These include NASICON type $Li_3Fe_2(PO_4)_3$,[9] lipscombite type $Fe_{1.18}(PO_4)(OH)$,[10, 11] other hydroxy-phosphate phases ($Fe_5(PO_4)_4(OH)_3 \cdot 2H_2O$),[12] tavorite type $LiFePO_4(OH)_{(1-x)}F_x$,[13-16] fluoro-phosphates (Na_2FePO_4F and $LiNaFePO_4F$),[17, 18] various hydrated phosphates,[19-22] pyro-phosphates ($LiFeP_2O_7$,[23] $Li_2FeP_2O_7$,[24] $Na_2FeP_2O_7$[25]) and some mixed polyanions consisting of phosphate and another polyanion, phosphate-pyrophosphate, e.g. $Na_4Fe_3(PO_4)_2(P_2O_7)$,[26] phosphate-carbonates,[27] phosphate-nitrate[28] and boro-phosphates.[29, 30] Besides these, a large number of phosphates and mixed-polyanion in combination with phosphates in known structure-types have been theoretically predicted

as potential cathode for Li-ion batteries.[31-33] Further development of a low-cost non-toxic electrode is thwarted due to lack of known materials in iron phosphate families. A large number of iron phosphates have been discovered in recent years using organo-ammonium cations but they are not very useful for battery applications since the organic cation occupy large volume of space in the structure and form strong hydrogen bonding with the framework oxygen making it impossible to exchange with smaller alkali ions.[4-6] Therefore, synthesis in presence of alkali ions remains a viable option to discover new iron phosphates. One can target certain compositions based on common knowledge or chemical intuition and attempt to synthesize them via high temperature solid-state synthesis route taking stoichiometric ratios of reactants. However, without a prior knowledge of the thermodynamic stability of the target phases such attempts often lead to formation of already known stable phase(s). On the other hand *chimie douce* or soft-chemical routes, for example, hydrothermal, low-melting flux, or ion-exchange can be employed to synthesize metastable phosphate phases.[34] There are several advantages of the *chimie douce* methods with respect to the number of variations of parameters (pH, temperature, solvent, etc.) that can be played upon while targeting new phases for synthesis. For example, recently we have demonstrated the synthesis of a highly fluorinated iron phosphate employing a low melting fluoride flux.[35] On the other hand, pH can be varied by controlling the amount of phosphoric acid or by the addition of a secondary modulating acid or by varying the amount of base, alkali metal hydroxide. Often highly acidic synthetic conditions result into crystallization of phases containing the protonated phosphates or hydrogen phosphate phases with or without incorporating alkali ions into the structure.[36] These protonated phosphates are important for further discovery of new phases through ion-exchange of

alkali ions and protons. Exploring such chemistry in iron phosphate families has far more implications since it can directly aid in discovering new phases with other transition metals bearing similarity of chemistry with iron. While exploring similar chemistry of iron hydrogen phosphate synthesis under highly acidic conditions Redrup and Weller synthesized $(NH_4)_3Fe_3(HPO_4)_6$ and predicted that successive ion-exchange of ammonium ions and protons could lead to synthesis of $Li_3Fe_3(HPO_4)_6$ and $Li_9Fe_3(PO_4)_6$, respectively, which were predicted to be potential cathode materials for Li-ion batteries.[36] In this article we are reporting synthesis of sodium iron hydrogen phosphate, $NaFe(HPO_4)_2$, by hydrothermal synthesis and its successful transformation to lithiated phases, $Li_2Fe(H_{0.5}PO_4)_2$[37] and $Li_3Fe(PO_4)_2$ *via* ion-exchange of Na^+ and protons by Li^+, thus demonstrating the versatility of soft chemical routes in discovering new and predicted phases. Detailed investigation of their structures employing single-crystal and synchrotron powder X-ray diffraction, ^{57}Fe Mössbauer spectroscopy and magnetic measurements are reported here along with their electrochemical activities with respect to lithium and sodium ion insertions and concomitant change in structures due to alkali ion insertions.

2. EXPERIMENTAL

2.1. MATERIALS

All the chemicals used in the syntheses were as purchased and without further purification. $FeSO_4 \cdot 7H_2O$, H_3PO_4 (85%), H_3BO_3 (Reagent grade) and $Fe(NO_3)_3 \cdot 9H_2O$ were purchased from Fischer Scientific. $LiOH \cdot H_2O$ (Reagent grade) and $LiNO_3$ (99%

anhydrous) were purchased from Strem chemicals and Alfa Aesar, respectively; NaF (99%, Reagent grade) and H_3PO_3 (98%, extra pure) were purchased from Aldrich.

2.2. SYNTHESIS

$NaFe(HPO_4)_2$ was synthesized hydrothermally from a mixture of 0.278 g of $FeSO_4 \cdot 7H_2O$ (1 mmol), 0.412 g of H_3BO_3 (6.66 mmol), 1.2597 g of NaF (30 mmol) and 3.1 ml of H_3PO_4 (45 mmol) in 5 ml of H_2O in a 23 ml capacity Teflon-lined stainless steel Paar acid digestion bomb. The reactants were first dissolved in 5 ml of water with constant stirring in a Teflon beaker covered with a lid, which was then placed in the steel autoclave, sealed tightly, and placed in a 185°C pre-heated oven. The autoclave was heated for 24 hours, followed by cooling down naturally to room temperature. The product of the reaction consisted of pink colored crystals, which was then filtered and washed with hot water, followed by drying in air at room temperature. A good quality crystal was selected for single-crystal X-ray diffraction study. It is to be noted here that the identity of the product does not change even if the hydrothermal reaction was carried out for six days or about a month. The product yield was 67% with respect to Fe.

$Li_2Fe(H_{0.5}PO_4)_2$-IEX has been synthesized following ion-exchange of the as-synthesized $NaFe(HPO_4)_2$ sample. 0.500 g (1.85 mmol) of finely ground $NaFe(HPO_4)_2$ was mixed with 1.2756 g (18.5 mmol) of $LiNO_3$ in water and stirred continuously for 48 hours at 75°C, which produced off white product which was then filtered and washed with excess of hot water in order to remove excess $LiNO_3$ used in the reaction, followed by drying in air at room temperature. The product yield was 74% with respect to Fe and has $FePO_4 \cdot 2H_2O$ as an impurity phase (*vide infra*, Figure 1).

$Li_2Fe(H_{0.5}PO_4)_2$-HT has been synthesized in pure phase employing hydrothermal route by mixing 2.0239 g (5 mmol) of $Fe(NO_3)_3 \cdot 9H_2O$, 0.6932 g (15 mmol) of $LiOH \cdot H_2O$, 1.257 g (15 mmol) of H_3PO_3, sealed tightly in a Teflon bomb. The bomb was then placed in an oven at 175°C for 6 days, followed by cooling down to room temperature produced white microcrystalline product which was then filtered and washed with hot water, followed by drying in air at room temperature. The product yield was 70% with respect to Fe.

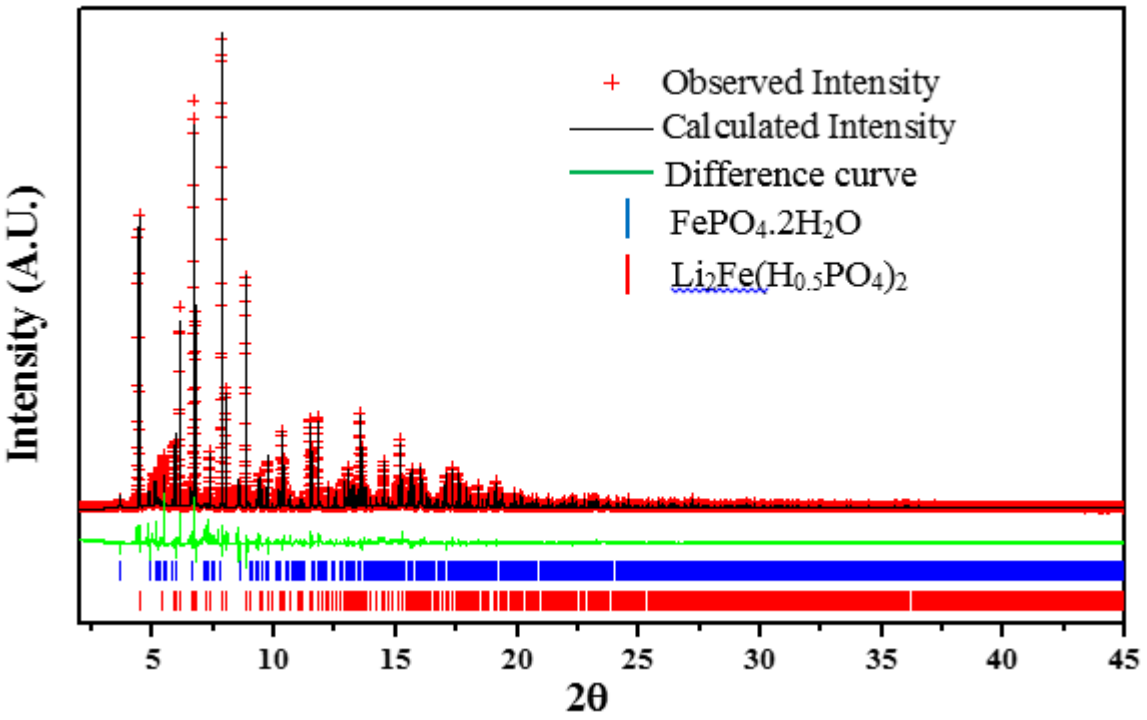

Figure 1. Rietveld refinement of synchrotron XRD data of $Li_2Fe(H_{0.5}PO_4)_2$-IEX showing the observed, calculated and difference curve. (λ = 0.41458Å, Rw = 15.578%)

$Li_3Fe(PO_4)_2$ was synthesized by the solid state ion exchange of $Li_2Fe(H_{0.5}PO_4)_2$-HT with $LiNO_3$. 1:10 molar ratio of $Li_2Fe(H_{0.5}PO_4)_2$-HT and $LiNO_3$ with a total amount of

~2g were taken in a agate mortar, ground together to make an intimate mixture and pressed into a pellet, which was then heated to 215°C for 3 days in air and cooled down to room temperature, produced light yellow colored product which was then filtered and washed with excess of hot water in order to remove excess $LiNO_3$ used in the reaction, followed by drying in air at room temperature. The product yield was 91% with respect to Fe.

Phase purity of all the samples were determined by laboratory and synchrotron powder X-ray diffraction (PXRD) data (discussed later).

2.3. MATERIAL CHARACTERIZATION

2.3.1. Single-Crystal X-ray Diffraction. The crystal structure of $NaFe(HPO_4)_2$ and $Li_2Fe(H_{0.5}PO_4)_2$-HT were solved from single-crystal intensity data sets collected on Bruker APEX II and Bruker Smart Apex diffractometer with monochromated Mo K_α radiation (0.7107 Å). Suitable crystals were selected and mounted on a glass fiber using epoxy-based glue. The data sets were collected using APEX II[38] and SMART[39] software at room temperature employing a scan of 0.3° in ω with an exposure time of 20 s per frame. The cell refinement and data reduction were carried out with SAINT,[40] while the program SADABS[40] was used for the absorption correction. The structures were solved by direct methods using SHELX-97 and difference Fourier syntheses.[41] Full-matrix least-squares refinement against $|F^2|$ was carried out using the SHELXTL-PLUS suit of programs.[41] Finally both structures were refined with SHELX-2014 using SHELXle.[42] The structures of $NaFe(HPO_4)_2$ and $Li_2Fe(H_{0.5}PO_4)_2$-HT crystallized in monoclinic crystal system and solved in Cc and $P2_1/n$ space group, respectively. However, before the final refinement the space group of $Li_2Fe(H_{0.5}PO_4)_2$-HT was transformed from $P2_1/n$ to $P2_1/c$ and refined again.

Details of final refinements and cell parameters of $NaFe(HPO_4)_2$ and $Li_2Fe(H_{0.5}PO_4)_2$-HT are given in Table 1. Final atomic coordinates and isotropic displacement parameters are given in Tables S1 and S2. Selected bond lengths are given in Tables 2 and 3.

Table 1. Crystal data and structure refinement for $NaFe(HPO_4)_2$ and $Li_2Fe(H_{0.5}PO_4)_2$-HT.

Emperical formula	$NaFe(HPO_4)_2$	$Li_2Fe(H_{0.5}PO_4)_2$-HT
Formula weight	270.80 g mol^{-1}	260.68 g mol^{-1}
Crystal system	Monoclinic	monoclinic
Space Group	*Cc*	$P2_1/c$
a	8.4320(9) Å	4.8239(9) Å
b	9.6941(10) Å	7.9988(15) Å
c	22.109(2) Å	7.8407(17) Å
$\alpha = \gamma$	90°	90°
β	90.231(10)°	112.315(2)°
Volume	1807.2(3) $Å^3$	279.88(10) $Å^3$
Z	12	2
ρ_{calc}	2.986 g cm^{-3}	3.093 g cm^{-3}
F(000)	1596	254
Temperature	120(2) K	296(2) K
GOF on F^2	1.128	1.147
R factors [I>2sigma(I)][a]	$R_1 = 0.0288$, $wR_2 = 0.0634$	$R_1 = 0.0241$, $wR_2 = 0.0654$
R factors [all data][b]	$R_1 = 0.0338$, $wR_2 = 0.0690$	$R_1 = 0.0273$, $wR_2 = 0.0663$

[a]$R_1 = \Sigma \, ||F_o| - |F_c| \, / \, \Sigma \, |F_o|$. [b]$wR_2 = \{\Sigma \, [w(F_o^2 - F_c^2)^2] \, / \, \Sigma \, [w(F_o^2)^2]\}^{1/2}$, $w = 1/[\sigma^2(F_o)^2 + (aP)^2 + bP]$, where $P = [F_o^2 + 2F_c^2]/3$.

Table 2. Selected bond lengths for Fe- and Na-centered polyhedral and their bond valence sum values for $NaFe(HPO_4)_2$.

Atom – Atom	*d* (Å)	Atom – Atom	*d* (Å)	Atom – Atom	*d* (Å)
Fe1 – O9	1.960(5)	Fe2 – O3	1.981(5)	Fe3 – O17	1.958(5)
Fe1 – O7$^{\#1}$	1.984(5)	Fe2 – O19	1.981(5)	Fe3 – O13	1.961(5)
Fe1 – O5	1.990(5)	Fe2 – O18	2.016(5)	Fe3 – O1	1.979(5)
Fe1 – O23	1.994(5)	Fe2 – O21	2.025(5)	Fe3 – O14$^{\#4}$	1.993(5)
Fe1 – O15	1.997(5)	Fe2 – O11	2.030(5)	Fe3 – O 6$^{\#5}$	2.025(5)
Fe1 – O10$^{\#2}$	2.065(5)	Fe2 – O22	2.047(5)	Fe3 – O2$^{\#6}$	2.067(5)
BVS sum, Fe1 = 3.16		BVS sum, Fe2 = 3.02		BVS sum, Fe3 = 3.16	
Na1 – O5	2.605(5)	Na2 – O7$^{\#5}$	2.272(6)	Na3 – O14$^{\#8}$	2.241(6)
Na1 – O8	2.468(5)	Na2 – O6$^{\#10}$	2.300(6)	Na3 – O15$^{\#4}$	2.278(5)
Na1 – O20	2.340(5)	Na2 – O12$^{\#10}$	2.517(6)	Na3 – O4$^{\#9}$	2.396(6)
Na1 – O23	2.346(5)	Na2 – O10$^{\#11}$	2.743(6)	Na3 – O2$^{\#12}$	2.628(6)
Na1 – O24	2.258(5)	Na2 – O5$^{\#5}$	2.828(6)	Na3 – O13$^{\#8}$	2.906(6)
Na1 – O12$^{\#2}$	2.505(6)	Na2 – O2	2.426(6)	Na3 – O10	2.533(6)
Na1 – O21$^{\#2}$	2.637(5)				
BVS sum, Na1 = 1.17		BVS sum, Na2 = 0.92		BVS sum, Na3 = 0.97	

Symmetry transformations used to generate equivalent atoms:

$^{\#1}$ x + 1/2, y + 1/2, z; $^{\#2}$ x + 1/2, y - 1/2, z; $^{\#4}$ x - 1/2, y + 1/2, z; $^{\#5}$x, -y + 1, z - ½; $^{\#6}$x - 1/2, y - 1/2, z; $^{\#8}$x, -y + 1, z + ½; $^{\#9}$x - 1/2, -y + 3/2, z + ½; $^{\#10}$x + 1/2, -y + 3/2, z - ½; $^{\#11}$x, -y + 2, z - ½; $^{\#12}$x, -y + 2, z + 1/2

Table 3. Selected bond lengths and bond valence sum values of Fe and Li in $Li_2Fe(H_{0.5}PO_4)_2$-HT.

Atom – Atom	*d* (Å)	Atom – Atom	*d* (Å)
Fe1 – O3$^{\#1}$	1.9725(16)	Li1 – O1	1.948(2)
Fe1 – O 3$^{\#2}$	1.9725(16)	Li1 – O4$^{\#7}$	1.970(4)
Fe1 – O2$^{\#3}$	2.0094(16)	Li1 – O3$^{\#8}$	1.986(4)
Fe1 – O2$^{\#4}$	2.0094(16)	Li1 – O2$^{\#9}$	2.062(2)
Fe1 – O1$^{\#5}$	2.0407(16)	Li1 – O4$^{\#10}$	2.347(3)
Fe1 – O1$^{\#6}$	2.0407(16)	Li1 – O3	2.871(5)
BVS, Fe1= 3.07		BVS, Li1 = 1.09	

$^{\#1}$1-x, -0.5+y, 0.5-z; $^{\#2}$-1+x, 0.5-y, -0.5+z; $^{\#3}$1-x, 1-y, 1-z; $^{\#4}$-1+x, -1+y, -1+z; $^{\#5}$x, 0.5-y, -0.5+z; $^{\#6}$-x, -0.5+y, 0.5-z; $^{\#7}$-1+x, 1.5-y, -0.5+z; $^{\#8}$1-x, 0.5+y, 1.5-z; $^{\#9}$-1+x, y, z; $^{\#10}$1-x, 0.5+y, 1.5-z;

2.3.2. Powder X-ray Diffraction (PXRD). Both laboratory and synchrotron powder X-ray diffraction have been used to evaluate the phase purity, quantitative phase analysis by Rietveld refinement, and *ab initio* structure solution. The laboratory PXRD pattern was obtained from a PANalytical X'Pert Pro diffractometer equipped with a Cu $K_{\alpha1,2}$ anode and a linear array PIXcel detector over a 2θ range of 5 to 90° with an average scanning rate of 0.0472°s^{-1}. Phase purity of samples, $NaFe(HPO_4)_2$ and $Li_2Fe(H_{0.5}PO_4)_2$-HT were evaluated by Rietveld refinement of laboratory PXRD, which indicated absence of any impurity line (Figure S1). Rietveld refinement of the synchrotron PXRD data of $Li_2Fe(H_{0.5}PO_4)_2$-IEX sample has been used to determine the fraction of the known impurity phase, $FePO_4{\cdot}2H_2O$ (monoclinic, unit cell dimensions: a = 5.335(5), b = 9.808(12), c =

8.720(7)Å, β = 90.54(5)°) (Figure 1).[19 - 21] For the solid state ion-exchanged sample, $Li_3Fe(PO_4)_2$, the acquired synchrotron PXRD data were used for structure solution by *ab initio* method followed by Rietveld refinement. Synchrotron data for $Li_2Fe(H_{0.5}PO_4)_2$-IEX and $Li_3Fe(PO_4)_2$ were collected from beamline, 11-BM, of Advanced Photon Source (APS) of Argonne National Laboratory (ANL). The powder pattern was collected in a kapton capillary under ambient conditions using a parallel monochromated X-ray beam with a calibrated wavelength of 0.41458Å over the Bragg angle range of 0.5 - 50°. The PXRD of $Li_3Fe(PO_4)_2$ was indexed in $P2_1/n$, intensities were extracted by Lebail method and atomic coordinates were found using Monte Carlo simulation embedded in FOX software.[43] The harvested atomic coordinates were then transformed into $P2_1/c$ cell setting and a Rietveld refinement was performed employing GSAS-II.[44] The lower final residuals from Rietveld refinement, chemically sensible geometrical parameters, bond-valence sum values, results from magnetic measurements and ^{57}Fe Mösssbauer spectroscopy indicated correctness of the model. A plot of Rietveld refinement of $Li_3Fe(PO_4)_2$ showing the excellent matching between the observed and calculated PXRD patterns is given in Figure 2. The details of refinement results and cell parameters of $Li_2Fe(H_{0.5}PO_4)_2$-IEX and $Li_3Fe(PO_4)_2$ are given in Table 4. Atomic coordinates and selected bond lengths along with their bond valence sum values of $Li_3Fe(PO_4)_2$ are given in Tables 5 and 6, respectively.

2.3.3. Mössbauer Spectroscopy. ^{57}Fe Mössbauer experiments were performed in transmission geometry at room temperature using a conventional constant acceleration spectrometer. The data were collected using a ^{57}Co (25 mCi) gamma-ray source embedded in a Rh matrix. Velocity calibration and isomer shifts are given with respect to α-Fe foil at

room temperature. The Mössbauer data were analyzed by Lorentzian line fitting using RECOIL software.[45]

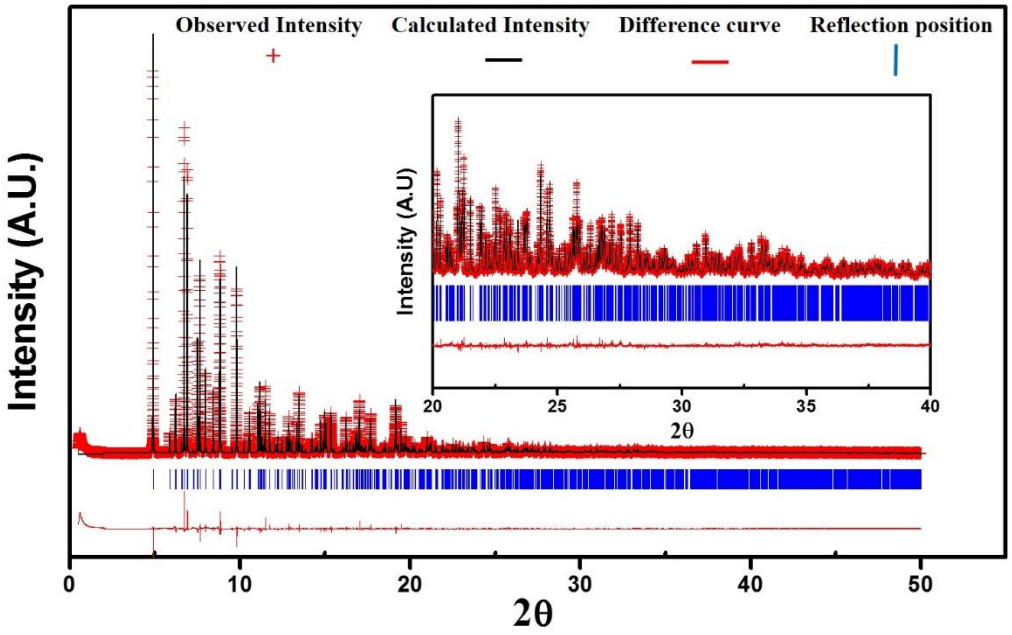

Figure 2. Rietveld refinement of synchrotron XRD data of $Li_3Fe(PO_4)_2$ showing the observed, calculated and difference curve. (λ = 0.41458Å, Rw = 10.717%). Inset shows enlarged view of segment from 2Θ = 20 to 40.

2.3.4. Magnetic Measurements. The variable temperature magnetic susceptibility measurements of the compounds (as-prepared) were carried out in the temperature range 2 – 300 K for $NaFe(HPO_4)_2$ and $Li_2Fe(H_{0.5}PO_4)_2$-IEX while 5 – 300 K for $Li_2Fe(H_{0.5}PO_4)_2$-HT and $Li_3Fe(PO_4)_2$ using Quantum Design SQUID magnetometer at 1T applied field while warming up under zero-field cooled (ZFC) conditions. Low applied field (0.05 T) ZFC and FC data sets were also collected while warming up over the temperature range from 5 – 50 K for $Li_2Fe(H_{0.5}PO_4)_2$-HT. Isothermal M-H data sets were collected at

increasing field from 0 to 5 T at 2 K for $NaFe(HPO_4)_2$ and $Li_2Fe(H_{0.5}PO_4)_2$-IEX, 5 K for $Li_3Fe(PO_4)_2$ and at 5, 100 and 300 K for $Li_2Fe(H_{0.5}PO_4)_2$-HT.

Table 4. Refined lattice constants and final Rietveld refinement parameters from the synchrotron powder XRD of $Li_2Fe(H_{0.5}PO_4)_2$-IEX and $Li_3Fe(PO_4)_2$.

Parameter	$Li_2Fe(H_{0.5}PO_4)_2$-IEX	$Li_3Fe(PO_4)_2$
a	4.8244(5) Å	5.0601(11) Å
b	7.9938(4) Å	8.0092(4) Å
c	7.8400(5) Å	8.1709(4) Å
$\alpha = \gamma$	90°	90°
β	112.357(2)°	117.641(29)°
V	279.62(8) $Å^3$	293.35(28) $Å^3$
Crystal system	Monoclinic	Monoclinic
Space group	$P2_1/c$	$P2_1/c$
Number of reflections	1841	1914
R_w	15.578 %	10.717 %
R_f^2	6.953 %	7.851 %
Number of data points	42066	47996

2.3.5. Thermogravimetric Analysis (TGA) & Differential Scanning Calorimetry (DSC). TGA has been performed on all the samples with a TA instruments

Q50 TGA and DSC on $Li_3Fe(PO_4)_2$ TA instruments Q600 SDT from room temperature to 800°C with a scan rate of 10°C min^{-1} under nitrogen atmosphere.

2.3.6. IR Spectroscopy. The IR spectrum was collected using Thermo Nicolet Nexus 470 FT-IR spectrometer over 400–4000 cm^{-1} on a sample embedded in KBr pellet.

Table 5. Atomic coordinates (x 10^4) and equivalent isotropic displacement parameters ($Å^2x10^3$) for $Li_3Fe(PO_4)_2$. U(eq) is defined as one third of the trace of the orthogonalized Uij tensor.

Atom	**Wyck.**	**Site**	**x/a**	**y/b**	**z/c**	**U [$Å^2$]**
Fe1	2*a*	-1	0	0	0	0.006(6)
P1	4*e*	1	0.64735(12)	0.68346(7)	0.72630(7)	0.005(6)
O1	4*e*	1	0.30198(25)	0.69446(14)	0.61348(16)	0.004(6)
O2	4*e*	1	0.77672(26)	0.86241(13)	0.76283(16)	0.003(6)
O3	4*e*	1	0.77987(27)	0.59002(16)	0.61915(18)	0.012(6)
O4	4*e*	1	0.73898(26)	0.58689(15)	0.90415(17)	0.006(6)
Li1	2*d*	-1	1/2	0	1/2	0.032(6)
Li2	4*e*	1	0.0648(8)	0.8775(4)	0.6411(4)	0.011(6)

2.3.7. SEM. The morphology of the powder samples was studied by scanning electron microscopy (Hitachi S 4700 FESEM) at 15 kV operating voltage.

2.3.8. UV-Visible Spectroscopy. Diffuse reflectance spectra on powdered samples were collected using a Praying Mantis accessory on Cary 5000 UV-Vis-NIR spectrophotometer over 200-1500 nm range.

2.3.9. Electrochemical Testing. To test the electrochemical performance of the four samples, cathode films of the active materials were first made on a sheet of carbon-coated aluminum current collector (MTI). The active material was subjected to ball-milling thoroughly after mixing with super P conductive carbon in a SPEX 8000 miller for 3 hours to reduce the particle size. The ball-milled samples were tested for structural stability using PXRD, which indicated that there is no structural change before and after ball milling (Figure S2, SI). Further details of the coin cell fabrication and electrochemical test are given in SI.

3. RESULTS AND DISCUSSION

3.1. SYNTHESIS AND STRUCTURE

The syntheses methods reported here for all samples are low temperature hydrothermal routes and simple ion-exchange reactions. The aim was to synthesize new iron hydrogen phosphate stabilized by alkali ions, especially with slightly bigger alkali ions, for example sodium or potassium to enable access to further new phases through ion-exchange of proton and alkali ion by a different alkali ions. To synthesize iron phosphates with acidic phosphate groups (HPO_4 or H_2PO_4) it is very important to have acidic medium but under hydrothermal condition it becomes somewhat challenging to have very acidic conditions and avoid formation of a clear solution at the end of digestion period extending over 24 hrs. To crystallize solids under acidic condition often requires a balance of pH and ionic strength of solutions. For this purpose weak acids such as boric acid, acetic acid etc. can act as very good pH modulator. Our synthesis strategy of using boric acid as pH

modulator and NaF as source of Na has allowed maintaining required acidic pH and high ionic strength enabling crystal growth of pure $NaFe(HPO_4)_2$. We also note here that use of boric acid can lead to formation of boro-phosphates and presence of fluoride can lead to fluoride phosphates besides acting as mineralizers. However, in this case, there was no F or B incorporated into the structure, which was also confirmed from the EDS (Figure S3, SI). We have also verified the need of each of these reactants for stabilization and crystallization of $NaFe(HPO_4)_2$ phase. Changing the reactants or omission of pH modulator leads to different phases as shown in Table S3.

Our aim was to exchange the Na and the protons with lithium to form successively $LiFe(HPO_4)_2$, $Li_2Fe(H_{0.5}PO_4)_2$, and $Li_3Fe(PO_4)_2$. To accomplish this goal we performed solution-based ion-exchange in aqueous medium employing $LiNO_3$ as lithiating agent. After several hours of stirring at 75 °C a visible color change from pink to whitish powder was observed. The PXRD analysis of the 48 hours ion-exchanged product indicated presence of $Li_2Fe(H_{0.5}PO_4)_2$ (80%) and $FePO_4{\cdot}2H_2O$ (20 %), both of which are known phases.[37, 19 -21] Our efforts to stop the exchange process at an intermediate time to isolate $LiFe(HPO_4)_2$ or increase the time to form a completely exchanged product, $Li_3Fe(PO_4)_2$, were unsuccessful. It was realized that as soon as the exchange process starts it forms $Li_2Fe(H_{0.5}PO_4)_2$ without going through $LiFe(HPO_4)_2$, which may be because of the somewhat greater thermodynamic stability of di-lithiated phase and further exchange of the remaining proton was impeded in acidic aqueous medium due to an equilibrium between the proton concentration and lithium ions. When stirred for longer duration $Li_2Fe(H_{0.5}PO_4)_2$ hydrolyzes to form the hydrated $FePO_4$. Realizing that aqueous solution route may not be ideal to form the completely exchanged product, $Li_3Fe(PO_4)_2$, we resort

to solid state ion-exchange starting with pure phase of $Li_2Fe(H_{0.5}PO_4)_2$ synthesized employing phosphorous acid route. Though the synthesis of $Li_2Fe(H_{0.5}PO_4)_2$ has been reported but in our laboratory we could not reproduce a pure form of the compound following the reported procedure.[37] Solid state ion-exchange of $Li_2Fe(H_{0.5}PO_4)_2$ with $LiNO_3$ at 210 °C produced pure form of $Li_3Fe(PO_4)_2$, the structure of which was solved from synchrotron powder X-ray diffraction data and the position of the lithium atoms were determined accurately. The structures of $Li_2Fe(H_{0.5}PO_4)_2$ and $Li_3Fe(PO_4)_2$ are remarkably similar in which lithium ions replace the protons to form the latter. Our efforts to synthesize $LiFe(HPO_4)_2$ by simple ion-exchange of $NaFe(HPO_4)_2$ has so far been unsuccessful. The efforts of ion-exchange in non-aqueous medium (methanol) carried out under solvothermal conditions also did not lead to any exchange with Li^+. On the other hand solid state ion-exchange of Na^+ from $NaFe(HPO_4)_2$ with Li^+ by adding excess $LiNO_3$ in pressed pellet at 215 °C led to complete structural transformation to NASICON type $Li_3Fe_2(PO_4)_3$. The various ion-exchange trials are listed in Table S3.

Figure 3 shows the asymmetric units of $NaFe(HPO_4)_2$, $Li_2Fe(H_{0.5}PO_4)_2$, and $Li_3Fe(PO_4)_2$. The asymmetric unit of $NaFe(HPO_4)_2$ (Figure 3a) contains 36 non-hydrogen atoms including three Fe, six P and three Na and 24 oxygen atoms of which 6 are protonated. All these crystallographically distinct atoms occupy general position, 3*a*. All the Fe atoms are in octahedral coordination with some degree of distortion with Fe – O distances in the range 1.960(5) – 2.065(5), 1.981(5) – 2.047(4), and 1.958(5) – 2.067(5) Å, respectively for Fe1, Fe2, and Fe3. Thus change in Fe – O bond lengths around Fe centers range between 0.1 – 0.06 Å with highest being 0.109 in Fe3, followed by 0.105 in Fe1 and 0.066 Å in Fe2 environments. Similarly variation in the angles around metal centers range

~5°. Depiction of environment around each Fe centers highlighting the distortion are shown in orthogonal projections and perspective views in Figures S4 – S6. All the P atoms are in tetrahedral coordination with average P – O distances in the range 1.511(5) – 1.602(5) Å, invariably containing one long P – O bond with the protonated oxygen. There are three crystallographically different sodium atoms present in the structure and the coordination environment of each sodium is unique. Both Na2 and Na3 has 6-fold coordination and Na1 has 7-fold coordination and none of them conform to any regular polyhedral shape.

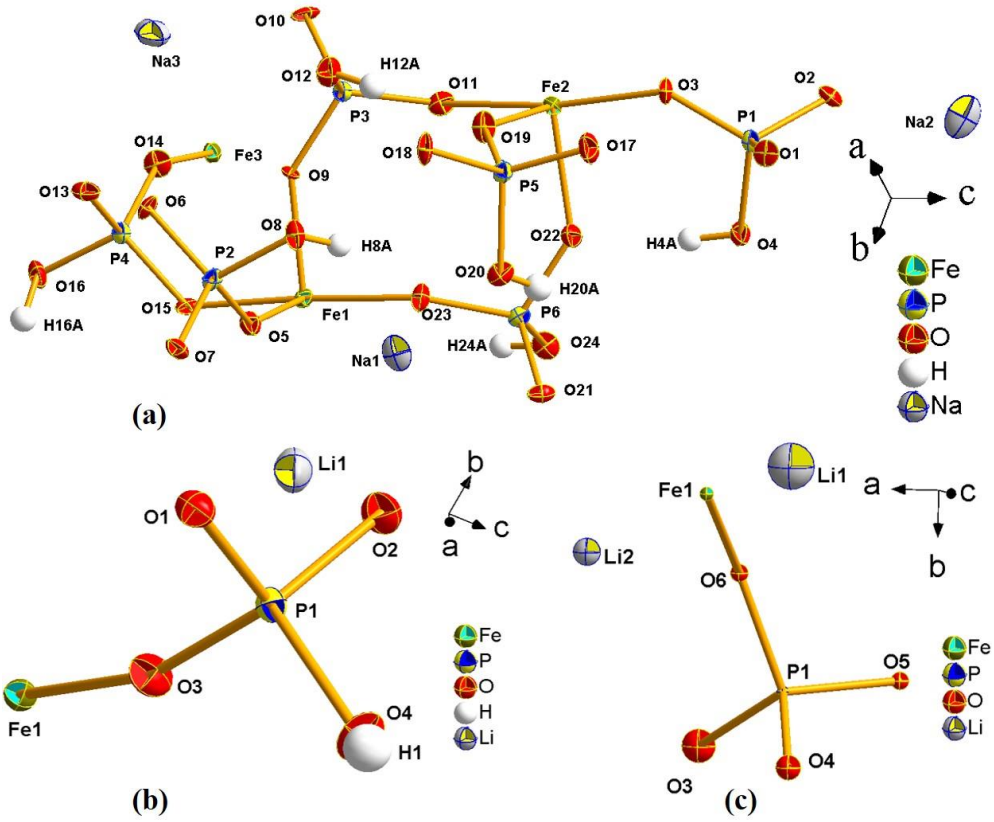

Figure 3. Asymmetric units of $NaFe(HPO_4)_2$ (a), $Li_2Fe(H_{0.5}PO_4)_2$ (b) and $Li_3Fe(PO_4)_2$ (c). Bonds with alkali ions have been removed for clarity. The thermal ellipsoids are given at 75 % probability. Note that for $Li_3Fe(PO_4)_2$ (c), atoms are only refined isotropically.

The Na – O distances are in the range 2.258(5) – 2.637(6), 2.272(6) – 2.828(6), and 2.241(6) – 2.906(6) Å for Na1, Na2, and Na3, respectively, with one of the Na – O distances (Na3 – O13) showing slightly longer than the average (2.906 Å). FeO_6 octahedra and PO_4 tetrahedra are alternatingly corner-shared to form a three-dimensional (3-D) structure with channels wherein reside the sodium ions. Each Fe atoms are connected to 6 phosphate groups through bridging Fe – O – P linkages; similarly each P atom is connected to three Fe atoms through bridging P – O – Fe linkages with one terminal protonated P – O bond with their protons (H4, H8, H12, H16, H20, H24) protruding into the cavities as shown in Figure 4a. On further inspection it revealed that each of the crystallographically distinct Fe atoms along with two crystallographically distinct P atoms form a slightly undulating layer containing exclusively 8-memberd ring (ring member is counted by connecting only Fe and P sites) through the alternate corner-sharing of FeO_6 octahedra and PO_4 tetrahedra (Figure 4a, left panel). Thus there are three such layers formed by Fe1, P2, and P3; Fe2, P5, and P6; and Fe3, P1, and P4 as indicated in Figure 4a, which are further cross-linked by the remaining P – O – Fe linkages along the *c*-axis. Cross-linking of 8-membered ring layers by the phosphates also create 8 and 4-membered ring channels when viewed along [5 5 0] direction. It is to be noted here that the 8-membered rings are not exactly on top of each other and rather they are shifted from one another preventing formation of 8-ring channel along the *c*-axis. However, the 8-membered rings are somewhat aligned when viewed along the [107] direction and forms a channel where all the sodium ions are located (Figure S7, SI). Recently isostructural vanadium analogue, $NaV(HPO_4)_2$ has been reported by zur Loye group.[46] Further literature survey reveals that there are few more examples of iron hydrogen phosphates templated by hydronium (H_3O^+)

or ammonium (NH_4^+) ions, but their anionic, $[Fe(HPO_4)_2]^{2-}$, frameworks are distinct from $NaFe(HPO_4)_2$. For example, $(NH_4)Fe(HPO_4)_2$ has two polymorphs both crystallize in triclinic crystal system with phosphate tetrahedra and FeO_6 octahedra alternately connected to create 8-membered ring channels along *a*- and *b*-axis in the former[47] and along all three crystallographic directions in the latter.[48] On the other hand the structure of $(H_3O)Fe(HPO_4)_2$ is built up of alternate corner-sharing of PO_4 and FeO_6 polyhedra forming a 3-D structure with a large 12-membered ring channel along the *a*-axis, which hosts the hydronium ions.[49] More importantly all the above known iron hydrogen phosphates are centrosymmetric while $NaFe(HPO_4)_2$ crystallizes in non-centrosymmetric space group, Cc, as can be judged by the lack of center of symmetry in the structure (Figure S8, SI).

The structure of $Li_2Fe(H_{0.5}PO_4)_2$ is known and has been adequately discussed in the literature with respect to iron and a recently published vanadium analogue.[37, 50] In this article our main objective is to see the similarities between $NaFe(HPO_4)_2$ and $Li_2Fe(H_{0.5}PO_4)_2$, the latter can be obtained by ion-exchange from the former. Similar to $NaFe(HPO_4)_2$, the structure of $Li_2Fe(H_{0.5}PO_4)_2$ is also built up of alternate corner-sharing of PO_4 tetrahedra and FeO_6 octahedra. Each FeO_6 octahedra is connected to six PO_4 tetrahedra through Fe – O – P linkages, similarly each PO_4 tetrahedra shares corner with three FeO_6 octahedra, leaving one terminal P – O – H bond. Similar to the parent structure ($NaFe(HPO_4)_2$), layers with 8-membered ring aperture can be discerned from $Li_2Fe(H_{0.5}PO_4)_2$, however, differences lie in the manner in which the layers are cross-linked. In $Li_2Fe(H_{0.5}PO_4)_2$ the layers are stacked and cross-linked along *a*-axis such that the 8-membered ring aperture is exactly aligned to form a channel wherein reside the lithium ions and protrude protons attached to the terminal P – OH bonds.

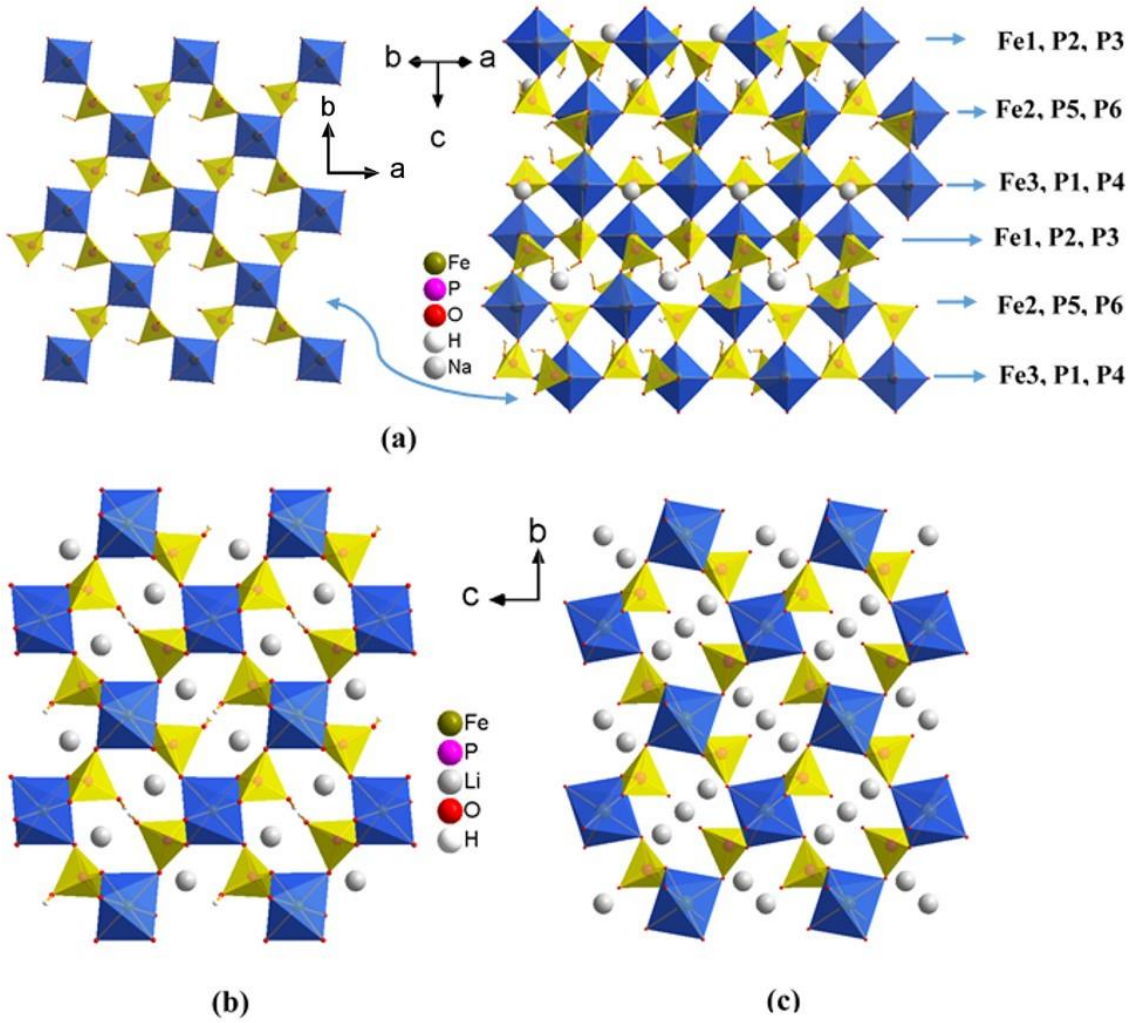

Figure 4. Perspective view of packing diagram for $NaFe(HPO_4)_2$ showing the cross-linking of layers (a); perspective view of structures of $Li_2Fe(H_{0.5}PO_4)_2$ (b) and $Li_3Fe(PO_4)_2$ (c) along *a*-axis.

On the other hand 8-member rings are shifted in the direction of stacking and channels containing the sodium can be observed at an angle from *c*-axis (compare Figure 4b with Figure 4a). The occupancy of protons are also different in these two structures, in $Li_2Fe(H_{0.5}PO_4)_2$ the occupancy of the hydrogen atom has been refined to be at 50%. Two such hydrogen atoms face each other in the channel with an apparent short contact

(0.957(5) Å) due to the disorder (partial occupancy of 50 %) while in $NaFe(HPO_4)_2$ all the protons are fully occupied. Thus we can say that one sodium ion and one of the protons can be exchanged from $NaFe(HPO_4)_2$ with lithium ions, $NaFe(HPO_4)_2 + 2LiNO_3 \rightarrow Li_2Fe(H_{0.5}PO_4)_2 + NaNO_3 + HNO_3$, to produce $Li_2Fe(H_{0.5}PO_4)_2$ in a topotactic manner considering the structural similarity. The protons protruding into the 8-membered channel of $Li_2Fe(H_{0.5}PO_4)$ were further exchanged with Li in a solid state reaction (*vide supra*, synthesis) and structure solution from powder X-ray diffraction data clearly indicated the position of new lithium ion in place of proton with the formation of a new phase, $Li_3Fe(PO_4)_2$ (compare asymmetric units in Figures 3b and c). The structure of $Li_2Fe(H_{0.5}PO_4)_2$ and $Li_3Fe(PO_4)_2$ are identical and thus transformation is topotactic. When viewed along the *a*-axis as in Figure 4 (compare Figure 4b and 4c), it clearly shows the position of the new lithium ion in slightly changed channel shape caused by little increase (~4%) of *a*- and *c*-axis lengths by the larger size of Li compared to proton. The coordination of the new Li site can be best described as square planar since two other Li – O distances (Li1 – O1 = 2.95(2) Å) are too long to be considered as bond whereas the coordination of the 2nd lithium ion (Li2) is a very distorted pentagonal pyramidal with one long Li – O distance (Li2 – O3 = 2.67(3) Å). Li in $Li_2Fe(H_{0.5}PO_4)_2$ has 5-fold coordination adopting an irregular polyhedral shape with one long Li – O distance (Li1 – O4 = 2.347(5) Å). The bond valence sum calculations reveal that the BVS value of 1.09 for Li1 in $Li_2Fe(H_{0.5}PO_4)$; 0.95 and 1.05 for Li1 and Li2 sites, respectively, in $Li_3Fe(PO_4)_2$ indicating slight under bonding of Li site (Li1) in square planar coordination. Such distorted square planar coordination of lithium is not new and has been found in lithium titanates, $Li_2Ti_6O_{13}$ and in Li_xTiO_2(B) ($x<0.25$).[51, 52] There exist an isostructural sulfate analogue of

$Li_2Fe(H_{0.5}PO_4)_2$ and $Li_3Fe(PO_4)_2$, which is a mineral called marinite, $Li_2Fe(SO_4)_2$, has identical framework but display subtle differences in the position of Li ions caused by the absence of proton in the sulfate structure.[53]

Table 6. Bond distances and bond valence sum for the coordination polyhedra in $Li_3Fe(PO_4)_2$.

Atom –Atom	d (Å)	Atom –Atom	d (Å)
Fe1 – O1$^{\#1, \#2}$ x 2	2.078(5)	P1 – O1	1.553(6)
Fe1 – O2$^{\#3, \#4}$ x 2	2.050(5)	P1 – O2	1.546(6)
Fe1 – O3$^{\#5, \#6}$ x 2	1.927(5)	P1 – O3	1.523(6)
BVS of Fe 1 = 3.03		P1 – O4	1.520(5)
		BVS of P1 = 5.20	
Li – O distances (Å)			
Li1 – O2$^{\#3, \#7}$ x 2	2.236(5)	Li2 – O3$^{\#10}$	2.438(5)
Li1 – O4$^{\#1, \#8}$ x 2	1.852(4)	Li2 – O4$^{\#11}$	1.895(3)
BVS of Li1 =	0.95	Li2 – O4$^{\#10}$	2.116(5)
Li2 – O1	1.967(3)	Li2 – O3	2.670(3)
Li2 – O2$^{\#9}$	2.116(5)	BVS of Li2 = 1.05	

$^{\#1}$x, 0.5-y, -0.5+z; $^{\#2}$-x, -0.5+y, 0.5-z; $^{\#3}$1-x, 1-y, 1-z; $^{\#4}$-1+x, -1+y, -1+z; $^{\#5}$-1+x, 0.5-y, -0.5+z;

$^{\#6}$1-x, -0.5+y, 0.5-z; $^{\#7}$x, -1+y, z; $^{\#8}$1-x, -0.5+y, 1.5-z; $^{\#9}$-1+x, y, z; $^{\#10}$1-x, 0.5+y, 1.5-z;

$^{\#11}$-1+x, 1.5-y, -0.5+z;

3.1.1. Spectroscopic and Thermogravimetric Analysis. FT-IR spectroscopy has been used (Figure S9, SI) to further characterize the chemical nature of the inter-atomic bonding in the as-prepared samples. The IR spectra of all compounds show prominent bands in 930 – 1100 cm^{-1} region which can be attributed to the P – O symmetric (ν_1) and anti-symmetric (ν_3) stretching modes, especially the strong modes in the range 930 – 1030 cm^{-1} can be attributed to ν_1. The weaker O – P – O bending modes can be seen in the range 400 – 650 cm^{-1}, which include symmetric bending (ν_2) between 400 – 465 cm^{-1} and antisymmetric bending (ν_4) in 500 – 650 cm^{-1} region, respectively. We observe broad shoulder for $Li_2Fe(H_{0.5}PO_4)_2$-HT or –IEX in the region 800 – 925 cm^{-1} for ν_{POH}, on the contrary we observe clear well-defined bands in the same region for ν_{POH} in the case of $NaFe(HPO_4)_2$. More importantly we do not see any broad/sharp bands in this region for $Li_3Fe(PO_4)_2$ phase confirming absence of any P-OH bonds in $Li_3Fe(PO_4)_2$. We also observe bands at 2919 and 2851 cm^{-1} in $Li_2Fe(H_{0.5}PO_4)_2$-IEX and $NaFe(HPO_4)_2$ for ν_{HO-P} modes. However, these bands did not show up for $Li_2Fe(H_{0.5}PO_4)_2$-HT. Except for $Li_3Fe(PO_4)_2$, all the compounds bear signature of stretching and bending P – O – H modes and weak shoulder centered at 1250 cm^{-1} for δ_{POH}, respectively, besides a broad O – H stretching modes centered around 3300 – 3400 cm^{-1}. An additional O–H stretching band at 3277 cm^{-1} and the more pronounced δ_{O-H} in $Li_2Fe(H_{0.5}PO_4)_2$-IEX at 1627 cm^{-1} also confirms the presence of H_2O from the $FePO_4 \cdot 2H_2O$ impurity. The IR spectra of the compounds bear close agreement with previously reported compounds containing acidic phosphate groups or hydrated iron phosphate.[21, 54, 55]

TGA has been utilized to determine the thermal stability of the compounds (Figure 5). The TGA curve of $NaFe(HPO_4)_2$ indicates that the compound is stable up to 425°C and after that it starts to lose weight, which can be attributed to the loss of one H_2O molecule based on the observed weight loss of 6.7% (theoretical = 6.65%) to form $NaFeP_2O_7$ as determined from the PXRD of heated residue. $Li_2Fe(H_{0.5}PO_4)_2$-HT shows a total weight loss of 4.52 %, of which, 3.52 % weight loss takes place between 480 to 520 °C and is attributed to the loss of ½ H_2O molecule (theoretical, 3.46%). The additional observed weight loss (< 1 %) may be due to the adsorbed water. The residue left after the TGA is a mixture of $LiFeP_2O_7$ and $Li_3Fe_2(PO_4)_3$ as determined by PXRD (data not shown). $Li_2Fe(H_{0.5}PO_4)_2$-IEX shows higher total weight loss (total 9.6 %) in two major steps, one below 200°C (5.2 %) and then there is a gradual drop in weight of about 2% between 180 to 480 °C followed by a sharp step at 490 °C accounting another 4.4 %. The excess weight loss compared to the $Li_2Fe(H_{0.5}PO_4)_2$-HT can be assigned to the loss of two H_2O molecules present in the impurity phase, $FePO_4 \cdot 2H_2O$. Considering ~20% impurity phase based on Rietveld refinement, the calculated weight loss due to water molecules would be 3.86 %, which corroborates well with our observed value (5.17%). The extra weight loss could be attributed to the adsorbed water. $Li_3Fe(PO_4)_2$ does not show any major weight loss till 800 °C except a small gradual loss of 1.28% between 30 – 800 °C of which initial weight loss of 0.4% can be attributed to adsorbed water and the remaining can be due to the presence of impurity/parent phase. Simultaneous DSC clearly, indicates that a peritectic decomposition is occurring at 550°C with an exothermic peak and the compound is decomposing into more stable $Li_3Fe_2(PO_4)_3$ and Li_3PO_4 as determined by the PXRD of

the heated residue (data not shown), which proves that $Li_3Fe(PO_4)_2$ is a metastable phase (Figure S10, SI).

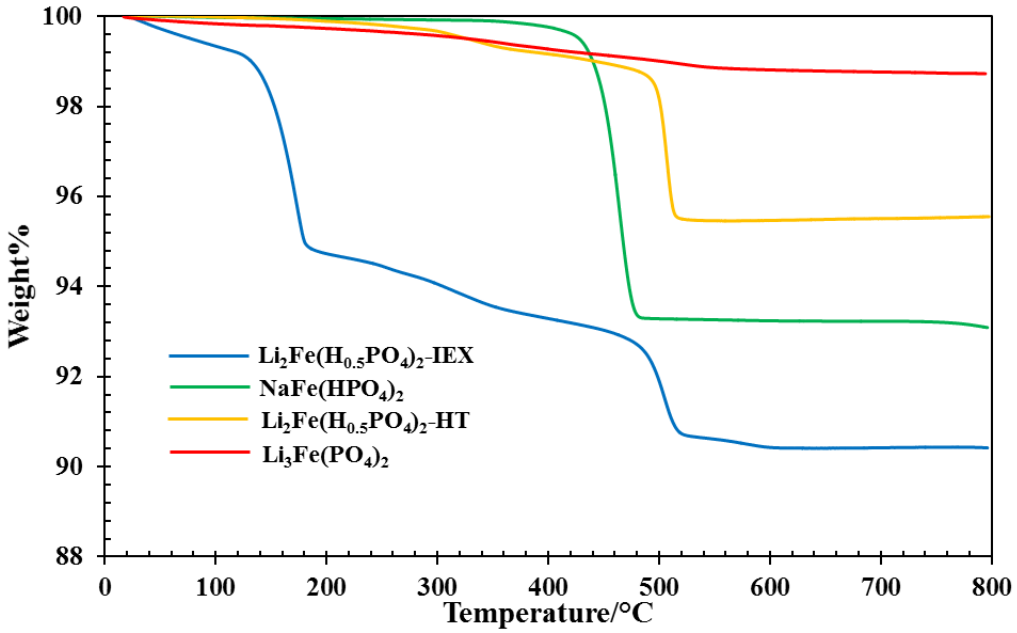

Figure 5. TGA analysis of the four compounds.

UV-Vis absorption spectra of the compounds as converted from the diffuse reflectance data employing Kubelka-Munk equation are given in Figure S11, SI.[56] The spectra of all the compounds are remarkably similar and can be explained assuming Fe in high spin configuration. Any *d-d* electronic transition would involve reversal of spin and the spin forbidden transitions will be extremely weak. The transition from ground state ^6S which transform into $^6A_{1g}$ to quartet state is conceivable due to change in only one spin. Accordingly, $NaFe(HPO_4)_2$ and $Li_2Fe(H_{0.5}PO_4)_2$-IEX exhibit two weak and broad absorption bands at 737 and 546 nm corresponding to transitions from ground state $^6A_{1g}$

(^{6}S) to $^4T_{1g}$ (^{4}G) and $^4T_{2g}$ (^{4}G), respectively; a strong and relatively sharp absorption peak at 417 nm corresponding to transition from $^6A_{1g}$ (^{6}S) to $^4A_{1g}$ (^{4}G), ^4E_g (^{4}G).[57] The corresponding transitions in $Li_2Fe(H_{0.5}PO_4)_2$-HT occur at 724, 535, and 423 nm, respectively. $Li_3Fe(PO_4)_2$, on the other hand has two broad absorption bands at 880 ($^6A_{1g}$ (^{6}S) to $^4T_{1g}$ (^{4}G)) and 660 nm ($^6A_{1g}$ (^{6}S) to $^4T_{2g}$ (^{4}G)), which are slightly lower in energy compared to $NaFe(HPO_4)_2$ or $Li_2Fe(H_{0.5}PO_4)_2$ phases and the appearance of shoulders at 465 and 420 nm on a rising ligand –metal charge transfer band can be attributed to transitions from ground $^6A_{1g}$ (^{6}S) to $^4T_{2g}$ (^{4}D) and $^4A_{1g}$ (^{4}G), ^4E_g (^{4}G), respectively.[58] The merging of the two peaks also represents the change in the electronic environment of Fe in $Li_3Fe(PO_4)_2$ with the new incoming Li.

3.1.2. SEM Analysis. As synthesized and hand-ground (using mortar pestle) materials were used for the SEM analysis (Figure 6). The average particle sizes of $NaFe(HPO_4)_2$, $Li_2Fe(H_{0.5}PO_4)_2$-IEX, $Li_2Fe(H_{0.5}PO_4)_2$-HT, $Li_3Fe(PO_4)_2$ are 70, 15, 5, and 8 µm, respectively. The hand ground sample of $NaFe(HPO_4)_2$ displayed larger crystallite size which is also manifested in its poor electrochemical activity, for the rest of the samples, as synthesized products were used for SEM analysis.

Synthetically different $Li_2Fe(H_{0.5}PO_4)_2$, however, have different morphologies, as seen in Figure 6b & c, the crystallites of $Li_2Fe(H_{0.5}PO_4)_2$-IEX have elongated shapes ranging between 20 - 25 µm in length and 3 – 6 µm in diameter, while that of $Li_2Fe(H_{0.5}PO_4)_2$-HT has large variation of particle sizes ranging from 10 nm to 5 µm. The electrochemistry of the ion-exchanged sample is more facile reaching close to the theoretical capacity, which can be attributed to this particular elongated morphology as has been seen in case of olivine, $LiFePO_4$.[59, 60]

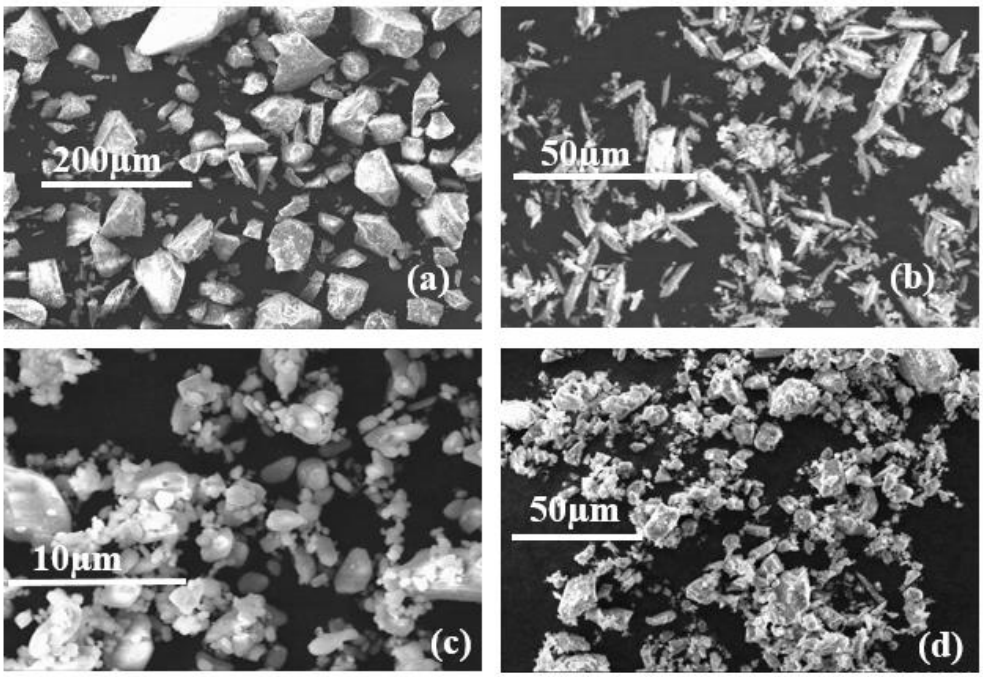

Figure 6. SEM micrographs of (a) $NaFe(HPO_4)_2$; (b) $Li_2Fe(H_{0.5}PO_4)_2$-IEX; (c) $Li_2Fe(H_{0.5}PO_4)_2$-HT; (d) $Li_3Fe(PO_4)_2$.

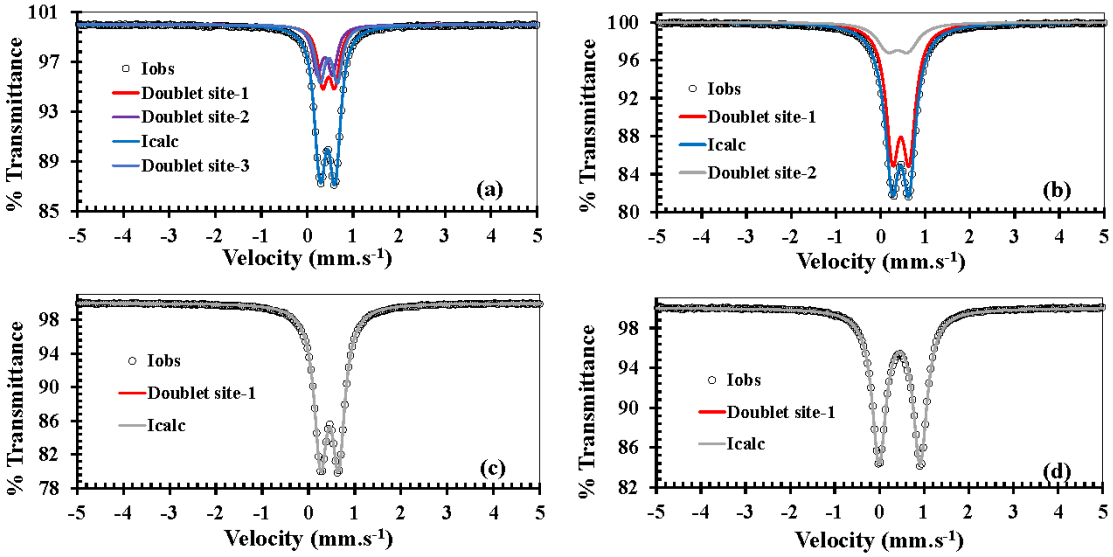

Figure 7. Mössbauer Spectra of (a) $NaFe(HPO_4)_2$; (b) $Li_2Fe(H_{0.5}PO_4)_2$-IEX; (c) $Li_2Fe(H_{0.5}PO_4)_2$-HT; (d) $Li_3Fe(PO_4)_2$.

3.1.3. Mössbauer Spectroscopy. Figure 7 shows the Mössbauer spectra for the four compounds; their isomer shift (IS) and quadrupole splitting (QS) parameters derived from the Lorentzian fittings of the peaks are listed in Table 7. As-prepared samples were used for all compounds except for $NaFe(HPO_4)_2$, which was ground into fine powder for measurement. Mössbauer spectra yielded valuable information about the oxidation states, spin states, coordination environments and local distortion of Fe centers through direct correlation of IS and QS values. In all samples, the spectrum can be fitted with one doublet, except for $NaFe(HPO_4)_2$, which is fitted with three doublets due to the presence of three crystallographically different iron centers in the structure. IS and QS values are in well accordance with the reported Fe^{+3} compounds in which Fe^{3+} is in high spin state in octahedral coordination surrounded by six oxo-ligands. The IS and QS values for $Li_2Fe(H_{0.5}PO_4)_2$-IEX and -HT are similar, but the width is larger for –IEX compared to the –HT phase, which may be because of the presence of $FePO_4{\cdot}2H_2O$ impurity phase. Therefore, spectrum of IEX phase was further fitted with two doublets and the ratio of the site populations of two doublets corresponds very close to the value (76.2:23.8) obtained by Rietveld refinement and the IS and QS values of the impurity phase corresponds well with the reported Mössbauer spectrum of $FePO_4{\cdot}2H_2O$.[61] The QS value of $Li_3Fe(PO_4)_2$ is significantly higher than the other two phases which also contain octahedral Fe^{3+} centers. Especially differences in the QS values between $Li_2Fe(H_{0.5}PO_4)_2$-IEX and -HT (ΔE_Q = 0.38(5)) and $Li_3Fe(PO_4)_2$ (ΔE_Q = 0.91(1)) are rather significant considering that there is hardly any difference in the distortion of FeO_6 octahedra and both iron have identical phosphate environment. However, removal of the proton by Li create a variation in the next nearest neighbor with respect to number of LiO_x polyhedra; for example, Fe in

$Li_2Fe(H_{0.5}PO_4)_2$ is surrounded by four LiO_x polyhedra which are edge-shared with FeO_6 octahedra while Fe in $Li_3Fe(PO_4)_2$ is surrounded by six LiO_x polyhedra, four of which are edge shared as before and two are corner-shared. This variation in the next neighbors can produce different electric field gradients and consequently a higher QS can be resulted in $Li_3Fe(PO_4)_2$. This is called next nearest neighbor (NNN) effect and has been found in many iron phosphate-based minerals.[62, 63]

Table 7. The fitted ^{57}Fe Mössbauer spectroscopic values for Isomer Shift (IS) and Quadrupole Splitting (QS) of the as-synthesized compounds.

Compounds	Sites	IS(δ) ($mm.s^{-1}$)	QS (ΔE_Q) ($mm.s^{-1}$)	Site population (%)
$NaFe(HPO_4)_2$	Doublet site-1	0.46(2)	0.26(3)	40
	Doublet site-2	0.38(4)	0.33(3)	29
	Doublet site-3	0.47(3)	0.38(2)	35
$Li_2Fe(H_{0.5}PO_4)_2$-IEX	Doublet site-1	0.45(2)	0.37(4)	76.2
	Doublet site-2	0.38(2)	0.40(3)	23.8
$Li_2Fe(H_{0.5}PO_4)_2$-HT		0.45(4)	0.38(4)	100
$Li_3Fe(PO_4)_2$		0.45(3)	0.91(1)	100

3.1.4. Magnetic Property. The temperature dependent ZFC magnetic susceptibility $\chi_M(T)$, the corresponding inverse molar susceptibility $\chi_M^{-1}(T)$ and isothermal field dependent magnetization $M(H)$ for the as-synthesized compounds are given in Figures 8 & 9. All the three compounds show signature of magnetic transition at low temperatures and paramagnetic susceptibility in the temperature range 50 – 300 K as evident from the perfectly linear $\chi_M^{-1}(T)$ plots in this temperature range, which starts to deviate from linearity as it approaches magnetic transition below 50 K. $\chi_M^{-1}(T)$ data in the paramagnetic region, 150 – 300 K, can be fitted to Curie-Weiss law to obtain paramagnetic Curie temperature Θ_p, the Curie constant C, and the effective paramagnetic moment, μ_{eff}, as calculated from C (Table 8). The effective magnetic moment calculated from the Curie constant for all the compounds are in agreement with the theoretical magnetic moment of 5.92 μ_B suggesting 3+ oxidation state of Fe with d^5 high spin configuration reinforcing the results of ^{57}Fe Mössbauer spectroscopy.

Table 8: Important magnetic parameters calculated from the magnetic measurements of the compounds.

Compound	T_N	θp	μ_{eff}	$N\beta$
$NaFe(HPO_4)_2$	32 K	-66.55	6.01	0.34
$Li_2Fe(H_{0.5}PO_4)_2$-IEX	22 K	-52.67	6.003	0.56
$Li_2Fe(H_{0.5}PO_4)_2$-HT	23 K	-33.13	5.896	0.57
$Li_3Fe(PO_4)_2$	28 K	-48.63	5.826	0.49

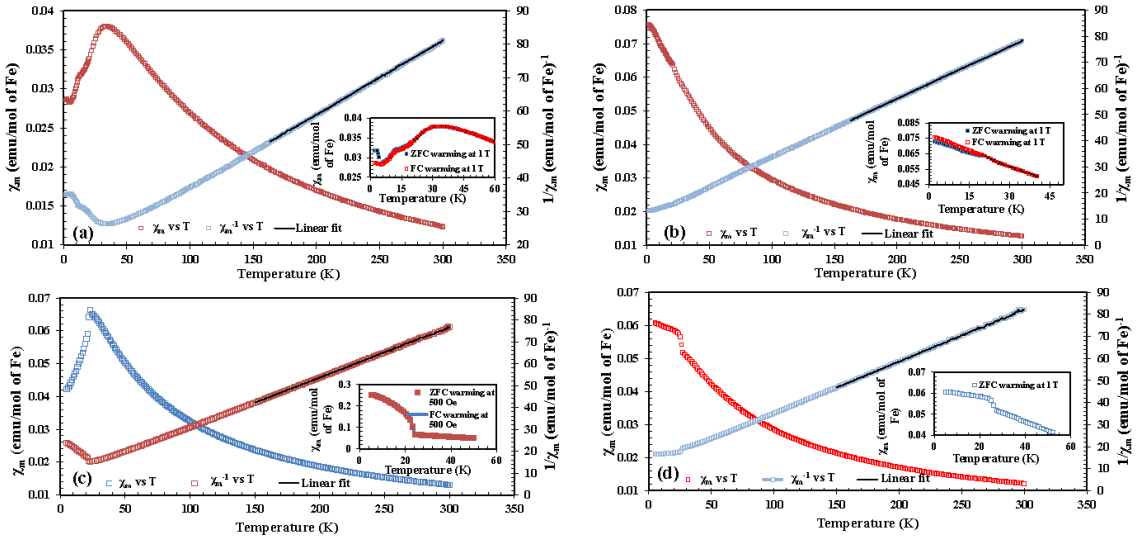

Figure 8. Temperature dependence of molar magnetic susceptibility (χ_m) and inverse molar magnetic susceptibility (χ_m^{-1}) of (a) $NaFe(HPO_4)_2$; (b) $Li_2Fe(H_{0.5}PO_4)_2$-IEX; (c) $Li_2Fe(H_{0.5}PO_4)_2$-HT; (d) $Li_3Fe(PO_4)_2$.

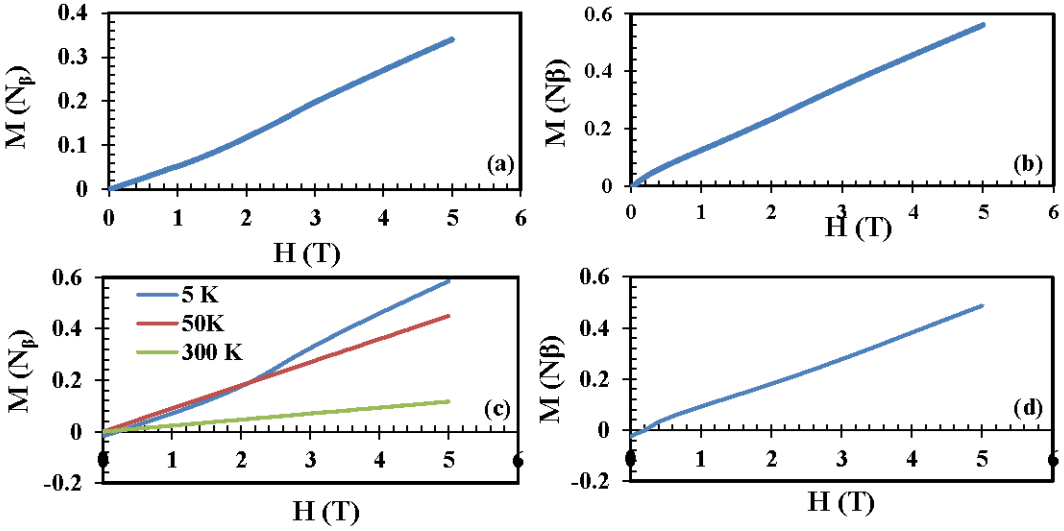

Figure 9. *M* vs *H* plots of (a) $NaFe(HPO_4)_2$; (b) $Li_2Fe(H_{0.5}PO_4)_2$-IEX; (c) $Li_2Fe(H_{0.5}PO_4)_2$-HT; (d) $Li_3Fe(PO_4)_2$.

The $\chi_M(T)$ plot for $NaFe(HPO_4)_2$ reveal that the compound shows an onset of a broad antiferromagnetic transition at 32 K, which is a signature of a low-dimensional short-

range ordering. The broad peak is followed by a small kink at 12 K, and a ZFC and FC divergence at 5 K (see inset of Figure 8a). The kink at 12 K may be assigned as an onset of 3-D antiferromagnetic ordering. The antiferromagnetic ordering is well corroborated with high negative Θ_p value of –66.5 K, sluggish and linear variation of $M(H)$ at 5 K with low saturation moment at 5 T (0.34 Nβ). In the case of $Li_2Fe(H_{0.5}PO_4)_2$-HT, we can observe an onset of antiferromagnetic transition at 23 K in ZFC warming up data at 1T applied field, however, at lower applied field of 500 Oe, the signature of transition changes to more like a ferromagnetic one with no divergence in ZFC and FC data. Such change in the nature of transition on increasing the applied field may indicate presence of weak ferromagnetic component. In the case of $Li_2Fe(H_{0.5}PO_4)_2$-IEX, the antiferromagnetic transition at 22 K is attenuated and not clearly visible when compared to the antiferromagnetic transition of phase pure $Li_2Fe(H_{0.5}PO_4)_2$-HT. This difference in magnetic properties can be attributed to the presence of $FePO_4{\cdot}2H_2O$ impurity in the ion-exchanged phase. The $\chi_M(T)$ plot of $Li_3Fe(PO_4)_2$ on the other hand show a weak ferromagnetic like transition at 28 K, however, negative value (–48.6 K) of the Weiss constant indicate predominant anti-ferromagnetic interactions between the Fe centers. The *M vs H* plots of $Li_2Fe(H_{0.5}PO_4)_2$-HT at different temperatures (5, 50, 300 K) reveal interesting observation specially at low temperature (5 K) where the magnetization is negative below 500 Oe and at 2.4 T there is an increase of magnetization which is reminiscent of meta magnetism. At higher temperatures the *M vs H* plots are perfectly linear with very sluggish change with field. Interestingly both $Li_2Fe(H_{0.5}PO_4)_2$-IEX and $Li_3Fe(PO_4)_2$ also show negative magnetization albeit less pronounced and becomes positive after application of 0.1 and 0.2 T field, respectively. Negative magnetization has been observed in several Fe(3+) compounds,[64 - 66] however, in

these present cases further detailed investigations are required to determine the cause of negative magnetization. The saturation magnetization M_S (~0.5 Nβ) for $Li_2Fe(H_{0.5}PO_4)_2$-HT, -IEX, and $Li_3Fe(PO_4)_2$ at 5 K under 5T applied field is only 10 % of the theoretical saturation moment expected for Fe^{3+} ($3d^5$) free ion magnetic moment (Ms = gS Nβ).

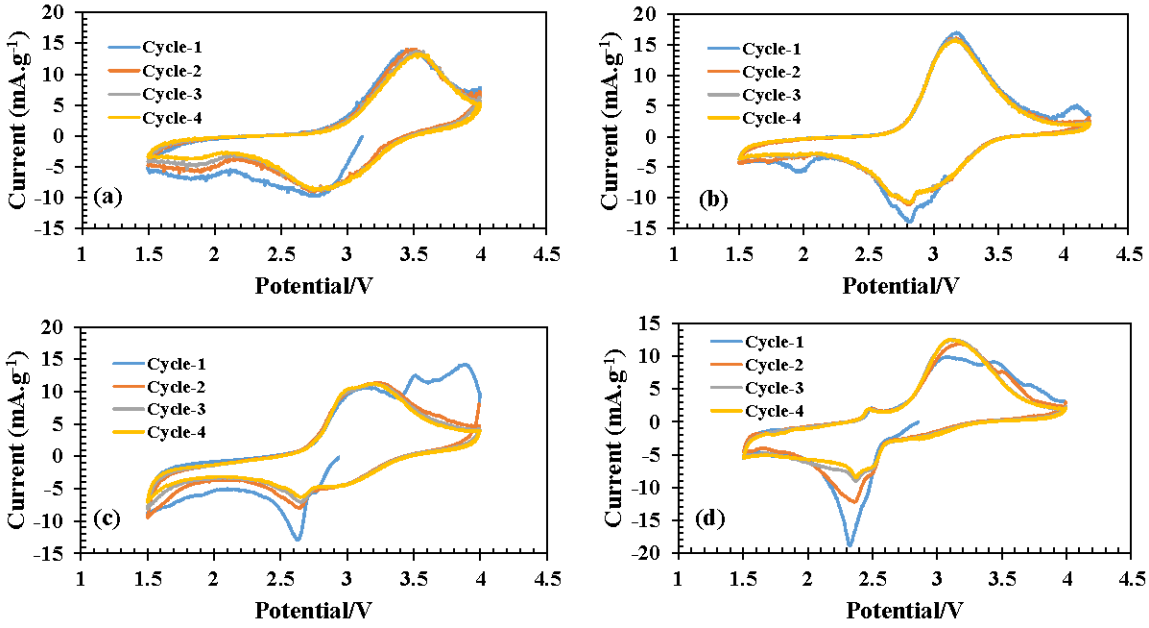

Figure 10. Cyclic Voltammograms of first four cycles of (a) $NaFe(HPO_4)_2$; (b) $Li_2Fe(H_{0.5}PO_4)_2$-IEX; (c) $Li_2Fe(H_{0.5}PO_4)_2$-HT; (d) $Li_3Fe(PO_4)_2$.

3.2. ELECTROCHEMISTRY

3.2.1. Cyclic Voltammetry. Figure 10 shows four cycles of voltammograms of the Li-ion cells made from the composites of compounds as cathode active material and metallic lithium as anode. The OCV of the cells are 3.11, 3.10, 2.94, and 2.85 V, respectively for $NaFe(HPO_4)_2$, $Li_2Fe(H_{0.5}PO_4)_2$-IEX, $Li_2Fe(H_{0.5}PO_4)_2$-HT and $Li_3Fe(PO_4)_2$. In the subsequent cycles the reduction onset (Li-insertion) is ~3.3 V for all

the compounds. The cathodic (Li-insertion) and anodic (Li-extraction) peaks are observed at 2.86 and 3.52 V for $NaFe(HPO_4)_2$, 2.8 and 3.17 V for $Li_2Fe(H_{0.5}PO_4)_2$-IEX, 2.65 and 3.23 V for $Li_2Fe(H_{0.5}PO_4)_2$-HT, 2.35 and 3.21 V for $Li_3Fe(PO_4)_2$. Apart from the main cathodic and anodic peaks, there is a broad peak at 1.9 V in $NaFe(HPO_4)_2$, which gradually attenuates in subsequent cycles (Figure 10a). A peak at 2.0 V for $Li_2Fe(H_{0.5}PO_4)_2$-IEX in the first reduction cycle can be observed (Figure 10b), which may be attributed to oxygen (dissolved in electrolyte) reduction peak or some irreversible reaction since it is absent in the subsequent cycles. An irreversible oxidation peak at 4.1 V is also observed in the first cycle of $Li_2Fe(H_{0.5}PO_4)_2$-IEX, whereas in the –HT phase irreversible oxidation peaks can be seen at 3.5 and 3.9 V in the first cycle. Similar features are also observed in $Li_3Fe(PO_4)_2$ at 3.5 and 3.8 V, which vanishes in subsequent cycles. $Li_2Fe(H_{0.5}PO_4)_2$-IEX, –HT and $Li_3Fe(PO_4)_2$ phases exhibit a broad peak centered around 3 V in the reduction cycle before the appearance of more pronounced somewhat sharp reduction peak at lower potentials. Ideally the reduction at ~3 V should be the main reduction peak for $Li_2Fe(H_{0.5}PO_4)_2$-IEX, –HT and $Li_3Fe(PO_4)_2$ based on their oxidation peaks. However, for both $Li_2Fe(H_{0.5}PO_4)_2$ and $Li_3Fe(PO_4)_2$ phases it seems that small amount of lithium ions are inserted at ~3 V and afterwards there may be some structural rearrangement which facilitates further Li-insertion at lower potential. This is also corroborated in the discharge curves of $Li_2Fe(H_{0.5}PO_4)_2$–HT and $Li_3Fe(PO_4)_2$, which are almost identical and exhibit ~0.25 Li insertions at ~3 V and the remaining lithium ions are inserted at lower potentials (*vide infra*). This also indicates that both $Li_2Fe(H_{0.5}PO_4)_2$-IEX, –HT and $Li_3Fe(PO_4)_2$ phases are going through similar structural changes during Li-insertions. This is somewhat substantiated by the Mössbauer spectral analysis of the reduced phases (*vide infra*). The

area under the cathodic and anodic peaks for $Li_2Fe(H_{0.5}PO_4)_2$-IEX (Figure 10b) is higher compared to $Li_2Fe(H_{0.5}PO_4)_2$-HT (Figure 10c), suggesting higher overall charge and discharge kinetic capabilities for the former. In addition we observe small peaks at both oxidation and reduction cycle at 2.5 V for $Li_3Fe(PO_4)_2$, which we speculate to be due to some reversible structural phase transition. However, more precise analysis of electrochemically reduced phases by PXRD and ^{57}Fe-Mössbauer spectroscopy (*vide infra*) will be required for a definitive answer.

3.2.2. Galvanostatic Charge-Discharge. The galvanostatic charge-discharge experiments were done at various slow C-rates and the cut-off potentials were set in the range 1.5 – 4.0 V for all the tests (Figure 11). Assuming complete one electron process per Fe atom, 1 lithium ion per formula unit gives a theoretical capacity of 98.97, 102.81 and 100.52 mAh/g, respectively, for $NaFe(HPO_4)_2$, $Li_2Fe(H_{0.5}PO_4)_2$ and $Li_3Fe(PO_4)_2$. $NaFe(HPO_4)_2$ shows achievable capacity of 60 mAh/g (61% of theoretical capacity) at C/50 rate (8.42 µA), which accounts for 0.6 Li insertion. However, it experiences an irreversible capacity loss of 7% in the second cycle. In the first discharge, we are certainly inserting Li-ions as we are using metallic Li anode and a lithium salt as an electrolyte, but while charging the cell the possibility of extracting part of Na-ion cannot be ruled out. At higher C-rates, the capacity achieved remains constant with 36 mAh/g at C/20 (21 µA), 26 mAh/g at C/10 (42 µA), 18 mAh/g at C/5 (84 µA), respectively. Upon returning to a slower C-rate (C/50) after completing all the faster C-rates, it showed a constant capacity of 45 mAh/g (Figure 11a).

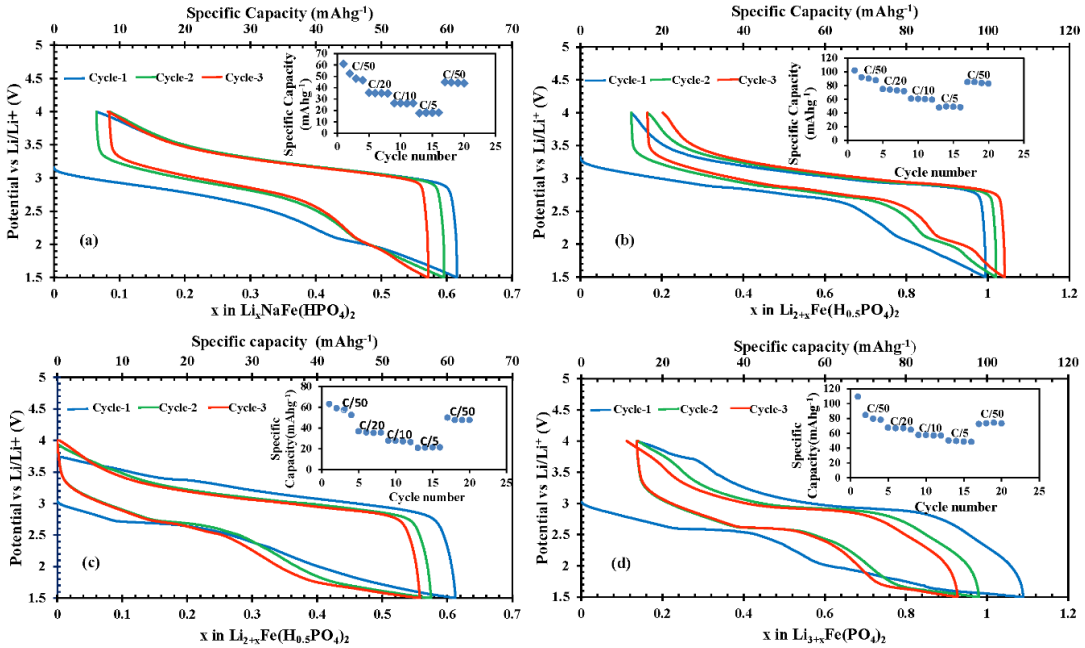

Figure 11. First three cycles of galvanostatic charge-discharge curves for $NaFe(HPO_4)_2$ (a), $Li_2Fe(H_{0.5}PO_4)_2$-IEX (b), $Li_2Fe(H_{0.5}PO_4)_2$-HT (c) and $Li_3Fe(PO_4)_2$ (d). Inset shows cycle life at different C-rates.

In contrary, $Li_2Fe(H_{0.5}PO_4)_2$-IEX achieves almost 100% (102.1 mAh/g) of the theoretical capacity in the first cycle at C/50 (8.29 µA), suffers a capacity loss of 10% in the 2nd cycle but remains constant thereafter. Even at faster C-rates the capacity fade is much less and at C/5 (82.9 µA), a capacity of 48 mAh/g can be achieved, which remains constant even after 100 cycles (Figure S12). Note that $Li_2Fe(H_{0.5}PO_4)_2$-IEX contains 20% of $FePO_4 \cdot 2H_2O$,[20, 21] which is also a electrochemically active phase. In calculating the capacity we took into account the percentage of the impurity phase. On the other hand, $Li_2Fe(H_{0.5}PO_4)_2$-HT shows an achievable capacity of 62 mAh/g (61% of theoretical capacity) at C/50 rate (8.55 µA), which accounts for 0.6 Li insertion. The cell experiences an irreversible capacity loss of about 10% in the fourth cycle. At higher C-rates, the capacity achieved remains constant with 37 mAh/g at C/20 (21.4 µA), 27 mAh/g at C/10

(42.8 µA), 21 mAh/g at C/5 (85.5 µA), respectively (see inset of Figure 11c). When the battery is cycled at a slower C-rate after completing all the faster C-rates, it showed a constant capacity of 47 mAh/g. Interestingly, there is a difference in the discharge profile of the –IEX and –HT phases of $Li_2Fe(H_{0.5}PO_4)_2$. In the –HT phase 40 % of the 62mAh/g discharge capacity can be accounted for in the voltage range below 2 V, while only 10% of the ~90 mAh/g capacity comes from below 2 V in the case of –IEX phase.

$Li_3Fe(PO_4)_2$ shows a high discharge capacity of 109 mAh/g in the first cycle at C/50 rate (8.62 µA), which is slightly higher than the theoretical capacity and 50 % of which appears below 2 V. This slight higher capacity can be attributed to the solid-electrolyte interface (SEI) formation in the first cycle. However, the capacity drops down to 80 mAh/g in the fourth cycle and remains constant and almost 30% of the total discharge capacity comes from second slopy voltage curve between 2 – 1.5 volt range. This part of the discharge curve is very similar to $Li_2Fe(H_{0.5}PO_4)_2$-HT and also consistent with their cyclic voltammograms, in which both display substantial Li-insertion at lower voltages. Similar to $Li_2Fe(H_{0.5}PO_4)_2$-IEX, $Li_3Fe(PO_4)_2$ also shows good capacity retention at faster C-rates with minimum capacity fading. It achieved 50 mAh/g at C/5 rate (86.2 µA) and after 100 cycles the achievable capacity was still 40 mAh/g (Figure S13). The large irreversible capacity for these two materials in the first cycle seems to be related to the smaller particle sizes and larger surface area that could lead to more SEI formation. $NaFe(HPO_4)_2$ and $Li_2Fe(H_{0.5}PO_4)_2$-IEX exhibit sloping voltage-capacity curve reminiscent of single phase solid-solution type mechanism during the entire charging and discharging cycles. However, $Li_2Fe(H_{0.5}PO_4)_2$-HT and $Li_3Fe(PO_4)_2$ after initial sloppy profile of up to 0.1 and 0.2 Li insertions, respectively, display flat plateaus that extend up to another 0.2 Li

insertions. Interestingly, for $Li_2Fe(H_{0.5}PO_4)_2$-HT after the 1st cycle the flat plateau tends to vanish but remains intact for $Li_3Fe(PO_4)_2$ phase. After the flat plateau both phases show sloping voltage profile till the end of achievable capacity. This flat plateau may suggest emergence of a two phase behavior in that voltage regime. All the samples start to discharge at 3.4 volt with gradual decrease in voltage profile till the lower cut off voltage of 1.5 V. The ion-exchanged derived, $Li_2Fe(H_{0.5}PO_4)_2$-IEX, showed the best performance with respect to achievable capacity and exhibited small polarization of 0.2 V. The superior performance of $Li_2Fe(H_{0.5}PO_4)_2$-IEX can be attributed to the smaller particle sizes and elongated particle morphology.[59, 60]

Sodium-ion batteries were also fabricated for $NaFe(HPO_4)_2$ and $Li_2Fe(H_{0.5}PO_4)_2$-IEX acting as cathode active material. Both cells are electrochemically active exhibiting 0.5 and 0.6 sodium insertion, respectively, at C/50 rate. The two phases show loss of capacity (~ 5%) irreversibly after the first cycle. When the cells are subjected to higher C-rates of charge–discharge tests, both phases lose some capacity with the former showing pronounced loss compared to the ion-exchanged phase. For example, at C/5 the ion-exchanged phase shows a stable capacity of 30 mAh/g, while $NaFe(HPO_4)_2$ phase exhibit negligible capacity under similar condition. When the cells are returned to the slow C/50 rate (cycles 17–20) after completing a series of relatively fast rates, both the cells recover their initial 4th cycle capacities of ~40 and ~55 $mAh \cdot g^{-1}$, respectively. This underpins the slow kinetics and added diffusion resistance brought by the presence of sodium ions in $NaFe(HPO_4)_2$. Both phases show very similar voltage–composition curves with sodiation starting at a potential of 2.8 V (vs Na^+/Na), which is about 0.3 V lower than the lithiation as expected from the lower reduction potential of sodium compared to the lithium (−2.71

vs −3.04 wrt SHE, respectively). The sloppy discharge profiles without any plateau also point towards a solid-solution formation between the oxidized and reduced phases (Figure 12).

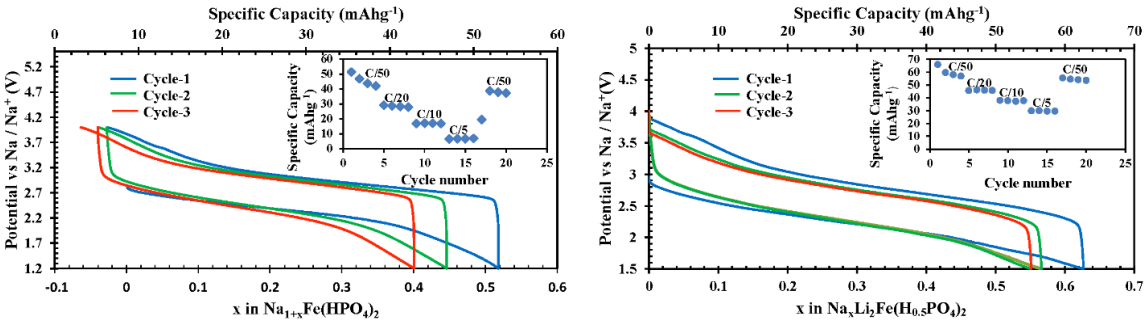

Figure 12. First three cycles of galvanostatic charge-discharge curves for $NaFe(HPO_4)_2$, $Li_2Fe(H_{0.5}PO_4)_2$-HT in Na-ion cell.

3.2.3. Ex-Situ Characterization of Discharged Cells. To further characterize the local environment of iron and structural changes occurring as a result of electrochemical reductions, ex-situ ^{57}Fe-Mössbauer spectroscopy and PXRD were carried out for all compounds (Table S4 & Figures S14 – S19). To analyze the reduced phases, the samples were prepared by extracting the cathodes from the cells discharged to lower cut-off potential. In all cases, the Mössbauer spectra indicated the emergence of Fe(II) centers in the cathode active material (Table S4 and Figure S14), which may have partly oxidized back to Fe(III) following exposure to air. This speculation is based on the fact that Mössbauer derived percentage of Fe(II) population is consistently less than the corresponding electrochemically achieved reduction of Fe(III). The PXRD pattern of the cathode film of $NaFe(HPO_4)_2$ retrieved from the discharged cell conserves its crystallinity

even after exposure to air, with the diffraction pattern of the presumably partly re-oxidized sample matching mostly with the as-prepared sample (Figure S15). The fitted Mössbauer spectrum of the discharged cathode film of $NaFe(HPO_4)_2$ contained signature of the parent $NaFe(HPO_4)_2$ and reduced phase, $LixNaFe(HPO_4)_2$, respectively, with IS and QS values matching with Fe^{3+} of $NaFe(HPO_4)_2$ and Fe^{2+} of $LixNaFe(HPO_4)_2$. Similarly, in the case of $Li_2Fe(H_{0.5}PO_4)_2$-IEX, -HT and $Li_3Fe(PO_4)_2$ (Figures S16 - S18) the reduced phases contain diffraction lines that are close to the as-synthesized cathodes, however, on close inspection it appears that reduced $Li_2Fe(H_{0.5}PO_4)_2$-HT exhibit some subtle differences compared to the simulated pattern of $Li_2Fe(H_{0.5}PO_4)_2$-HT, especially the intensities of the (020) and (110) lines are interchanged in the reduced phase. The Mössbauer spectra of electrochemically reduced $Li_2Fe(H_{0.5}PO_4)_2$-IEX and -HT are remarkably similar to that of the reduced phase of $Li_3Fe(PO_4)_2$, specially the IS and QS values of the Fe^{3+} sites of $Li_{2+x}Fe(H_{0.5}PO_4)_2$-IEX and -HT are quite similar to the IS and QS values of pristine, $Li_3Fe(PO_4)_2$ or the reduced form, $Li_{3+x}Fe(PO_4)_2$. This can be explained if the $Li_2Fe(H_{0.5}PO_4)_2$ phases have undergone ion-exchange reaction partially or fully with Li^+ from the electrolyte to form $Li_3Fe(PO_4)_2$ during reductive insertion. Another possibility could be that upon Li-insertion in $Li_2Fe(H_{0.5}PO_4)_2$, the resulting phase, $Li_{2+x}Fe(H_{0.5}PO_4)_2$ has similar structure as $Li_{3+x}Fe(PO_4)_2$, such that Fe site has similar electric field gradient in both. The intensity reversal of diffraction lines in the reduced phase resembling the $Li_3Fe(PO_4)_2$ phase also supports this assertion. However, besides the intensity switching (Figure S17) in the reduced phase of $Li_2Fe(H_{0.5}PO_4)_2$-HT there appears to be couple of more features, for example, merging of two diffraction lines, (10-2) and (021), into one and splitting (022) line into two lines in the reduced phase, which are not particularly

related to $Li_3Fe(PO_4)_2$ or reduced phase of $Li_3Fe(PO_4)_2$ (Figure S19). Therefore, high resolution powder X-ray diffraction data and structure solution of the reduced phases of $Li_2Fe(H_{0.5}PO_4)_2$-HT and $Li_3Fe(PO_4)_2$ would yield more accurate information and more importantly in-operando Mössbauer and PXRD study can be conclusive in determining the oxidation state and nature of crystalline phases during the electrochemical process.

4. CONCLUSIONS

In this article we have reported the pure phase syntheses of three iron phosphates, $NaFe(HPO_4)_2$, $Li_2Fe(H_{0.5}PO_4)_2$ and $Li_3Fe(PO_4)_2$. Two of these iron phosphates, $NaFe(HPO_4)_2$ and $Li_3Fe(PO_4)_2$ are new and their structures have been solved from single-crystal and synchrotron powder X-ray diffraction data, respectively. The structure of $Li_2Fe(H_{0.5}PO_4)_2$ was known but we have presented new hydrothermal (-HT) and ion-exchange (-IEX) routes of synthesis. All the structures are mutually related and can be derived from one another *via* simple ion-exchange routes, for example, aqueous phase ion exchange of Na^+ ion from $NaFe(HPO_4)_2$ with Li^+ ion produces $Li_2Fe(H_{0.5}PO_4)_2$, while solid-state proton exchange from $Li_2Fe(H_{0.5}PO_4)_2$ with Li-ion produces $Li_3Fe(PO_4)_2$, which is a metastable phase. $Li_3Fe(PO_4)_2$ was a compositionally predicted phase, which is synthetically realized by our soft-chemical approach. These compounds were also characterized by Mössbauer and magnetic measurements, which unequivocally proved +3 oxidation state and high spin configuration of iron present in all three compositions. All the synthesized compounds were tested as cathode materials in lithium ion batteries and

two of them were also tested for sodium ion batteries. Since the as-synthesized compounds contained alkali ions and Fe in 3+ oxidation state, an oxidative de-insertion was attempted but could not be achieved while charging the cells up to 4.5 V. However, our efforts to insert lithium reductively have resulted insertion of up to 0.6 – 1.0 lithium equivalents per Fe when the cells were discharged first to 1.5 V. The cells displayed reversible electrochemical activity of the Fe^{3+}/Fe^{2+} couple when cycled between 1.5 – 4 V vs Li+/Li. All the compounds show very similar charge-discharge profiles due to similarities in the structure; differences in the achievable capacity and kinetics of electrochemical reactions occur due to particle sizes and presence of ions in the channels impeding incoming lithium ions. Interestingly the same compound, $Li_2Fe(H_{0.5}PO_4)$, synthesized in two different ways show remarkably different electrochemical behavior, the ion-exchanged derived sample shows almost 100% theoretical capacity at slow rate and slightly better average voltage and less polarizations, all of which can be attributed to the elongated particle shape underscoring the importance of synthesis routes in electrochemistry. We have also demonstrated reversible electrochemical activity of Fe^{3+}/Fe^{2+} couple in $NaFe(HPO_4)_2$ and $Li_2Fe(H_{0.5}PO_4)_2$ in Na-ion cells. In principle all the compounds reported here are two electron candidates and further capacity enhancement is possible by replacing Fe with V, where higher oxidation states are more easily achieved.

ACKNOWLEDGEMENTS

The authors acknowledge the funding from University of Missouri Research Board and Energy Research and Development Center, Missouri S&T. Use of the Advanced

Photon Source at Argonne National Laboratory was supported by the U.S. Department of Energy, Office of Science, Office of Basic Energy Sciences, under Contract No. DE-AC02-06CH11357.

SUPPLEMENTARY INFORMATION

Coin Cell fabrication and electrochemical test.

To the finely ground active material, Poly-vinylidene fluoride (PVDF) was added as the binder and an optimum amount of N-methyl-2-pyrrolidone (NMP) was added to dissolve the PVDF. The resulting slurry was further ball milled for another 20 minutes to obtain a homogeneous viscous mixture. The ratio of the active material, conducting carbon, and the binder in the cathode mix was 75: 15: 10. The cathode mix was then spread as a film of uniform thickness with the help of a glass rod onto a flat sheet of carbon-coated aluminum current collector and transferred into a vacuum oven and dried overnight at 85°C.

For electrochemical tests, CR2032 type coin cells were fabricated. The composite cathode film was cut into circular disks (3/8 inch diameter) with 4.0–5.0 mg of active material loading and transferred into an argon filled glove box with an oxygen concentration below 2.0 ppm. The cathode disk and Li anode (0.75 mm thickness Li ribbon cut into circular disk) were assembled in the coin cell casing with a Celgard® 2325 circular sheet placed between the two electrodes as the separator. The electrolyte, 1 M solution of $LiPF_6$ in DMC–EC (1:1) was then added and the cell was sealed with a coin cell crimper. The prepared cells were aged for equilibration for about 12 hours before electrochemical

testing. Similarly Na ion batteries were also made using Na anode and 1 M solution of $NaClO_4$ in DMC–EC (1:1) was used as the electrolyte.

Cyclic voltammograms were obtained using a PAR EG&G potentiostat/galvanostat model 273 in the potential range of 1.5 – 4.0 V (vs. Li/Li^+) and (vs. Na/Na^+) with a scan rate of 0.05 mV s^{-1}. Voltage composition profiles were obtained using galvanostatic charge/discharge experiments on an Arbin Instruments battery tester, model BT2043, on the same potential limits as CV at various C-rates.

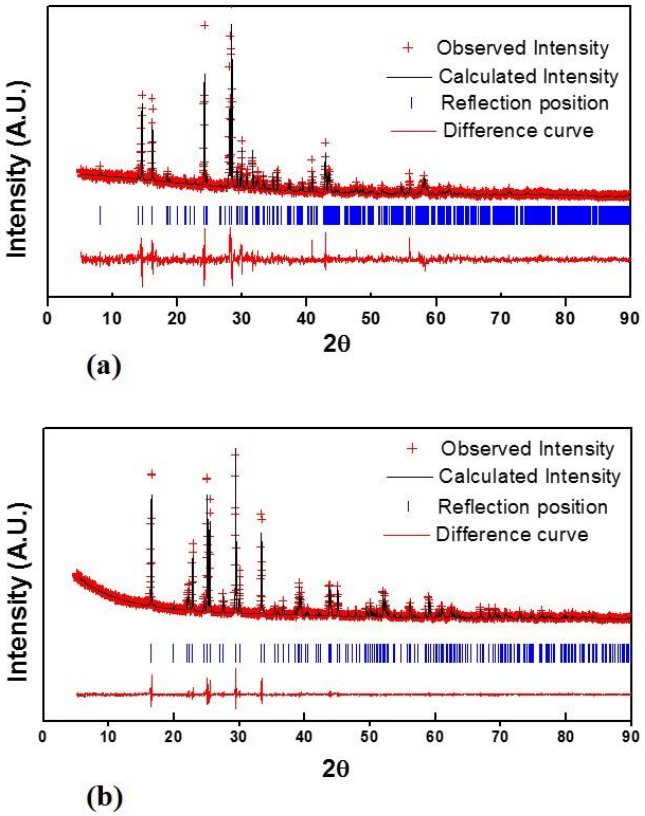

Figure S1. Rietveld refinement of low-resolution powder X-ray diffraction patterns of (a) $NaFe(HPO_4)_2$ (λ = 1.54059Å, Rw = 12.858%) and (b) $Li_2Fe(H_{0.5}PO_4)_2$-HT (λ = 1.54059Å, Rw = 12.246%)

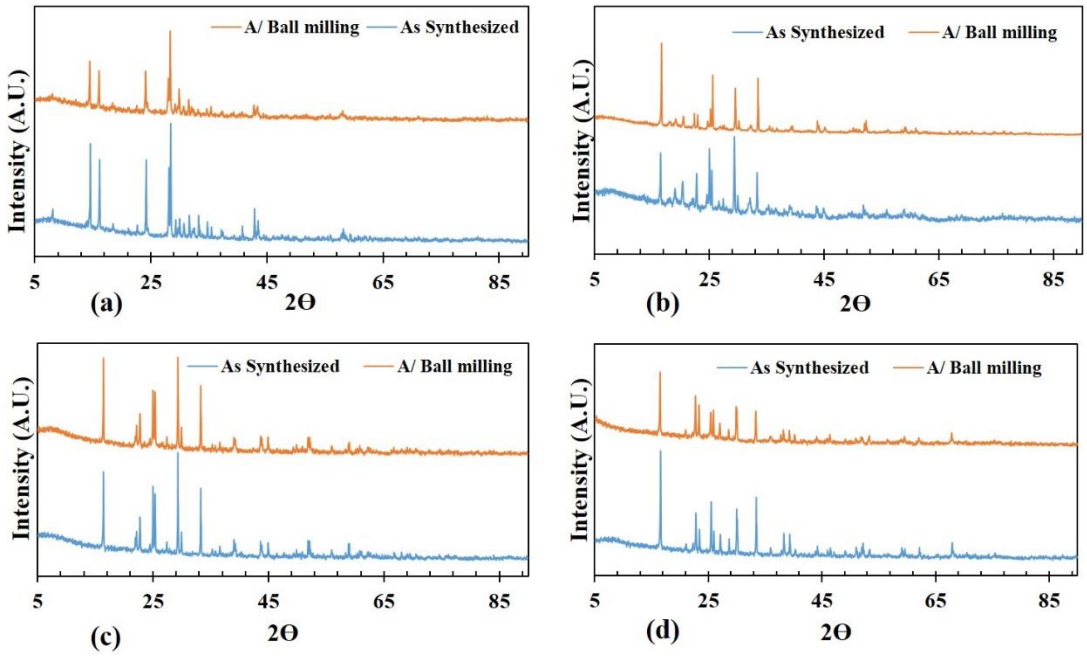

Figure S2. Powder XRDs of As Synthesized and After Ball milling samples for (a) $NaFe(HPO_4)_2$; (b) $Li_2Fe(H_{0.5}PO_4)_2$-IEX, (c) $Li_2Fe(H_{0.5}PO_4)_2$-HT; (d) $Li_3Fe(PO_4)_2$.

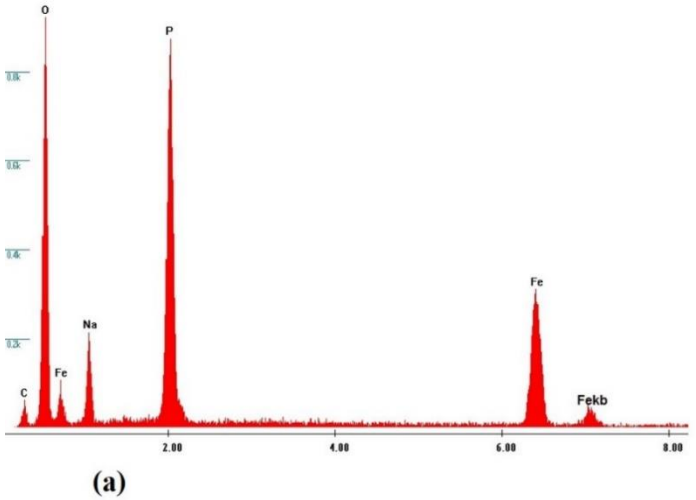

Element	Wt %	At %
B K	0.00	0.00
C K	8.36	14.93
O K	39.88	53.50
F K	0.00	0.00
NaK	9.50	8.87
P K	20.94	14.51
FeK	21.32	8.19
Total	100.00	100.00

(b)

Figure S3. EDS spectra of $NaFe(HPO_4)_2$.

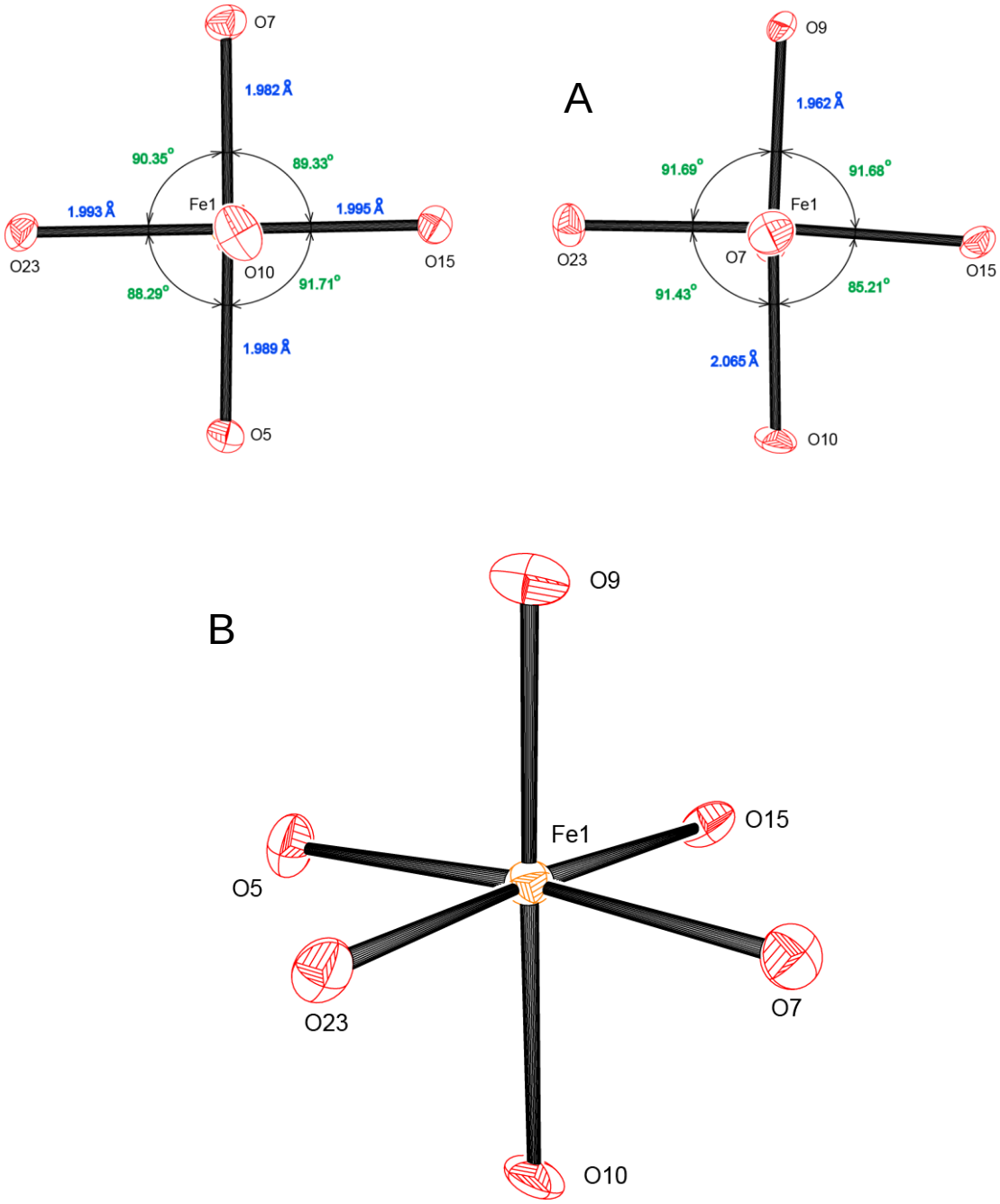

Figure S4. Environment of Fe1 center in the structure: **A** – two orthogonal projections, **B** – prospective view showing small distortions of octahedral polyhedron of the metal center.

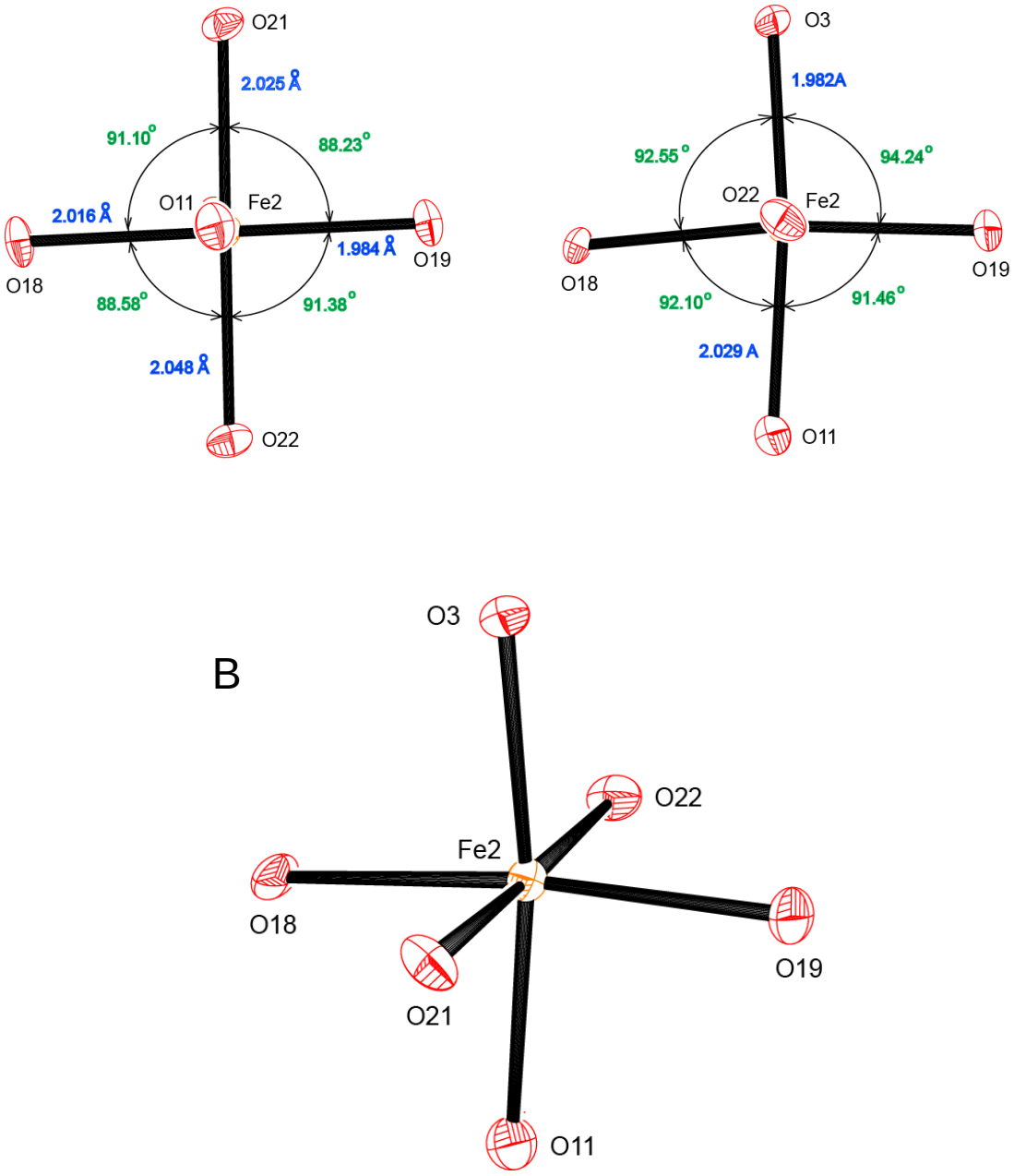

Figure S5. Environment of Fe2 center in the structure: **A** – two orthogonal projections, **B** – prospective view showing small distortions of octahedral polyhedron of the metal center.

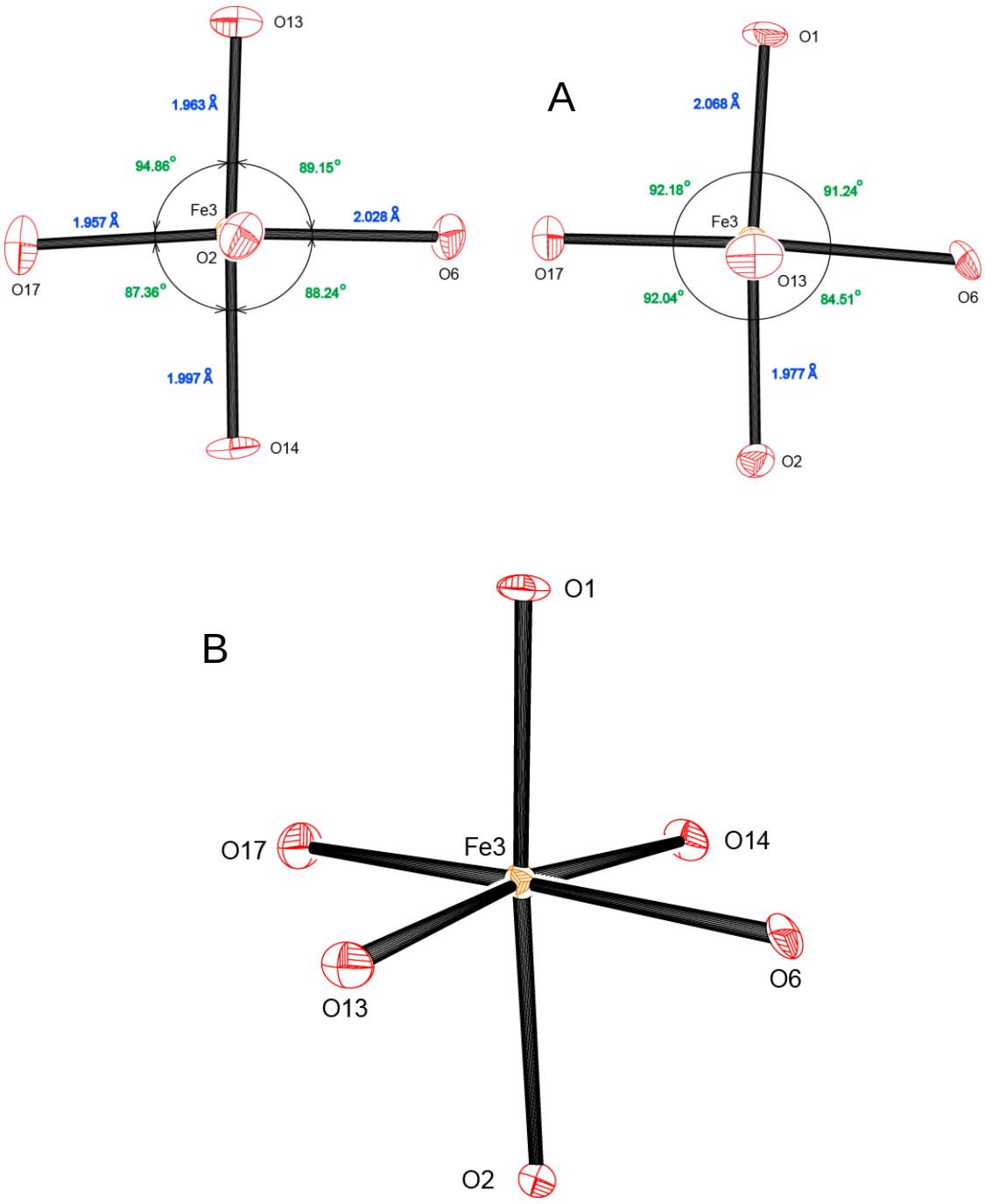

Figure S6. Environment of Fe3 center in the structure: **A** – two orthogonal projections, **B** – prospective view showing small distortions of octahedral polyhedron of the metal center.

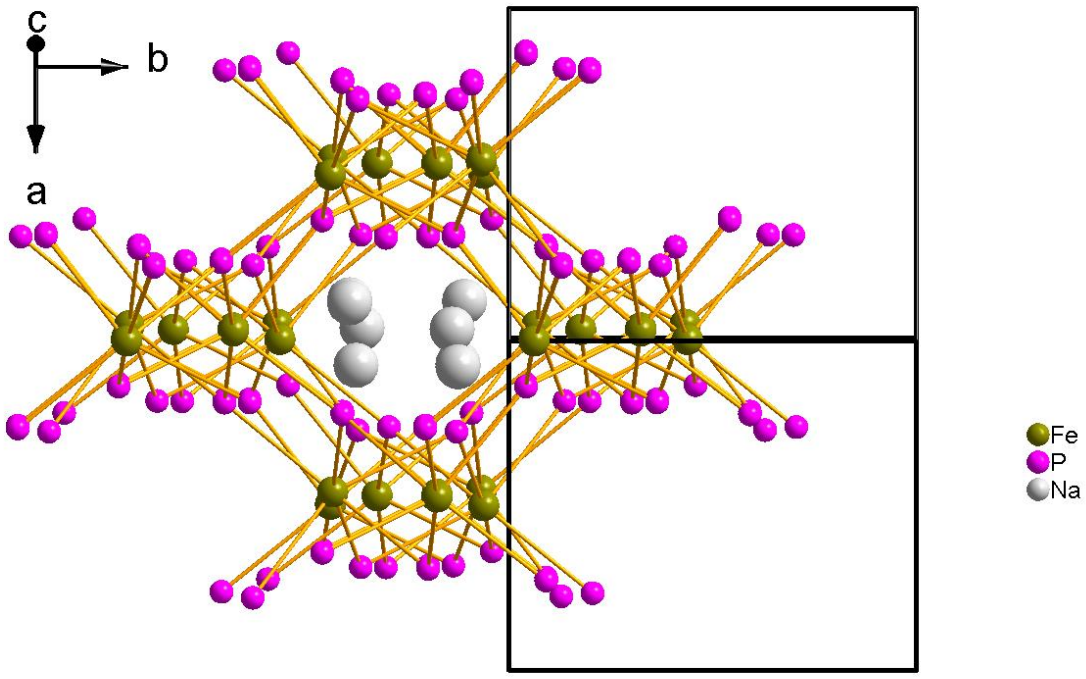

Figure S7. View of the structure of $NaFe(HPO_4)_2$ along [1 0 7] direction showing the channel filled with sodium ions. Note that oxygen atoms have been removed from the structure for clarity in visualization.

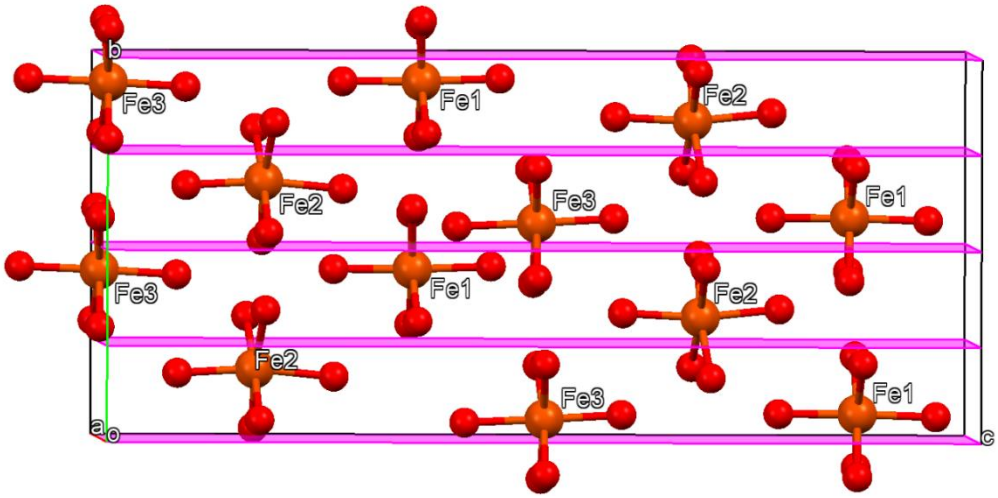

Figure S8. Structure of $NaFe(HPO_4)_2$ viewed along the a-axis showing only the Fe-centered octahedra. Purple planes indicate glide planes. Note the orientation of the crystallographically distinct Fe-octahedra display lack of center of symmetry in the structure.

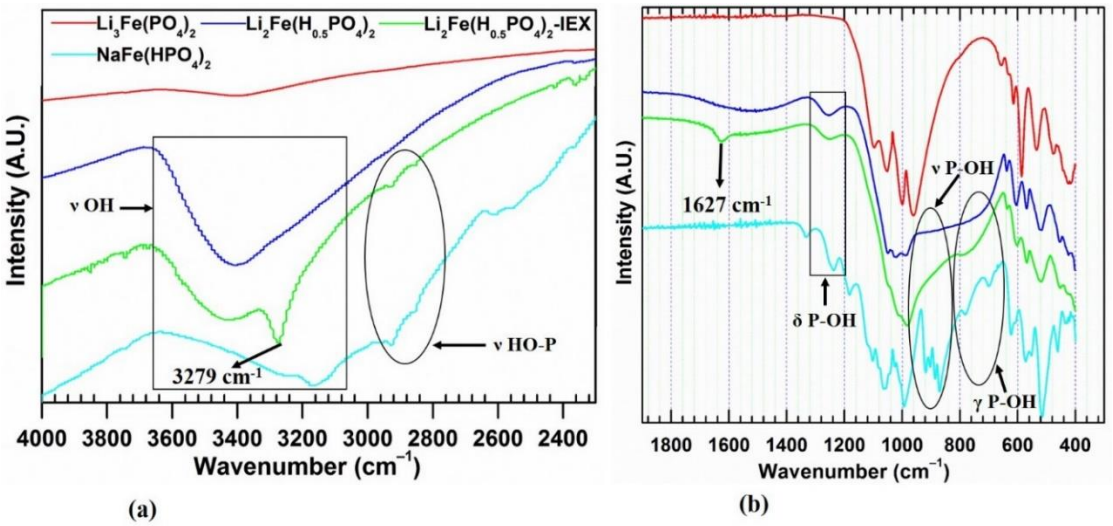

Figure S9. FT-IR spectra for the four compounds.

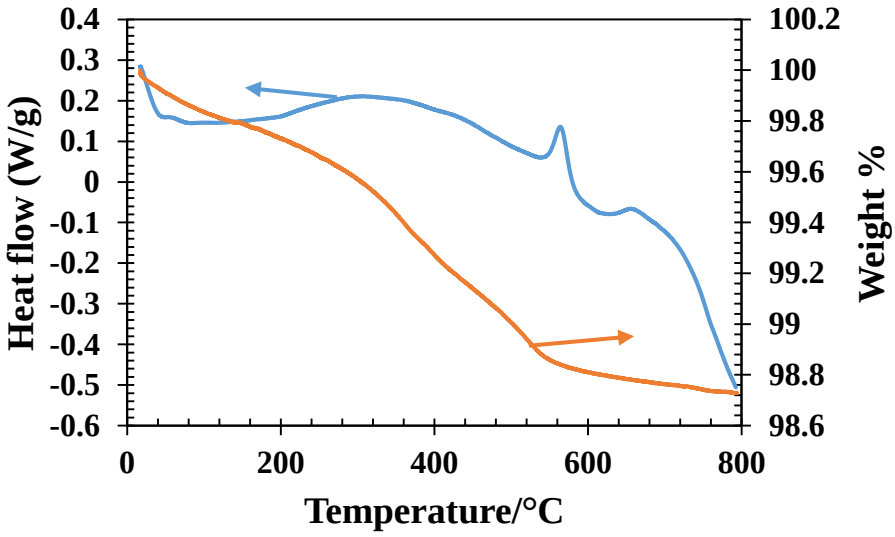

Figure S10. Simultaneous TGA/DSC curves for $Li_3Fe(PO_4)_2$.

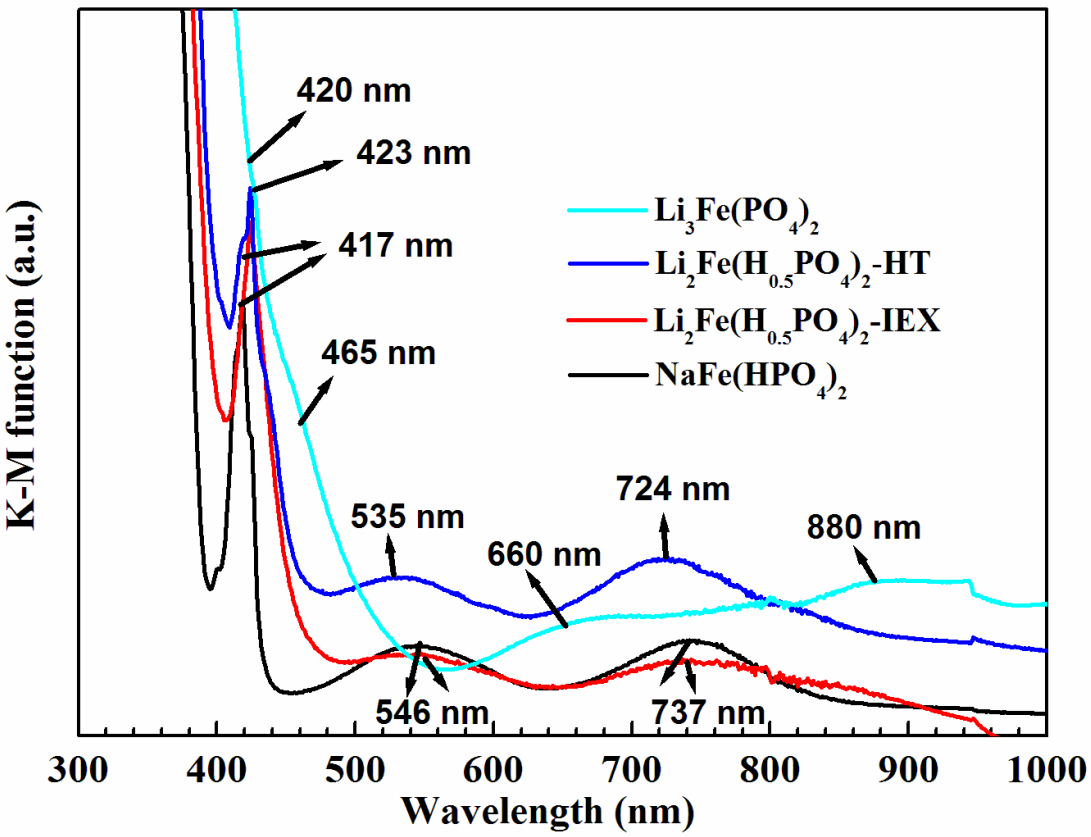

Figure S11: DRS spectra for the compounds.

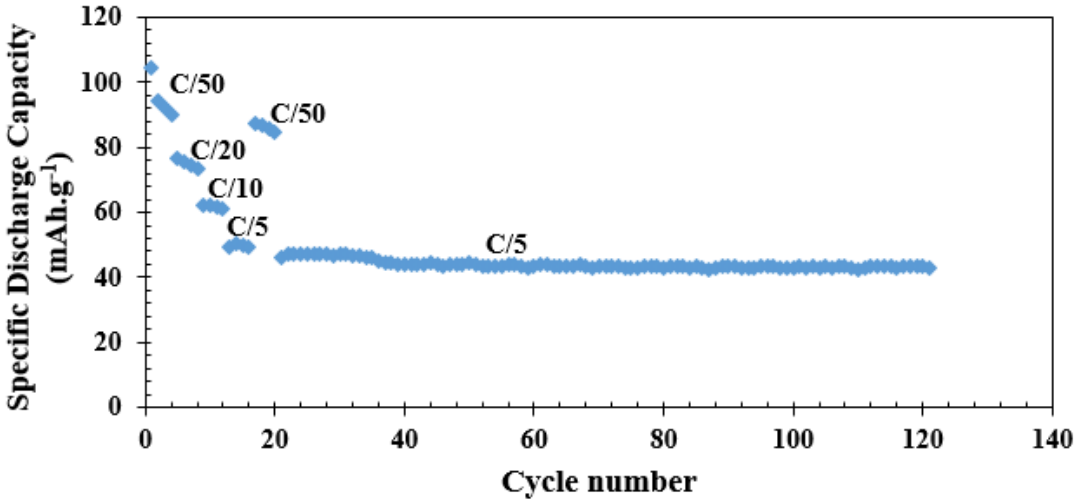

Figure S12. Discharge profile showing 100 cycles at C/5 rate after 20 cycles (four each of C/50, C/20, C/10, C/5) for $Li_2Fe(H_{0.5}PO_4)_2$-IEX.

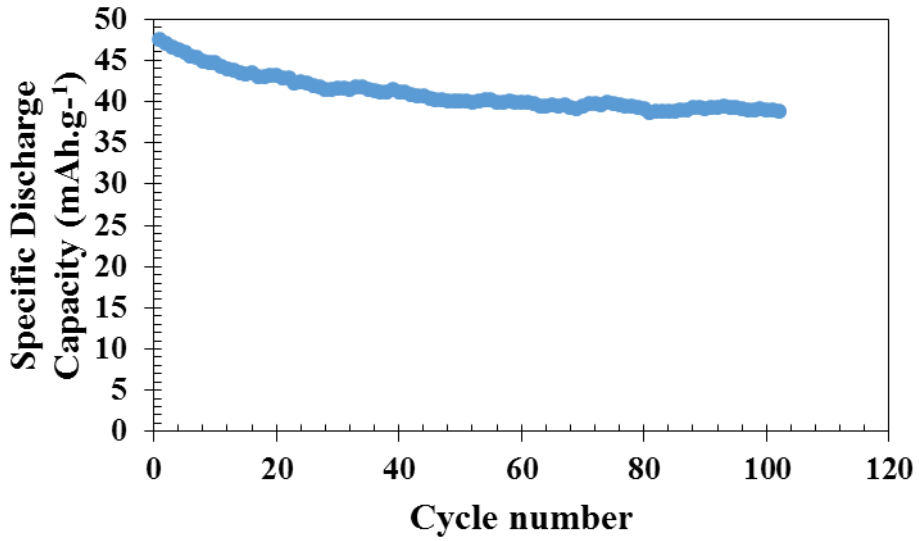

Figure S13. Discharge profile showing 102 cycles at C/5 rate for $Li_3Fe(PO_4)_2$.

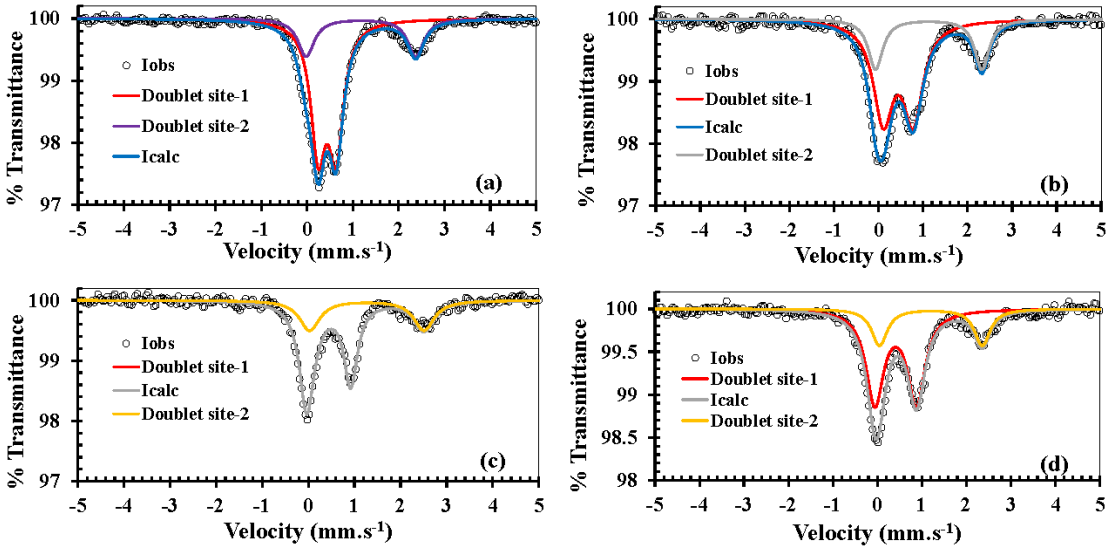

Figure S14. Mossbauer spectra of discharged phases for (a) $NaFe(HPO_4)_2$; (b) $Li_2Fe(H_{0.5}PO_4)_2$-IEX, (c) $Li_2Fe(H_{0.5}PO_4)_2$-HT; (d) $Li_3Fe(PO_4)_2$.

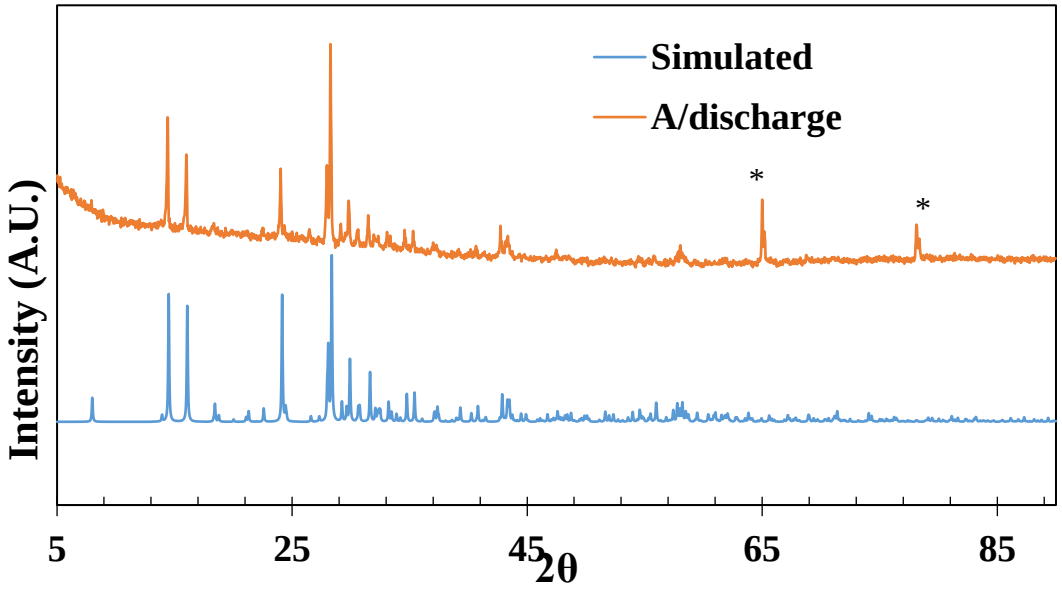

Figure S15. Powder XRD of discharged cathode material for $NaFe(HPO_4)_2$. (* Aluminum peaks).

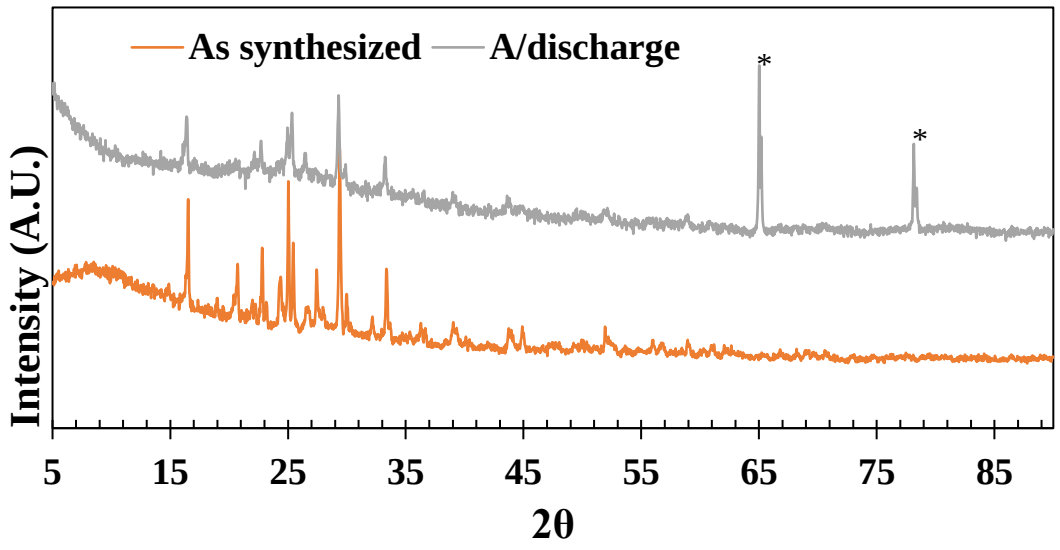

Figure S16. Powder XRD of discharged cathode material for $Li_2Fe(H_{0.5}PO_4)_2$-IEX. (* Aluminum peaks).

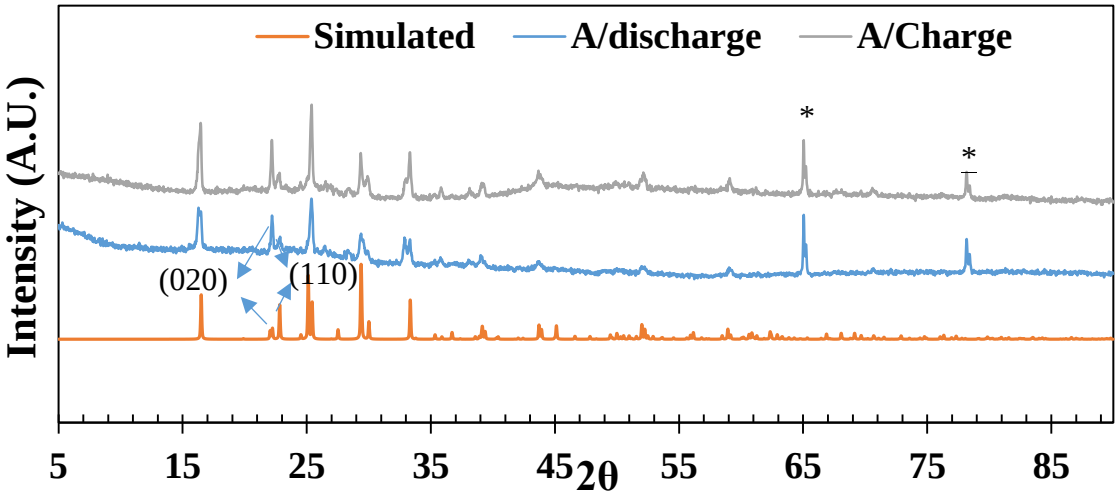

Figure S17. Powder XRD of discharged and charged cathode material for $Li_2Fe(H_{0.5}PO_4)_2$-HT. (* Aluminum peaks).

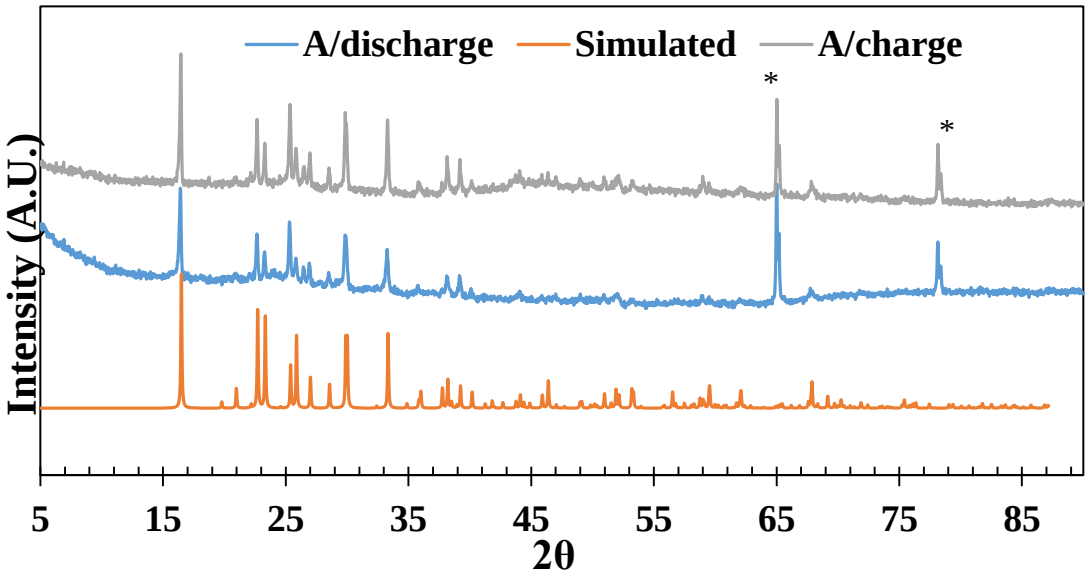

Figure S18. Powder XRD of discharged and charged cathode material for $Li_3Fe(PO_4)_2$. (* Aluminum peaks).

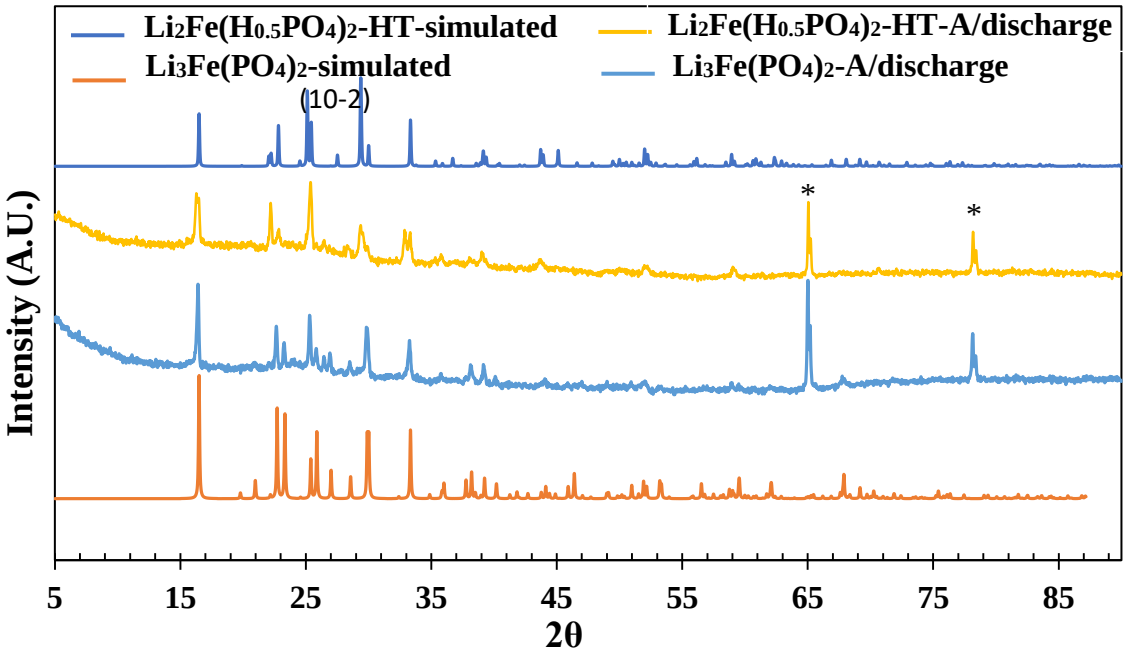

Figure S19. Powder XRDs of discharged cathode materials for $Li_2Fe(H_{0.5}PO_4)_2$-HT and $Li_3Fe(PO_4)_2$ showing the presence of same set of diffraction lines in the reduced phases indicating structurally same reduced phase for the compounds.

Table S1. Atomic coordinates (x 10^4) and equivalent isotropic displacement parameters ($Å^2x10^3$) for $NaFe(HPO_4)_2$. U(eq) is defined as one third of the trace of the orthogonalized Uij tensor.

$NaFe(HPO_4)_2$					
Atoms	x	y	z	U(eq)	Wyckoff
Fe1	9083(1)	5678(1)	8660(1)	6(1)	4*a*
Fe2	7109(1)	8236(1)	6821(1)	6(1)	4*a*
Fe3	5001(1)	5619(1)	5000(1)	6(1)	4*a*
P1	7712(2)	7945(2)	5351(1)	6(1)	4*a*
P2	5868(2)	3715(2)	8628(1)	6(1)	4*a*
P3	6413(2)	8020(2)	8301(1)	6(1)	4*a*
P4	8172(2)	3636(2)	5022(1)	6(1)	4*a*
P5	5144(2)	5417(2)	6535(1)	7(1)	4*a*
P6	9927(2)	5913(2)	7161(1)	7(1)	4*a*
O1	6747(5)	6979(5)	4959(2)	9(1)	4*a*
O2	8167(6)	9204(5)	4974(2)	8(1)	4*a*
O3	6844(5)	8343(5)	5932(2)	7(1)	4*a*
O4	9297(5)	7178(5)	5550(2)	9(1)	4*a*
O5	7616(5)	4071(5)	8636(2)	9(1)	4*a*
O6	4868(5)	4472(5)	9086(2)	8(1)	4*a*
O7	5717(5)	2151(5)	8660(2)	8(1)	4*a*
O8	5304(6)	4218(5)	7977(2)	10(1)	4*a*
O9	7333(6)	7007(5)	8688(2)	9(1)	4*a*
O10	5897(5)	9247(5)	8680(2)	9(1)	4*a*
O11	7323(5)	8443(5)	7731(2)	9(1)	4*a*
O12	4828(6)	7266(5)	8075(2)	11(1)	4*a*
O13	6442(5)	4032(5)	4990(2)	9(1)	4*a*
O14	8333(5)	2075(5)	4975(2)	10(1)	4*a*
O15	9212(5)	5605(5)	9561(2)	7(1)	4*a*
O16	8722(6)	4101(5)	5679(2)	11(1)	4*a*
O17	4911(6)	5739(5)	5883(2)	12(1)	4*a*
O18	8671(5)	9810(5)	6833(2)	9(1)	4*a*
O19	5604(5)	6682(5)	6916(2)	9(1)	4*a*
O20	6514(5)	4313(4)	6596(2)	13(1)	4*a*
O21	5235(5)	9540(5)	6845(2)	8(1)	4*a*
O22	8983(5)	6901(4)	6759(2)	8(1)	4*a*
O23	9058(6)	5678(5)	7758(2)	8(1)	4*a*
O24	6620(5)	1566(4)	7293(2)	10(1)	4*a*
Na1	7820(3)	3606(2)	7479(1)	14(1)	4*a*
Na2	8129(4)	8752(3)	3895(1)	20(1)	4*a*
Na3	5964(4)	8911(3)	9816(2)	20(1)	4*a*

Table S2. Atomic coordinates (x 10^4) and equivalent isotropic displacement parameters ($Å^2x10^3$) for $Li_2Fe(H_{0.5}PO_4)_2$-HT. U(eq) is defined as one third of the trace of the orthogonalized Uij tensor.

$Li_2Fe(H_{0.5}PO_4)_2$-HT					
Atoms	x	y	z	U(eq)	Wyckoff
Fe1	0	0	0	6(1)	2*a*
P1	6335(1)	6540(1)	7652(1)	6(1)	4*e*
O1	2979(3)	6763(2)	6511(2)	9(1)	4*e*
O2	7937(4)	8225(2)	8136(2)	10(1)	4*e*
O3	7762(4)	5465(2)	6594(2)	10(1)	4*e*
O4	6900(4)	5605(2)	9478(2)	11(1)	4*e*
Li1	479(10)	8656(6)	6578(6)	16(1)	4*e*

Table S3. Set of reactions carried out at different pH, temperature and other different conditions.

S.No.	Reactants	Conditions	Product (s)
1	$FeSO_4 \cdot 7H_2O + H_3PO_4 + H_3BO_3 + NaF + H_2O$	185°C, 24 h- 6 days, HT	$NaFe(HPO_4)_2$*
2	$FeSO_4 \cdot 7H_2O + H_3PO_4 + NaF + H_2O$	185°C, 24 h, HT	Na_3FeF_6
3	$FeSO_4 \cdot 7H_2O + H_3PO_4 + CH_3COOH + NaF + H_2O$	185°C, 24 h, HT	Na_3FeF_6 & $Na_3Fe_2(PO_4)_2(OH)_2F$
5	$FeSO_4 \cdot 7H_2O + H_3PO_4 + H_3BO_3 + LiF + H_2O$	185°C, 24 h, HT	$LiFe(PO_4)(OH)_xF_{1-x}$
6	$FeSO_4 \cdot 7H_2O + H_3PO_4 + H_3BO_3 + NaOH + H_2O$	185°C, 24 h, HT	$NaFeBP_2O_7(OH)_3$
7	$FeSO_4 \cdot 7H_2O + H_3PO_4 + H_3BO_3 + NaF + H_2O$	145°C, 24 h, HT	No solid product
9	$NaFe(HPO_4)_2 + LiNO_3 + H_2O$	185°C, 24 h, HT	$LiFe(PO_4)(OH)$
10	$NaFe(HPO_4)_2 + LiNO_3 + H_2O$	75°C, 8 h, IEx, stir	$NaFe(HPO_4)_2$
11	$NaFe(HPO_4)_2 + LiNO_3 + H_2O$	75°C, 16 h, IEx, Stir	$NaFe(HPO_4)_2$
12	$NaFe(HPO_4)_2 + LiNO_3 + H_2O$	75°C, 24 h, IEx, Stir	$NaFe(HPO_4)_2$ + $Li_2Fe(H_{0.5}PO_4)_2$
13	$NaFe(HPO_4)_2 + LiNO_3 + H_2O$	75°C, 48 h, IEx, Stir	$Li_2Fe(H_{0.5}PO_4)_2$ (major) & $Fe(PO_4).2H_2O$(minor)
14	$Fe(NO_3)_3 \cdot 9H_2O + LiOH \cdot H_2O + H_3PO_3$	175°C, 6 days	$Li_2Fe(H_{0.5}PO_4)_2$*
15	$Li_2Fe(H_{0.5}PO_4)_2 + LiNO_3$	215°C, 3 days Solid state IEX	$Li_3Fe(PO_4)_2$*

*This work

Table S4. The fitted ^{57}Fe Mössbauer spectroscopic values for Isomer Shift (IS) and Quadrupole Splitting (QS) of the electrochemically discharged cells.

Compounds	No of sites	Isomer Shift ($mm.s^{-1}$)	Quadrupole Splitting ($mm.s^{-1}$)	Site population (%)
$NaFe(HPO_4)_2$	Doublet site-1	0.43(4)	0.39(4)	75
	Doublet site-2	1.17(1)	2.39(2)	25
$Li_2Fe(H_{0.5}PO_4)_2$-IEX	Doublet site-1	0.44(4)	0.67(1)	72.4
	Doublet site-2	1.12(1)	2.38(2)	27.6
$Li_2Fe(H_{0.5}PO_4)_2$-HT	Doublet site-1	0.43(2)	0.96(2)	64.7
	Doublet site-2	1.26(1)	2.47(3)	35.3
$Li_3Fe(PO_4)_2$	Doublet site-1	0.41(2)	0.93(3)	73.9
	Doublet site-2	1.20(2)	2.3(5)	26.1

REFERENCES

1. Padhi, A. K.; Nanjundaswamy, K. S.; Goodenough, J. B. Phospho-olivines as Positive-Electrode Materials for Rechargeable Lithium Batteries, *J. Electrochem. Soc.* **1997**, *144*, 1188 - 1194.

2. Padhi, A. K.; Manivannan, V.; Goodenough, J. B. Tuning the position of the redox couples in materials with NASICON structure by anionic substitution, *J. Electrochem. Soc*. **1998**, *145*, 1518 - 1520.

3. Masquelier, C.; Croguennec, L. Polyanionic (phosphates, silicates, sulfates) frameworks as electrode materials for rechargeable Li (or Na) batteries, *Chem. Rev.* **2013**,*113*, 6552 - 6591.

4. Riou-Cavellec, M.; Riou, D.; Férey, G. Magnetic iron phosphates with an open framework, *Inorganica Chimica Acta*. **1999**, *291 (1-2)*, pp. 317-325.

5. Murugavel, R.; Choudhury, A.; Walawalkar, M. G.; Pothiraja, R.; Rao, C. N. R. Metal Complexes of Organophosphate Esters and Open-Framework Metal Phosphates: Synthesis, Structure, Transformations, and Applications, *Chem. Rev.* **2008**, *108*, 3549 - 3655.

6. Natarajan, S.; Mandal, S. Open-framework structures of transition-metal compounds, *Angew. Chem. Int. Ed.* **2008**, *47*, 4798 – 4828.

7. Keates, A. C.; Armstrong, J. A.; Weller, M. T. Iron fluorophosphates, *Dalton Trans.*, **2013**, *42*, 10715 – 10724.

8. Xie, H.; Li, Y.; Goodenough, J. B. NASICON-type $Li_{1+2x}Zr_{2-x}Ca_x(PO_4)_3$ with high ionic conductivity at room temperature, *RSC Adv.*, **2011**, ***1***, 1728 – 17.

9. Padhi, A. K.; Nanjundaswamy, K. S.; Masquelier, C.; Okada, S.; Goodenough, J. B. Effect of Structure on the Fe^{3+}/Fe^{2+} Redox Couple in Iron Phosphates, *J. Electrochem. Soc.* **1997**, *144*, 1609 - 1613.

10. Song, Y.; Zavalij, P. Y.; Chernova, N. A.; Whittingham, M. S. Synthesis, Crystal Structure, and Electrochemical and Magnetic Study of New Iron (III) Hydroxyl-Phosphates, Isostructural with Lipscombite, *Chem. Mater*. **2005**, *17*, 1139 - 1147.

11. Dollé, M.; Patoux, S.; Richardson, T. J. Lithium insertion chemistry of phosphate phases with the lipscombite strucrure, *J. Power Sources* **2005**, *144*, 208 – 213.

12. Han, S.; Wang, J.; Li, S.; Wu, D.; Feng, X. Graphene aerogel supported $Fe_5(PO_4)_4(OH)_3 \cdot 2H_2O$ microspheres as high performance cathode for lithium ion batteries, *J. Mater. Chem. A.* **2014**, *2*, 6174 – 6179.

13. Ramesh, T. N.; Lee, K. T.; Ellis, B. L.; Nazar, L. F. Tavorite lithium iron fluorophosphate cathode materials: Phase transition and electrochemistry of $LiFePO_4F$-Li_2FePO_4F, *Electrochem. Solid-State Lett.* **2010**, *13*, A43 – A47.

14. Marx, N.; Croguennec, L.; Carlier, D.; Wattiaux, A.; Le Cras, F.; Suard, E.; Delmas, C. The structure of tavorite $LiFePO_4(OH)$ from diffraction and GGA + *U* studies and its preliminary electrochemical characterization, *Dalton Trans.* **2010**, *39*, 5108 - 5116.

15. Ellis, B. L.; Nazar, L. F. Anion-Induced Solid Solution Electrochemical Behavior in Iron Tavorite Phosphates, *Chem. Mater.*, **2012**, *24*, 966 - 968.

16. Yaghoobnejad-Asl, H.; Choudhury, A. Phosphorous acid route synthesis of iron tavorite phases, $LiFePO_4(OH)_xF_{1-x}$ $[0 \leq x \leq 1]$ and comparative study of their electrochemical activities, *RSC Adv*. **2014**, *4* , 37691 - 37700.

17. Ellis, B. L.; Makahnouk, W. R. M.; Rowan-Weetaluktuk, W. N; Ryan, D. H.; Nazar, L. F. Crystal Structure and Electrochemical Properties of A_2MPO_4F Fluorophosphates (A = Na, Li; M = Fe, Mn, Co, Ni), *Chem. Mater.* **2010**, *22*, 1059 – 1070.

18. Khasanova, N. R.; Drozhzhin, O. A.; Storozhilova, D. A.; Delmas, C.; Antipov, E. V. New Form of $Li_2FePO4F$ as Cathode Material for Li-Ion Batteries, *Chem. Mater*. **2012**, *24*, 4271 – 4273.

19. Song, Y.; Zavalij, P. Y.; Suzuki, M.; Whittingham, M. S. New Iron(III) Phosphate Phases: Crystal Structure and Electrochemical and Magnetic Properties, *Inorg. Chem.* **2002**, *41*, 5778 – 5786.

20. Reale, P.; Scrosati, B.; Delacourt, C; Wurm, C.; Morcrette, M.; Masquelier, C. Synthesis and Thermal Behavior of Crystalline Hydrated Iron(III) Phosphates of interest as Positive Electrodes in Li Batteries, *Chem. Mater.* **2003,** *15*, 5051-5058.

21. Zaghib, K.; Julien, C. M.; Structure and electrochemistry of $FePO_4 \cdot 2H_2O$ hydrate, *J. Power Sources* **2005**, *142*, 279 – 284.

22. Marx, N.; Croguennec, L.; Carlier, D.; Bourgeois, L.; Kubiak, P.; Le Cras, F.; Delmas, C. Structural and Electrochemical Study of a New Crystalline Hydrated Iron(III) Phosphate $FePO_4 \cdot H_2O$ Obtained from $LiFePO_4(OH)$ by Ion Exchange, *Chem. Mater.* **2010**, *22*, 1854 - 1861.

23. Wurm, C.; Morcrette, M.; Rousse, G.; Dupont, L.; Masquelier, C. Lithium Insertion/Extraction into/from $LiMX_2O_7$ Compositions (M = Fe, V; X = P, As) Prepared via a Solution Method, *Chem. Mater.* **2002**, *14*, 2701 - 2710.

24. Nishimura, S. -I.; Nakamura, M.; Natsui, R.; Yamada, A. New Lithium Iron Pyrophosphate as 3.5 V Class Cathode Material for Lithium Ion Battery, *J. Am. Chem. Soc.* **2010**, *132*, 13596 – 13597.

25. Barpanda, P.; Ye, T.; Nishimura, S.; Chung, S. C.; Yamada, Y.; Okubo, M.; Zhou, H. S.; Yamada, A. Sodium iron pyrophosphate: A novel 3.0 V iron-based cathode for sodium-ion batteries, *Electrochem. Commun.* **2012**, *24*, 116 – 119.

26. Kim, H.; Park, I.; Lee, S.; Kim, H.; Park, K. – Y.; Park, Y. – U.; Kim, H.; Kim, J.; Lim, H. – D.; Yoon, W. – S.; Kang, K. Understanding the Electrochemical Mechanism of the New Iron-Based Mixed-Phosphate $Na_4Fe_3(PO_4)_2(P_2O_7)$ in a Na Rechargeable Battery, *Chem. Mater.* **2013**, *25*, 3614 – 3622.

27. Hailong Chen, H.; Hautier, G.; Jain, A.; Moore, C.; Kang, B.; Doe, R.; Wu, L.; Zhu, Y.; Tang, Y.; Ceder, G. Carbonophosphates: A New Family of Cathode Materials for Li-Ion Batteries Identified Computationally, *Chem. Mater.* **2012**, *24*, 2009 – 2016.

28. Yaghoobnejad Asl, H.; Choudhury, A. A Combined Theoretical and Experimental Approach to the Discovery of Electrochemically Active Mixed Polyanionic Phosphatonitrates, $A FePO_4NO_3$ (A = NH_4/Li, K), *Chem. Mater.* **2016**, *28*, 5029 – 5036.

29. Yaghoobnejad Asl, H.; Stanley, P.; Ghosh, K.; Choudhury, A. Iron Borophosphate as a Potential cathode for Lithium- and Sodium-ion Batteries, *Chem. Mater.* **2015**, *27*, 7058 – 7069.

30. Tao, L.; Rousse, G.; Sougrati, M. T.; Chotard, J. -N.; Masquelier, C. $(NH_4)_{0.75}Fe(H_2O)_2[BP_2O_8]\cdot 0.25H_2O$, a Fe3+/Fe2+ mixed valence cathode material for Na-ion battery exhibiting a helical structure, *J. Phys. Chem. C* **2015**, *119*, 4540 – 4549.

31. Hautier, G.; Jain, A.; Ong, S. P.; Kang, B.; Moore, C.; Doe, R.; Ceder, G. Phosphates as Lithium-ion Battery Cathodes: An Evaluation Based on High-Throughput *ab Initio* Calculations, *Chem. Mater.* **2011**, *23*, 3495 – 3508.

32. Hautier, G.; Jain, A.; Chen, H.; Moore, C.; Ong, S. P.; Ceder, G. Novel mixed polyanions lithium-ion battery cathode materials predicted by high-throughput ab initio computations, *J. Mater. Chem.* **2011**, *21*, 17147 – 17153.

33. Mueller, T.; Hautier, G.; Jain, A.; Ceder, G. Evaluation of tavorite-structured cathode materials for lithium-ion batteries using high-throughput computing, *Chem. Mater.* **2011,** *23*, 3854 – 3862.

34. Gopalakrishnan, J. Chimie Douce approaches to the synthesis of metastable oxide materials, *Chem. Mater*, **1995**, *7*, 1265 – 1275.

35. Yaghoobnejad Asl, H.; Ghosh, K.; Choudhury, A. A highly fluorinated lithium iron phosphate with interpenetrating lattices: electrochemistry and ionic conductivity, *Dalton Trans.*, **2017**, *46*, 12588 – 12596.

36. Redrup, K. V.; Weller, M. T. Synthesis and crystal structures of iron hydrogen phosphates, *Dalton Trans.*, **2009**, 3786–3792.

37. Mi, J. -X.; Borrmann, H.; Zhang, H.; Huang, Y. -X.; Schnelle, W.; Zhao, J. -T.; Kniep, R. Synthesis, magnetism, and crystal structure of $Li_2Fe[(PO_4)(HPO_4)]$ and its hydrogen position refinement, *Z. Anorg. Allg. Chem.* **2004**, *630*, 1632 – 1636.

38. Bruker (2017). APEX3, SAINT and SHELXTL. Bruker AXS Inc., Madison, Wisconsin, USA.

39. Bruker- SMART. Bruker AXS Inc., Madison, Wisconsin, USA. **2002**.

40. Bruker- SAINT and SADABS. Bruker AXS Inc., Madison, Wisconsin, USA, **2008**.

41. Sheldrick, G.M. A short history of SHELX, *Acta Cryst.*, **2008**, *A64*, 112.

42. Sheldrick, G.M.; Hubshle, C. B.; Dittrich, B. Shelxle: A Qt graphical user interface for SHELXL , *J. Appl. Cryst.* **2011**, *44*, 1281 – 1284.

43. Favre-Nicolin, V.; Cerny, R. Free objects for crystallography: A modular approach to ab initio structure determination from powder pattern, *J. Appl. Cryst*, **2002**, *35*, 734 – 743.

44. Toby, B. H.; Von Dreele, R. B. GSAS-II: the genesis of a modern open-source all-purpose crystallography software package, *J. Appl. Cryst*. **2013**, *46*, 544-549.

45. Lagarec, K.; Rancourt, D. G. Extended Voigt-based analytic lineshape method for determining N-dimensional correlated hyperfine parameter distributions in Mössbauer spectroscopy. *Nucl. Instrum. Methods Phys. Res., Sect. B,* **1997,** *129*, 266-280.

46. Abeysinghe, D.; Smith, M. D.; zur Loye, H. -C. One-step mild hydrothermal method to prepare low valent sodium vanadium(III) monohydrogenphosphate: $NaV(HPO_4)_2$, *Solid State Sci.*, **2017**, *69*, 1 – 6.

47. Yakubovich, O. V. Crystal structure of $(NH_4)Fe(HPO_4)_2$, *Kristallografiya*, **1993**, *38*, 43 – 48.

48. Alfonso, B. F.; Blanco, J. A.; Fernández-Díaz, M. T.; Trobajo. C.; Khainakov, S. A.; García, J. R. On the crystal structure and thermal decomposition of ammonium-iron(III)bis(hydrogenphosphate), *Dalton Trans.*, **2010**, *39*, 1791 – 1796.

49. Jones, C. W.; Battle, P. D.; Lightfoot, P.; Harrison, W. T. A. The Structure of Ferric Oxonium Bis(hydrogenphosphate), $Fe^{3+}.(H_30)^{+}.2(PO_4H)^{2-}$, *Acta Cryst.* **1989**, *C45*, 367 – 371.

50. Boivin, E.; Masquelier, C.; Croguennec, L.; Chotard, J. -N. Crystal Structure and Lithium Diffusion Pathways of a Potential Positive Electrode Material for Lithium-Ion Batteries: $Li_2V^{III}(H_{0.5}PO_4)_2$, *Inorg. Chem.* **2017**, *56*, 6776 – 6779.

51. Pérez-Flores, J. C.; García-Alvarado, F.; Hoelzel, M.; Sobrados, I.; Sanz, J.; Kuhn, A. Insight into the channel ion distribution and influence on the lithium insertion properties of hexatitanates $A_2Ti_6O_{13}$(A = Na, Li, H) as candidates for anode materials in lithium-ion batteries, *Dalton Trans.*, **2012**, *41*, 14633 – 14642.

52. Armstrong, A. R.; Arrouvel, C.; Gentili, V.; Parker, S. C.; Islam, M. S.; Bruce, P. G. Lithium coordination sites in Li_xTiO_2(B): A structural and computational study, *Chem. Mater.*, **2010**, *22*, 6426 – 6432.

53. Reynaud, M.; Rousse, G.; Sougrati, M. T.; Chotard, J. N.; Carvajal, J. R.; Tarascon, J. -M. Marinite $Li_2M(SO_4)_2$ (M = Co, Fe, Mn) and $Li_1Fe(SO_4)_2$: Model Compounds for Super-Super- Exchange Magnetic Interactions, *Inorg. Chem.*, **2013**, *52* (18), 10456–10466.

54. Ait Salah, A.; Jozwiak, P.; Zaghib, K.; Garbarczyk, J.; Gendron, F.; Mauger, A.; Julien, C. M. FTIR features of lithium-iron phosphates as electrode materials for rechargeable lithium batteries, *Spectrochimica Acta - Part A: Molecular and Biomolecular Spectroscopy*, **2006**, *65*, 1007 – 1013.

55. Filaretov, A. A.; Rusakov, D. A.; Simonov, S. V.; Khasanov, S. S.; Komissarova, L. N. Hydrothermal synthesis and crystal structure of lithium scandium orthophosphate $Li_2Sc[H(PO_4)_2]$. The $Li_2M^{III}[H(PO_4)_2]$ family (M^{III}= Fe, Sc, In), *Russ. J. Inorg. Chem.*, **2009**, *54*, 1750 – 1762.

56. Kubelka, P.; Munk, F. Ein Beitrag Zur Optik Der Farbanstriche. *Z. Techn. Phys.*, **1931**. *12*, 593 – 601.

57. Sherman, D. M.; Waite, T. D. Electronic spectra of Fe^{3+} oxides and oxide hydroxides in the near IR to near UV, *Am. Mineralogist*, **1985**, *70*, 1262 – 1269.

58. Lever, A. B. P. *Inorganic Electronic Spectroscopy*; Elsevier Science Publisher BV: Amsterdam, The Netherlands, 1984.

59. Nan, C.; Lu, J.; Chen, C.; Peng, Q.; Li, Y. Solvothermal synthesis of lithium iron phosphate nanoplates, *J. Mater. Chem.*, **2011**, *21*, 9994 – 9996.

60. Wang, L.; He, X.; Sun, W.; Wang, J.; Li, Y.; Fan, S. Crystal orientation tuning of $LiFePO_4$ nanoplates for high rate lithium battery cathode materials, *Nano Lett.*, **2012,** *12*, 5632 – 5636.

61. Delacourt, C.; Poizot, P.; Bonnin, D.; Masquelier, C. Lithium-Insertion Mechanism in Crystalline and Amorphous $FePO_4 \cdot nH_2O$, *J. Electrochem. Soc.*, **2009**, *156*, A595 – A605.

62. Li, Z.; Shinno, I. Next nearest neighbor effects in triphylite and related phosphate minerals, *Mineralogical Journal*, **1997**, *19*, 99 – 107.

63. Hermann, R. P.; Hatert, F.; Fransolet, A. -M.; Long, G. J.; Grandjean, F. Mössbauer spectral evidence for next-nearest neighbor interactions within the alluaudite structure of $Na_{1-x}Li_xMnFe_2(PO_4)_3$, *Solid State Sci.*, **2002**, 4, 507 – 513.

64. Bhattacharjee, A.; Feyerherm, R.; Steiner, M. Study of the negative magnetization phenomenon in $NBu_4[Fe^{II}Fe^{III}(ox)_3]$, *J. Phys. Soc. Jpn*. **1999**, *68*, 1679.

65. Hagen, K. S.; Naik, S. G.; Huynh, B. H.; Masello, A.; Christou, G. Intensely colored mixed-valence Iron(II) Iron(III) formate analogue of prussian blue exhibits Néel N-Type ferrimagnetism, *J. Am. Chem. Soc.* **2009,** *131*, 7516 – 7517.

66. Albino, M.; Clark, L.; Lhoste, J.; Payen, C.; Grenèche, J. -M.; Lightfoot, P.; Maisonneuvea, V.; Leblanca, M. A magnetisation and Mössbauer study of triazole $(M_{1-x}^{2+}M_x^{3+})M^{3+}F_5(Htaz)_{1-x}(taz)_x$ weberites (M = Fe, Co, Mn, Zn, Ga, V), *Dalton Trans*., **2017**, *46*, 5352.

III. ELECTROCHEMISTRY OF ILLUSIVE BARBOSALITE, $FE^{2+}FE^{3+}_2(PO_4)_2(OH)_2$: AN IRON PHOSPHATE RELATED TO LIPSCOMBITE STRUCTURE

Prashanth Sandineni[a], Kartik Ghosh[b], and Amitava Choudhury[a,*]

[a]Department of Chemistry, Missouri University of Science and Technology, Rolla, MO 65409, USA.

[b]Department of Physics, Astronomy and Materials Science and Center for Applied Science and Engineering, Missouri State University, Springfield, Missouri 65897, USA.

ABSTRACT

Barbosalite, an iron hydroxy-phosphate belonging to the family of Lazulite has been synthesized using hydrothermal route and its electrochemical property is investigated for the first time with respect to Li-ion batteries. The structure, as determined from single-crystal X-ray diffraction data, built up of undulating layer of FeO_6 octahedra, consisting of trimers and PO_4 tetrahedral units. Magnetic susceptibility measurements show predominant overall anti-ferromagnetic interactions and room temperature ^{57}Fe Mössbauer spectroscopic studies confirm the mixed 3+ and 2+ oxidation states of Fe in the compound. The compound is stable up to 400 °C and undergo facile electrochemical lithium insertion. Galvanostatic charge-discharge studies indicate that up to 0.7 lithium ions per formula unit can be inserted at an average voltage of 2.6 V. The barbosalite phase seems to undergo irreversible phase transition upon lithiation as evident from the powder X-ray diffraction pattern of the reduced and oxidized phases.

1. INTRODUCTION

Iron phosphates are extensively investigated as electrode materials for Li-ion batteries since Goodenough's group discovery of $LiFePO_4$ as an inexpensive and environmentally friendly 3.5 V cathode material for Li-ion batteries.[1] Iron hydroxy phosphates, often called basic iron phosphates,[2] are interesting class of materials that have found applications in catalysis and also tested for cathodes for rechargeable lithium-ion batteries.[3−7] These basic phosphates of iron are widespread in mineral kingdom and display rich crystal chemistry.[2] By virtue of the presence of hydroxide ion in these iron phosphates, FeO_n polyhedra are either corner- or edge-/face-shared to yield finite or infinite chains of iron-centered polyhedra.[2] Amongst the various hydroxy phosphates, the presence of a face-shared trimeric unit, termed as *h*-cluster by P. B. Moore, is quite common and different connectivities between the *h*-clusters with other iron-oxo clusters and phosphate tetrahedral unit create different structure types.[2] Mineral families of basic iron phosphates that contain the octahedral face-sharing three-cluster include rockbridgeite ($FeFe_4(OH)_5(PO_4)_3$),[2] beraunite ($Fe_3(OH)_{2.5}(PO_4)_2(H_2O)_3$),[8] lipscombite ($Fe^{2+}Fe^{3+}{}_2(PO_4)_2(OH)_2$)[9,10] and barbosalite ($Fe^{2+}Fe^{3+}{}_2(PO_4)_2(OH)_2$)[11] etc and all of them seem to have mixed valency of iron. In lipscombite, the face-shared trimeric units are further face-shared to form the infinite face-shared chain of octahedra where Fe is partially occupied with ¾ Fe/octahedra in 1:2 ratio of Fe^{2+} and Fe^{3+} in the chain. Barbosalite, a member of Lazulite family, is related to lipscombite in which instead of disordered face-shared chain, iron octahedra are ordered and they form isolated trimer of *h*-cluster. The ferric end members ($Fe_{2-y}\square_y(PO_4)(OH)_{3-3y}(H_2O)_{3y-2}$ (y = 2/3 or 0.82)] of the lipscombite structure type with

tetragonal symmetry has been extensively studied as cathode for Li-ion batteries.[6, 12 – 20] Apart from this, hydroxy Tavorite has been studied in recent years as cathodes for Li-ion batteries.[7, 21 – 24] Tavorite, unlike lipscombite, has an infinite chains of corner-shared Fe-octahedra. This iron Tavorite structure-type has been a hallmark of voltage tuning through substitution of OH by more electronegative F.[21, 23] Surprisingly besides these two hydroxy phosphates, no other basic iron phosphate has been investigated for lithium or sodium ion batteries. Barbosalite with ordered Fe-sites can be considered a relative of lipscombite with every fourth octahedral site of which being empty. Therefore, intuitively it should show similar electrochemical activities as the ferric end member of lipscombite but with reduced capacity due to 1/3rd of Fe in +2 oxidation state. However, most of the studies reported on barbosalite are on naturally occurring minerals, there is just one report of synthetic barbosalite which involves a two-step process with two different precursors of iron.[25] In this article we report one-step syntheses of pure barbosalite and study their electrochemistry for the first time with respect to Li-ion insertion. Our synthetic barbosalite has little variation in composition with slightly increased amount of Fe^{2+} due to the dehydroxylation-hydration reaction. The synthetic barbosalite has been characterized by Mössbauer spectroscopy, magnetic measurements, IR and thermogravimetric analysis.

2. EXPERIMENTAL

2.1. MATERIALS

All the chemicals used in the syntheses were as-purchased and without further purification. $FeSO_4 \cdot 7H_2O$, H_3PO_4 (85%), and H_3BO_3 (Reagent grade) were purchased

from Fischer Scientific. $LiOH \cdot H_2O$ and NaF (99%, Reagent grade) were purchased from Alfa Aesar and Aldrich, respectively.

2.1.1. Synthesis. We have employed two different one-step hydrothermal syntheses routes to prepare phase pure barbosalite. In the first approach the compound was synthesized from a mixture of 0.278 g of $FeSO_4 \cdot 7H_2O$ (1 mmol), 0.062 g of H_3BO_3 (1 mmol), 0.042 g of NaF (1 mmol) and 0.13 ml of H_3PO_4 (2 mmol) in 5 ml of H_2O in a 23 ml capacity Teflon-lined stainless steel Paar acid digestion bomb. The reactants were first dissolved in 5 ml of water with constant stirring in a Teflon beaker covered with a lid, which was then placed in the steel autoclave, sealed tightly, and placed in a 185°C pre-heated oven. The autoclave was heated for 24 hours, followed by cooling down to room temperature in ambient air. The product of the reaction consisted of dark colored crystals, which was then filtered and washed with hot water (yield 72%). Since both sodium and fluorine were absent (from EDS analysis) in the final composition, we explored the synthesis with NaOH instead of NaF but it led to a different phase (see Table S1). Subsequently we used LiOH and was able to produce pure phase of barbosalite. In this second approach, hydrothermal reaction was carried out at 175 °C for 3 days by taking a mixture of 1.39 g of $FeSO_4 \cdot 7H_2O$ (5 mmol), 1 ml of H_3PO_4 (10 mmol), 0.31 g of H_3BO_3 (5 mmol), and 0.21 g of $LiOH \cdot H_2O$ (5 mmol) in 9 ml H_2O in a 23 ml capacity vessel. The dark color product (yield 75%) was isolated following similar work up approach as above. It is to be noted here that in both approach, presence of H_3BO_3 was essential to produce barbosalite. Both the methods produce crystals amenable for single-crystal X-ray diffraction study. Various trials of syntheses are given in Table S1 (S.I.)

2.1.2. Chemical Reduction. The compound was subjected to chemical reduction using $LiAlH_4$. 0.1842 g (0.94 mmol) of the compound was mixed with 0.03567 g (0.94 mmol) of $LiAlH_4$ in Tetrahydrofuran (THF) and was stirred continuously at room temperature in an argon filled glovebox for 3 days and then the reaction mixture was filtered, washed with THF and dried under vacuum without exposing to air.

2.2. MATERIAL CHARACTERIZATION

2.2.1. Single-Crystal X-ray Diffraction. Single-crystal X-ray diffraction data were collected from crystals obtained from both the syntheses. The intensity data sets were collected on Bruker Smart Apex diffractometer with monochromated Mo K_α radiation (0.7107 Å). The data sets were collected at room temperature using SMART[26] software employing a scan of 0.3° in ω with an exposure time of 20 s per frame. The cell refinement and data reduction were carried out with SAINT[27] and the program SADABS[27] was used for the absorption correction. The structures were solved by direct methods using SHELX-97 and difference Fourier syntheses.[28] Full-matrix least-squares refinement against $|F^2|$ was carried out using the SHELXTL-PLUS suite of programs.[27] The compound crystallizes in monoclinic crystal system and solved in $P2_1/n$ space group. However, before the final refinement the space group was transformed from $P2_1/n$ to $P2_1/c$ and refined again. Crystals were twinned and a TWIN law was determined using TwinRotMat routine in PLATON[29] and utilized in the final refinement performed with SHELXL-2014 using shelXle software.[30] The crystallographic parameters for the structure solution are given in Table 1. The final atomic coordinates and selected interatomic distances are given in Tables 2 and 3 for the structure solution from the crystals of NaF-based synthesis, while same data

for LiOH-based synthesis are supplied as supplementary materials (see Tables S2, S3, and S4 in S.I.) It is to be noted here that crystal structure solutions from both the syntheses indicate absence of alkali ions, which is supported by EDS for Na and chemical analysis for Li. The final composition derived from crystal structure solutions was $Fe_{0.5}^{2+}Fe^{3+}(PO_4)(OH)$ or $Fe_3(PO_4)_2(OH)_2$, however, Mössbauer spectroscopic data (discussed later) indicated presence of slightly excess Fe^{2+} (Fe^{3+}:Fe^{2+} = 61.8:38.2) than crystallographically derived composition. Due to the absence of any alkali ions into the structure, the only way the excess Fe^{2+} can be explained is by invoking partial replacement of hydroxyl by water through the reduction of Fe^{3+} leading to a final composition of $Fe_{1.5}(PO_4)(OH)_{0.93}(H_2O)_{0.07}$ or $Fe_3(PO_4)_2(OH)_{1.86}(H_2O)_{0.14}$.

2.2.2. Powder X-ray Diffraction (PXRD). The laboratory PXRD pattern was obtained from a PANalytical X'Pert Pro diffractometer equipped with a Cu $K_{\alpha 1,2}$ anode and a linear array PIXcel detector over a 2θ range of 5 to 90° with an average scanning rate of $0.0472°s^{-1}$. Phase purity of the samples was evaluated by laboratory PXRD through the direct comparison with the simulated pattern generated from the atomic coordinates of single-crystal XRD solution (Figure S1, supporting information). However, to confirm the validity of single-crystal structure solution and to determine absence of any impurity phase(s) we have employed high-resolution synchrotron PXRD (S-PXRD) data collected from Advanced Photon Source (APS) in Argonne National Laboratory. Rietveld refinement using GSAS-II[31] of the S-PXRD data from the NaF-based synthesis route converged very well and confirmed absence of any impurity phase(s). A plot of Rietveld refined data of S-PXRD converted into Cu Kα wavelength over a 2θ range of 2 to 90° is

given in Figure 1, however the whole range of S-PXRD from 2θ = 0.5 to 50° in λ = 0.412832 Å has been provided in supporting information (Figure S2).

Table 1. Crystal data and structure refinement for $Fe_3(PO_4)_2(OH)_2$ from NaF route.

Empirical formula	$Fe_3(PO_4)_2(OH)_2$
Formula weight	391.51
Temperature	298(2) K
Wavelength	0.71073 Å
Crystal system	Monoclinic
Space group	*P* 2_1/c
a/Å	7.309(4)
b/Å	7.479(4)
c/Å	7.497(5)
β/°	119.836(6)
Volume	355.5(4) $Å^3$
Z	2
Density (calculated)	3.657 g/cm^3
Absorption coefficient	6.535 mm^{-1}
F(000)	380
Goodness-of-fit on F^2	1.044
Final R indices [I>2sigma(I)]	R1 = 0.0487, wR2 = 0.1284
R indices (all data)	R1 = 0.0574, wR2 = 0.1365

2.2.3. Mössbauer Spectroscopy. ^{57}Fe Mössbauer experiment was performed in transmission geometry at room temperature using a conventional constant acceleration spectrometer. The data were collected using a ^{57}Co (25 mCi) gamma-ray source embedded

in a Rh matrix. Velocity calibration and isomer shifts are given with respect to α-Fe foil at room temperature. The Mössbauer data were analyzed by Lorentzian line fitting using RECOIL software.[32]

Table 2. Atomic coordinates and equivalent isotropic displacement parameters ($Å^2$) of $Fe_3(PO_4)_2(OH)_2$. U(eq) is defined as one third of the trace of the orthogonalized U^{ij} tensor.

Atom	Wyckoff	x/a	y/b	z/c	U(eq)
P(1)	4*e*	0.2465(3)	0.3846(3)	0.2441(3)	0.008(1)
Fe(1)	2*a*	0.0000	0.0000	0.0000	0.011(1)
Fe(2)	4*e*	0.7319(2)	0.2320(1)	0.5069(2)	0.009(1)
O(1)	4*e*	0.3035(11)	0.4960(8)	0.1090(9)	0.014(1)
O(2)	4*e*	0.4304(9)	0.2624(8)	0.3786(9)	0.015(1)
O(3)	4*e*	0.1955(10)	0.5111(8)	0.3749(9)	0.014(1)
O(4)	4*e*	0.0500(9)	0.2679(7)	0.1142(9)	0.011(1)
O(5)	4*e*	0.7375(8)	0.1337(8)	0.7603(8)	0.010(1)

2.2.4. Magnetic Measurements. The variable temperature magnetic susceptibility measurements of the compound (as-prepared) was carried out in the temperature range 5 – 300 K using Quantum Design SQUID magnetometer at 1T applied field while warming up from 5 – 300 K while the sample was cooled under zero applied field (ZFC). Isothermal magnetization measurements were performed at 5 K between 0 to 5 T applied field.

2.2.5. Thermogravimetric Analysis (TGA). TGA has been performed with a TA instruments Q50 TGA from room temperature to 800°C with a scan rate of 10°C min^{-1} under nitrogen atmosphere.

Table 3. Selected bond lengths [Å] and Bond Valence Sum values for the compound.

Atom-Atom	*d* (Å)	Atom-Atom	*d* (Å)	Atom-Atom	*d* (Å)
P1 – O2	1.520(6)	Fe1 – O3$^{\#1}$	2.065(7)	Fe2 – O1$^{\#7}$	1.927(6)
P1 – O1	1.521(6)	Fe1 – O3$^{\#2}$	2.065(7)	Fe2 – O2	1.929(6)
P1 – O3	1.536(6)	Fe1 – O5$^{\#3}$	2.116(5)	Fe2 – O5	2.018(5)
P1 – O4	1.543(6)	Fe1 – O5$^{\#4}$	2.116(5)	Fe2 – O4$^{\#8}$	2.048(6)
		Fe1 – O4$^{\#5}$	2.138(5)	Fe2 – O3$^{\#9}$	2.071(6)
		Fe1 – O4$^{\#6}$	2.138(5)	Fe2 – O5$^{\#1}$	2.122(5)
BVS, P1 = 5.062		BVS, Fe1 = 1.846		BVS, Fe2 = 3.025	

Symmetry transformations used to generate equivalent atoms: $^{\#1}$ x, -y+1/2, z-1/2, $^{\#2}$ -x, y-1/2, -z+1/2, $^{\#3}$ -x+1, -y, -z+1, $^{\#4}$ x-1, y, z-1, $^{\#5}$ -x, -y, -z, $^{\#6}$ x-1, -y+1/2, z-1/2, $^{\#7}$ -x+1, y-1/2, -z+1/2, $^{\#8}$ x+1, -y+1/2, z+1/2, $^{\#9}$ -x+1, -y+1, -z+1.

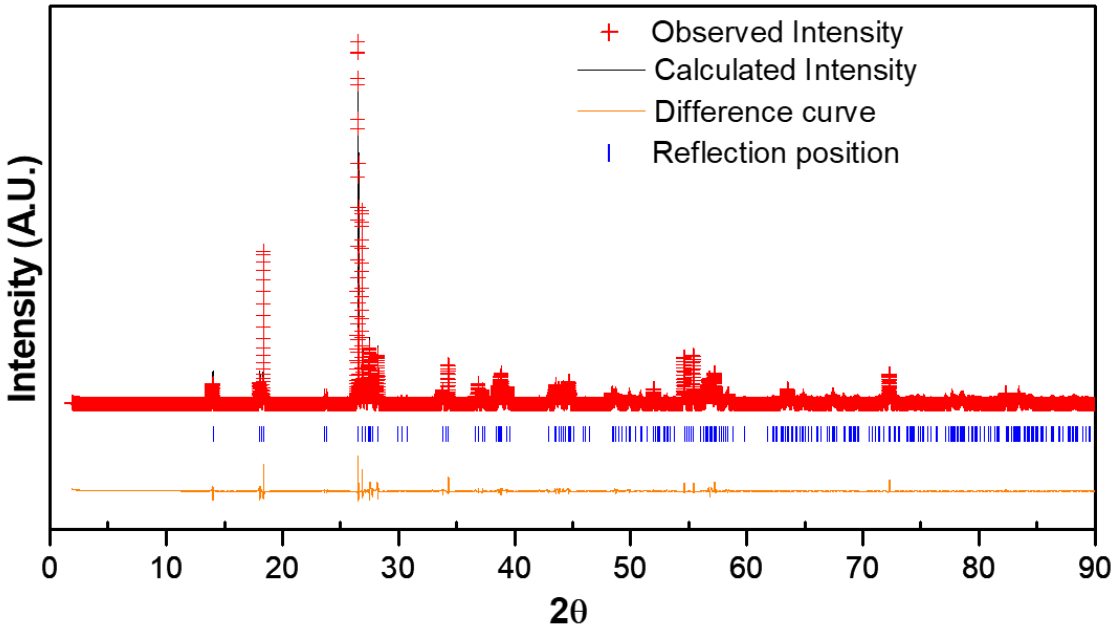

Figure 1. Rietveld refinement of synchrotron XRD data converted to standard PXRD with Cu Kα (λ = 1.540598 Å) of $Fe_3(PO_4)_2(OH)_{1.86}(H_2O)_{0.14}$ showing the observed, calculated and difference curve.

2.2.6. IR Spectroscopy. The IR spectrum was collected using Thermo Nicolet iS50 FT-IR spectrometer over 400–4000 cm^{-1} on a sample using ATR mode.

2.2.7. SEM. The morphology of the powder sample was studied by scanning electron microscopy (Hitachi S 4700 FESEM) at 5 kV operating voltage.

2.2.8. Electrochemical Testing. To evaluate the electrochemical activities of the samples, the as-synthesized compounds were subjected to ball-milling thoroughly after mixing with super P conductive carbon in a SPEX 8000 miller for 3 hours to reduce the particle size. Poly-vinylidene fluoride (PVDF) was then added to the active material as the binder and an optimum amount of N-methyl-2-pyrrolidone (NMP) was added to dissolve the PVDF. The resulting slurry was further ball milled for another 20 minutes to obtain a homogeneous viscous mixture. The ratio of the active material, conducting carbon, and the binder in the cathode mix was 75: 15: 10 and 65:25:10. The slurry of cathode mix was then spread onto a flat sheet of carbon-coated aluminum current collector with help of a glass rod, transferred into a vacuum oven and dried overnight at 85°C.

For electrochemical tests, CR2032 type coin cells were fabricated. The composite cathode film was cut into circular disks (3/8 inch diameter) with 4.0–5.0 mg of active material loading and transferred into an argon filled glove box with an oxygen concentration below 2.0 ppm. The cathode disk and Li anode (0.75 mm thickness Li ribbon cut into circular disk) were assembled in the coin cell casing with a Celgard® 2325 circular sheet placed between the two electrodes as the separator. The electrolyte, 1 M solution of $LiPF_6$ in DMC–EC (1:1) was then added and the cell was sealed with a coin cell crimper. The prepared cells were aged for equilibration for about 12 hours before electrochemical testing.

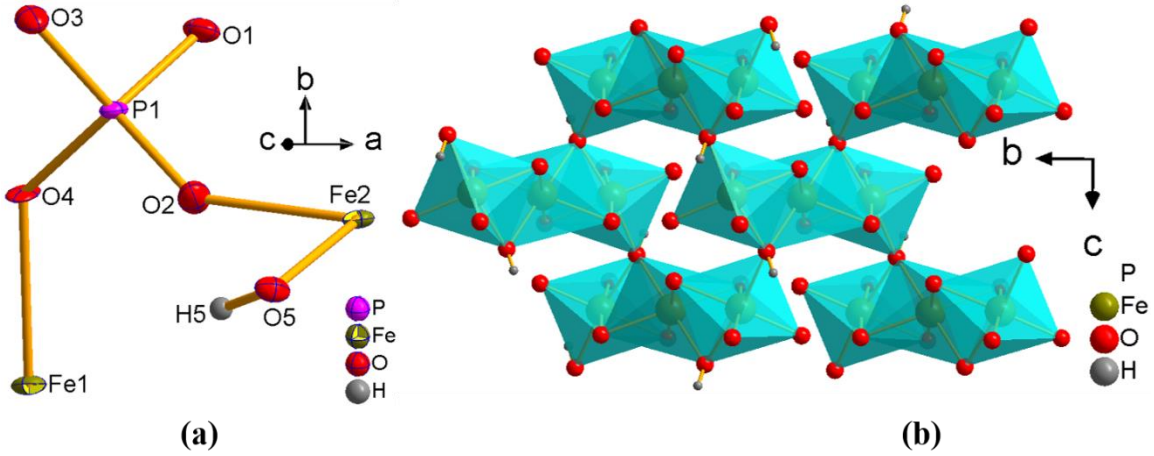

Figure 2. Asymmetric unit (a) and the interconnectivity of the trimers of Fe1-Fe2-Fe1 along *a*-axis (b) of the compound, $(Fe_3(PO_4)_2(OH)_{1.86}(H_2O)_{0.14})$.

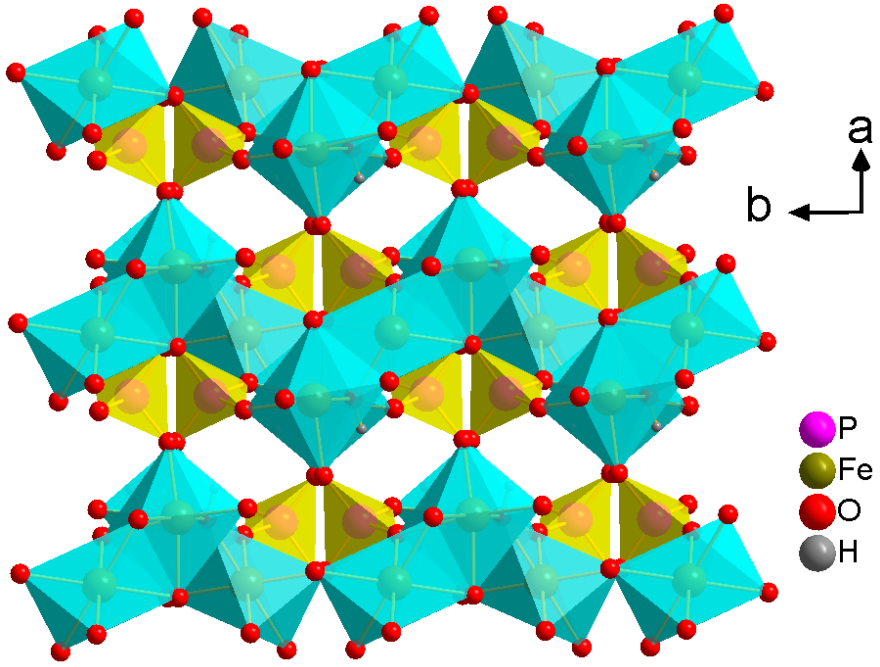

Figure 3. Perspective view of the structure of $Fe_3(PO_4)_2(OH)_{1.86}(H_2O)_{0.14}$ showing packing diagram along *c*-axis.

Cyclic voltammograms were obtained using a PAR EG&G potentiostat/galvanostat model 273 in the potential range of 1.5 – 4.0 V (vs. Li/Li^+) with a scan rate of 0.05 mV s^{-1}. Voltage composition profiles were obtained using galvanostatic charge/discharge experiments on an Arbin Instruments battery tester, model BT2043, on the same potential limits as CV at various C-rates. EIS spectra were obtained using biologic instruments SP-150 with the coin cells in the frequency range from 0.1 Hz to 1 MHz, by applying 5 mV AC amplitude.

3. RESULTS AND DISCUSSION

3.1. SYNTHESIS AND STRUCTURE

Only synthesis of barbosalite reported in the literature involves a two-step lengthy process. An Fe(II)-phosphate precursor, $Fe_3(PO_4)_2 \cdot 8H_2O$ (vivianite) and an amorphous Fe(III)-phosphate precursor was digested first and then the product from the first step was again digested with additional phosphoric acid with a total duration of 10 days at 200 °C.[25] On the other hand, we have used a low temperature one-step hydrothermal route for synthesis of barbosalite. Our initial aim was to partly substitute bridging hydroxide with fluoride to boost the insertion voltage similar to tavorite or kagomé lattice.[23, 33]

However, fluoride could not be inserted but the role of NaF was essential as a mineralizer for the barbosalite phase formation. Similarly, boric acid was also essential as a pH modulator and mineralizer which allowed maintenance of required acidic pH and high ionic strength enabling crystal growth of pure crystals. Since neither Na nor F got

incorporated into the structure, we could successfully synthesize barbosalite using LiOH in place of NaF. However, there is a subtle difference in the composition of our barbosalite ($Fe_3(PO_4)_2(OH)_{1.86}(H_2O)_{0.14}$) compared to naturally occurring or previously reported synthetic barbosalite ($Fe_3(PO_4)_2(OH)_2$). From Mössbauer study we have found slight excess of Fe(II) in our synthetic barbosalite which can be attributed to the exchange of hydroxide with water, since we have used almost 18 ml and 6.5 ml/g of $FeSO_4 \cdot 7H_2O$, respectively, for the NaF and LiOH-based synthesis, which is quite an excess compared previously reported synthesis (2ml/g of Fe-phosphate precursor). Similar dehydroxylation-hydration has been previously found in the ferric end member of lipscombite compensated by iron vacancy.[6]

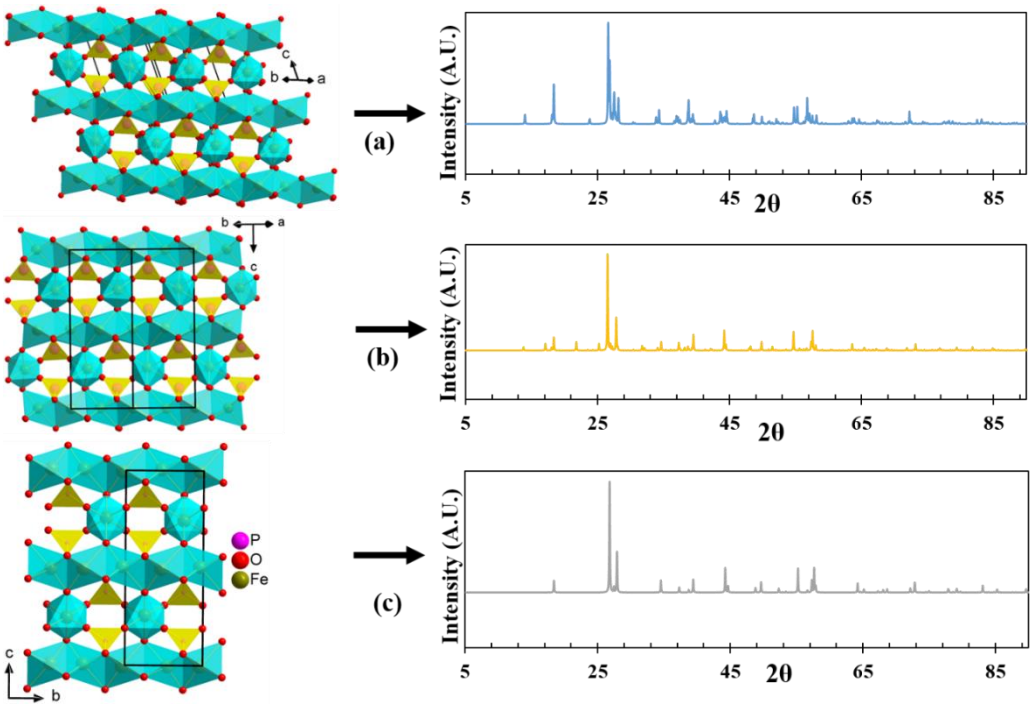

Figure 4. Comparison of 3D structures of barbosalite (a), lipscombite (b), and ferric lipscombite (c) with their simulated PXRD patterns.

The crystal structure of barbosalite has been adequately discussed in the literature. Here, we will briefly discuss the structure and highlight the differences with lipscombite phase. Figure 2a shows the asymmetric unit of the compound, which contains seven non-hydrogen atoms, 2 Fe, 1 P, and 5 O. Out of two Fe, one is located in a special position on the center of inversion (2*a*, Wyckoff site), while rest of the atoms are in general position, (4*a*, Wyckoff site). Out of 5 oxygen atoms, four belong to the phosphate moiety and the 5th oxygen is part of a mixed hydroxide/water. All the Fe atoms are in octahedral coordination with some degree of distortion with Fe – O distances in the range 1.926(5) – 2.157(5) and 2.056(5) – 2.109(4) Å, respectively, for Fe1 and Fe2. Figure 3 shows the packing diagram where the structure can be described as consisting of undulating layers of FeO_6 octahedra formed by the trimers of Fe1-Fe2-Fe1-centered face-shared octahedra (Figure 2b) connected through Fe-O-Fe linkages. Each trimer is connected to 4 different trimers through corner sharing at the hydroxide (O5-H) oxygen. Such layers are cross linked through corner sharing of PO_4 tetrahedra yielding a three dimensional framework of octahedra and tetrahedra with a narrow 4-membered ring channel along *c*-axis. This channel is a consequence of ordering of Fe sites in barbosalite with one Fe in +2 and the other in +3 oxidation state, unlike lipscombite where that empty site is occupied by another Fe but with two Fe sites having partial occupancy. As a result instead of an isolated trimer of face-shared octahedra, lipscombite contain infinite chains of face-shared octahedra of Fe^{2+} and Fe^{3+} which are crosslinked by both FeO_6 octahedra and PO_4 tetrahedra. In the ferric end member of lipscombite there is only one crystallographically distinct Fe site with partial occupancy resulting in infinite face-shared octahedral chain with high concentration of Fe vacancy. Besides the narrow channel along the *c*-axis, barbosalite has another four-

membered ring channel when viewed along [-2, -2, 1] direction, this channel is a common feature in barbosalite and lipscombite as can be seen along [1 1 0] plane and *a*-axis for mixed valent and ferric lipscombite, respectively (Figure 4). This remarkable similarity has also been reflected in the PXRD patterns of these compounds as shown Figure 4. When viewed along the [0 1 0] direction, we can clearly see the ordering of trimers which is not clearly visible from [-2, -2, 1] direction (Figure S3, S.I.).

3.1.1. Spectroscopic and Thermogravimetric Analysis. FT-IR spectroscopy has been used (Figure S4, S.I.) to further characterize the chemical nature of the inter-atomic bonding in the as-prepared sample. The IR spectra of the compounds from the two syntheses routes show prominent bands at 3300 cm^{-1} region which can be attributed to the O – H stretching mode and band at 1585 cm^{-1} to O – H bending modes from the bridging H_2O. The peaks at 900 – 1100 can be attributed to the symmetric and antisymmetric stretching modes of P – O in phosphate group. The symmetric and antisymmetric bending modes of P – O can be seen from 400-600 cm^{-1}.

TGA has been performed to determine the thermal stability of the compounds (Figure 5). The TGA curves indicate that the compound is stable up to 400 °C irrespective of synthetic routes and after that it starts to lose weight till 650 °C which can be attributed to the loss of one H_2O molecule based on the observed weight loss of 4.1% (theoretical = 4.6%) to form Fe_2OPO_4 and $FePO_4$ as determined from the PXRD of heated residue. (Figure S5, S.I.)

3.1.2. SEM Analysis. To evaluate the particle size, hand-ground (using mortar pestle) material was used for the SEM analysis (Figure S6, S.I.). The average particle size of the compound ranged from 3-20 μm in the hand-ground sample.

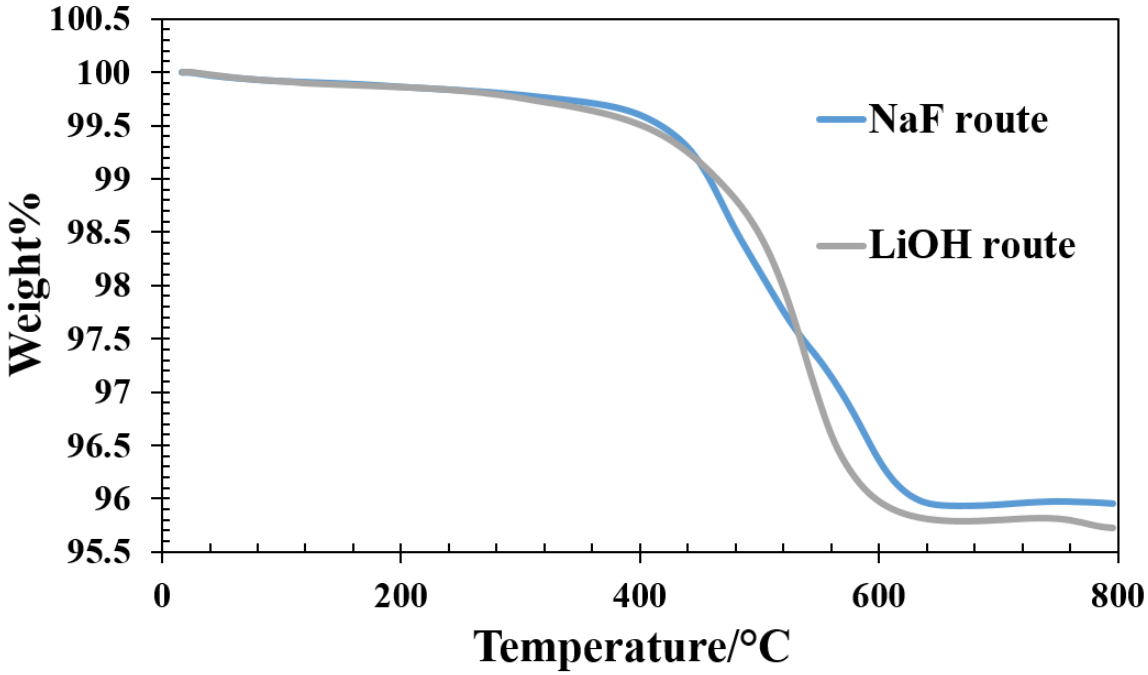

Figure 5. TGA curves of the compound $Fe_3(PO_4)_2(OH)_{1.86}(H_2O)_{0.14}$ from NaF and LiOH routes.

3.1.3. Mössbauer Spectroscopy. Figure 6 shows the Mössbauer spectra for the compounds synthesized by two different routes. Isomer shift (IS) and quadrupole splitting (QS) parameters derived from the Lorentzian fittings of the peaks are listed in Table 4. Well-ground powder of as-prepared samples were used for measurements. IS and QS values are in well accordance with the Fe^{+3} and Fe^{2+} sites of barbosalite reported by Redhammer *et al.*[34] However, our samples yielded slightly higher percentage of Fe^{2+} population, which is stabilized by the exchange of hydroxide with water. The IS and QS values also correlate with the high spin Fe^{2+} and Fe^{3+} ions in octahedral coordination.[35]

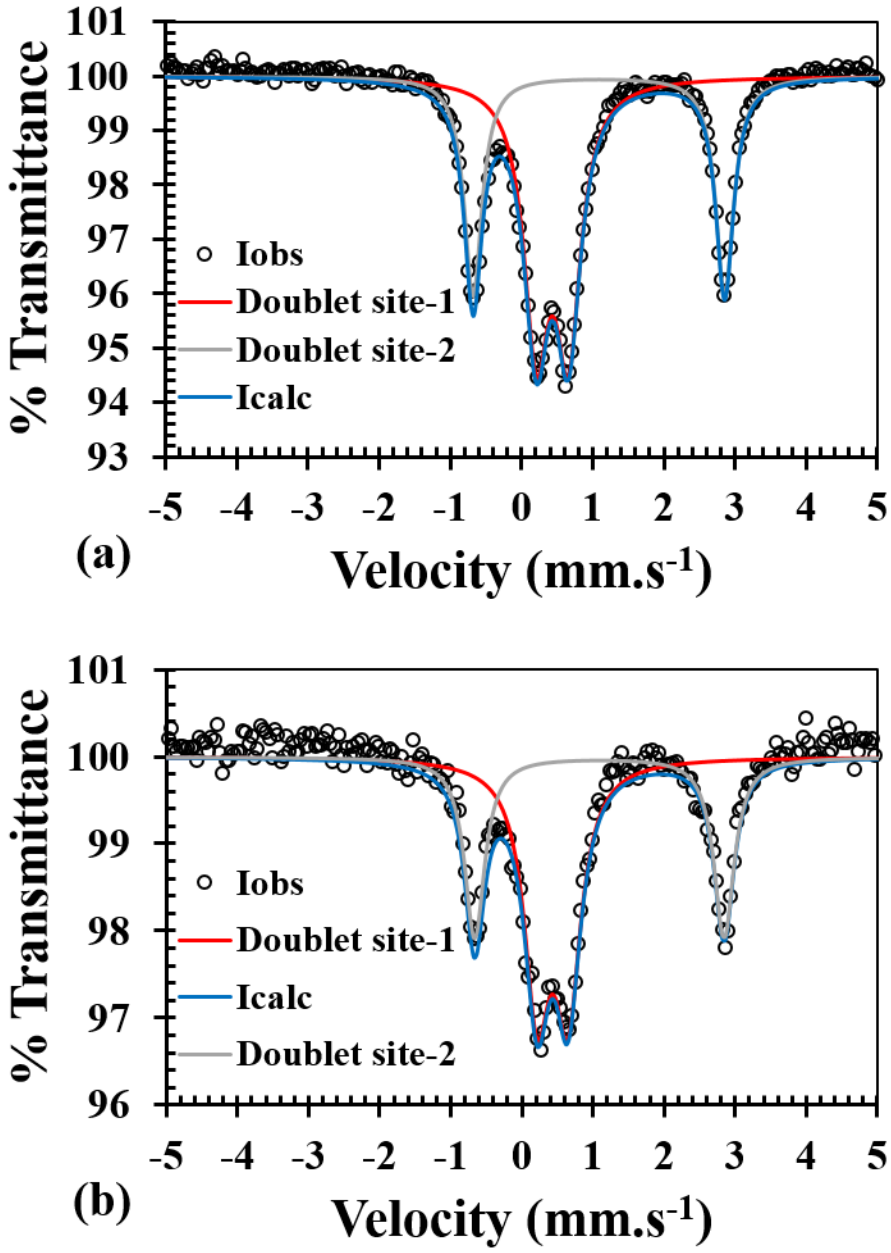

Figure 6. Mössbauer spectra of the compounds prepared from NaF route (a) and LiOH route (b).

Table 4. The fitted ^{57}Fe Mössbauer spectroscopic values for Isomer Shift (IS) and Quadrupole Splitting (QS) of the as-synthesized compounds.

NaF route	Sites	IS(δ) (mm.s^{-1})	QS (ΔE_Q) (mm.s^{-1})	Site population (%)
Fe^{3+}	Doublet site-1	0.433(3)	0.449(5)	61.8
Fe^{2+}	Doublet site-2	1.087(3)	3.533(3)	38.2
LiOH route	Sites	IS(δ) (mm.s^{-1})	QS (ΔE_Q) (mm.s^{-1})	Site population (%)
Fe^{3+}	Doublet site-1	0.429(3)	0.435(5)	62.4
Fe^{2+}	Doublet site-2	1.087(3)	3.506(3)	37.6

3.1.4. Magnetic Properties. The temperature dependent ZFC magnetic susceptibility $\chi_M(T)$, the corresponding inverse molar susceptibility $\chi_M^{-1}(T)$ and isothermal field dependent magnetization $M(H)$ for the as-synthesized compound (NaF route) is given in Figure 7. The onset of magnetic ordering can be seen at 169 K with a jump in magnetic susceptibility as shown in Figure 7 at an applied field of 1 T. This jump resembles more like a ferromagnetic transition but the linear fitting of the inverse susceptibility above 250 K yields a high negative Θ_p value (-332 K) indicating predominant antiferromagnetic interactions. Magnetic moment/Fe (6.63 μ_B) as calculated from the curie constant, C, derived from the linear fit yields a higher value than theoretically expected for a 62% Fe^{3+} and 38% Fe^{2+} iron site. This may be due to the fact that the temperature region between 250 – 300 K does not reside on a paramagnetic region and one has to go above the room

temperature to be in the purely paramagnetic region. The overall interactions can be described as antiferromagnetic with a ferromagnetic component due to competing anti-ferromagnetic and ferromagnetic interactions between the Fe^{3+} centers (inter-trimer) and Fe^{2+} and Fe^{3+} (within the trimer). The saturation magnetization at 5 K is about 0.12 Nβ, which is quite less than the theoretical saturation magnetization (*M*s = *gS* Nβ) of fully ordered magnetic moment of either four (high spin Fe^{2+}) or five (high spin Fe^{3+}) unpaired electrons (inset of Figure 7). More interestingly the magnetization curve remains negative up to an applied field of 1000 Oe, after which it becomes positive. The negative magnetization in barbosalite has been observed previously,[34] however, actual cause of negative magnetization needs further investigation.

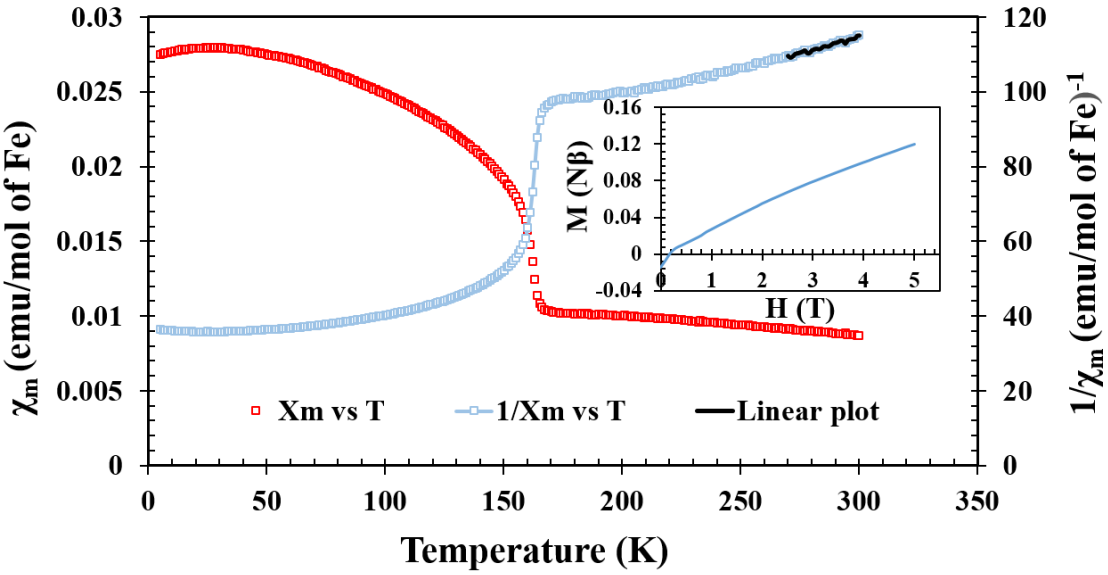

Figure 7. Temperature dependence of molar magnetic susceptibility (χ_m) and inverse molar magnetic susceptibility (χ_m^{-1}) of $Fe_3(PO_4)_2(OH)_{1.86}(H_2O)_{0.14}$ synthesized by NaF route. (Inset shows M vs H plot).

3.2. ELECTROCHEMISTRY

3.2.1. Cyclic Voltammetry. Cyclic voltammetry tests were conducted on the fabricated Li-ion coin cells to get an idea of the Li-insertion (cathodic reduction) and Li-extractions (anodic oxidation) voltages. Figure 8 shows the first three cycles of cyclic voltammograms, when the cell was subjected to a voltage scanning between 1.5 – 4.0 V. Open circuit voltage (OCV) was at 2.99 V. The battery was discharged first yielding an onset of reductive lithiation at 2.55 V with a peak at 2.45 V and the corresponding oxidation peak was at 2.75 V. The potential at the reduction peak increased in the subsequent cycle to 2.5 V and at same time oxidation peak decreased to 2.7 V, with an onset of oxidation at 2.3 volt. From the oxidation and reduction peaks, the average voltage can be estimated to be around 2.6 V. It is also to be noted here that during reduction it exhibit strong cathodic current with a sharp peak while during the anodic oxidation it shows a broad peak spanning between 2.3 to 3.5 volt.

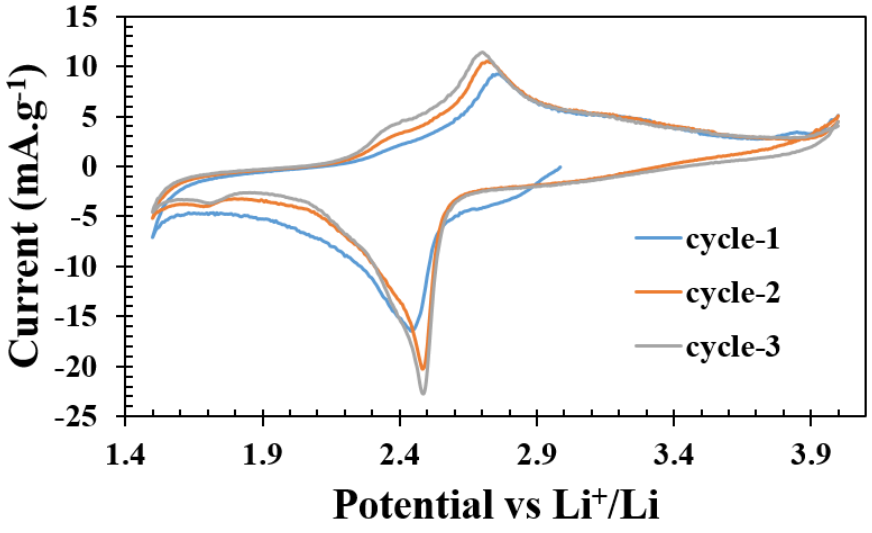

Figure 8. First three cycles of cyclic voltammogram of Li-ion cell made with $Fe_3(PO_4)_2(OH)_{1.86}(H_2O)_{0.14}$ as cathode and pure Li as anode.

3.2.2. Galvanostatic Charge-Discharge. The galvanostatic charge-discharge experiments were done at various slow C-rates and the cut-off potentials were set in the range 1.5 – 4.0 V for all the tests (Figure 9). Assuming a complete one electron process per Fe atom, the theoretical capacity of the compound can be calculated to be 136.90 $mAh.g^{-1}$. Figure 9 shows the charge-discharge profiles at C/50. The first discharge delivered a capacity of 47 $mAh.g^{-1}$, which on subsequent cycles increased to 55 $mAh.g^{-1}$. Subsequently at various comparatively faster C-rates specifically, at C/20, C/10 and C/5, a very stable capacity of 52, 50 and 46 $mAh.g^{-1}$, respectively, was achieved (Figure 10). The decrease in capacity with the increasing C-rate was minimum. After several cycles of faster C-rates when we returned to slower C-rate (C/50), the capacity further increased to 69 $mAh.g^{-1}$, which is equivalent to insertion of 0.5 lithium (Figure 10). To further increase the capacity, we increased the percentage of carbon in the cathode composite from 15% to 25% assuming electronic conductivity could be a factor impeding achievement of full theoretical capacity. Similar charge-discharge tests on the higher carbon percentage in the cathode mix resulted in substantial enhancement in the achievable capacity (Figures 9 and 10). In the respective C-rates starting from C/50 and going through C/20, C/10, C/5 and again returning to C/50 in the 20^{th} cycle we observed an increase of 10 -15 $mAh.g^{-1}$ capacity. More interestingly when the cell was further cycled for another 20 cycles in similarly varying C-rates the capacity further jumped to 95 $mAh.g^{-1}$ in the 40^{th} cycle in C/50 rate. Even in C/5 rate a capacity of 65 $mAh.g^{-1}$ can be achieved, which was the best performance in C/50 rate with 15% carbon content (Figures 9 and 10). The final achievable capacity of 95 $mAh.g^{-1}$ is equivalent to 70% of the theoretical capacity. The cell was tested for cycle-life for 300 cycles at C/5 rate, where it continued to show capacity increase till

150 cycles and then stabilize to the initial capacity of C/5 rate (inset of Figure 10). The increase in the capacity during successive charge-discharge cycles is quite intriguing and might be associated with particle size reduction occurring during cycling or creation of conducting pathways with successive cycling or increased exposure of active materials in the electrolyte.

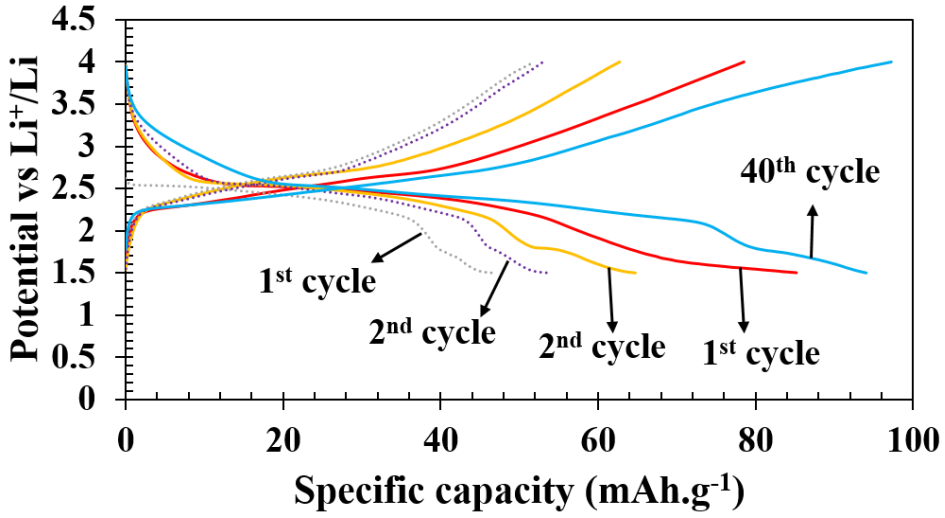

Figure 9. Galvanostatic charge-discharge profiles for Li-ion batteries at C/50 with 75:15:10 composition (shown with dotted lines, 1st and 2nd cycles) and 65:25:10 (shown with continuous lines, 1st, 2nd, and 40th cycles).

The capacity can also increase on successive cycling due to structural transformation from a poorly electrochemically active phase to a phase with facile electrochemical activity. Another possibility could be that the active materials had some Na-substitution to begin with in the as-synthesized phase, which on successive cycling slowly got exchanged with Li and capacity increased due to decrease of equivalent weight of active material. We, therefore, also charged the battery first, which didn't yield any capacity eliminating the possibility of having Na-ion into the as-synthesized compound as

was also supported by our EDS analysis (absence of Na). To better understand the capacity increase phenomena we carried out several tests with the cells that were tested for cycle-life.

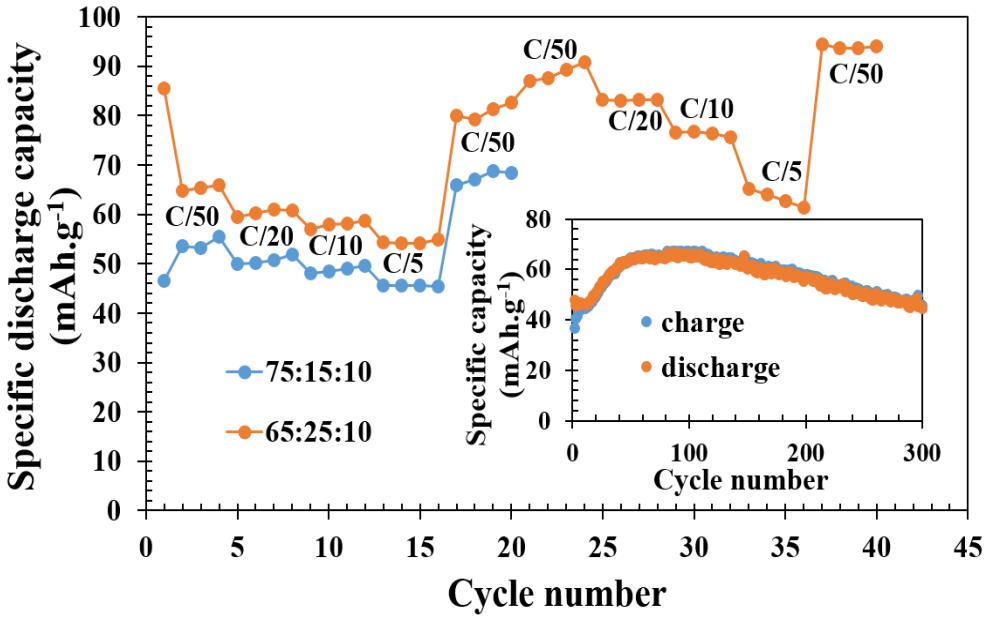

Figure 10. Cycle index showing capacity retention at different C-rates with 75:15:10 composition (20 cycles) and 65:25:10 composition (40 cycles). (Inset shows capacity retention for 300 cycles at C/5).

3.3. POST ANALYSIS OF CYCLED CELLS

3.3.1. Cyclic Voltammetry. We collected cyclic voltammograms for the coin cells after 100 cycles and 300 cycles from two different cells, which displayed remarkably different shape from the initial (fresh) cells (Figure S7, S.I.). The noticeable features of the cycled cells include change in the oxidation (2.5 V) and reduction (2.3 V) peaks with a decrease from the initial values of 2.8 and 2.5 V, respectively, along with a development of a very symmetric CV with broad rounded oxidation and reduction peaks. The area under

the anodic oxidation and cathodic reduction are almost equal indicating equal kinetics of oxidation and reduction and facile electrochemistry with less polarization. More importantly lithium insertion and extraction potentials are a function of structure type and a substantial shift in their values (See Figure 11) may indicate a structural rearrangement.

3.3.2. Electro-Impedance Study. In order to understand the kinetics of processes inside the battery, we performed electro-impedance studies on a freshly fabricated and cycled (100, 300 cycles) cells (Figure 12, fitted parameters are supplied in Table S5, S.I.). The freshly fabricated cell was fitted with one R/C element at mid frequency to high frequency region with one semicircle corresponding to the charge transfer resistance, with a low frequency tail fitted with Warburg impedance corresponding to Li-ion diffusion inside the cathode material. For the cycled cells, based on the two partially overlapped semicircle we used an extra R/C element at high frequency corresponding to SEI resistance (R_{SEI}), and the other semicircle for charge transfer (R_{ct}) following previous well-document work.[36, 37] During cycling, the cell is expected to develop SEI (solid electrolyte interface) and thereby the combined resistance increased (R_{SEI} + R_{ct}). However, if we consider R_{ct} alone in all three cells, it decreases with cycling from 342 (fresh battery) to 202 ohm after 100 cycles, and showing further reduced value of 112 ohm after 300 cycles, which explains that the kinetics of the Li^+ charge transfer becoming facile on cycling. Such values of R_{ct} has been observed previously in phosphate-based cathode in Li-ion batteries.[38] From this observation it can be concluded that the charge-transfer in the electrolyte-electrode interface especially at cathode may be related to the transformation of the cathode materials to a more electrochemically facile phase as supported by the CV and PXRD of the cycled

cell (discussed below). During cycling R_{SEI} has increased from 421 (100 cycles) to 484 ohm (300 cycles), which may be affecting capacity retention after 200 cycles.

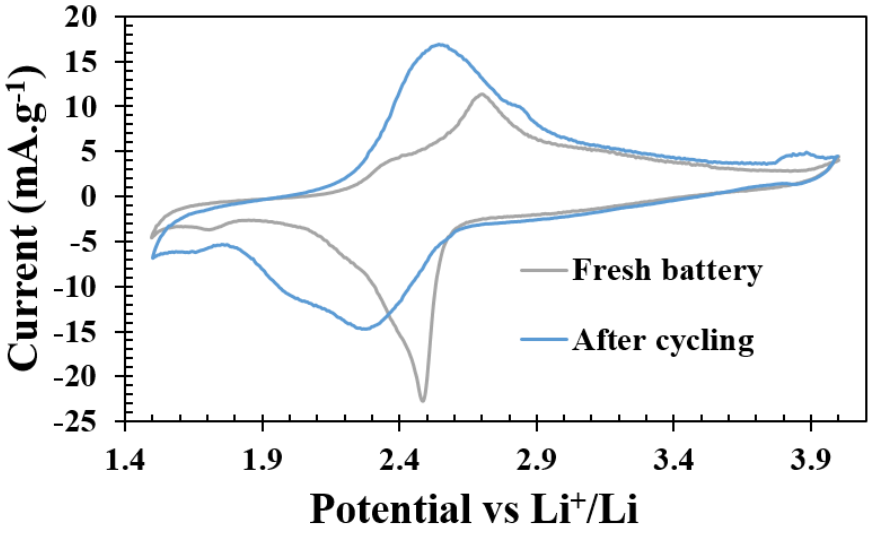

Figure 11. Comparison of cyclic voltammograms for the batteries, freshly fabricated and after cycling. (Second cycle).

3.3.3. Ex-Situ PXRD Characterization of Discharged and Charged Cells. To further understand the mechanism of the charge-discharge profiles and to evaluate if there is any structural phase transition, the ex-situ PXRDs of the charged and discharged cells were carried out. For this, the coin cells were cracked-opened inside the argon filled glovebox and the cathode material in the charged and discharge state of the cells were recovered, washed with the acetone, and dried. The cathode material was then placed in an air tight cell holder, and PXRD was collected. The PXRD of the discharged phase indicates that due to successive charge-discharge process there may be structural rearrangement as evident by the emergence of a new line at $2\Theta = 25.8°$ and the new line is retained even in

the charged state, supporting that the structural rearrangement is irreversible. The overall PXRDs look mostly similar to the as synthesized sample, except the development of a new peak at 2Θ = 25.8°. To validate the hypothesis that the structural transformation is due to lithium insertion, we carried out chemical reductive lithiation with $LiAlH_4$ by stirring the as-synthesized sample in THF with 1:1 ratio of barbosalite and $LiAlH_4$ inside Ar-filled glovebox. The PXRD (Figure S8, S.I.) of the chemically reduced phase bear remarkable similarity with the electrochemically reduced/oxidized phase, corroborating well with the hypothesis that lithium insertion is causing a structural phase transition. It is to be noted here that similar phase transition has been observed recently in a vanadium oxy-phosphate, $V_4O_3(PO_4)_3$, which also belongs to lipscombite-lazulite family of structures.[39]

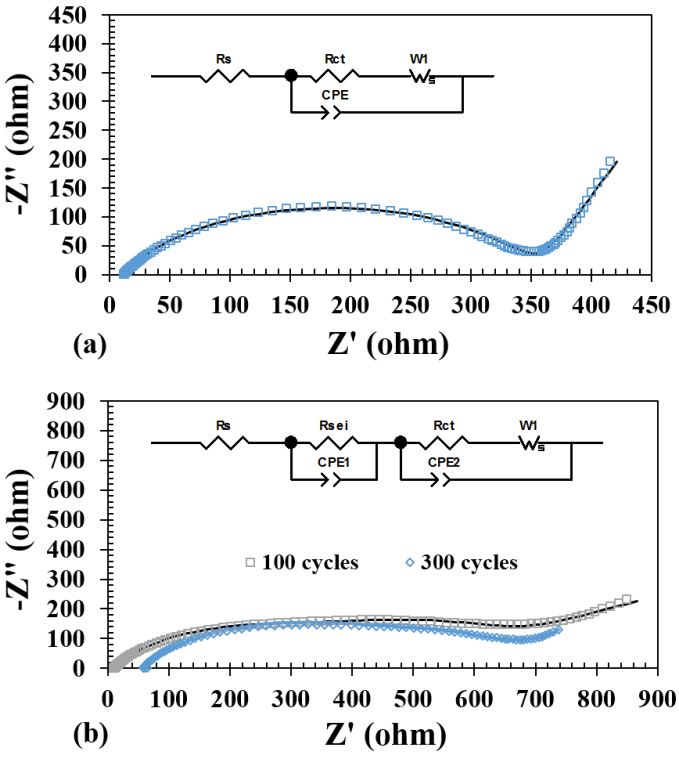

Figure 12. Nyquist plot of freshly fabricated (a) and cycled Li-ion cells (b).

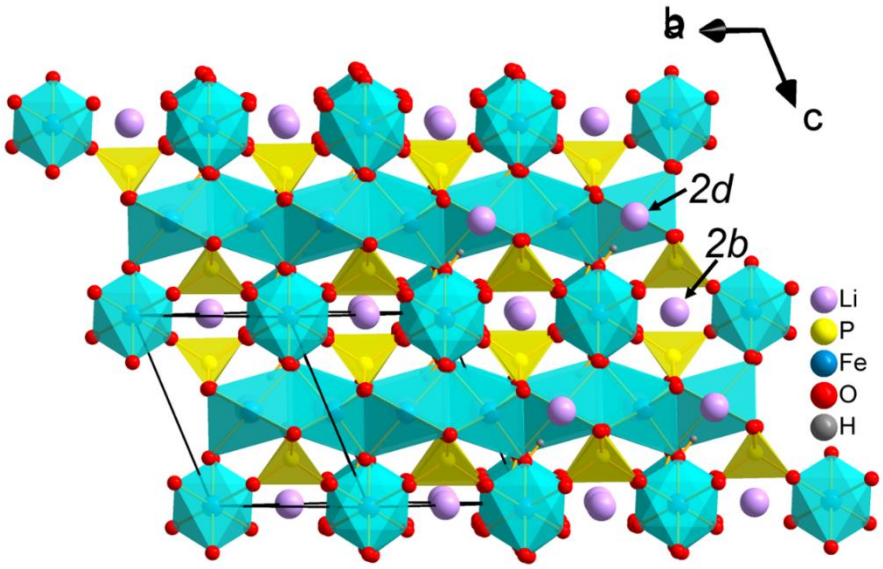

Figure 13. Perspective view of the structure of $Fe_3(PO_4)_2(OH)_{1.86}(H_2O)_{0.14}$ showing possible Li sites.

3.3.4. Possible Li-Sites in the Structure. It is worth discussing here the possible sites for Li-ion intercalation in barbosalite. Since the Fe-sites are ordered it has an empty site at every fourth position (Wyckoff, 2*d*) of an infinite hypothetical face-shared chain of octahedra, the volume of which is appropriate for the accommodation of a lithium ion. Besides the 2*d* site there is another empty site, namely 2*b* Wyckoff site, similar to 8*c* empty channel site of the ferric end member of the lipscombite. This 8*c* site has been theoretically predicted to be the site for Li-intercalation in lipscombite.[20] Some authors also hypothesized that Li can also occupy the iron vacancy sites along with the empty channel sites in lipscombite.[19] Intuitively it is possible for Li to go either in the 2*b* empty channel site or the empty metal site, 2*d* in barbosalite, as shown in Figure 13. However, unoptimized structure with two inserted lithium ions do not produce the new line that we have observed in electrochemically/chemically reduced phase. Therefore, it can be

concluded that a structural re-arrangement may be happening which may include movement of Fe-atoms in the face-shared chain. Obviously more sophisticated experiments for example, high resolution synchrotron PXRD data of the reduced Li-intercalated phase will be required to understand the structural rearrangement and locate the exact position of the Li-ion which is beyond the scope of this manuscript.

4. CONCLUSIONS

In this article, we have reported the synthesis of barbosalite through low-temperature hydrothermal routes. The compound has shown good achievable capacities for the Li-ion batteries with 0.7 Li insertion at an average voltage of 2.6 V. Charge-discharge profile, CV and PXRD of the cycled cell indicate structural re-arrangement due to lithium insertion. Though due to the lower capacity and smaller insertion voltage, it will not be competitive for Li-ion battery cathode but from fundamental solid state electrochemistry perspective it is an important system which complements the electrochemistry of the lipscombite structure type and reminds us about the fact that subtle difference in structure from well-studied lipscombite can have substantial impact on electrochemistry.

ACKNOWLEDGEMENTS

The authors acknowledge the funding from University of Missouri Research Board and Energy Research and Development Center, Missouri S&T. Use of the Advanced Photon Source at Argonne National Laboratory was supported by the U.S. Department of

Energy, Office of Science, Office of Basic Energy Sciences, under Contract No. DE-AC02-06CH11357.

SUPPLEMENTARY INFORMATION

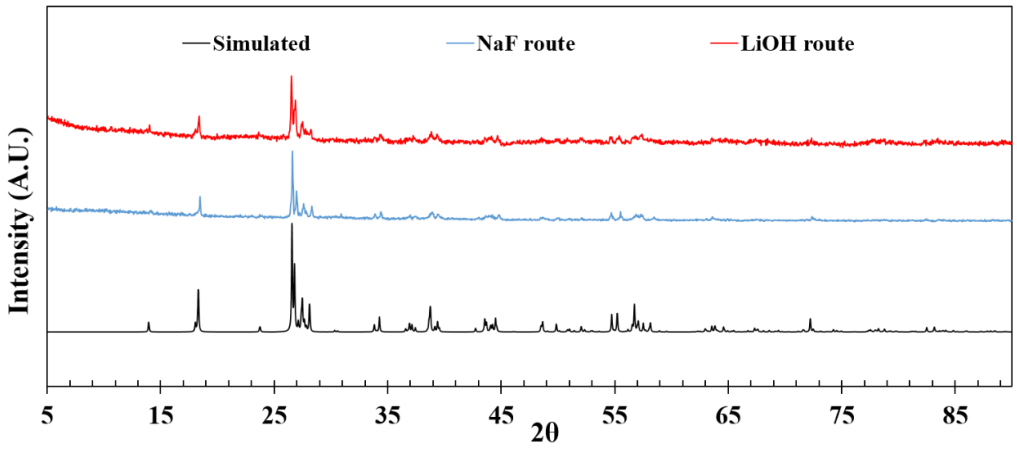

Figure S1. Comparison of laboratory PXRD of $Fe_3(PO_4)_2(OH)_{1.86}(H_2O)_{0.14}$ from NaF and LiOH routes with simulated pattern.

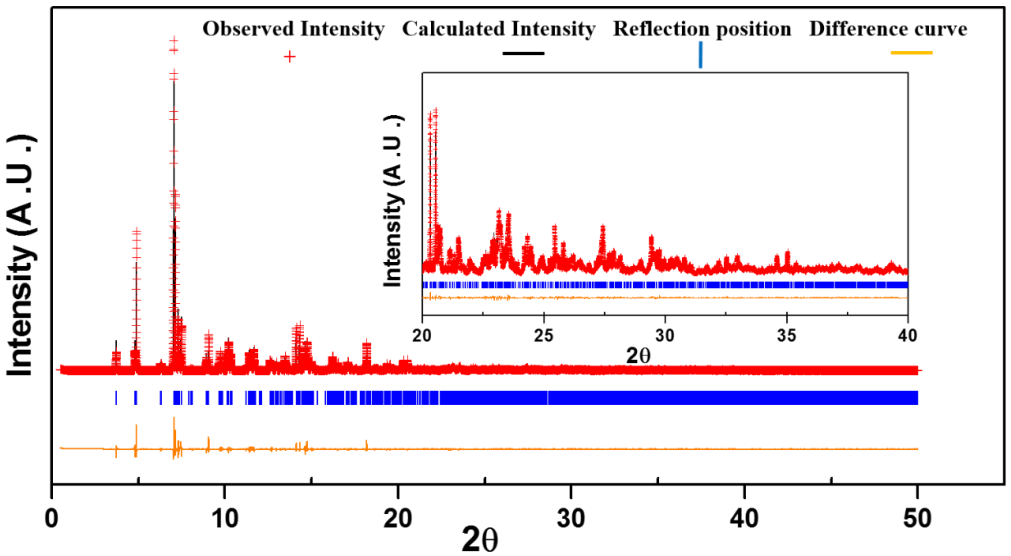

Figure S2. Rietveld refinement of synchrotron XRD data of $Fe_3(PO_4)_2(OH)_{1.86}(H_2O)_{0.14}$ showing the observed, calculated and difference curve. Inset shows enlarged view of the segment for 2θ = 20 to 40°. (Refined parameters: a = 7.308(9) Å, b = 7.468(8) Å, c = 7.519(1) Å, β = 120.163 (5)°, V = 354.88 (5) Å^3, Rw = 15.341%, λ = 0.412832 Å).

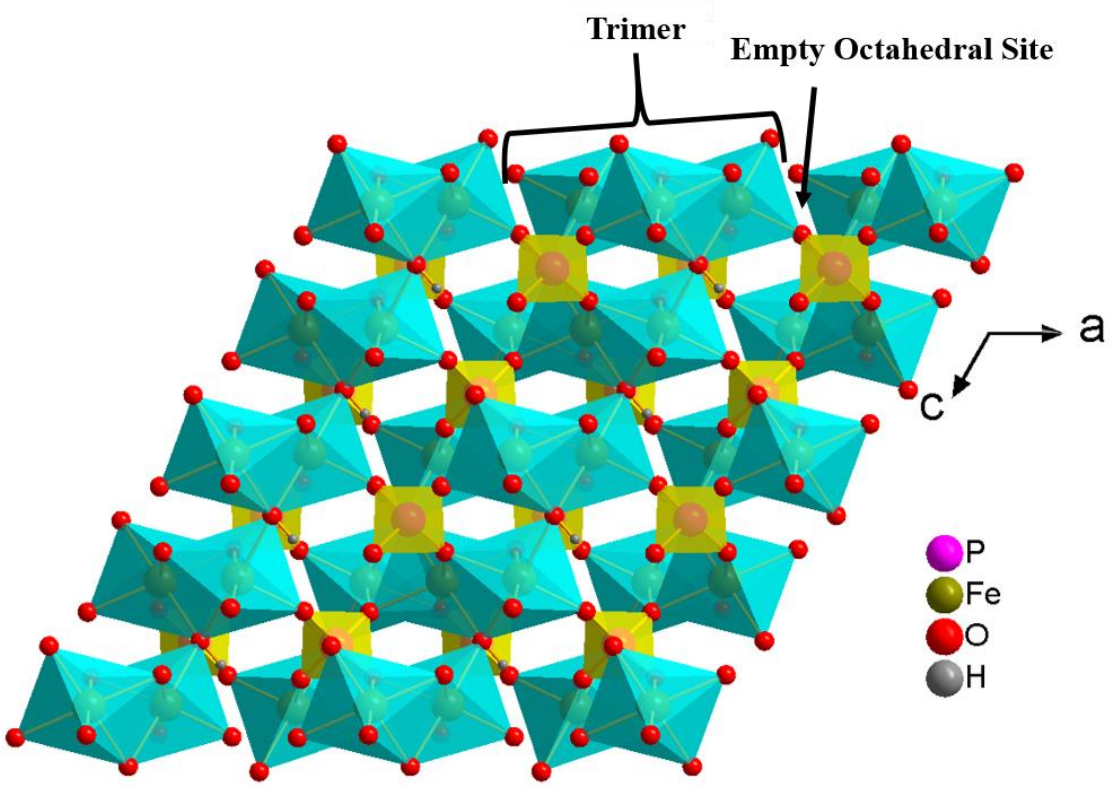

Figure S3. Perspective view of $Fe_3(PO_4)_2(OH)_{1.86}(H_2O)_{0.14}$ along [0 1 0] direction.

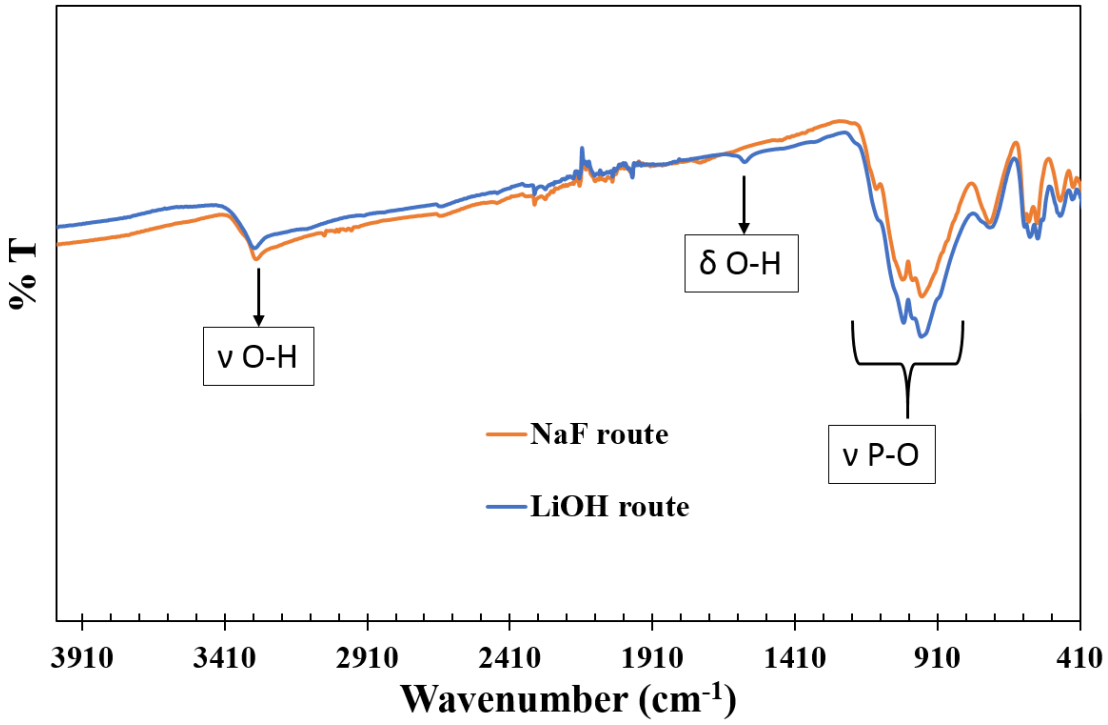

Figure S4. FTIR spectra of the compound $Fe_3(PO_4)_2(OH)_{1.86}(H_2O)_{0.14}$ from NaF and LiOH routes.

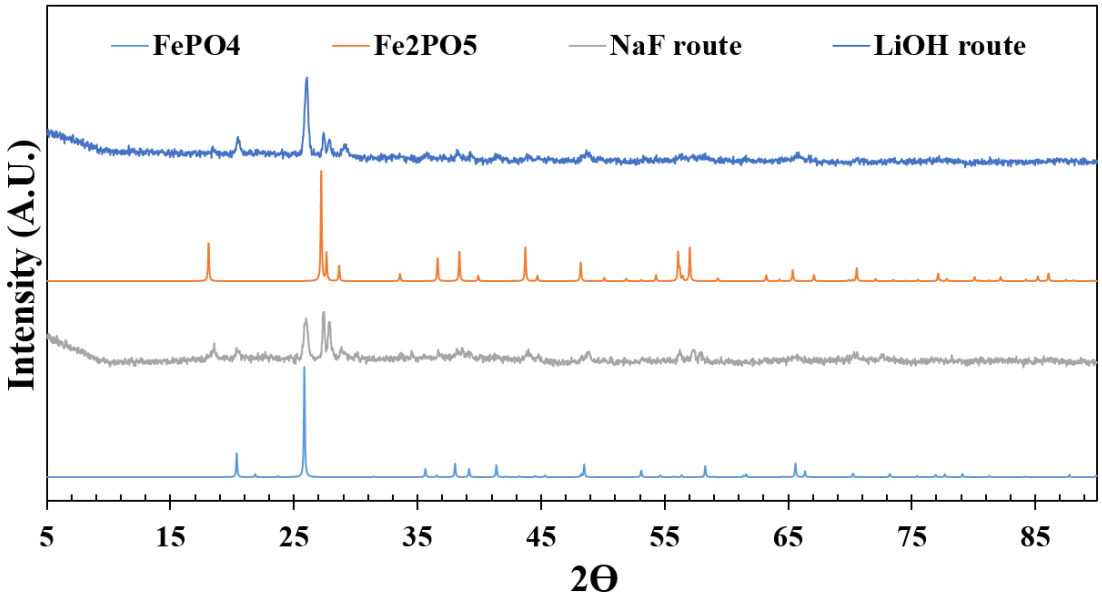

Figure S5. PXRD spectra of the compound $Fe_3(PO_4)_2(OH)_{1.86}(H_2O)_{0.14}$ from NaF and LiOH routes after TGA.

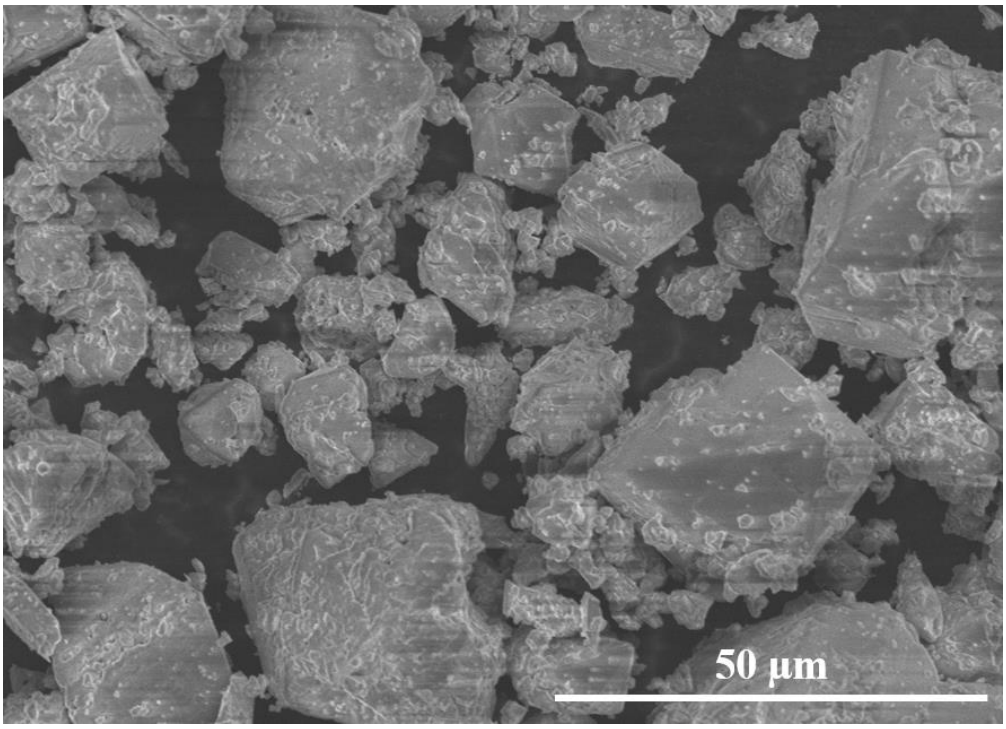

Figure S6. SEM micrograph of the compound $Fe_3(PO_4)_2(OH)_{1.86}(H_2O)_{0.14}$ synthesized by NaF route.

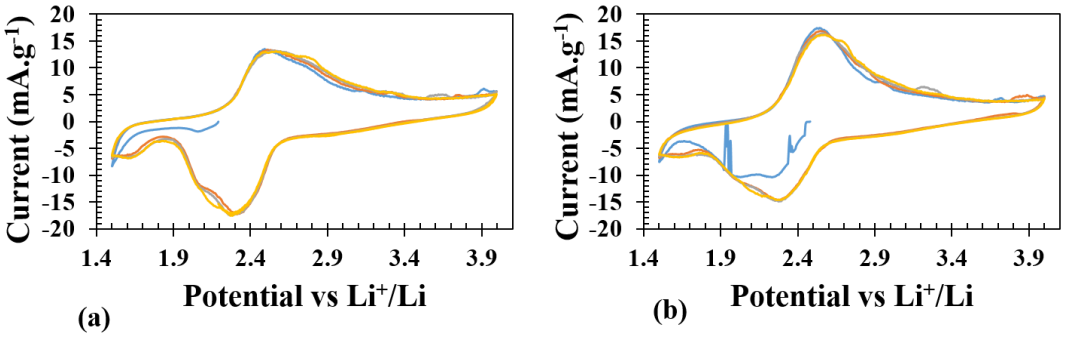

Figure S7. Cyclic voltammogram after 100 cycles (a) and 300 cycles (b).

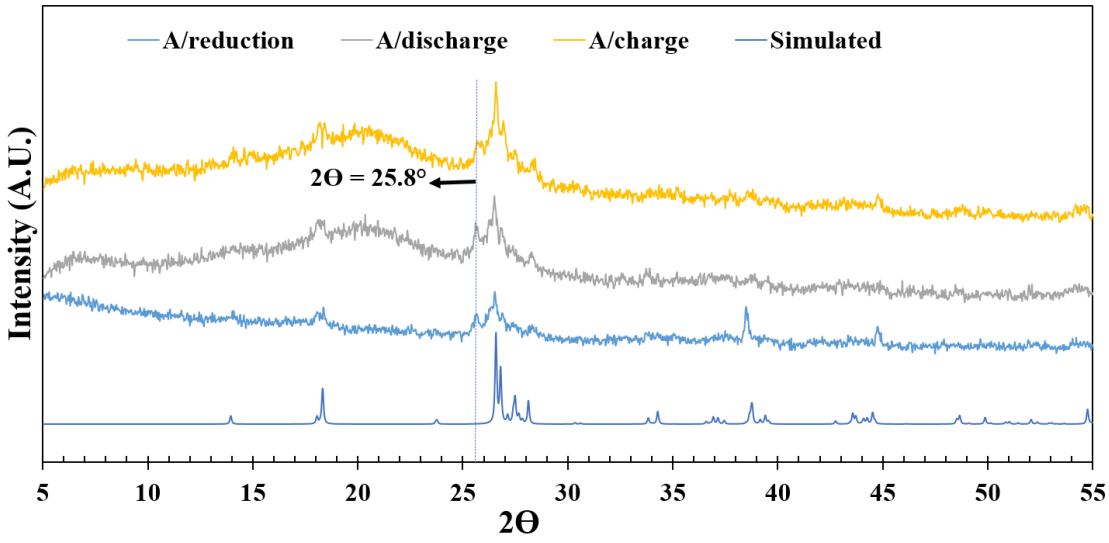

Figure S8. Ex-situ PXRDs of the compound, $Fe_3(PO_4)_2(OH)_{1.86}(H_2O)_{0.14}$, in chemically reduced form, electrochemically reduced and oxidized form along with simulated PXRD of barbosalite.

Table S1. Various trials of synthesis while targeting $Fe_3(PO_4)_2(OH)_2$ (* this work)

S.No.	Reactants	Conditions	Product (s)
1	$FeSO_4.7H_2O + H_3PO_4 + H_3BO_3 + NaF + H_2O$	185°C, 24 h	$Fe_3(PO_4)_2(OH)_{1.86}(H_2O)_{0.14}$*
2	$FeSO_4.7H_2O + H_3PO_4 + NaF + H_2O$	185°C, 24 h	$Fe_3(PO_4)_2(OH)_2$, $Fe_4(PO_4)_2O$ & $Na_3PO_4 \cdot 5H_2O$
3	$FeSO_4.7H_2O + H_3PO_4 + H_3BO_3 + NaOH + H_2O$	175°C, 72 h	$Fe_5(PO_4)_4(OH)_2 \cdot 2H_2O$
4	$FeSO_4.7H_2O + H_3PO_4 + H_3BO_3 + LiOH.H_2O + H_2O$	175°C, 72 h	$Fe_3(PO_4)_2(OH)_{1.86}(H_2O)_{0.14}$*
5	$FeCl_3.6H_2O + H_3PO_4 + H_3BO_3 + LiOH.H_2O + H_2O$	175°C, 72 h	$Fe_5(PO_4)_4(OH)_3 \cdot 2H_2O$
6	$FeCl_3.6H_2O + H_3PO_4 + H_3BO_3 + H_2O$	175°C, 72 h	$Fe(PO_4) \cdot 2H_2O$

Table S2. Crystal data and structure refinement for $Fe_3(PO_4)_2(OH)_2$ from LiOH route.

Empirical formula	$Fe_3(PO_4)_2(OH)_2$	
Formula weight	391.51	
Temperature	295(2) K	
Wavelength	0.71073 Å	
Crystal system	Monoclinic	
Space group	*P* 2_1/c	
Unit cell dimensions	a = 7.301(10) Å	α= 90°.
	b = 7.470(10) Å	β= 119.45(9)°.
	c = 7.466(7) Å	γ = 90°.
Volume	354.6(8) $Å^3$	
Z	2	
Density (calculated)	3.667 g/cm^3	
F(000)	380	
Goodness-of-fit on F^2	1.008	
Final R indices [I>2sigma(I)]	R1 = 0.0617, wR2 = 0.1415	
R indices (all data)	R1 = 0.0870, wR2 = 0.1543	

Table S3. Atomic coordinates (x 10^4) and equivalent isotropic displacement parameters ($Å^2$x 10^3) of $Fe_3(PO_4)_2(OH)_2$ synthesized from LiOH route. U(eq) is defined as one third of the trace of the orthogonalized U^{ij} tensor.

Atom	x	y	z	U(eq)
P(1)	2474(4)	3847(5)	2450(5)	12(1)
Fe(1)	0	0	0	15(1)
Fe(2)	7318(2)	2323(2)	5068(3)	13(1)
O(1)	3037(18)	4958(11)	1074(13)	15(2)
O(2)	4299(14)	2644(12)	3797(12)	16(2)
O(3)	1959(18)	5117(11)	3766(13)	16(2)
O(4)	508(15)	2712(11)	1146(13)	17(2)
O(5)	7342(12)	1342(11)	7583(11)	16(2)

Table S4. Selected Bond lengths [Å] and Bond Valence sum values for the compound, $Fe_3(PO_4)_2(OH)_2$ synthesized from LiOH route.

Atom-Atom	*d* (Å)	Atom-Atom	*d* (Å)	Atom-Atom	*d* (Å)
P(1)-O(2)	1.509(9)	Fe(1)-O(3)$^{\#1}$	2.049(11)	Fe(2)-O(1)$^{\#7}$	1.923(9)
P(1)-O(1)	1.526(10)	Fe(1)-O(3)$^{\#2}$	2.049(11)	Fe(2)-O(2)	1.939(10)
P(1)-O(3)	1.534(9)	Fe(1)-O(5)$^{\#3}$	2.141(8)	Fe(2)-O(5)	2.007(8)
P(1)-O(4)	1.540(10)	Fe(1)-O(5)$^{\#4}$	2.141(8)	Fe(2)-O(4)$^{\#8}$	2.057(10)
		Fe(1)-O(4)$^{\#5}$	2.159(9)	Fe(2)-O(3)$^{\#9}$	2.059(9)
		Fe(1)-O(4)	2.159(9)	Fe(2)-O(5)$^{\#1}$	2.114(8)
BVS, P1 = 5.104		BVS, Fe1 = 1.821		BVS, Fe2 = 3.042	

Symmetry transformations used to generate equivalent atoms:
#1 x, -y+1/2, z-1/2; #2 -x, y-1/2, -z+1/2; #3 -x+1, -y, -z+1; #4 x-1, y, z-1; #5 -x, -y, -z; #6 x-1, -y+1/2, z-1/2; #7 -x+1, y-1/2, -z+1/2; #8 x+1, -y+1/2, z+1/2; #9 -x+1, -y+1, -z+1

Table S5. Impedance equivalent circuit parameters for freshly fabricated and cycled cells.

				CPE1		CPE2		Ws		
	R_s (Ω)	R_{SEI} (Ω)	R_{Ct} (Ω)	C (μF)	P	C (μF)	P	R (Ω)	τ (s)	P
Fresh battery	25.12		342			25.38	0.75	1182	14.48	0.75
After 100 cycles	9.109	421.8	202.5	22.64	0.71	27.14	0.73	1374	26.95	0.40
After 300 cycles	52.41	484	112.1	51.65	0.68	43.89	0.70	476.8	15.19	0.41

REFERENCES

1. A. K. Padhi, K. S. Nanjundaswamy, J. B. Goodenough, "Phospho-olivines as positive-electrode materials for rechargeable lithium batteries," *J. Electrochem. Soc.,* **144 (4)**, 1188 (1997).

2. P. B. Moore, "Crystal chemistry of the basic iron phosphates," *Am. Mineral.*, **55 (1-2)**, 135 (1970).

3. J. M. M. Millet, D. Rouzies, J. C. Vedrine, "Isobutyric acid oxidative dehydrogenation over iron hydroxyphosphates. II. Tentative description of the catalytic sites based on Mössbauer spectroscopic study," *Appl. Catal., A.,* **124**, 205 (1995).

4. D. Rouzies, J. M. M. Millet, D. Siew Hew Sam, J. C. Védrine, "Isobutyric acid oxidative dehydrogenation over iron hydroxyphosphates. I. Catalytic properties and role of water," *Appl. Catal., A.,* **124 (2)**, 189 (1995).

5. J. -M. M. Millet, "FePO catalysts for the selective oxidative dehydrogenation of isobutyric acid into methacrylic acid," *Catal. Rev. – Sci. Eng.*, **40 (1-2)**, 1 (1998).

6. Y. Song, P. Y. Zavalij, N. A. Chernova, M. S. Whittingham, "Synthesis, Crystal Structure, and Electrochemical and Magnetic Study of New Iron (III) Hydroxyl-Phosphates, Isostructural with Lipscombite," *Chem. Mater.,* **17 (5)**, 1139 (2005).

7. N. Marx, L. Croguennec, D. Carlier, A. Wattiaux, F. L. Cras, E. Suard, C. Delmas, "The structure of tavorite $LiFePO_4(OH)$ from diffraction and GGA + U studies and its preliminary electrochemical characterization," *Dalton Trans.*, **39 (21)**, 5108 (2010).

8. P. B. Moore and A. R. Kampf, "Beraunite: Refinement, comparative crystal chemistry, and selected bond valences, *Z. Kristallogra.*, **201**, 263 (1992).

9. I. Vencato, E. Mattievich, Y. P. Mascarenhas, "Crystal structure of synthetic lipscombite: a redetermination," *Am. Mineral.,* **74 (3-4)**, 456 (1989).

10. I. Vencato, E. Mattievich, Y. P. Mascarenhas, "Crystal structure of synthetic lipscombite: a redetermination," *Acta Cryst. A,* **43**, C153 (1987).

11. M. L. Lindberg, C. L. Christ, "Crystal structures of the isostructural minerals lazulite, scorzalite and barbosalite," *Acta Cryst.,* **12**, 695 (1959).

12. M. Dollé, S. Patoux, T. J. Richardson, "Lithium insertion chemistry of phosphate phases with the lipscombite structure," *J. Power Sources*, **144 (1)**, 208 (2005).

13. Z. Wang, S. Sun, F. Li, G. Chen, D. Xia, T. Zhao, W. Chu, Z. Wu, "Stability, electrochemical behaviors and electronic structures of iron hydroxyl-phosphate," *Mater. Chem. Phys.*, **123 (1)**, 28 (2010).

14. S. Sun, Z. Wang, D. Xia, "Theoretical study of a new cathode material of li-battery: Iron hydroxyl-phosphate," *J. Phys. Chem. C*, **114 (1)**, 587 (2010).

15. S. M. Zhang, J. X. Zhang, S. J. Xu, X. J. Yuan, T. Tan, "Synthesis, morphological analysis and electrochemical performance of iron hydroxyl phosphate as a cathode material for lithium ion batteries," *J. Power Sources*, **243**, 274 (2013).

16. S. Han, J. Wang, S. Li, D. Wu, X. Feng, "Graphene aerogel supported $Fe_5(PO_4)_4(OH)_3 \cdot 2H_2O$ microspheres as high performance cathode for lithium ion batteries," *J. Mater. Chem. A*, **2**, 6174 (2014).

17. Yu, Y. D.; Zhu, Y. J.; Wu, J. Glycerin-assisted solvothermal synthesis of $Fe_3(PO_4)_2(OH)_2$ microspheres, *Materials Letters*, **205**, 158 (2017).

18. C. Karegeya, A. Mahmoud, R. Cloots, B. Vertruyen, F. Boschini, "Hydrothermal synthesis in presence of carbon black: Particle-size reduction of iron hydroxyl phosphate hydrate for Li-ion battery," *Electrochim. Acta*, **250**, 49 (2017).

19. A. Mahmoud, C. Karegeya, M. T. Sougrati, J. Bodart, B. Vertruyen, R. Cloots, P. E. Lippens, F. Boschini, "Electrochemical Mechanism and Effect of Carbon Nanotubes on the Electrochemical Performance of $Fe_{1.19}(PO_4)(OH)_{0.57}(H_2O)_{0.43}$ Cathode Material for Li-Ion Batteries," *ACS Appl. Mater. Interfaces*, **10 (40)**, 34202 (2018).

20. C. Henriksen, C. Wegeberg, D. B. Ravnsbæk, "Phase Transformation Mechanism of Li-Ion Storage in Iron(III) Hydroxide Phosphates," *J. Phys. Chem. C*, **122 (4)**, 1930 (2018).

21. B. L. Ellis, L. F. Nazar, "Anion-induced solid solution electrochemical behavior in iron tavorite phosphates," *Chem. Mater.*, **24 (6)**, 966 (2012).

22. G. Zhou, X. Duan, B. Liu, Q. Li, T. Wang, "Architectures of tavorite $LiFe(PO_4)(OH)_{0.5}F_{0.5}$ hierarchical microspheres and their lithium storage properties," *Nanoscale*, **6 (19)**, 11041 (2014).

23. H. Yaghoobnejad Asl, A. Choudhury, "Phosphorous acid route synthesis of iron tavorite phases, $LiFePO_4(OH)_xF_{1-x}$ $[0 \leq x \leq 1]$ and comparative study of their electrochemical activities," *RSC Adv.*, **4 (71)**, 37691 (2014).

24. M. -Y. Cho, Y. S. Lim, S. –M. Park, K. –B. Kim, K. C. Roh, "Size-tunable tavorite LiFe(PO4)(OH) microspheres with a core-shell structure," *CrystEngComm*, **17 (32)**, 6149 (2015).

25. J. M. M. Millet, D. Rouzies, “Mössbauer spectroscopic study of synthetic lipscombite and barbosalite at room temperature,” *Hyperfine Interact.*, **77**, 11 (1993).

26. Bruker- SMART. Bruker AXS Inc., Madison, Wisconsin, USA. **2002**.

27. Bruker- SAINT, SADABS and SHELXTL. Bruker AXS Inc., Madison, Wisconsin, USA, **2008**.

28. G. M. Sheldrick, “A short history of SHELX,” *Acta Cryst*., **A64**, 112 (2008).

29. A. L. Spek, “Structure validation in chemical crystallography,” *Acta Cryst.*, **65D**, 148 (2009).

30. G. M. Sheldrick, C. B. Hubshle, B. Dittrich, “Shelxle: A Qt graphical user interface for SHELXL,” *J. Appl. Cryst*., **44**, 1281 (2011).

31. B. H. Toby, R. B. Von Dreele, “GSAS-II: the genesis of a modern open-source all-purpose crystallography software package,” *J. Appl. Cryst*., **46**, 544 (2013).

32. K. Lagarec, D. G. Rancourt, “Extended Voigt-based analytic lineshape method for determining N-dimensional correlated hyperfine parameter distributions in Mössbauer spectroscopy.” *Nucl. Instrum. Methods Phys. Res., Sect. B,* **129**, 266 (1997).

33. P. Sandineni, H. Yaghoobnejad Asl, A. Choudhury, “Kagomé lattices as cathode: Effect of particle size and fluoride substitution on electrochemical lithium insertion in sodium- and ammonium Jarosites,” *J. Solid State Chem.,* **242**, 78 (2016).

34. G. J. Redhammer, G. Tippelt, G. Roth, W. Lottermoser, G. Amthauer, “Structure and Mössbauer spectroscopy of barbosalite $Fe^{2+}Fe_2^{3+}(PO_4)(OH)$ between 80 K and 300 K,” *Phys. Chem. Miner.,* **27 (6)**, 419 (2000).

35. F. Menil, “Systematic trends of the ^{57}Fe Mössbauer isomer shifts in (FeO_n) and (FeF_n) polyhedra. Evidence of a new correlation between the isomer shift and the inductive effect of the competing bond T −X (→ Fe) (where X is O or F and T any element with a formal positive charge).” *J. Phys. Chem. Solids,* **46**, 763 (1985).

36. M. C. Smart, B. V. Ratnakumar, S. Surampudi, “Electrolytes for Low-Temperature Lithium Batteries Based on Ternary Mixtures of Aliphatic Carbonates,” *J. Electrochem. Soc.*, **146**, 486, (1999).

37. T. R. Jow, S. A. Delp, J. L. Allen, J. –P. Jones, M. C. Smart, “Factors limiting Li^+ charge transfer kinetics in Li-ion batteries,” *J. Electrochem. Soc.*, **165**, A361, (2018).

38. W. Yang, Y. Bi, Y, Qin, Y. Liu, X. Zhang, B. Yang, Q. Wu, D. Wang, S. Shi, "$LiMn_{0.8}Fe_{0.2}PO4/C$ cathode material synthesized via co-precipitation method with superior high-rate and low-temperature performances for lithium-ion batteries," *J. of Power Sources*, **275**, 785, (2015).

39. M. Satyanarayana, R. S. Rao, V. Pralong, U. V. Varadaraju, "Reversible Li Insertion Studies on $V_4O_3(PO_4)_3$ as High Energy Storage Material for Li-Ion Battery Applications," *J. Electrochem. Soc.*, **164**, A6201 (2017).

IV. A SQUARE CHANNEL VANADIUM PHOSPHITE FRAMEWORK AS HIGH VOLTAGE CATHODE FOR Li- AND Na- ION BATTERIES

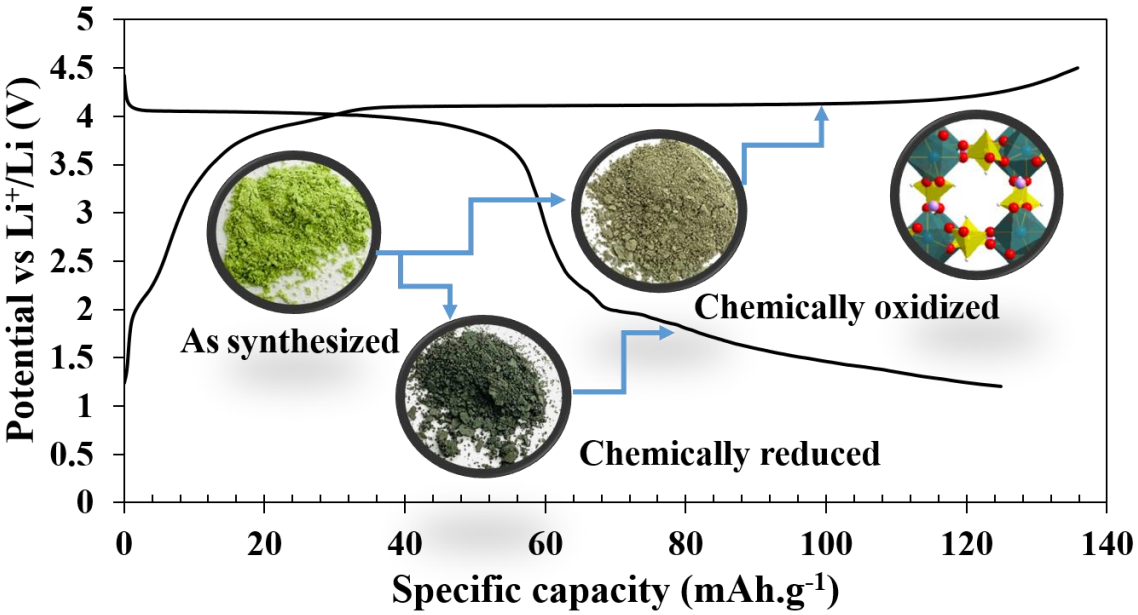

Prashanth Sandineni[a], Pranal Madria[a], Kartik Ghosh[b], and Amitava Choudhury[a,*]

[a]Department of Chemistry, Missouri University of Science and Technology, Rolla, MO 65409, USA.

[b]Department of Physics, Astronomy and Materials Science and Center for Applied Science and Engineering, Missouri State University, Springfield, Missouri 65897, USA.

ABSTRACT

A vanadium phosphite compound, $LiV(HPO_3)_2$, has been synthesized using low-melting flux comprised of phosphorous acid and lithium hydroxide. The crystal structure

of the compound is as refined by Rietveld method matched with the previously reported unit cell parameters (space group: $I\bar{4}2d$, $a = b = 10.5987(4)$, $c = 9.9843(5)$ Å). It has a 3-dimensional open-framework structure with intersecting channels. Eight-membered ring square channels along the *c*-axis and 6-membered ring channels along the *a*- and *b*-axis. The Li-ions are located in the six-membered ring channels exactly at the opening window to the eight-membered ring channels. The magnetic property measurement confirmed the +3 oxidation state of vanadium. The synthesized V-phosphite display facile electrochemical properties with an average voltage of 4.05 V vs Li^+/Li and 3.7 V vs Na^+/Na in Li- and Na–ion batteries, respectively, when cycled between 4.5 and 1.2 V. The galvanostatic charge-discharge profile indicates that $LiV(HPO_3)_2$ can be cycled between $V(HPO_3)_2$ and $Li_2V(HPO_3)_2$. The compound was further characterized by TGA, IR, and diffuse reflectance spectroscopy.

1. INTRODUCTION

Over the past two decades, Li-ion batteries (LIB) have been touted as the primary source for energy storage and power supply owing to its high energy density.[1–7] Depending on the intended applications, batteries can be designed with optimum energy density. For example, high energy density is required for portable applications while low cost, long cycle life, fast charge-discharge capability precedes over high energy density for stationary devices like smart grids.[5, 8] Layered Li-rich oxides, $xLi_2MnO_3\cdot(1–x)LiMO_2$ ($0 < x < 1$, M = $Ni_{0.5}Mn_{0.5}$, $Mn_{x'}Ni_{y'}Co_{1–x'–y'}$, $0 < x', y' < 1$) have attracted great deal of interest for their high specific capacities and low-cost, but there are still challenges related to capacity

fading and safety hazards need to be addressed before they can be used commercially in LIBs.[9 – 13] Polyanion-based (PO_4^{3-}, SO_4^{2-}, SiO_4^{4-} etc.) cathode materials have attracted lot of attention owing to their higher electrochemical stability and achievable capacities as first demonstrated by Goodenough in the case of olivine, $LiFePO_4$.[14] Compared to layered lithium metal oxides, polyanion-based materials are inherently safer because of the strong covalent bond between the oxygen and the central element of the polyanionic moiety. Another significance of the polyanion chemistry is that the electronegativity of the central atom can tune the redox potential of the transition metal couple by changing the iono-covalency of metal – ligand bond through the relay of inductive effect in $M-O-X$ linkage (M = transition metal; X = central atom of polyanion).[3, 15] Besides safety and voltage tuneability, polyanioinc compounds are great playground for solid state chemists as they can be synthesized under mild reaction conditions such as hydrothermal. A large number of structure types encompassing 3-dimensional (3-D) structures with channels or layered 2-dimensional structures can be accessed by varying the reaction conditions. Using this strategy various electroactive compounds have been synthesized with a variety of polyanions,[16] for example, phosphates,[17-19] pyrophosphates,[20, 21] sulfates,[22] borates,[23, 24] silicates,[25, 26] as well as a range of mixed polyanions such as carbono-phosphates, [27, 28] phosphate-pyrophosphates,[29, 30] phosphatonitrate[31] and so on.[32] Polyanions in combination with another electronegative element such as fluoride has been successfully used to further boost insertion voltage through inductive effect.[33, 34] Polyanion-based electrodes are also excellent host for Na-ion batteries because of the availability of channel dimension/volume appropriate for the size of Na-ion.[35]Amidst all the development of polyanion electrodes, one important family of polyanions namely phosphites in which one of the oxygen of

phosphate is replaced by a hydrogen, has remained largely unexplored. Phosphites are known to form very stable 3-dimensional structure with channels through vertex-sharing between the pseudo tetrahedral HPO_3^{2-} and metal-oxygen polyhedra. Rojo *et al.* first reported the electrochemical activity in an open-framework iron phosphite, $Li_{1.43}[Fe_{4.43}^{II}Fe_{0.57}^{III}(HPO_3)_6]\cdot 1.5H_2O$,[36] but with a limited specific capacity. We have recently demonstrated facile electrochemical activities in two more iron phosphites $Li_3Fe_2(HPO_3)_3Cl$ and $LiFe(HPO_3)_2$[37, 38] with an average voltage of 3V and capacity exceeding 70 $mAhg^{-1}$. There has been few more reports of phosphites with encouraging electrochemistry.[39 - 41] Both $Li_3Fe_2(HPO_3)_3Cl$ and $LiFe(HPO_3)_2$ are two electron candidates, however, their 2nd electron could not be extracted because often it is very difficult to access 3+/4+ couple of iron. Vanadium compounds, on the other hand are known to exhibit multi electron process more readily. Multi-electron process has been touted to be one of the ways to invent next generation high-capacity Li-ion batteries by Whittingham.[42, 43] We, therefore, sought to synthesize $LiV(HPO_3)_2$, isostructural to $LiFe(HPO_3)_2$ to access both +4 and +2 oxidation states through oxidative de-insertion of Li and reductive insertion of Li, respectively.

In this article, we report reversible (de)intercalation of Li at a high average voltage of ~4.1 V with reasonable capacity exceeding 80 $mAhg^{-1}$ when $LiV(HPO_3)_2$ is cycled between 4.5 to 2 V. A capacity of >125 $mAhg^{-1}$ can be harnessed when a 2nd lithium is inserted demonstrating possibility of accessing multiple redox couples (V^{2+}/V^{3+}, V^{3+}/V^{4+}) in vanadium phosphites to increase the capacity. The compound also exhibited its electrochemical activity toward reversible insertion of Na^+ ions at an average voltage of 3.7 V in a hybrid cell when V^{3+}/V^{4+} couple is accessed.

2. EXPERIMENTAL

2.1. MATERIALS

VCl_3 (97%), H_3PO_3 (98% extra pure) and $LiOH \cdot H_2O$ (98% reagent grade) were purchased from Acros Organics. All the chemicals used in the syntheses were as-purchased and without further purification.

2.1.1. Synthesis. A mixture of 0.7870 g of VCl_3 (5 mmol), 1.2304 g of H_3PO_3 (15 mmol), and 0.6295 g of $LiOH \cdot H_2O$ (15 mmol) were ground in an agate mortar pestle, and the resulting paste was transferred into a 23 ml capacity Teflon-lined stainless steel Paar acid digestion bomb, which was then sealed tightly, and placed in a 175 °C pre-heated oven for 24 hours, followed by cooling down naturally to room temperature. The product of the reaction was then filtered and washed with hot water to remove any unreacted reagents and dried at room temperature (yield 94%).

10% Fe-substituted compound was also synthesized similarly. A mixture of 0.6292 g of VCl_3 (4 mmol), 0.1988 g of $FeCl_2.4\ H_2O$ (1 mmol), 1.2304 g of H_3PO_3 (15 mmol), and 0.6295 g of $LiOH \cdot H_2O$ (15 mmol) were ground in an agate mortar pestle, and the resulting paste was transferred into a 23 ml capacity Teflon-lined stainless steel Paar acid digestion bomb, which was then sealed tightly, and placed in a 175°C pre-heated oven for 24 hours, followed by cooling down naturally to room temperature. The product of the reaction was then filtered and washed with hot water to remove any unreacted reagents and dried at room temperature. The Fe^{3+} salt ($FeCl_3 \cdot 6H_2O$) was intentionally avoided because it was absorbing too much water during the mixing and the desired product was not forming. Fe^{2+} salt was presumed aerially oxidized to Fe^{3+} during reaction.

2.1.2. Chemical Oxidation and Reduction. The compound was subjected to chemical oxidation using NO_2BF_4. 0.2460 g (1.13 mmol) of the compound was mixed with 0.1740 g (1.31 mmol) of NO_2BF_4 in acetonitrile and was stirred continuously at room temperature in an argon filled glovebox for 5 days and then the reaction mixture was filtered, washed with acetonitrile and dried under vacuum without exposing to air. Chemical reduction was carried out using $LiAlH_4$. 0.2048 g (0.94 mmol) of the compound was mixed with 0.03567 g (0.94 mmol) of $LiAlH_4$ in tetrahydrofuran (THF) and was stirred continuously at room temperature in an argon filled glovebox for 3 days and then the reaction mixture was filtered, washed with THF and dried under vacuum without exposing to air.

2.1.3. Electrochemical Testing. To test the electrochemical performance of the sample, the compound was subjected to ball-milling thoroughly after mixing with super P conductive carbon in a SPEX 8000 miller for 1 hour to reduce the particle size. Ball milling was done only for 1 hour, as we observed the development of new peaks in the PXRD after 1 hour of milling (Figure S1, S.I.). Poly-vinylidene fluoride (PVDF) was then added to the active material as the binder and an optimum amount of N-methyl-2-pyrrolidone (NMP) was added to dissolve the PVDF. The resulting slurry was further ball milled for another 20 minutes to obtain a homogeneous viscous mixture. The ratio of the active material, conducting carbon, and the binder in the cathode mix was 75: 15: 10. The cathode mix was then spread as a film of uniform thickness with the help of a glass rod onto a flat sheet of carbon-coated aluminum current collector and transferred into a vacuum oven and dried overnight at 85 °C.

For electrochemical tests, CR2032 type coin cells were fabricated. The composite cathode film was cut into circular disks (3/8 inch diameter) with 4.0–5.0 mg of active material loading and transferred into an argon filled glove box with an oxygen concentration below 0.1 ppm. The cathode disk and Li anode (0.75 mm thickness Li ribbon cut into circular disk) were assembled in the coin cell casing with a Celgard® 2325 circular sheet placed between the two electrodes as the separator. The electrolyte, 1 M solution of $LiPF_6$ in DMC–EC (1:1) was then added and the cell was sealed with a coin cell crimper. The prepared cells were aged for equilibration for about 12 hours before electrochemical testing. Similarly Na-ion batteries were also made using Na anode and 1 M solution of $NaClO_4$ in PC was used as the electrolyte.

Cyclic voltammograms were obtained using a PAR EG&G potentiostat/galvanostat model 273 in the potential range of 1.2 – 4.5 V (vs. Li/Li^+) and (vs. Na/Na^+) with a scan rate of 0.05 mV s^{-1}. Voltage composition profiles were obtained using galvanostatic charge/discharge experiments on an Arbin Instruments battery tester, model BT2043, on the same potential limits as CV at various C-rates.

2.2. MATERIAL CHARACTERIZATION

Single-crystal structure determination of $LiV(HPO_3)_2$ has been reported[45] but the article only lists the unit cell parameters and no atomic coordinates. The atomic coordinates were also not found in any database. Therefore, to determine the structure and establish absence of any impurity phase(s) Rietveld refinement was employed on high-resolution synchrotron PXRD (S-PXRD) data collected from Advanced Photon Source (APS) in Argonne National Laboratory. The atomic coordinates of $LiFe(HPO_3)_2$ were used in the

initial model and refinement of S-PXRD data using GSAS-II[46] converged very well, which also showed absence of any impurity phase (Figure 1). The final refined unit cell parameters are in agreement with the reported one[45] and are listed with final refinement parameters of the compound in Table 1. Atomic coordinates and isotropic displacement parameters are given in Table S1. Selected bond lengths are given in Table 2.

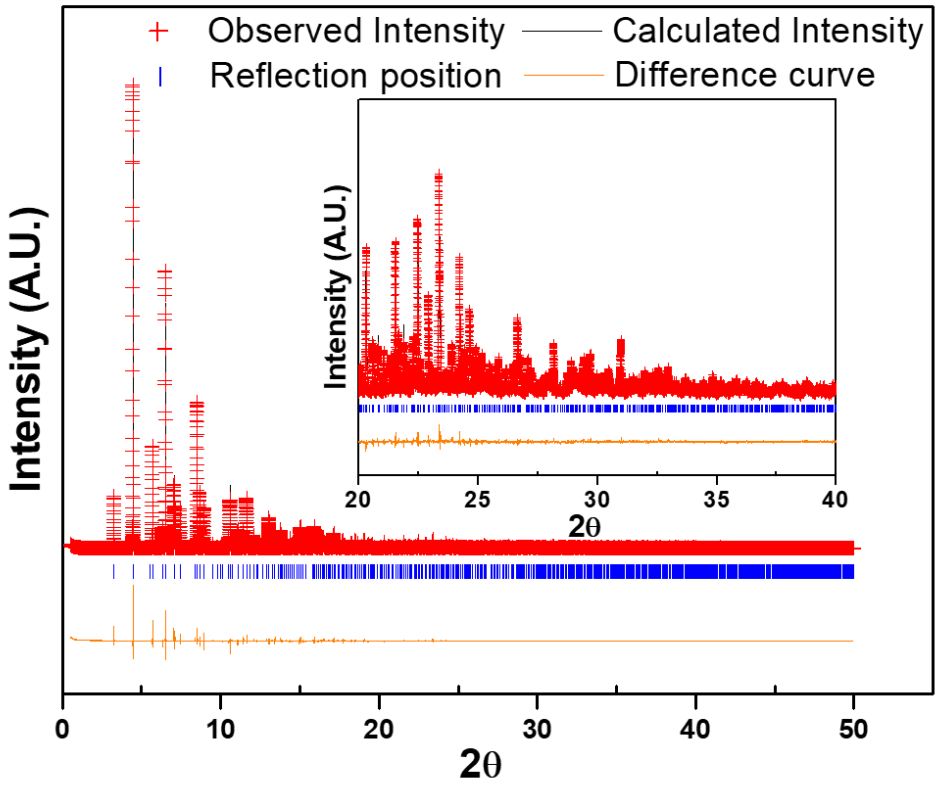

Figure 1. Rietveld refinement of synchrotron XRD data of $LiV(HPO_3)_2$ showing the observed, calculated and difference curve. Inset shows enlarged view of the segment for 2θ = 20 to 40°. (λ = 0.412834 Å)

2.2.1. Thermogravimetric Analysis (TGA). TGA has been performed with a TA instruments Q50 TGA from room temperature to 800 °C with a scan rate of 10 °C min^{-1}

under nitrogen atmosphere. The TGA curve of the sample shows that it is stable up to 400 °C (Figure 2a). On further heating from 400 to 800 °C, a mass gain is observed due to the presumed oxidation of P(III) to P(V) forming $LiV(P_2O_7)$. The oxidation may have caused as result of reaction with oxygen impurity (see eqn. 1) from the nitrogen gas used for purging, as confirmed by the PXRD of the residue remained after TGA. Similar oxidation of phosphite has been previously observed in phosphite-based materials.[36, 38, 47, 48]

$LiV(HPO_3)_2 + O_2 = LiV(P_2O_7) + H_2O$ …….. 1

Table 1. Refined lattice constants and final Rietveld refinement parameters from the synchrotron powder XRD for $LiV(HPO_3)_2$.

Empirical formula	$LiV(HPO_3)_2$
Formula weight	217.84
Crystal system	Tetragonal
Space group	$I\bar{4}2d$
a/Å	10.5987(4)
b/Å	10.5987(4)
c/Å	9.9843(5)
Volume	1121.57(4) $Å^3$
Z	8
Number of reflections	1399
R_w	12.450 %
R_f^2	6.411 %
Number of data points	47571

Table 2. Selected bond lengths [Å] for the compound.

Atom-Atom	*d* (Å)	Atom-Atom	*d* (Å)	Atom-Atom	*d* (Å)
P1 – O1	1.5215(8)	2 x V1 – O1	2.0195(5)	2 x Li1 – O1	2.0092(1)
P1 – O2	1.5260(2)	2 x V1 – O2	2.0106(4)	2 x Li1 – O2	2.0155(7)
P1 – O3	1.5205(8)	2 x V1 – O3	1.9583(5)		
P1 – H1	1.3339(5)				

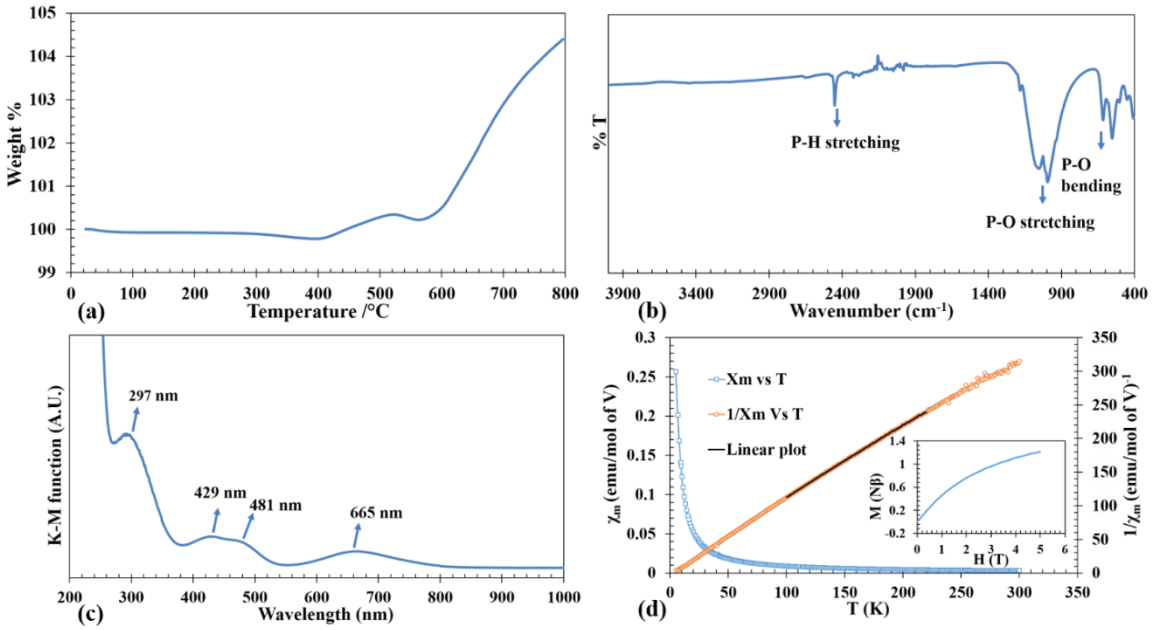

Figure 2. TGA curve (a), FT-IR spectrum (b), DRS spectrum (c), Temperature dependence of molar magnetic susceptibility (χ_m) and inverse molar magnetic susceptibility (χ_m^{-1}) of $LiV(HPO_3)_2$ (d). Inset of Figure 2(d) shows *M* vs *H* plot.

2.2.2. IR Spectroscopy. The IR spectrum was collected using Thermo Nicolet iS50 FT-IR spectrometer over 400–4000 cm^{-1} on a sample using ATR mode. The IR spectrum in Figure 2b clearly shows the signature P – H stretching at 2450 cm^{-1}. P – O stretching modes are observed from 900 – 1100 cm^{-1}. The region from 500 – 600 cm^{-1} corresponds to P – O bending modes.

2.2.3. UV-Visible Spectroscopy. Diffuse reflectance spectrum on powdered sample was collected using a Praying Mantis accessory on Cary 5000 UV-Vis-NIR spectrophotometer over 200 – 1500 nm range. UV-Vis absorption spectrum of the compound as converted from the diffuse reflectance data employing Kubelka-Munk equation is given in Figure 2c. Considering the normal valencies of the elements in $LiV(HPO_3)_2$, the oxidation state of V can be discerned as +3, which is a d^2 ion. The spin allowed electronic transition from the ground state $^3T_{1g}(3F)$ to the excited states of the same spin multiplicities $^3T_{2g}(3F)$, $^3T_1g(^3P)$ and $^3A_{2g}(^3F)$ take place at wavelengths 665, 481 and 429 nm. Besides these, the weak spin forbidden transition from $^3T_{1g}(3F)$ to ^1E_g (1G) is observed at high energy (297 nm) as a shoulder in ligand-metal charge transfer band.[49, 50]

2.2.4. Magnetic Measurements. The variable temperature magnetic susceptibility measurements of the compound (as-prepared) was carried out in the temperature range 5 – 300 K using Quantum Design SQUID magnetometer at 1T applied field while warming up under zero-field cooled (ZFC) conditions. Isothermal magnetization measurements were performed at 5 K between 0 to 5 T applied field. The plots of temperature dependent ZFC magnetic susceptibility $\chi_M(T)$, the corresponding inverse molar susceptibility $\chi_M^{-1}(T)$ and isothermal field dependent magnetization $M(H)$ for the as-synthesized compound are given in Figure 2d. The magnetic susceptibility χ_M vs T plot is asymptotic from 5 to 300 K with

an applied field of 1 T which indicate paramagnetic region without any ordering. The small negative Θ_p value (-3.68 K) suggests that there may exist antiferromagnetic correlation in the paramagnetic region and an antiferromagnetic ordering may exist below 2K. Magnetic moment/V (2.74 μ_B) as calculated from the curie constant, C, derived from the linear fit yields a value closer to the theoretical magnetic moment of 2.83 μ_B corresponding to d^2 configuration thus supporting +3 oxidation state of V as also observed in DRS. The saturation magnetization at 5 K is about 1.21 Nβ, which is about 60% of the theoretical saturation magnetization ($Ms = gS$ Nβ) of 2 Nβ as calculated for V^{3+} with 2 unpaired electrons of parallel spins (inset of Figure 2d).

3. RESULTS AND DISCUSSION

3.1. SYNTHESIS AND STRUCTURE

A low temperature solvent free synthesis route was used to produce the compound, $LiV(HPO_3)_2$. The reported synthesis was also a low temperature route using molten boric acid flux and HF as mineralizer.[45] The synthesis method reported here is a straight forward one and devoid of use of corrosive HF. VCl_3 was used as V source hence no reducing agent was needed. $LiOH{\cdot}H_2O$ as Li source and H_3PO_3, which has a low melting point of 73.6 °C, as phosphite source were mixed together to form a low-melting flux. The reaction was carried out at 175 °C for one day to produce the desired product, and the identity of the product did not change even if the reaction was carried out for seven days.

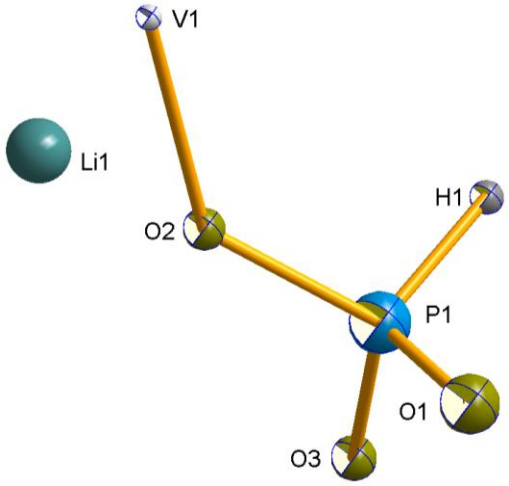

Figure 3. Asymmetric unit of $LiV(HPO_3)$.

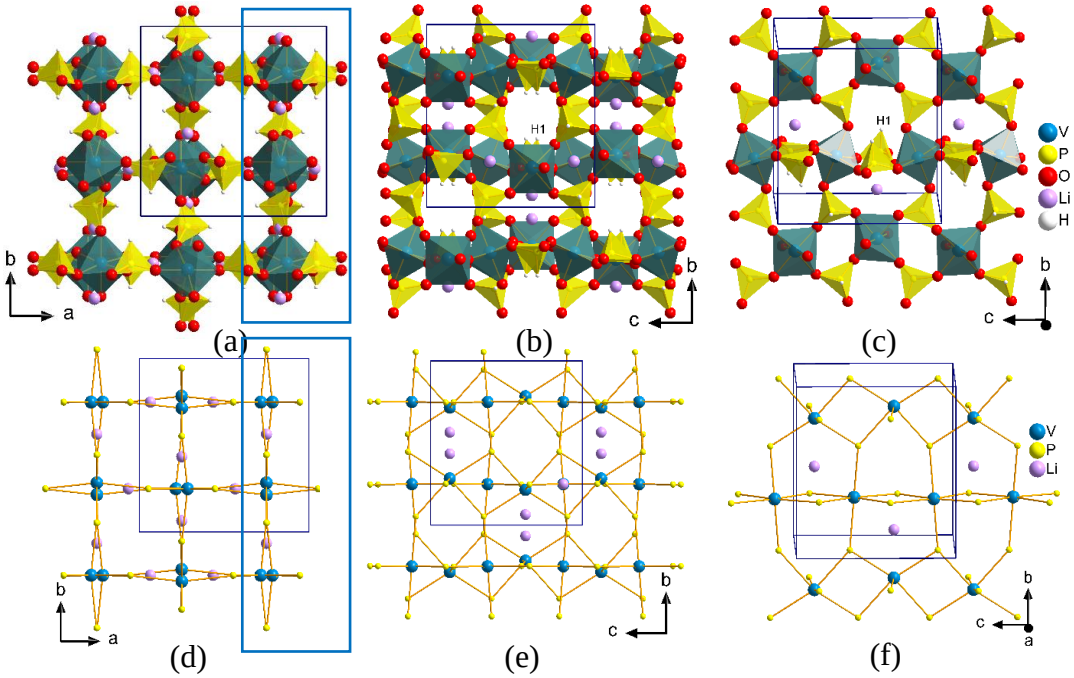

Figure 4. Perspective view of packing diagram of $LiV(HPO_3)_2$ along *c*-axis (a, d) and along *a*-axis (b, e). A slice of layer from Figures 4a and b (blue rectangles) projected onto *bc* plane are shown in Figures 4c and 4f.

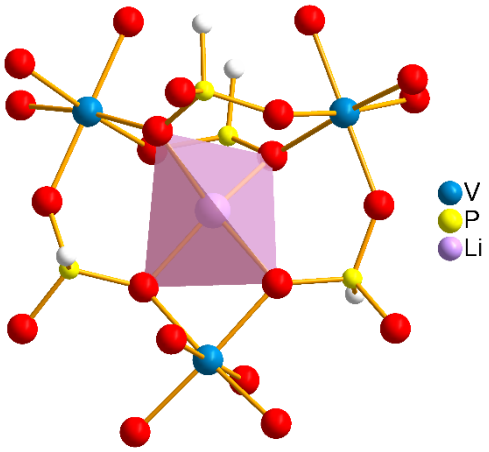

Figure 5. Li-coordination in $LiV(HPO_3)_2$.

The structure of $LiV(HPO_3)_2$ has been discussed already in the literature.[45] The asymmetric unit consists of seven atoms, one V, one P, three O, one Li, and one H (Figure 3). It has a 3-dimensional framework made up of alternating vertex-sharing VO_6 octahedra and HPO_3 psuedopyramidal units with Li-ions located in the channels (Figure 4). The V – O bond distances are in the range of 1.9583(5) – 2.0195(5) Å which are in agreement with the reported V – O distances in V^{3+} compounds.[49 – 51] P – O bond distances in the phosphite group are in the range of 1.5205(8) – 1.5260(2) Å and P – H bond distance is 1.3339(5) Å in agreement with the reported metal phosphites.[36, 38, 48, 49, 51] Vertex sharing alternating VO_6 octahedra and HPO_3 units form 4-membered rings (connecting only V and P), which are further connected to form a chain, and the chains are further connected through HPO_3 units forming a layer (Figures 4 c and 4f). These layers are connected by HPO_3 groups to produce a 3-D structure with intersecting channels; 8-membered ring square-shaped channel along *c*-axis (Figures 4a and 4d) and 6-membered ring bifurcated channel along *a*- and *b*-axis (Figures 4b and 4e). Li-ions are located exclusively in the 6-membered ring

channel in the opening window to the 8- membered ring channel and adopts a very distorted tetrahedral coordination (Figure 5). The 8- membered ring channels are empty and the hydrogen atoms from the HPO_3 groups protrude into this channel (Figure 4a and 4d).

3.2. ELECTROCHEMISTRY

3.2.1. Cyclic Voltammetry. Cyclic voltammetry tests were conducted on the fabricated Li-ion coin cells to get an idea of the Li-insertion (cathodic reduction) and Li-extractions (anodic oxidation) voltages. Figure 6a shows the first four cycles of cyclic voltammograms, when the cell was subjected to a voltage scanning between 1.2 – 4.5 V. The open circuit voltage (OCV) was observed at 2.99 V. The battery was discharged first on the assumption that one more Li can be inserted to further reduce the V^{3+} to V^{2+}, however, a clear reduction peak could not be observed due to very low current (inset of Figure 6a). It is to be noted here that previous work on isostructural host with Fe^{3+} in place of V^{3+} displayed facile reductive Li-insertion through the reduction of Fe^{3+} to Fe^{2+}.[38] However, upon charging one could see a high intense peak current at 4.3 V due to V^{3+} to V^{4+} oxidation and a corresponding reduction peak at 3.97 V.

Similarly, Na-ion cells were subjected to the same voltage scanning from 1.2 – 4.5 V, and the battery was charged first to remove the Li and during the reduction cycle it was presumed that insertion of Na^+ would take place. The first oxidation peak was similar to the Li-ion cell, at 4.3 V, but on subsequent oxidation the peaks shifted to 4.15 V, which was consistent with the notion that during the first oxidation Li was extracted while in the 2^{nd} cycle Na^+ was extracted. The corresponding reduction peaks are at 3.63 V, which is ~.34 volt less than Li-ion cell and does not show any shift during cycling indicating that

the inserted ion was Na^+ (Figure 6b), consistent with the lower redox potential of Na/Na^+ couple (2.71 V) compared to Li/Li^+ (3.04 V) with respect to SHE.

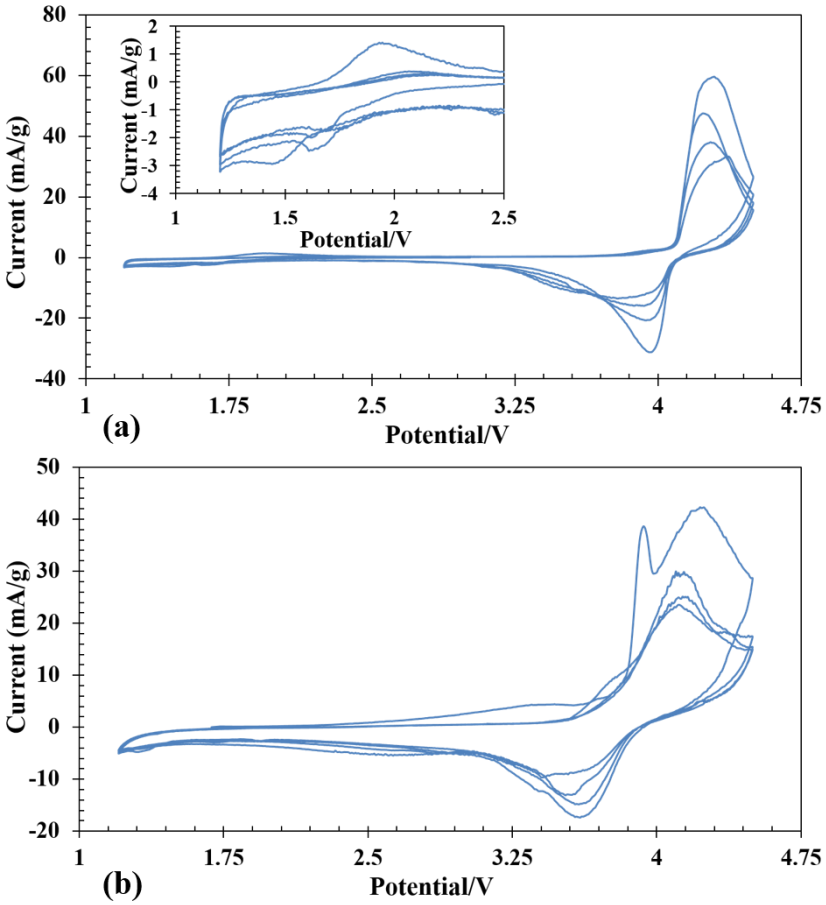

Figure 6. First four cycles of cyclic voltammograms of Li-ion cell (a) (Inset shows enlarged view from 1.2 to 2.5 V) and Na-ion cell made with $LiV(HPO_3)_2$ as cathode and pure Li and Na as anodes, respectively.

3.2.2. Galvanostatic Charge-Discharge. The galvanostatic charge-discharge experiments were done at various slow C-rates and the cut-off potentials were set in the range 2.0 – 4.5 V or 1.2 – 4.5 V in different tests (Figure 7). Assuming a complete one electron process per V atom, the theoretical capacity of the compound can be calculated to

be 122.96 mAh.g^{-1}. Figure 7 shows the charge-discharge profiles at C/50. The battery was charged first and the first charge delivered a capacity of 137 mAh.g^{-1}, which on subsequent cycles decreased to 90, 84, and 79 mAh.g^{-1}. The extra capacity during the first charge can be attributed to the oxidation of the electrolyte and formation of cathode electrolyte interface (CEI). The corresponding discharge capacities were 75, 77, 75, and 72 mAh.g^{-1}, respectively. Subsequently at various comparatively faster C-rates specifically, at C/20, C/10 and C/5, a very stable discharge capacity of 55, 42 and 30 mAh.g^{-1}, respectively, (inset of Figure 7) were observed. After all the faster C-rates, the cell was again cycled at C/50 which achieved a capacity of 66 mAh.g^{-1} suffering a loss of 6 mAh.g^{-1} and a stable capacity thereafter indicating decrease of capacity at faster C-rate may be associated with the polarization within the cell and not due to any crystal structure degradation of the host. This was also reflected in the ex-situ PXRD of the cycled cells which showed retention of crystallinity (discussed later). After 20 cycles of various C-rates, the battery was cycled at C/10 for 150 cycles to evaluate the capacity retention and the results indicated that it maintained a steady capacity 33 mAh.g^{-1} with 100 % coulombic efficiency after an initial loss of 9 mAh.g^{-1} (Figure S4, S.I.).

In order to check the possibility of second electron process (V^{3+}/V^{2+}), the battery was discharged until 1.2 V. Figure 8 shows the charge-discharge profiles of battery cycled between 4.5 to 1.2 V. The discharge curves exhibit a flat plateau from 4.5 to 3.5 V indicating a two phase behavior of V^{4+}/V^{3+} couple with a sharp fall till 2.0 V and a second rather sloppy discharge profile from 2.0 V to 1.2 V corresponding to the insertion of second lithium ion. The sloppy profile of the second electron process indicate a solid solution for the V^{3+}/V^{2+} couple. The total discharge capacity observed in the first run was 125 mAh.g^{-}

[1], which can be exactly divided into capacity ranges due to two redox processes $V^{4+/3+}$ and $V^{3+/2+}$, respectively, indicating that the percentage (~50 %) of V^{4+} reduced in the high voltage plateau to V^{3+} has been fully converted to V^{+2}. However, there is a loss in the capacity on successive cycling when V^{2+} was accessed. Further optimization in terms of particle sizes, conductivities, and degree of SEI formation of the cathode active material need to be improved to fully access the $V^{4+/3+}$ couple to take advantage of the two full lithium insertion and double the capacity.

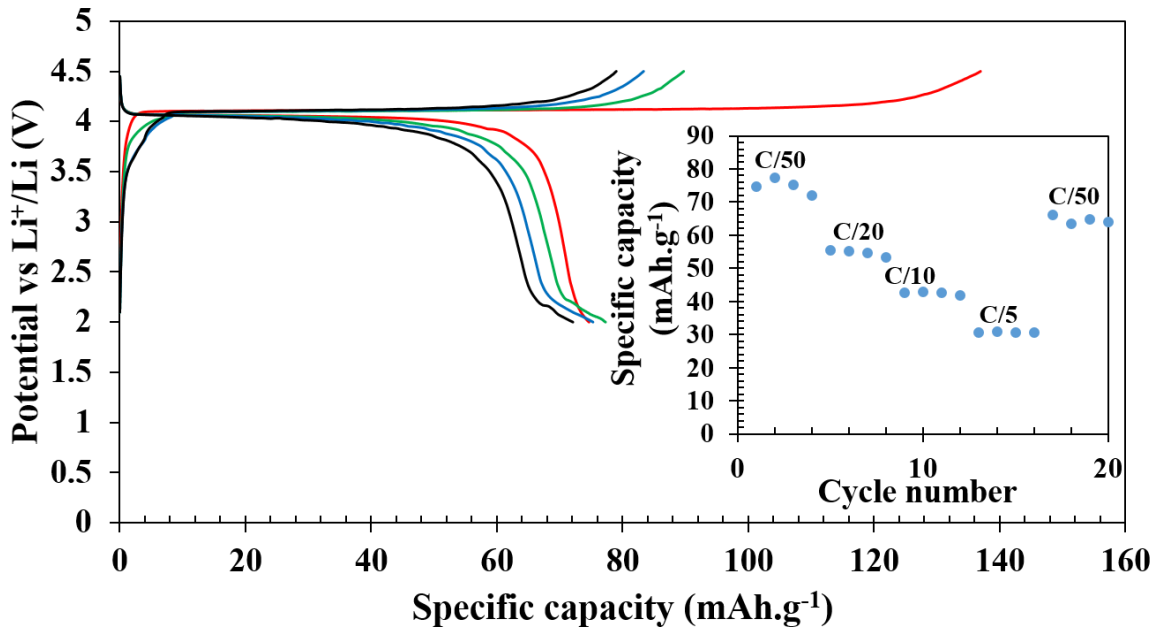

Figure 7. Galvanostatic charge-discharge profiles for Li-ion batteries at C/50. (Inset shows discharge specific capacity at different c-rates).

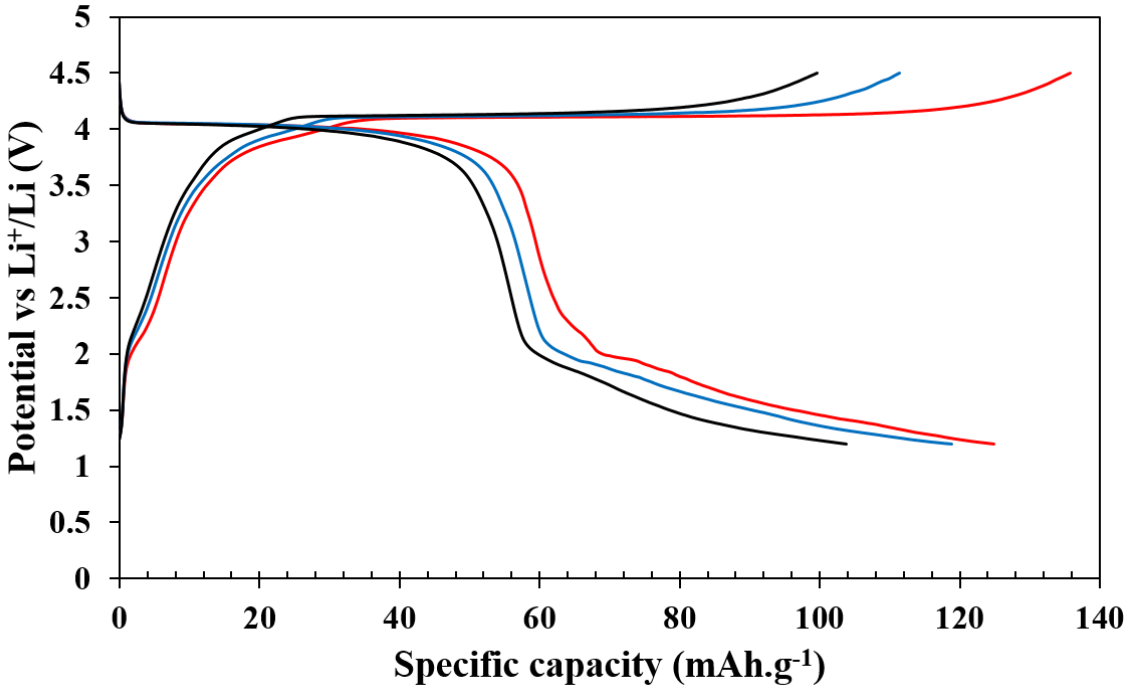

Figure 8. Galvanostatic charge-discharge profiles for Li-ion batteries at C/50 cycled between 1.2 to 4.5 V.

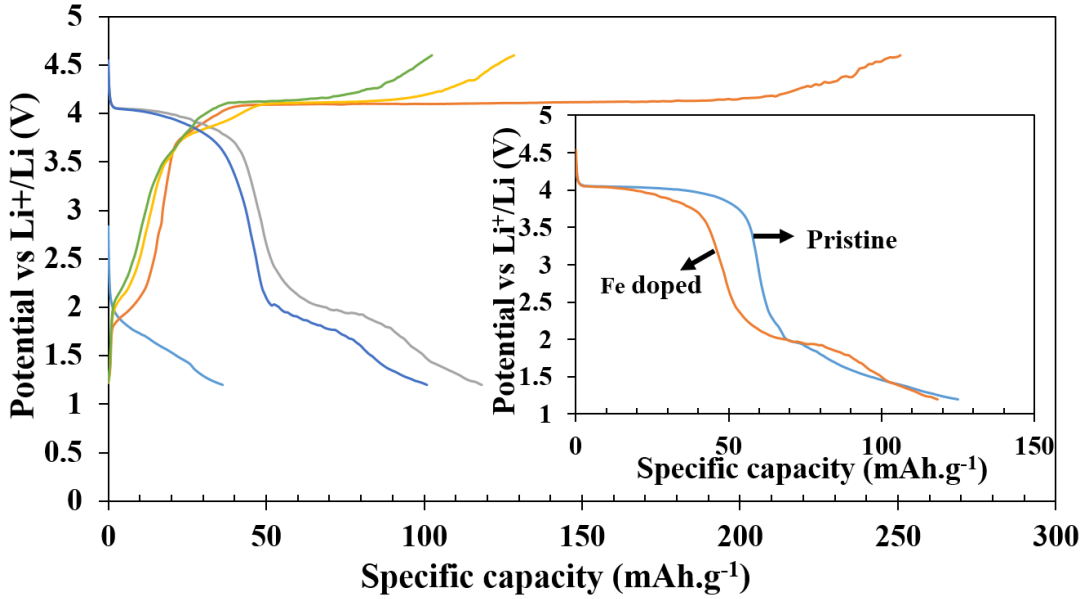

Figure 9. Galvanostatic charge-discharge profiles for Fe doped Li-ion batteries at C/50. (Inset shows comparison of discharge curves for Fe doped and pristine compounds).

To improve the cycle stability a small percentage (~10 %) of Fe^{3+} was doped in $LiV(HPO_3)_2$, taking clue from $LiFe(HPO_3)_2$ which exhibited a facile $Fe^{3+/2+}$ redox couple during Li-ion insertion. The charge-discharge profile of the battery made with the doped-material is shown in Figure 9. The battery was discharged first and a capacity of ~40 $mAh.g^{-1}$ was observed, which can be attributed exclusively to $V_{1-x}Fe_x^{3+/2+}$ (x = 0.1) couple. The discharge capacities increased to ~100 $mAh.g^{-1}$ in successive discharge cycles after the battery was charged to 4.5 volt. The first charging was again long due to CEI formation. The flat plateau for V^{4+}/V^{3+} from 4.5 to 3.5 V observed in the pristine battery has become somewhat sloppy during 2nd discharge and the average voltage also decreased to 3.9 V. The capacity at high voltage due to V^{4+}/V^{3+} couple has also decreased by ~10 $mAh.g^{-1}$ because of the substitution by Fe^{3+}, which is only active for Fe^{3+}/Fe^{2+} reduction (inset of Figure 9). The discharge profile for V^{3+}/V^{2+} couple starts from 2.5 V, which is an effect of small percentage of active Fe^{3+}/Fe^{2+} couple. However, 2.5 V is still less than the onset discharge voltage (~3 V) of Fe^{3+}/Fe^{2+} couple in $LiFe(HPO_3)_2$ but consistent with small percentage of Fe^{3+}-substitution in polyanion-based V^{3+} compound.[52] Instead of a rather sharp fall, a gradual sloppy profile in transitioning from V^{4+}/V^{3+} to V^{3+}/V^{2+} redox couple compared to pristine also supports doping of Fe^{3+} in the structure. Such transformation from sharp fall to slopping voltage profile can be a useful strategy for successful utilization in practical applications. The Fe-substitution, therefore, can be helpful for the V^{3+}/V^{2+} couple to achieve better capacity in the lower voltage window, but the overall achievable capacity will be diminished because of the loss in V^{4+}/V^{3+} couple activity due to Fe^{3+} substitution.

Na-ion cells, on the other hand were cycled between 1.75 to 4.5 V in a hybrid cell starting with Li-containing host. The battery was charged first to remove the Li, and the first charge capacity (166 mAh.g^{-1}) was more than the theoretical capacity at C/50 rate, presumably due the electrolyte decomposition and CEI formation as observed in Li-ion cells. In subsequent charging the capacity reduced to 84, 75, and 73 mAh.g^{-1} and the corresponding discharge capacities were 87, 68, 63, 61 mAh.g^{-1} (Figure 10). At various comparatively faster C-rates specifically, at C/20, C/10 and C/5, a very stable discharge capacities of 46, 35 and 25 mAh.g^{-1}, respectively, (inset of Figure 10) were observed. After all the faster C-rates, the cell was again cycled at C/50 which achieved a capacity of 54 mAh.g^{-1} suffering a loss of 7 mAh.g^{-1} and there is a gradual decrease in capacity thereafter. The slightly lower average voltage, ~3.65 V for V^{4+}/V^{3+} couple compared to 4 V in Li-ion cell also supports the intercalation of Na^+ ions after the first discharge.

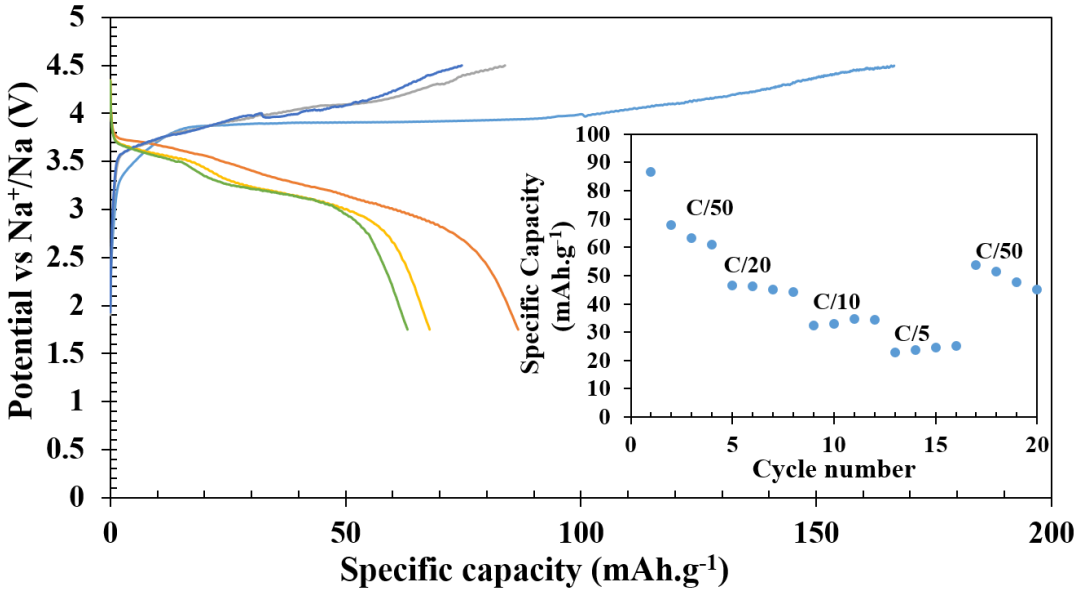

Figure 10. Galvanostatic charge-discharge profiles for Na-ion batteries at C/50. (Inset shows discharge specific capacity at different c-rates).

3.3. EX-SITU PXRD CHARACTERIZATION OF DISCHARGED AND CHARGED CELLS

The ex-situ PXRDs of the charged (to 4.5 V) and discharged (to 1.2 V) cells were carried out to further understand the mechanism of the charge-discharge profiles and to evaluate if there is any structural phase transition. For this, the coin cells were cracked-opened inside the argon filled glovebox and the cathode materials in the charged and discharged state of the cells were recovered, washed with dry acetonitrile, and dried under vacuum without exposing to air. The cathode material was then placed in an air tight cell holder, and PXRD was collected. The overall PXRDs look similar to the as-synthesized sample (Figure 11), except the shift in the peaks towards lower two-theta angles in the case of electrochemically reduced phase (lithiated) indicating an increase in the volume as supported by the Rietveld refinement values (Table S2, S.I.). The opposite effect (volume decrease) was observed in the case of electrochemically reduced phase (delithiated). However, the overall volume change is very minimal indicating the structure is very rigid. One of the lingering question in the phosphite-based cathode is the stability of the P-H bond during the electrochemical oxidation and reduction. To verify the intactness of the P – H bond, the IR-spectroscopy was run under ATR mode on the cathode materials in charged and discharged conditions on which ex-situ PXRD was conducted. The IR-spectra clearly showed the presence of P – H stretching confirming that along with crystallinity of the structure it also retains the P – H bond (Figure S5, S.I.). The ex-situ PXRDs of chemically reduced/oxidized phases also corroborate well with the electrochemically reduced/oxidized phases in terms of volume change. The color of the reduced and oxidized phase also supports that the chemical reduction/oxidation has occurred (Figure S6, S.I.).

The chemically reduced sample has an extra line at 2Θ = 38.58° which could be because of the unreacted $LiAlH_4$.

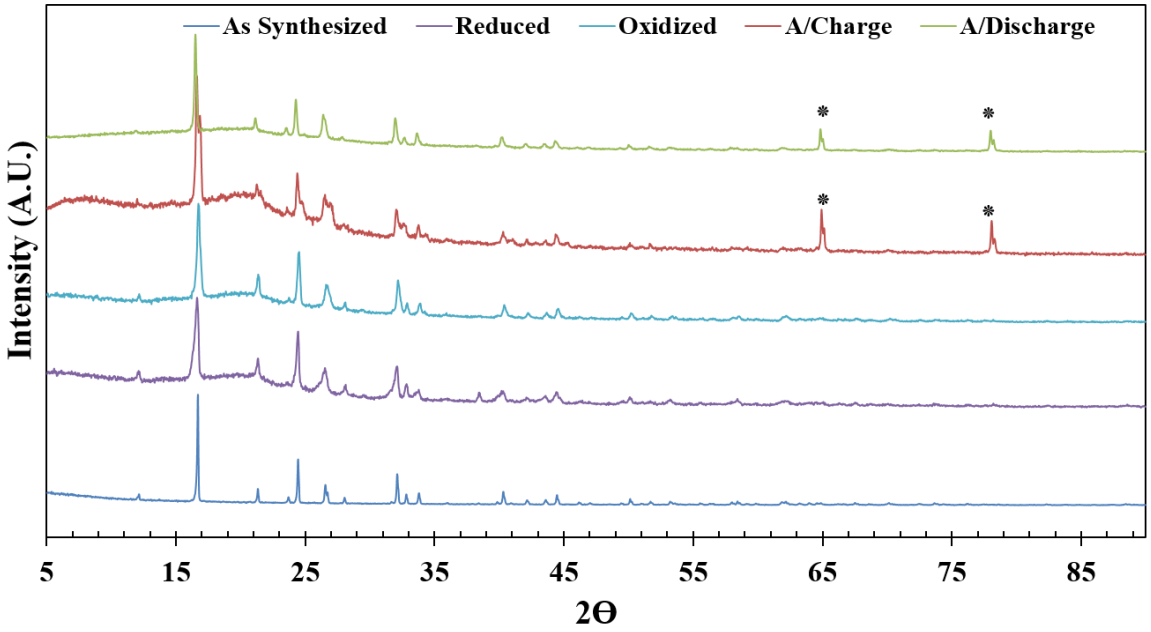

Figure 11. Comparison of PXRDs of oxidized and reduced (chemically & electrochemically) samples with as synthesized. (* indicates Al peaks)

4. CONCLUSIONS

In this article, we have reported the synthesis of $LiV(HPO_3)_2$ through low-temperature route. The compound has shown good achievable capacities for the Li- and Na-ion batteries with average voltage of 4.0 V and 3.7 V, respectively. In the case of Li-ion batteries, the compound did exhibit two electron process when the battery was discharged to 1.2 V. Li-ion battery showed better rate capabilities compared to Na-ion, but considering the higher average voltage for Na-ion, this material can't be overlooked.

Further modification in terms of crystal sizes and improving the electronic conductivities via doping can lead to further useful improvements.

ACKNOWLEDGEMENTS

The authors acknowledge the funding from University of Missouri Research Board and Energy Research and Development Center, Missouri S&T. Use of the Advanced Photon Source at Argonne National Laboratory was supported by the U.S. Department of Energy, Office of Science, Office of Basic Energy Sciences, under Contract No. DE-AC02-06CH11357.

SUPPLEMENTARY INFORMATION

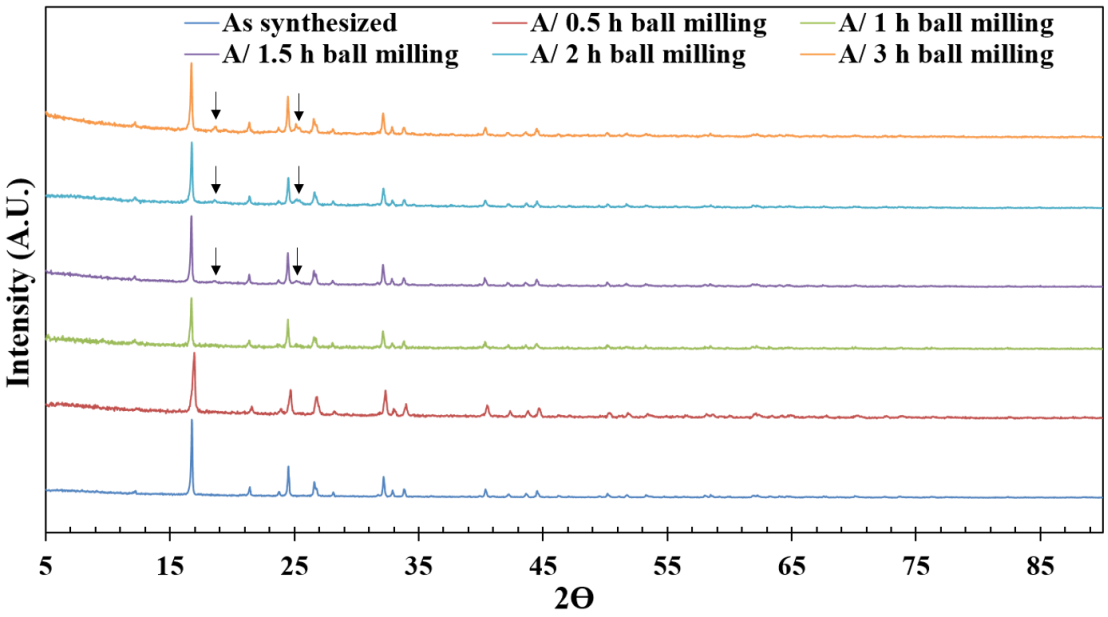

Figure S1. Comparison of PXRD data of ball milled samples with as synthesized

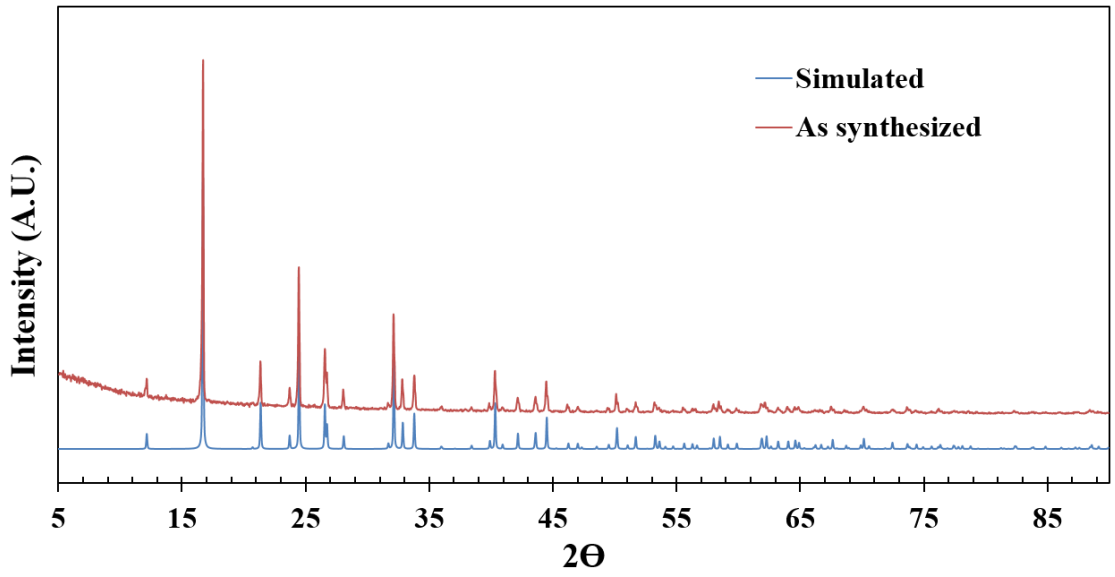

Figure S2. Comparison of PXRD data of as synthesized $LiV(HPO_3)_2$ with simulated.

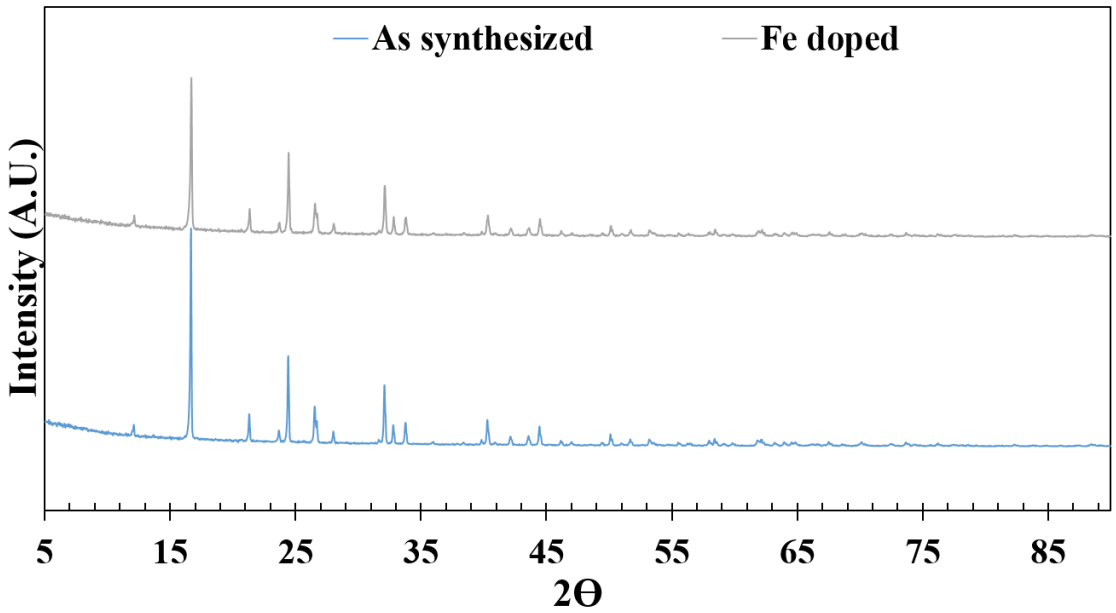

Figure S3. Comparison of PXRD data of as synthesized 10 % Fe-substituted $LiV(HPO_3)_2$ with simulated pattern of $LiV(HPO_3)_2$.

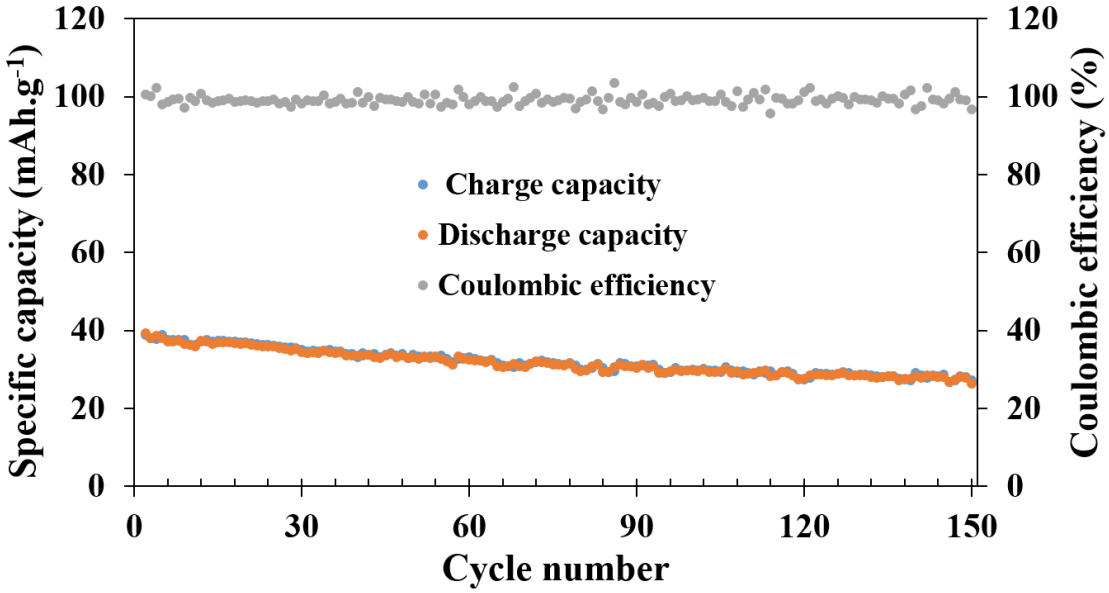

Figure S4. Cycle index of Li-ion battery along with coulombic efficiency at C/10 rate for 150 cycles after initial 20 cycles at different c-rates.

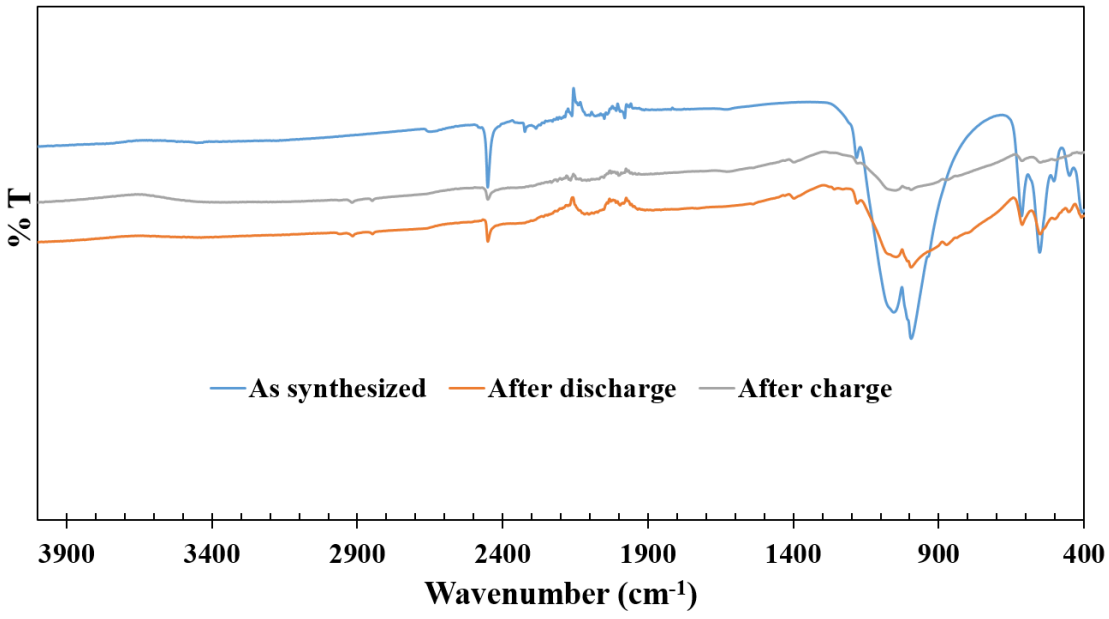

Figure S5. FT-IR spectra of cathode materials (after charge & discharge) in comparison with as synthesized sample of $LiV(HPO_3)_2$.

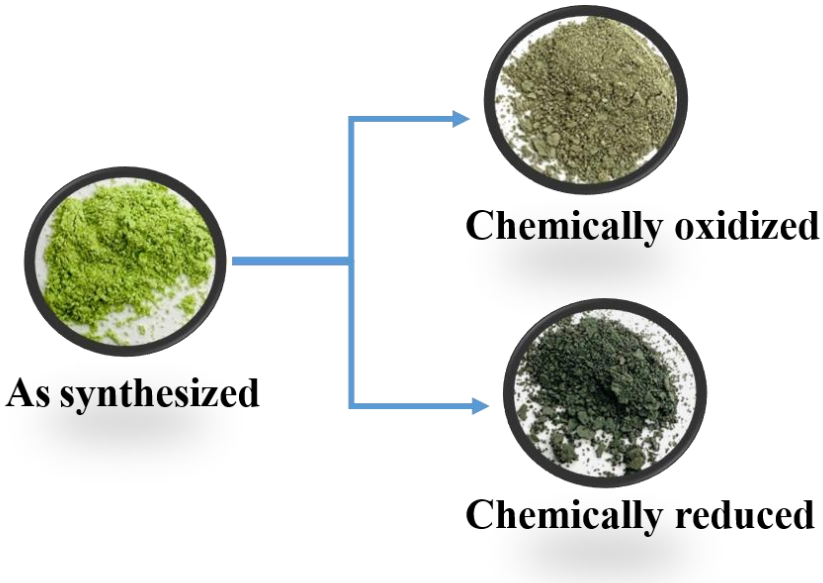

Figure S6. A photograph of the as-synthesized, chemically reduced and chemically oxidized $LiV(HPO_3)_2$.

Table S1. Atomic coordinates and equivalent isotropic displacement parameters ($Å^2$) of $LiV(HPO_3)_2$. U(eq) is defined as one third of the trace of the orthogonalized U^{ij} tensor.

Atom	Wyckoff	x/a	y/b	z/c	U(eq)
V(1)	8d	0.2843(3)	0.2500(3)	0.1250(3)	0.004(1)
P(1)	16e	0.4463(3)	0.2479(8)	0.4011(8)	0.015(1)
O(1)	16e	0.3431(7)	0.1911(8)	0.4882(9)	0.014(1)
O(2)	16e	0.4244(9)	0.2126(2)	0.2548(9)	0.007(1)
O(3)	16*e*	0.5787(2)	0.2154(8)	0.4485(9)	0.008(1)
Li(1)	8d	0.5651(3)	0.2500(3)	0.1250(3)	0.025(1)
H(1)	16e	0.4440(8)	0.3736(8)	0.4090(8)	0.007(1)

Table S2. Rietveld refinement values of oxidized and reduced (chemically & electrochemically) samples in comparison with as synthesized sample of $LiV(HPO_3)_2$.

Cell parameters	As synthesized	Chemically Oxidized	Electrochemically Oxidized (charged)	Chemically Reduced	Electrochemically Reduced (discharged)
$a = b$ (Å)	10.5987(4)	10.5883(4)	10.5691(5)	10.6208(5)	10.6169(5)
c (Å)	9.9843(5)	9.9975(3)	10.0072(4)	9.9769(4)	10.0012(4)
V (Å3)	1121.57(4)	1120.84(5)	1117.87(5)	1125.43(3)	1127.34(5)
wR	12.450 %	9.748 %	13.121 %	10.706 %	17.057 %

REFERENCES

1. Whittingham, M. S. Lithium Batteries and Cathode Materials. *Chem. Rev*. **2004**, *104*, 4271-4302.

2. Armand, M.; Tarascon, J. M. Building better batteries. *Nature* **2008**, *451*, 652-657.

3. Goodenough, J. B.; Kim, Y. Challenges for rechargeable Li batteries. *Chem. Mater*. **2010**, *22*, 587-603.

4. Ellis, B. L.; Lee, K. T.; Nazar, L. F. Positive electrode materials for Li-ion and Li-batteries. *Chem. Mater*. **2010**, *22*, 691-714.

5. Dunn, B.; Kamath, H.; Tarascon, J. M. Electrical energy storage for the grid: A battery of choices. *Science* **2011**, *334*, 928-935.

6. Goodenough, J. B.; Park, K. -S. The Li-ion rechargeable battery: A perspective. *J. Am. Chem. Soc.* **2013**, *135* (4), 1167 – 1176.

7. Larcher, D.; Tarascon, J. M. Towards greener and more sustainable batteries for electrical energy storage. *Nat. Chem*. **2015**, *7*, 19-29.

8. Yang, Z.; Zhang, J.; Kintner-Meyer, M. C. W.; Lu, X.; Choi, D.; Lemmon, J. P.; Liu, J. Electrochemical energy storage for green grid. *Chem. Rev.*, **2011**, *111*(5), 3577 – 3613.

9. Rozier, P.; Tarascon, J. M. Review-Li-rich layered oxide cathodes for next-generation Li-ion batteries: Chances and challenges. *J. Electrochem. Soc.*, **2015**, *162*(14), A2490 - A2499.

10. Li, W.; Song, B.; Manthiram, A. High-voltage positive electrode materials for lithium-ion batteries. *Chem. Soc. Rev.*, **2017,** *46*(10), 3006 – 3059.

11. Schipper, F.; Erickson, E. M.; Erk, C.; Shin, J. -Y.; Chesneau, F. F.; Aurbach, D. Review-Recent advances and remaining challenges for lithium ion battery cathodes I. Nickel-rich, $LiNi_xCo_yMn_zO_2$. *J. Electrochem. Soc.*, **2017**, *164*(1), A6220 - A6228.

12. Erickson, E. M.; Schipper, F.; Penki, T. R.; Shin, J. -Y.; Erk, C.; Chesneau, F. -F.; Markovsky, B.; Aurbach, D. Review-Recent advances and remaining challenges for lithium ion battery cathodes II. Lithium-Rich, $xLi_2MnO_3 \cdot (1-x)LiNi_aCo_bMn_cO_2$. *J. Electrochem. Soc.* **2017**, *164*(1), A6341 - A6348.

13. Zheng, J.; Myeong, S.; Cho, W.; Yan, P.; Xiao, J.; Wang, C.; Cho, J.; Zhang, J. -G. Li- and Mn-Rich Cathode Materials: Challenges to Commercialization. *Adv. Energy Mater.* **2017**, *7*(6), 1601284 (1-25).

14. Padhi, A. K.; Nanjundaswamy, K. S.; Goodenough, J. B. Phospho-olivines as Positive-Electrode Materials for Rechargeable Lithium Batteries. *J. Electrochem. Soc.* **1997**, *144*, 1188–1194.

15. Padhi, A. K.; Manivannan, V.; Goodenough, J. B. Tuning the position of the redox couples in materials with NASICON structure by anionic substitution. *J. Electrochem. Soc.* **1998,** *145*, 1518-1520.

16. Masquelier, C.; Croguennec, L. Polyanionic (phosphates, silicates, sulfates) frameworks as electrode materials for rechargeable Li (or Na) batteries. *Chem. Rev.* **2013**, *113*(8), 6552 – 6591.

17. Morcrette, M.; Wurm, C.; Masquelier, C. On the way to the optimization of $Li_3Fe_2(PO_4)_3$ positive electrode materials. *Solid State Sci.* **2002**, *4*, 239-246.

18. Ramesh, T. N.; Lee, K. T.; Ellis, B. L.; Nazar, L. F. Tavorite lithium iron fluorophosphate cathode materials: Phase transition and electrochemistry of $LiFePO_4F$-Li_2FePO_4F. *Electrochem Solid St.* **2010**, *13*, A43-A47.

19. Hidalgo, M. F. V.; Lin, Y. -C.; Grenier, A.; Xiao, D.; Rana, J.; Tran, R.; Xin, H.; Zuba, M.; Donohue, J.; Omenya, F. O.; Chu, I. -H.; Wang, Z.; Li, X.; Chernova, N. A.; Chapman, K. W.; Zhou, G.; Piper, L.; Ong, S. P. Whittingham, M. S., Rational synthesis and electrochemical performance of LiVOPO4 polymorphs. *J. Mater. Chem. A* **2019**, *7*(14), 8423 – 8432.

20. Nishimura, S.; Nakamura, M.; Natsui, R.; Yamada, A. New Lithium Iron Pyrophosphate as 3.5 V Class Cathode Material for Lithium Ion Battery. *J. Am. Chem. Soc.* **2010**, *132*, 13596-13597.

21. Tamaru, M.; Chung, S. C.; Schimizu, D.; Nishimura, S. I.; Yamada, A. Pyrophosphate Chemistry toward Safe Rechargeable Batteries. *Chem. Mater.* **2013**, *25*, 2538-2543.

22. Rousse, G.; Tarascon, J. M. Sulfate-Based Polyanionic Compounds for Li-Ion Batteries: Synthesis, Crystal Chemistry, and Electrochemistry Aspects. *Chem. Mater.* **2014**, *26*, 394-406.

23. Legagneur, V.; An, Y.; Mosbah, A.; Portal, R.; Le Gal La Salle, A.; Verbaere, A.; Guyomard , D.; Piffard, Y. $LiMBO_3$ (M=Mn, Fe, Co): synthesis, crystal structure and lithium deinsertion/insertion properties. *Solid State Ionics* **2011**, *139*, 37-46.

24. Yamada, A.; Iwane, N.; Harada, Y.; Nishimura, S.; Koyama, Y.; Tanaka, I. Lithium Iron Borates as High-Capacity Battery Electrodes. *Adv. Mater.* **2010**, *22*, 3583-3587.

25. Nytén, A.; Abouimrane, A.; Armand, M.; Gustafsson, T.; Thomas, J. Electrochemical performance of Li_2FeSiO_4 as a new Li-battery cathode material. *Electrochem. Commun.* **2005**, *7*, 156-160.

26. Sirisopanaporn, C.; Masquelier, C.; Bruce, P.; Armstrong, A.; Dominko, R. Dependence of Li_2FeSiO_4 Electrochemistry on Structure. *J. Am. Chem. Soc.* **2011**, *133*, 1263-1265.

27. Chen, H.; Hautier, G.; Ceder, G. Synthesis, Computed Stability, and Crystal Structure of a New Family of Inorganic Compounds: Carbonophosphates. *J. Am. Chem. Soc.* **2012**, *134*, 19619-19627.

28. Huang, W.; Zhou, J.; Li, B.; Ma, J.; Tao, S.; Xia, D.; Chu, W.; Wu, Z. Detailed investigation of $Na_{2.24}FePO_4CO_3$ as a cathode material for Na-ion batteries. *Scientific Reports* **2014**, *4*, 4188.

29. Kim, H.; Park, I.; Seo, D.; Lee, S.; Kim, S.; Kwon, W.; Park, Y.; Kim, C.; Jeon, S.; Kang, K. New Iron-Based Mixed-Polyanion Cathodes for Lithium and Sodium Rechargeable Batteries: Combined First Principles Calculations and Experimental Study. *J. Am. Chem. Soc.* **2012**, *134*, 10369-10372.

30. Kim, H.; Park, I.; Lee, S.; Kim, H.; Park, K.; Park, Y.; Kim, H.; Kim, J.; Lim, H.; Yoon, W.; Kang, K. Understanding the Electrochemical Mechanism of the New Iron-Based Mixed-Phosphate $Na_4Fe_3(PO_4)_2(P_2O_7)$ in a Na Rechargeable Battery. *Chem. Mater.* **2013**, *25*, 3614-3622.

31. Yaghoobnejad Asl, H.; Choudhury, A. Combined Theoretical and Experimental Approach to the Discovery of Electrochemically Active Mixed Polyanionic Phosphatonitrates, $AFePO_4NO_3$ (A = NH_4/Li, K). *Chem. Mater.* **2016**, *28* (14), 5029-5036.

32. Senthilkumar, B.; Murugesan, C.; Sharma, L.; Lochab, S.; Barpanda, P. An Overview of Mixed Polyanionic Cathode Materials for Sodium-Ion Batteries. *Small Methods* **2019**, *3*, 1800253 (1 – 23).

33. Ellis, B. L.; Nazar, L. F. Anion-induced solid solution electrochemical behavior in iron tavorite phosphates. *Chem. Mater.* **2012**, *4*(6), 966 – 968.

34. Yaghoobnejad Asl, H.; Choudhury, A. Phosphorous acid route synthesis of iron tavorite phases, $LiFePO_4(OH)_xF_{1-x}$ [$0 \leq x \leq 1$] and comparative study of their electrochemical activities. *RSC Advances*, **2014**, *4* (71), 37691 – 37700.

35. Barpanda, P.; Lander, L.; Nishimura, S. -I.; Yamada, A. Polyanionic Insertion Materials for Sodium-Ion Batteries. *Adv. Energy Mater.* **2018**, *8*(17), art. no. 1703055.

36. Chung, U. C.; Mesa, J. L.; Pizarro, J. L.; de Meatza, I.; Bengoechea, M.; Fernández, J. R.; Arriortua, M. I.; Rojo, T. $Li_{1.43}[Fe^{II}_{4.43}Fe^{III}_{0.57}(HPO_3)_6]\cdot 1.5H_2O$: A Phosphite Oxoanion-Based Compound with Lithium Exchange Capability and Spin-Glass Magnetic Behavior. *Chem. Mater.* **2011**, *23*, 4317-4330.

37. Yaghoobnejad Asl, H.; Ghosh, K.; Meza, M. V.; Choudhury, A. $Li_3Fe_2(HPO_3)_3Cl$: an electroactive iron phosphite as a new polyanionic cathode material for Li-ion battery. *J. Mater. Chem. A* **2015**, *3*, 7488-7497.

38. Yaghoobnejad Asl, H.; Choudhury, A. Phosphite as Polyanion-Based Cathode for Li-Ion Battery: Synthesis, Structure, and Electrochemistry of $LiFe(HPO_3)_2$. *Inorg. Chem*. **2015**, *54*, 6566–6572.

39. Hameed, A. S.; Reddy, M. V.; Sarkar, N.; Chowdari, B. V. R.; Vittal, J. J. Synthesis and electrochemical investigation of novel phosphite based layered cathodes for Li-ion batteries. *RSC Advances* **2015**, *5* (74), 60630 – 60637.

40. Munaò, I.; Zvereva, E. A.; Volkova, O. S.; Vasiliev, A. N.; Armstrong, A. R.; Lightfoot, P. $NaFe_3(HPO_3)_2((H,F)PO_2OH)_6$: A Potential Cathode Material and a Novel Ferrimagnet. *Inorg. Chem.* **2016**, *55* (5), 2558-2564.

41. Lallaoui, A.; Edfouf, Z.; Benabdallah, O.; Idrissi, S.; Saadoune, I.; Abd-Lefdil, M.; El Moursli, F. C. New titanium (III) phosphite structure and its application as anode for lithium ion batteries, *Int. J. Hydrog. Energy*, (in press), **2018**.

42. Whittingham, M. S. Ultimate limits to intercalation reactions for lithium batteries. *Chem. Rev.*, **2014**, *114*(23), 11414 – 11443.

43. Whittingham, M.S.; Siu, C.; Ding, J. Can Multielectron Intercalation Reactions Be the Basis of Next Generation Batteries? *Acc. Chem. Res.* **2018**, *51*(2), 258 – 264.

44. Geister, G. Crystal structure of $LiFe^{3+}(SeO_3)_2$, *Monatshefte für Chemie* - Chemical Monthly. **1994**, *125* (5), 535-538.

45. Huang, H. L.; Huang, S. H.; Lai, C. W.; Wu, J. R.; Lii, K. H.; Wanga, S. L. Alkali Transition Metal Phosphites as Potential Cathode Materials Grown from Molten Boric Acid. *J. Chin. Chem. Soc*. **2013**, *60*, 691-694.

46. Toby, B. H.; Von Dreele, R. B. "GSAS-II: the genesis of a modern open-source all-purpose crystallography software package". *J. Appl. Cryst*., **2013**, *46*, 544.

47. Yaghoobnejad Asl, H.; Morries, R.; Tran, T. T.; Halasyamani, P. S.; Ghosh, K.; Choudhury, A. A Cubic Non-Centrosymmetric Mixed-valence Iron Borophosphate-Phosphite. *Cryst. Growth Des.* **2016**, *16*(3), 1187 – 1194.

48. Hamchaoui, F.; Alonzo, V.; Venegas-Yazigi, D.; Rebbah, H.; Fur, E. L. Six novel transition-metal phosphite compounds, with structure related to yavapaiite: Crystal structures and magnetic and thermal properties of $A^{I}[M^{III}(HPO_3)_2]$ (*A*=K, NH_4, Rb and *M*=V, Fe). *J. Solid State Chem*. **2013**, *198*, 295-302.

49. Fernandez, S.; Mesa, J. L; Pizarro, J. L.; Lezama, L.; Arriortua, M. I.; Rojo, T. Two New Three-Dimensional Vanadium(III) and Iron(III) Phosphites Templated by Ethylenediamine: $(C_2H_{10}N_2)_{0.5}[M(HPO_3)_2]$. Ab Initio Structure Determination, Spectroscopic, and Magnetic Properties. *Chem. Mater*. **2002**, *14*, 2300-2307.

50. Alda, E.; Bazan, B.; Mesa, J. L; Pizarro, J. L.; Lezama, L.; Arriortua, M. I.; Rojo, T. A new vanadium(III) fluorophosphate with ferromagnetic interactions, $(NH_4)[V(PO_4)F]$. *J. Solid State Chem*. **2003**, *173* (1), 101-108.

51. Armas, S. F.; Mesa, J. L.; Pizarro, J. L.; Clemente-Juan, J. M.; Coronado, E.; Arriortua, M. I.; Rojo, T. Parametrization of the Magnetic Behavior of the Triangular Spin Ladder Chains Organically Templated: $(C_2N_2H_{10})[M(HPO_3)F_3]$ (MIII) Fe, Cr, and V). Crystal Structure and Thermal and Spectroscopic Properties of the Iron(III) Phase. *Inorg. Chem*. **2006**, *45*, 3240-3248.

52. Yan, J. -L.; Shao, G. -Q.; Fan, S. -H.; Zhu, C.; Zhang, Y.; Wang, J.; Liu, Q. Structure, shift in redox potential and Li-ion diffusion behavior in tavorite $LiFe_{1-x}V_xPO_4F$ solid-solution cathodes. *Molecules* **2019** 24 (10), art. no. 1893.

V. $Na_3V_2O_2(PO_4)_2F$ AS A HIGH VOLTAGE CATHODE FOR Na- AND Li-ION BATTERIES

Prashanth Sandineni and Amitava Choudhury*

Department of Chemistry, Missouri University of Science and Technology, Rolla, MO 65409, USA.

ABSTRACT

Fine powder of $Na_3V_2O_2(PO_4)_2F$ in highly pure phase has been synthesized by a facile one-step soft chemical route. The as-synthesized compound crystallizes in tetragonal crystal system ($a = b = 6.3882(3)$, $c = 10.6244(2)$ Å) in $I4/mmm$ space group as confirmed by Rietveld refinement from the high resolution synchrotron powder X-ray diffraction. The electrochemical performances of $Na_3V_2O_2(PO_4)_2F$ have been investigated in sodium and lithium ion batteries, which exhibit high reversible capacities of more than 90 and 115 $mAh.g^{-1}$ with an average voltage of 3.8 and 4 V, respectively when cycled between 4.5 to 2.2 V. When the batteries are cycled between 4.5 to 1 V capacity exceeding 150 and 160 $mAh.g^{-1}$ can be achieved for Na- and Li-ion batteries showing the capability of accommodating one more alkali ion in the structure. In addition the compound showed excellent capacity retention with faster C-rates and on cycling in a Li-ion hybrid cell. These results demonstrate the importance of structural framework of polyanion-compounds that favor ion-conduction for both Li- and Na-ion in their channels without degradation on repeated cycling.

1. INTRODUCTION

The great concern about the availability of lithium is leading to an increasing interest in sodium ion batteries. Sodium is very abundant and widely available throughout the world, which make sodium-ion technology an attractive candidate for the development of large battery systems.[1-3] Owing to this, several materials were tested as electrodes for sodium ion batteries recently.[4-9] Currently, the lack of well-performing cathode has been a limiting factor in the successful implementation of Na-ion technology. Therefore, there is a need to develop cathode materials in sodium ion batteries that can sustain long cycle life and display reasonable gravimetric capacity that can potentially challenge the lithium ion battery technology.[10] Oxides of P2 type and O3 type are being studied extensively as a cathode for sodium ion batteries[11-14] because of their high gravimetric density. However, these oxide materials suffer from capacity fade upon cycling, therefore, much of the attention are now shifted towards polyanion compounds. Polyanions can form numerous structures with different frameworks.[15] Vanadium based compounds, for example, NASICON structure type, $Na_3V_2(PO_4)_3$ [16-18] and a fluoro phosphate, $Na_3V_2(PO_4)_2F_3$[19,20] have been studied extensively in the recent times as electrode material. $Na_3V_2(PO_4)_2F_3$ in particular has attracted more attention since it showed higher energy density of 500 Wh Kg^{-1} and high average potential of 3.9 V vs Na. The oxy-fluoro version of the same compound, $Na_3V_2O_2(PO_4)_2F$[21-26] is also emerging as a viable candidate due to its high gravimetric capacity and long cycle-life. Recently it has been shown that $Na_3V_2O_2(PO_4)_2F$ can be cycled between $NaV_2O_2(PO_4)_2F$ and $Na_4V_2O_2(PO_4)_2F$ leading to the possibility of achieving a theoretical energy density of 600 Wh Kg^{-1}.[27] However, there is a challenge in

the synthesis of phase pure composition of $Na_3V_2O_2(PO_4)_2F$. The propensity to form solid solution between the two end members, full fluoro and the oxo-fluoro derivatives, $Na_3V_2O_{2x}(PO_4)_2F_{3-2x}$ ($0 \leq x \leq 1$) along with undesired by-products in solution mediated synthesis have created some challenges on the optimum performance of this material. In this manuscript we report a one-step soft chemical approach for the synthesis of phase pure $Na_3V_2O_2(PO_4)_2F$. We demonstrated herein that $Na_3V_2O_2(PO_4)_2F$ is multifunctional and can act as high energy density cathode for both Li- and Na- ion batteries. The possibility of insertion of second alkali ion to double the capacities has been explored. Herein we also report the excellent capacity retention when $Na_3V_2O_2(PO_4)_2F$ is used as a cathode for Li-ion batteries in a hybrid cell.

2. EXPERIMENTAL

2.1. MATERIALS

VCl_3 (97%) was purchased from Acros Organics, H_3PO_4 (85%), and H_3BO_3 (Reagent grade) were purchased from Fischer Scientific. NaF (99%, Reagent grade) was purchased from Aldrich.

2.1.1. Synthesis. The compound was synthesized from a mixture of 0.1573 g of VCl_3 (1 mmol), 0.412 g of H_3BO_3 (6.66 mmol), 1.2597 g of NaF (30 mmol) and 3.1 ml of H_3PO_4 (45 mmol) in 5 ml of H_2O in a 23 ml capacity Teflon-lined stainless steel Paar acid digestion bomb which was placed in a 185 °C pre-heated oven. The autoclave was heated for 24 hours followed by cooling down to room temperature in natural air. The green

colored powder product of the reaction was then filtered, washed with hot water to remove any unreacted reagents and dried at room temperature.

2.1.2. Electrochemical Testing. To test the electrochemical performance of the sample, the compound was subjected to ball-milling thoroughly after mixing with super P conductive carbon in a SPEX 8000 miller for 2 hours to reduce the particle size. Poly-vinylidene fluoride (PVDF) was then added to the active material as the binder and an optimum amount of N-methyl-2-pyrrolidone (NMP) was added to dissolve the PVDF. The resulting slurry was further ball milled for another 20 minutes to obtain a homogeneous viscous mixture. The ratio of the active material, conducting carbon, and the binder in the cathode mix was 75: 15: 10. The cathode mix was then spread as a film of uniform thickness with the help of a glass rod onto a flat sheet of carbon-coated aluminum current collector and transferred into a vacuum oven and dried overnight at 85 °C. For electrochemical tests, CR2032 type coin cells were fabricated. The composite cathode film was cut into circular disks (3/8 inch diameter) with 4.0–5.0 mg of active material loading and transferred into an argon filled glove box with an oxygen concentration below 0.1 ppm. The cathode disk and Li anode (0.75 mm thickness Li ribbon cut into circular disk) were assembled in the coin cell casing with a Celgard® 2325 circular sheet placed between the two electrodes as the separator. The electrolyte, 1 M solution of $LiPF_6$ in DMC–EC (1:1) was then added and the cell was sealed with a coin cell crimper. The prepared cells were aged for equilibration for about 12 hours before electrochemical testing. Similarly Na-ion batteries were also made using Na anode and using 1 M solution of $NaClO_4$ in DMC–EC (1:1) as the electrolyte.

Cyclic voltammograms were obtained using a PAR EG&G potentiostat/galvanostat model 273 in the potential range of 1.2 – 4.6 V (vs. Li/Li^+) and (vs. Na/Na^+) with a scan rate of 0.05 mV s^{-1}. Voltage composition profiles were obtained using galvanostatic charge/discharge experiments on an Arbin Instruments battery tester, model BT2043, on the same potential limits as CV at various C-rates.

2.2. MATERIAL CHARACTERIZATION

2.2.1. Powder X-ray Diffraction (PXRD). The laboratory PXRD pattern was obtained from a PANalytical X'Pert Pro diffractometer equipped with a Cu $K_{\alpha 1,2}$ anode and a linear array PIXcel detector over a 2θ range of 5 to 90° with an average scanning rate of 0.0236°s^{-1}. The PXRD pattern matched well with the reported $Na_3V_2O_2(PO_4)_2F$ and to check the absence of any impurity phase(s) Rietveld refinement was employed on high-resolution synchrotron PXRD (S-PXRD) data collected from 11 BM beamline of Advanced Photon Source (APS) in Argonne National Laboratory. The refinement of S-PXRD data using GSAS-II[28] converged well but on close comparison few minor peaks were observed at lower 2θ values which matched with the complete fluorine version of the compound, $Na_3V_2(PO_4)_2F_3$ (Figure 1). The final refined unit cell parameters of the compound are in Table 1. Atomic coordinates and isotropic displacement parameters are given in Table 2. Selected bond lengths are given in Table 3.

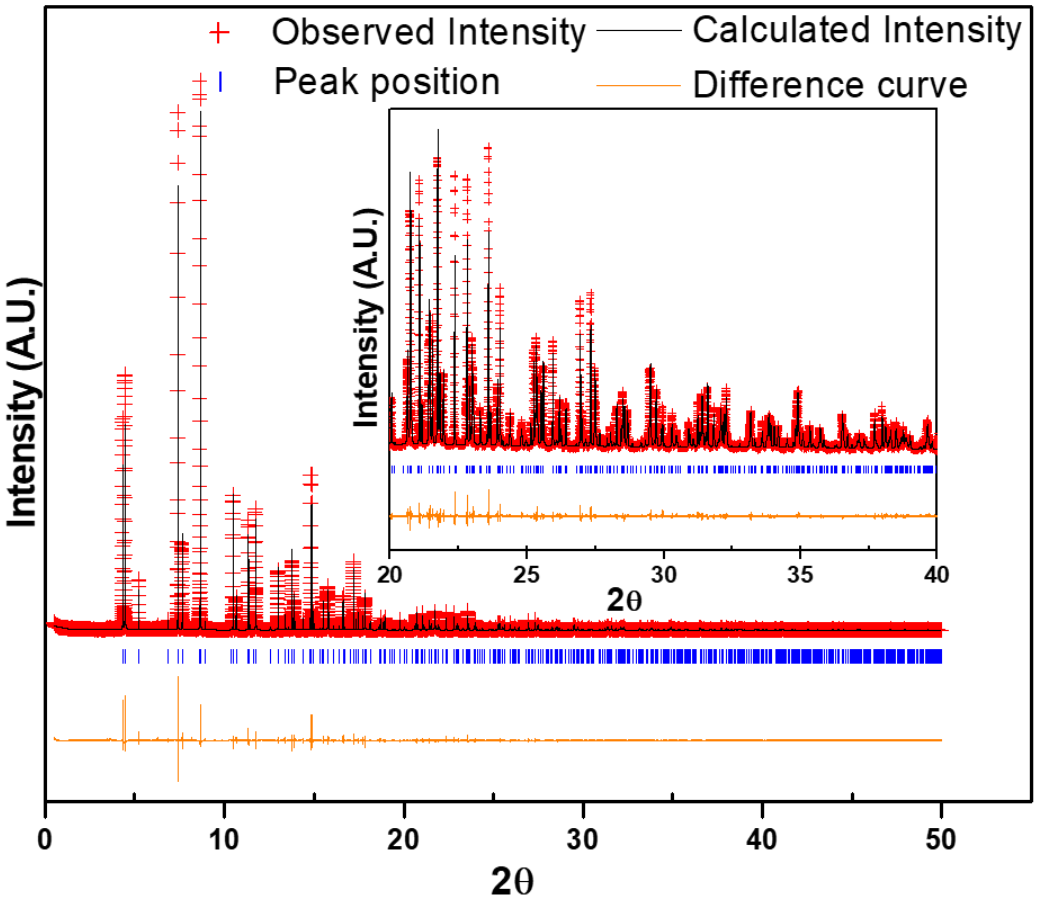

Figure 1. Rietveld refinement of synchrotron XRD data of $Na_3V_2O_2(PO_4)_2F$ showing the observed, calculated and difference curve. Inset shows enlarged view of the segment for $2\theta = 20$ to $40°$. ($\lambda = 0.412834$ Å)

Table 1. Atomic coordinates and equivalent isotropic displacement parameters ($Å^2$) of $Na_3V_2O_2(PO_4)_2F$. U(eq) is defined as one third of the trace of the orthogonalized U^{ij} tensor.

Atom	Wyck.	Site	x/a	y/b	z/c	U(eq) [$Å^2$]
V1	4e	4mm	0	0	0.19894(12)	0.007(4)
P1	4d	-4m2	0	1/2	1/4	0.004(5)
O1	16n	.m.	0	0.3093(5)	0.1625(8)	0.011(6)
O2	4e	4mm	0	0	0.3508(9)	0.021(14)
F1	2a	4/mmm	0	0	0	0.010(13)
Na1	8h	m.2m	0.2688(6)	0.2688(6)	0	0.049(13)

Table 2. Refined lattice constants and final Rietveld refinement parameters from the synchrotron powder XRD for $Na_3V_2O_2(PO_4)_2F$.

Empirical formula	$Na_3V_2O_2(PO_4)_2F$
Formula weight	411.79
Crystal system	Tetragonal
Space group	*I*4/*mmm*
a/Å	6.38823(5)
b/Å	6.38823(5)
c/Å	10.6244(2)
Volume	433.57(9) $Å^3$
Z	2
Number of reflections	609
R_w	12.924 %
R_f^2	4.912 %
Number of data points	49575

Table 3. Selected bond lengths [Å] for the compound.

Atom-Atom	*d* (Å)	Atom-Atom	*d* (Å)	Atom-Atom	*d* (Å)
4 x P1 – O1	1.5316(8)	4 x V1 – O1	2.0136(5)	4 x Na1 – O1	2.4495(8)
		V1 – O2	1.6144(2)	2 x Na1 – O2	2.6210(7)
		V1 – F1	2.1136(5)	Na1 – F1	2.429(2)

2.2.2. Thermogravimetric Analysis (TGA). TGA has been performed with a TA instruments Q50 TGA from room temperature to 800 °C with a scan rate of 10 °C min^{-1} under nitrogen atmosphere. The TGA curve of the sample shows that the compound starts to lose weight immediately after room temperature and till 100 °C it loses almost 0.6%

weight presumably due to adsorbed water (Figure 2). This sluggish water loss continues till 320 °C at which point it loses 1.1 % water. On further heating over 320 °C till 800 °C, a total weight loss of 4.25 % was observed.

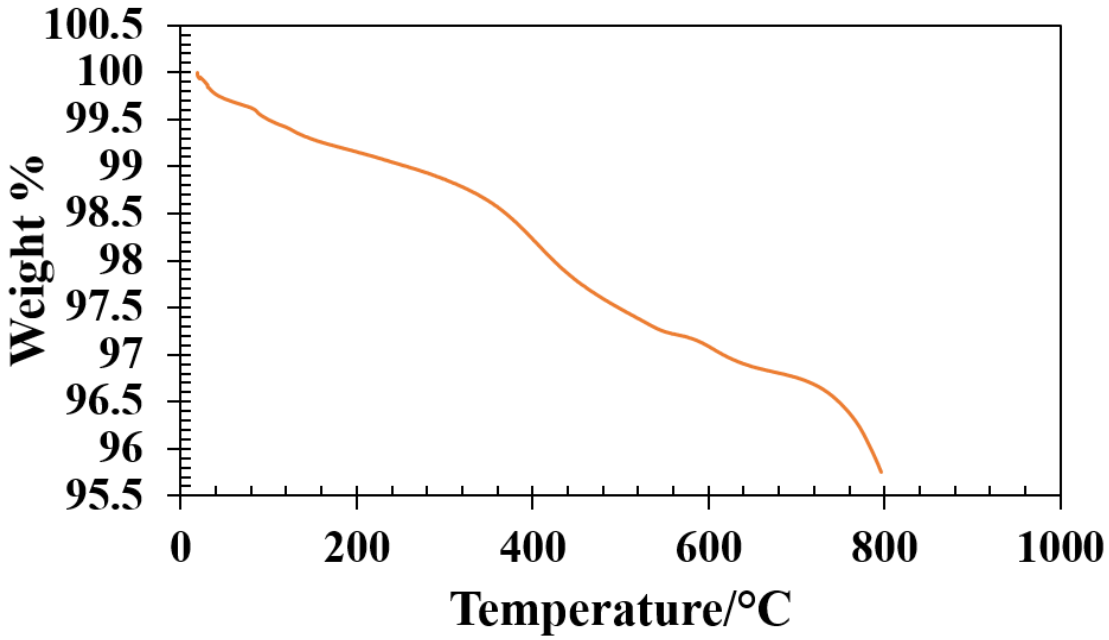

Figure 2. TGA of $Na_3V_2O_2(PO_4)_2F$.

2.2.3. IR Spectroscopy. The IR spectrum was collected using Thermo Nicolet iS50 FT-IR spectrometer over 400–4000 cm^{-1} on a sample using ATR mode. The peak around 903 cm^{-1} corresponds to V = O stretching (Figure 3). The broad band near 1000 – 1100 cm^{-1} is due to P – O asymmetric stretching vibrations.[29-31] The peaks around 550 cm^{-1} corresponds to asymmetric P – O bending mode while a band at 665 cm^{-1} can be assigned to symmetric stretching. The peak near 3500 cm^{-1} suggests the presence of OH or adsorbed water in the sample.

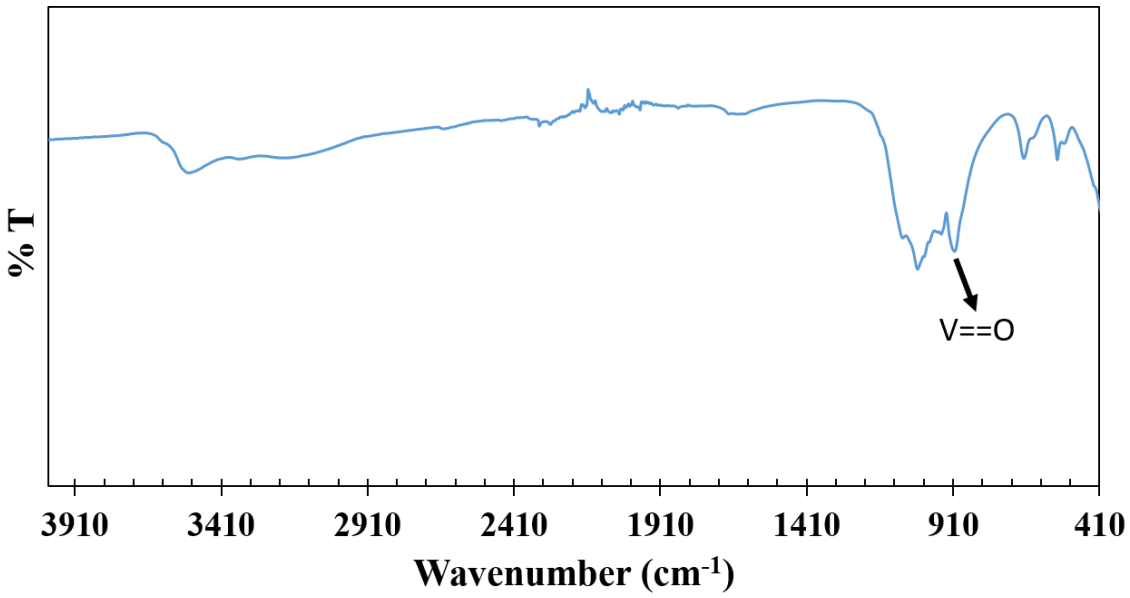

Figure 3. FT-IR spectrum of $Na_3V_2O_2(PO_4)_2F$.

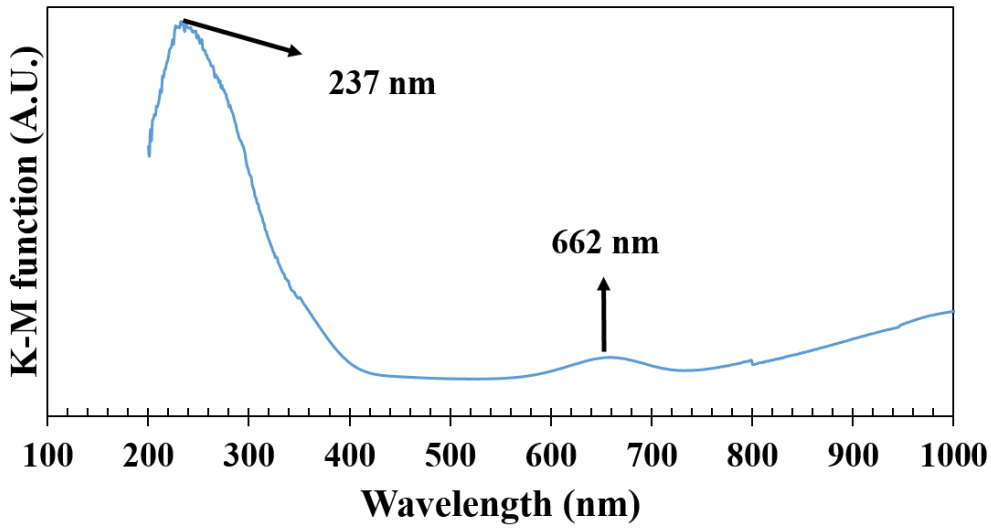

Figure 4. DRS spectrum of $Na_3V_2O_2(PO_4)_2F$.

2.2.4. UV-Visible Spectroscopy. Diffuse reflectance spectrum on powdered sample was collected using a Praying Mantis accessory on Cary 5000 UV-Vis-NIR

spectrophotometer over 200 – 1000 nm range. UV-Vis absorption spectrum of the compound as converted from the diffuse reflectance data employing Kubelka-Munk equation is given in Figure 4. The oxidation state of V in $Na_3V_2O_2(PO_4)_2F$ is +4, which is a d^1 ion. The peak at 662 nm was attributed for the electronic transition from the ground state $^2T_{2g}$ to the excited states ^2E_g.The peak observed at high energy 297 nm is because of ligand-metal charge transfer band.[31]

2.2.5. Magnetic Measurements. The variable temperature magnetic susceptibility measurements of the compound (as-prepared) was carried out in the temperature range 5 – 300 K using Quantum Design SQUID magnetometer at 1T applied field while warming up under zero-field cooled (ZFC) conditions. Isothermal magnetization measurements were performed at 5 K between 0 to 5 T applied field. The plots of temperature dependent ZFC magnetic susceptibility $\chi_M(T)$, the corresponding inverse molar susceptibility $\chi_M^{-1}(T)$ and isothermal field dependent magnetization $M(H)$ for the as-synthesized compound are given in Figure 5. The magnetic susceptibility χ_M vs T plot is asymptotic from 5 to 300 K with an applied field of 1 T which indicate paramagnetic region without any ordering. The small negative Θ_p value (-1.43 K) suggests that there may exist antiferromagnetic correlation in the paramagnetic region. Magnetic moment/V (1.66 μ_B) as calculated from the curie constant, C, derived from the linear fit yields a value closer to the theoretical magnetic moment of 1.733 μ_B corresponding to d^1 configuration thus supporting +4 oxidation state of V as also observed in DRS. The saturation magnetization at 5 K is about 0.25 Nβ, which is about 25% of the theoretical saturation magnetization (Ms = gS Nβ) of 1 Nβ as calculated for V^{4+} with 1 electron (inset of Figure 5).

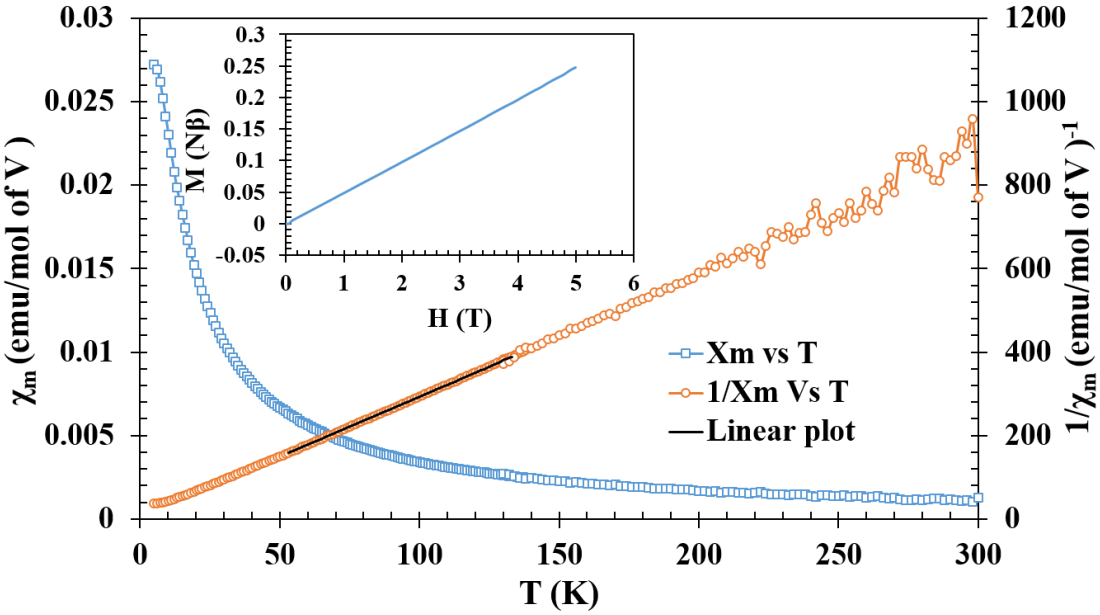

Figure 5. Temperature dependence of molar magnetic susceptibility (χ_m) and inverse molar magnetic susceptibility (χ_m^{-1}) of $Na_3V_2O_2(PO_4)_2F$. (Inset shows M vs H plot).

3. RESULTS AND DISCUSSION

3.1. SYNTHESIS AND STRUCTURE

Unlike the reported syntheses where carbothermal reduction was carried out at high temperatures, a low temperature hydrothermal synthesis route used here is energy sustainable. In our synthesis, VCl_3 was used as V source where V is in +3 oxidation state and our desired product, $Na_3V_2O_2(PO_4)_2F$ has a higher oxidation state of +4 indicating that the V has been oxidized during the course of reaction.

The asymmetric unit consists of six atoms, one V, one P, two O, one F and one Na (Figure 6). Our Rietveld refined solution has only one crystallographically distinct Na, whereas the crystal structures reported by Massa *et al*[32], Sauvage *et al*[24] have two Na sites.

This difference may originate from the different syntheses routes adopted in the two cases. Higher temperature synthesis may produce compounds with disordered Na positions if they are very mobile, while low temperature route can have ordered Na site. The structure is made of $V_2O_{10}F$ bi-octahedra (two VO_5F octahedra shared with a bridging F) bridged by PO_4 tetrahedra, which creates a 3-dimensional framework (closely related to NASICON structure type) with pseudo layers where the Na ions are present (Figure 7). The four equivalent V– O(1) bond distance and the terminal V= O(2) bond distance are 2.0136(5) and 1.6144 (2) Å, respectively, the latter is normally shorter as it accounts for a double bond between V = O. The bridging V – F bond distance is at 2.1136(5) Å. All P – O(1) bond distances are same as 1.5316(8) Å representing a perfect tetrahedron without any distortion.

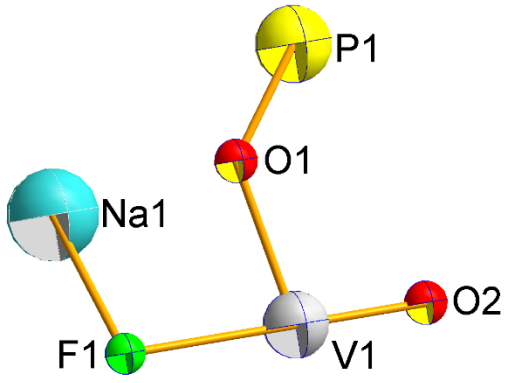

Figure 6. Asymmetric unit of $Na_3V_2O_2(PO_4)_2F$.

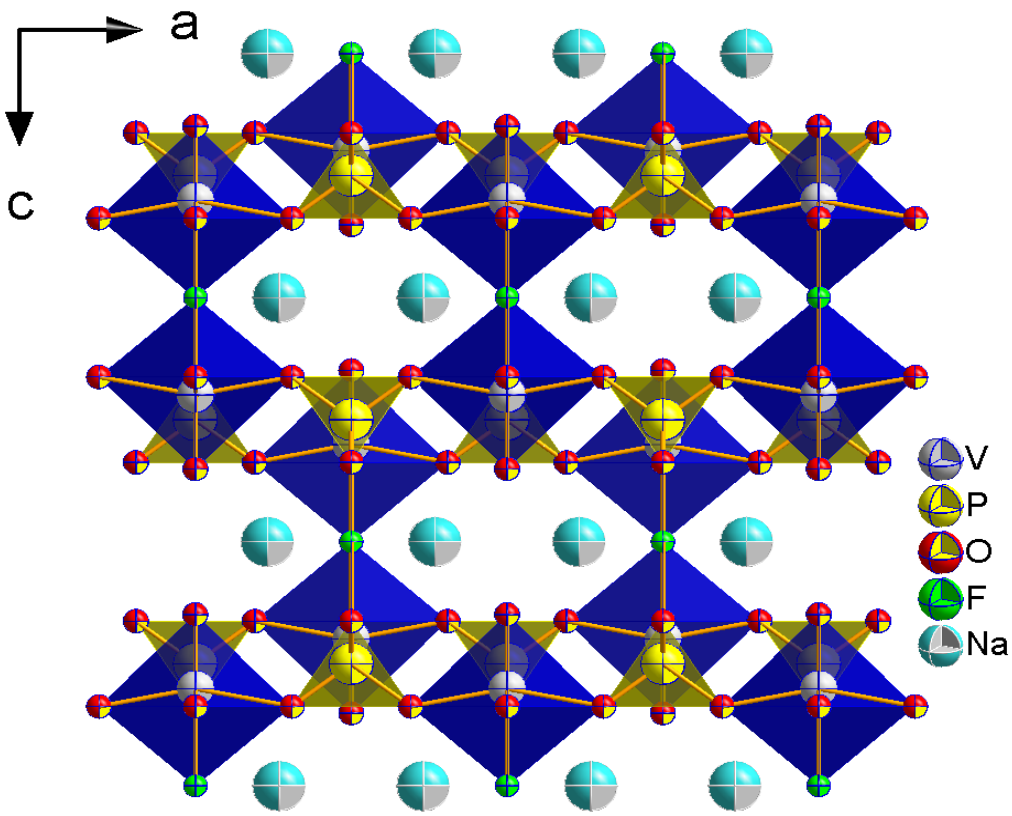

Figure 7. Perspective view of packing diagram of $Na_3V_2O_2(PO_4)_2F$ along b-axis.

3.2. ELECTROCHEMISTRY

3.2.1. Cyclic Voltammetry. Cyclic voltammetry tests were conducted on the fabricated Na-ion coin cells to get an idea of the Na-insertion (cathodic reduction) and Na-extractions (anodic oxidation) voltages. Figure 8 shows the cyclic voltammograms of the battery when subjected to a voltage scanning between 1.2 – 4.6 V. The cell was discharged first, and a small peak current at 1.42 V (reduction) and 1.68 V (oxidation) were observed corresponding to V^{4+}/ V^{3+} couple, and on further charging, the anodic peaks (oxidation) corresponding to Na extraction are observed at 3.82 V and 4.2 V. The corresponding

reduction peaks are observed at 3.76 V and 3.37 V. The reduction peak intensity at 3.37 V disappeared upon cycling.

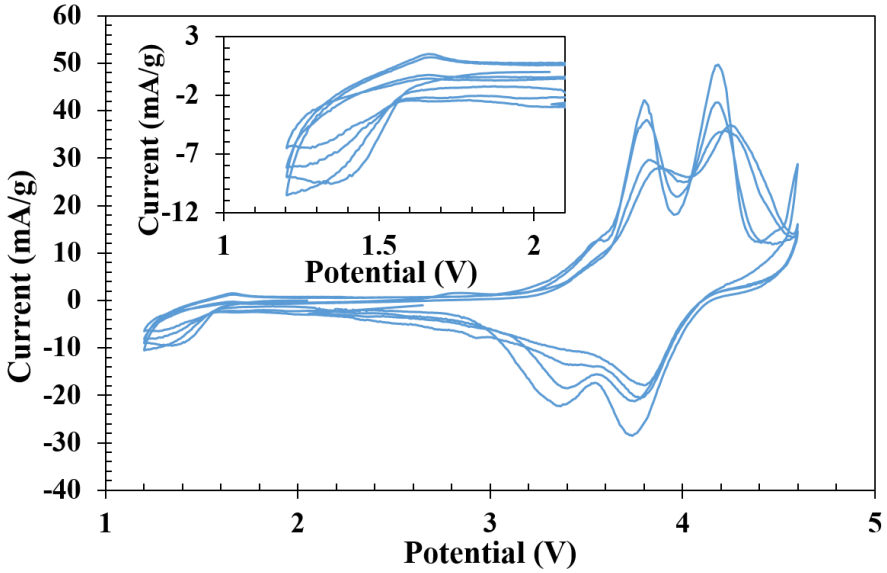

Figure 8. First four cycles of cyclic voltammograms of Na-ion battery. (Inset shows enlarged view from 1.2 to 2.1 V)

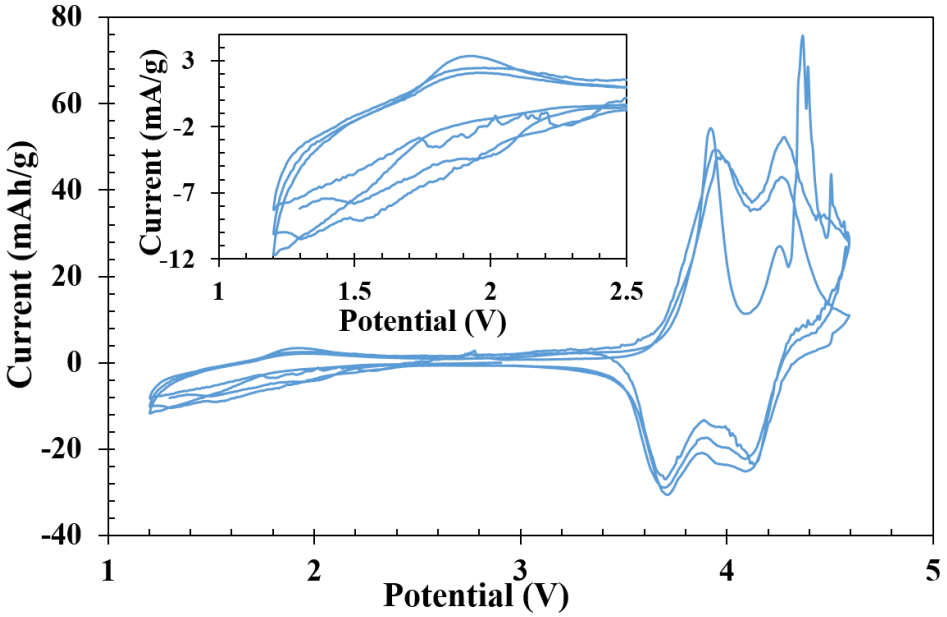

Figure 9. First three cycles of cyclic voltammograms of hybrid-ion (Li-) battery. (Inset shows enlarged view from 1.2 to 2.5 V)

Similarly, Li-ion (also called hybrid ion; since cathode is a sodiated compound, $Na_3V_2O_2(PO_4)_2F$) cells were prepared and subjected to the same voltage scanning from 1.2 – 4.6 V. Similar to Na-ion, it is also discharged first, and small peak currents at 1.57 V (reduction) and 1.91 V (oxidation) are observed. On further charging, the oxidation peaks are observed at 3.97 V and 4.28 V with the corresponding reduction peaks at 4.12 V and 3.72 V. (Figure 9).

3.2.2. Galvanostatic Charge-Discharge. The galvanostatic charge-discharge experiments were done for Na-ion cells at various slow C-rates and the cut-off potentials were set in the range 2.2 – 4.5 V. Assuming one electron process per V atom (1 Na per V), the theoretical capacity of the compound can be calculated to be 130.16 $mAh.g^{-1}$. Figure 10 shows the charge-discharge profiles at C/50. We charged the battery first and the first charge delivered a capacity of 148 $mAh.g^{-1}$, and the extra capacity could be because of the electrolyte oxidation. The corresponding discharge yielded 101 $mAh.g^{-1}$. Subsequent cycles were almost stable with a loss of 10 $mAh.g^{-1}$ in the fourth cycle yielding 91 $mAh.g^{-1}$. Subsequently at various comparatively faster C-rates specifically, at C/20, a very stable discharge capacity of 63 $mAh.g^{-1}$was achieved. At relatively faster C-rates like C/10, a capacity of 23 $mAh.g^{-1}$ was achieved, but dropped down to 17 $mAh.g^{-1}$. At C/5, a minimal capacity of 8 $mAh.g^{-1}$ was achieved. After all the faster C-rates when the cell was cycled again at C/50 it achieved a capacity of 63 $mAh.g^{-1}$ and on further cycling at the same rate, it reached the initial capacity of 91 $mAh.g^{-1}$. It can be inferred from this observation that at faster C-rates the mobility of ions are hindered and lower achievable capacity is not due to any structural degradation.

In order to check the possibility of insertion of 4th Na in $V_2O_2(PO_4)_2F$ framework as reported in by Bianchini et al,[27] another Na-ion battery was discharged to 1.0 V, and a discharge capacity of 157 mAh.g^{-1} was achieved, which decreased to 150 mAh.g^{-1} on further cycling. (Figure 11). Nonetheless, a gain of another 50 mAh.g^{-1} due to the 2nd electron process though at a lower voltage adds up to the overall energy density of the Na-ion battery. Li-ion cells (hybrid ion) were also cycled in the voltage range of 2.2 to 4.5 V.

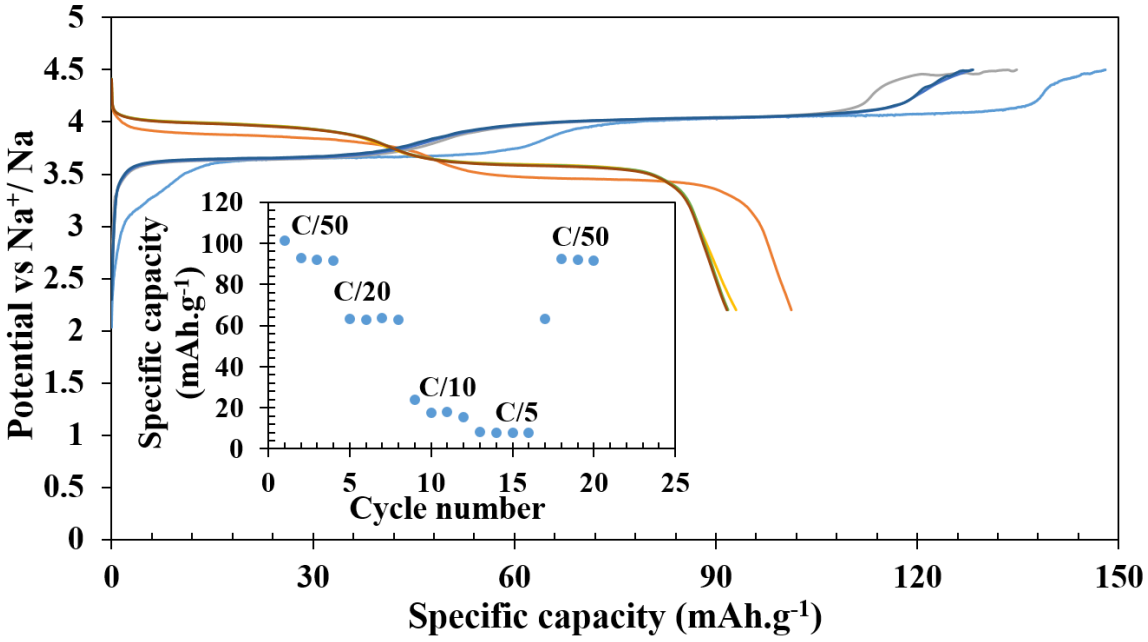

Figure 10. First three cycles of galvanostatic charge-discharge (C/50), capacity at different C-rates (inset) of Na-ion cell of $Na_3V_2O_2(PO_4)_2F$.

Figure 12a shows the first four cycles at C/50 rate, with a first discharge capacity of 115 mAh.g^{-1}, which reduced to 113 mAh.g^{-1} with a minimal loss of 2 mAh.g^{-1}. At relatively faster C-rates of C/20, C/10, C/5 a stable capacity of 112, 107, 95 mAh.g^{-1}were achieved. After all the faster C-rates, when the cell was cycled at C/50 again it achieved

the exact initial capacity of 113 mAh.g^{-1} without any fading. The first charge was removal of Na^+ ions and quite evidently the profile looked similar to the Na-ion battery with two plateaus. However, on further cycling, the two plateaus were disappeared and a sloping charge-discharge curves became more prominent proving that only the first charge involved Na-ions while successive cycling involved insertion-(de)-insertion of Li-ions. When the cell was subjected for a long cycle-life testing at C/5 rate, it was observed that for initial 20 cycles the battery achieved a more or less constant capacity of 93 mAh.g^{-1} (Figure 12b). However, as the cycling continued, the capacity increased to 100 mAh.g^{-1} by the end of 30th cycle and was constant thereafter with 100 % coulombic efficiency. This increased capacity may be due to complete leaching out of the Na-ions in exchange for Li-ions in the structure allowing a facile electrochemical activity.

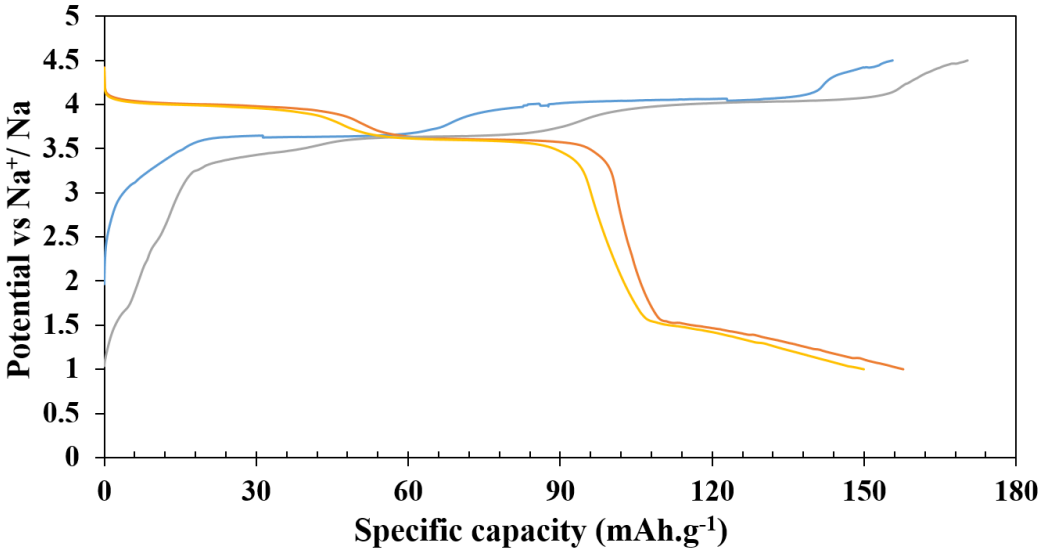

Figure 11. Galvanostatic charge-discharge profiles for Na-ion batteries at C/50 cycled between 1.0 to 4.5 V.

To test the possibility of insertion of another Li^+, another Li-ion battery was cycled between 1.0 to 4.5 V similar to the Na-ion battery. It achieved a capacity of 118 $mAh.g^{-1}$ in the first charge cycle and when the battery was discharged all the way to 1.0 V, a capacity of 187 $mAh.g^{-1}$ was achieved indicating the insertion of 4^{th} alkali-ion leading to the composition, $NaLi_3V_2O_2(PO_4)_2F$. However, the capacity was gradually decreased to 166 $mAh.g^{-1}$ in the 4^{th} cycle (Figure 13) indicating capacity fading when V(3+) was accessed. The open framework structure of $Na_3V_2O_2(PO_4)_2F$ provides acceptable mobility of Na^+ and Li^+ ions. The charge-discharge profile for Na-ion exhibit two-voltage discharge/charge plateaus at 3.6 and 4 V, while in the case of Li-ion batteries it only shows one sloping discharge profile. The two-voltage plateaus are not due to two oxidation state change of V, they still represent $V^{4+/5+}$ to $V^{5+/4+}$ redox couples during charging and discharging, respectively. The step of 0.4 V in the charge-discharge profile for Na-ion battery is a consequence of Na^+-Na^+ coulombic interactions[24] which results in a series of Na-ordered phases upon sodiation and de-sodiation. This is also interesting to note that though in our structure there is only one crystallographically distinct fully ordered Na site but it turns out that the moment Na is being extracted the remaining sodium starts to scramble and becomes disordered. The same thing happens during the insertion instead of sodium ion going into one site it go into two sites after the initial insertion. This stepped profiles are frequently observed in oxide host cathode of Na-ions. This is less pronounced in Li-ion batteries because Li^+-Li^+ coulombic interactions are much weaker compared to Na^+-Na^+ in oxide host cathodes. The Na^+-Na^+ coulombic interactions and subsequent Na- disorder becomes more prominent when the structure is more open framework than tightly bound channel for Na-ion**.**

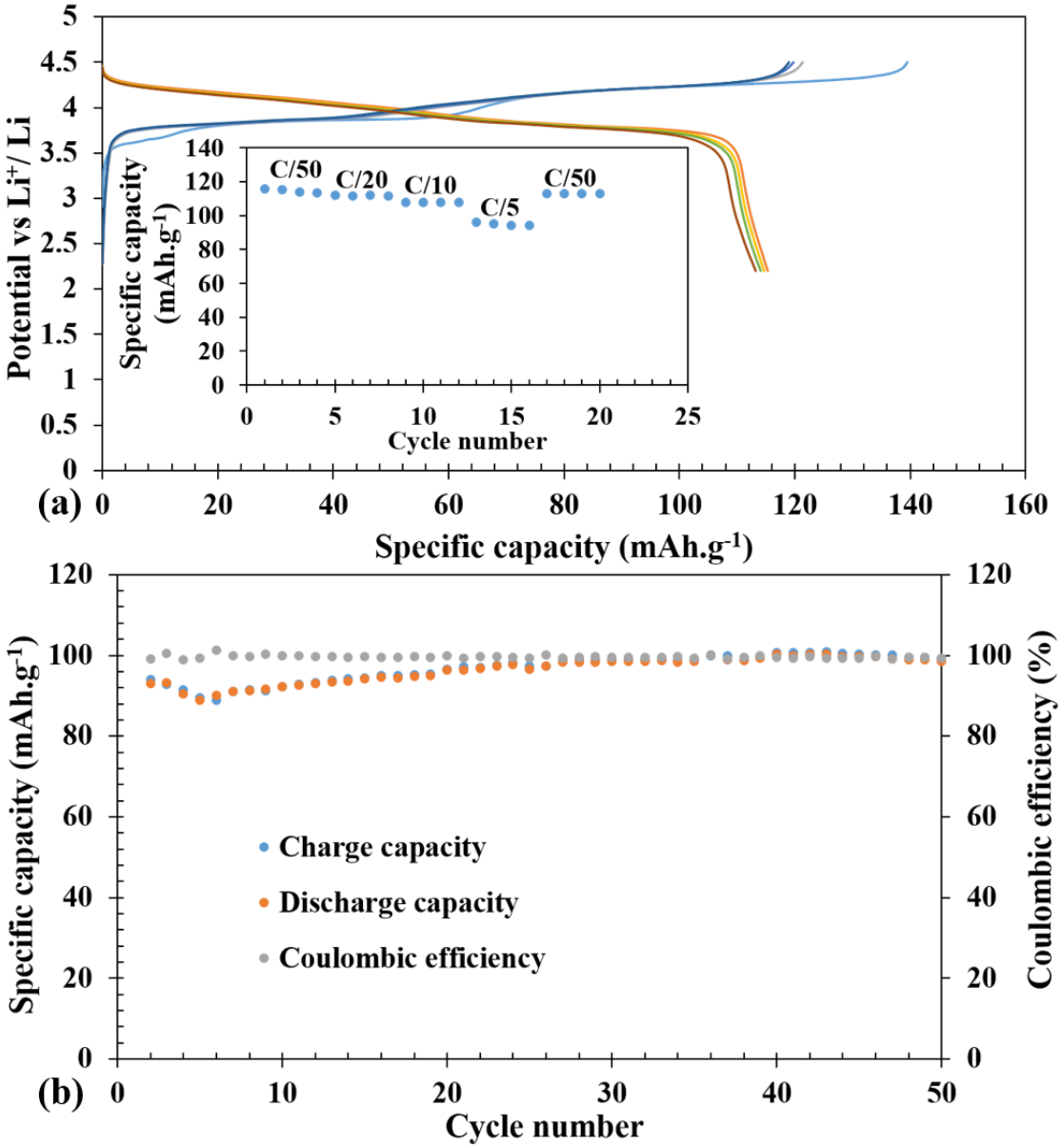

Figure 12. First three cycles of galvanostatic charge-discharge (C/50), capacity at different C-rates (inset) of Li-ion cell of $Na_3V_2O_2(PO_4)_2F$ (a). Cycle index along with coulombic efficiency at C/5 rate for 50 cycles after initial 20 cycles at different c-rates (b).

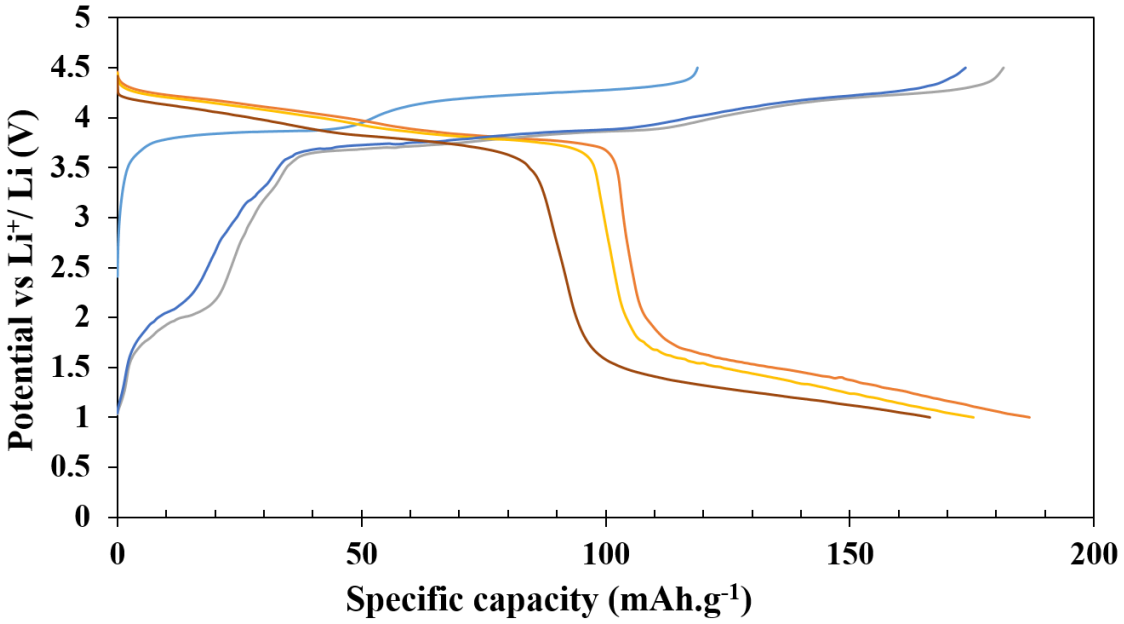

Figure 13. Galvanostatic charge-discharge profiles for Li-ion batteries at C/50 cycled between 1.0 to 4.5 V.

4. CONCLUSIONS

In this article, we report one step soft chemical route for the synthesis of $Na_3V_2O_2(PO_4)_2F$. The electrochemistry of the compound with respect to Na and Li-ion batteries show a high discharge capacity when operated between 4.5 to 1 V and evidently showed two electron process with a discharge curve below 2 V. Hybrid-ion battery showed excellent stability in the capacity retention even at higher C-rates and the capacity increased upon cycling. Even though, Na-ion battery did not perform well in faster C-rates, the capacity retention at slower C-rates is comparable. The possibility of achieving extra capacity by discharging to lower potential as shown in both Li- and Na-ion batteries makes $Na_3V_2O_2(PO_4)_2F$ a high energy density candidate for potential applications.

ACKNOWLEDGEMENTS

The authors acknowledge the funding from University of Missouri Research Board and Energy Research and Development Center, Missouri S&T. The authors acknowledge Dr. Kartik Ghosh of Missouri State University for his help with the magnetic measurements.

REFERENCES

1. B. L. Ellis, L. F. Nazar, *Curr. Opin. Solid State Mater. Sci.* **2012**, *16*, 168.
2. J.-M. Tarascon, *Nat. Chem.* **2010**, *2*, 510.
3. H. Pan, Y.-S. Hu, L. Chen, *Energy Environ. Sci.* **2013**, *6*, 2338.
4. S.-W. Kim, D.-H. Seo, X. Ma, G. Ceder, K. Kang, *Adv. Energy Mater.***2012**, *2*, 710.
5. M. D. Slater, D. Kim, E. Lee, C. S. Johnson, *Adv. Funct. Mater.* **2013**, *23*, 947.
6. N. Yabuuchi, K. Kubota, M. Dahbi, S. Komaba, *Chem. Rev.* **2014**,*114*, 1163611682.
7. E. Irisarri, A. Ponrouch, M. R. Palacin, *J. Electrochem. Soc.* **2015**,*162*, A2476.
8. K. Kubota, S. Komaba, *J. Electrochem. Soc.* **2015**, *162*, A2538.
9. D. Kundu, E. Talaie, V. Duffort, L. F. Nazar, *Angew. Chem., Int. Ed.***2015**, *54*, 3431.
10. X. Xiang, K. Zhang, J. Chen, *Adv. Mater.* **2015**, *27*, 5343.
11. J. J. Braconnier, C. Delmas, C. Fouassier, P. Hagenmuller, *Mater.Res. Bull.* **1980**, *15*, 1797.
12. R. Berthelot, D. Carlier, C. Delmas, *Nat. Mater.* **2011**, *10*, 74.
13. J. Billaud, R. J. Clement, A. R. Armstrong, J. Canales-Vazquez,P. Rozier, C. P. Grey, P. G.Bruce, *J. Am. Chem. Soc.* **2014**, *136*, 17243.

14. R. J. Clement, P. G. Bruce, C. P. Grey, *J. Electrochem. Soc.* **2015**, *162*, A2589.

15. C. Masquelier, L. Croguennec, *Chem. Rev.* **2013**, *113*, 6552.

16. Y. Uebou, T. Kiyabu, S. Okada, J.-I. Yamaki, *Rep. Inst. Adv. Mater.Study, Kyushu Univ.* **2002**, *16*, 1.

17. Z. Jian, W. Han, X. Lu, H. Yang, Y.-S. Hu, J. Zhou, Z. Zhou, J. Li,W. Chen, D. Chen, L. Chen, *Adv. Energy Mater.* **2013**, *3*, 156.

18. F. Lalere, V. Seznec, M. Courty, R. David, J. N. Chotard,C. Masquelier, *J. Mater. Chem. A* **2015**, *3*, 16198.

19. R. K. B. Gover, A. Bryan, P. Burns, J. Barker, *Solid State Ionics* **2006**,*177*, 1495.

20. J. M. Le Meins, M. P. Crosnier-Lopez, A. Hemon-Ribaud,G. Courbion, *J. Solid State Chem.***1999**, *148*, 260.

21. Y.-U. Park, D.-H. Seo, H. Kim, J. Kim, S. Lee, B. Kim, K. Kang, *Adv.Funct. Mater.* **2014**, *24*, 4603.

22. Y. Qi, L. Mu, J. Zhao, Y.-S. Hu, H. Liu, S. Dai, *Angew. Chem.* **2015**,*127*, 10049.

23. J. Zhao, L. Mu, Y. Qi, Y.-S. Hu, H. Liu, S. Dai, *Chem. Commun.* **2015**,*51*, 7160.

24. F. Sauvage, E. Quarez, J. M. Tarascon, E. Baudrin, *Solid State Sci.***2006**, *8*, 1215.

25. P. Serras, V. Palomares, P. Kubiak, L. Lezama, T. Rojo, *Electrochem.Commun.* **2013**, *34*, 344.

26. M. Xu, P. Xiao, S. Stauffer, J. Song, G. Henkelman,J. B. Goodenough, *Chem. Mater.* **2014**,*26*, 3089.

27. M. Bianchini, P. Xiao, Y. Wang, G. Ceder, *Adv. Energy Mater.* **2017**, *7*, 1700514

28. Toby, B. H.; Von Dreele, R. B. "GSAS-II: the genesis of a modern open-source all-purpose crystallography software package". *J. Appl. Cryst*., **2013**, *46*, 544.

29. S. Y. Lim, H. Kim, R. A. Shakoor, Y. Jung and J. W. Choi, *J. Electrochem. Soc*., **2012**, *159*, A1393–A1397.

30. Z.-m. Liu, X.-y. Wang, Y. Wang, A.-p. Tang, S.-y. Yang and L.-f. He, *Trans. Nonferrous Met. Soc. China*, **2008**, *18*, 346–350.

31. D. L. Calero, S. Bruque, M. A. G. Aranda, M. M. Lara, L. Moreno, *J. Solid State Chem*. **1993**, *103*, 481-489.

32. W. Massa, O. V. Yakubovich, O. V. Dimitrova, *Solid State Sci.* **2002**,*4*, 495.

SECTION

2. CONCLUSIONS AND RECOMMENDATIONS

2.1. CONCLUSIONS

Transition metal polyanion-based cathode materials are receiving greater attention compared to traditional oxide-based cathodes regarding achievable capacities and sustainable syntheses conditions. We employed soft chemical routes, for example, hydrothermal and ion-exchange reactions for synthesizing metastable phases, which could not be prepared using high temperature synthesis route. Polyanion chemistry provides better alternatives to the existing energy storage materials in regards to the formation of new structures and many compositions that are yet to be explored. Using the phenomenon, inductive effect, different polyanions namely sulfates, phosphates, phosphites which we reported here can make a broader impact on the improving the average voltage and capacities of the batteries. As the electronegativity of the central atom of the polyanion increases, the average voltage increases and with the introduction of another electronegative moiety such as F can significantly improve the average voltage. The achievable capacity also depends on the interlayer space in case of 2D materials, and size of the channel in 3D materials, which should be capable of (de)intercalating alkali-ion, thereby showing the significance of structure. Synthesis conditions are also important when choosing the polyanion, for example, if phosphites are used, there is a high chance of their conversion to phosphates if a temperature of > 200 °C is used. The fate of product also depends on the oxidation state of starting transition metal, which tends to form the

compound in the same oxidation state unless an oxidizing/reducing agent is used. The main focus was on Fe based cathode materials, but we tried two compositions with V as well to check the existence of multi electron process.

Using these criteria we successfully synthesized some new compositions namely $AFe_3(SO_4)_2(OH)_6$ (A = Na/NH_4), $NaFe(HPO_4)_2$, $Li_2Fe(H_{0.5}PO_4)_2$, $Li_3Fe(PO_4)_2$, $Fe_3(PO_4)_2(OH)_2$, $LiV(HPO_3)_2$ and $Na_3(VO)_2(PO_4)_2F$. For all compounds, single-crystal and powder (synchrotron and laboratory) X-ray diffraction techniques have been used to determine the crystal structures. All the compounds were characterized with spectroscopic techniques (FT-IR, TGA/DSC, UV-Visible), microscopic (SEM), magnetic measurements and ex-situ characterization of cathode films was done with powder XRD. In the case of metastable phases like phosphites, TGA and FT-IR, plays an important role as they are not stable at high temperatures, and to check the intactness of P – H bonding, FT-IR is essential. Many researchers are finding new avenues towards Na-ion technology compared to Li-ion because of the cost-effectiveness and availability. Keeping this in mind, we studied the electrochemical activities in both Li- and Na-ion batteries.

$AFe_3(SO_4)_2(OH)_6$ (A = Na/NH_4) has been synthesized using hydrothermal conditions and their electrochemistry was reported for the first time. The sluggish kinetics of $NH_4Fe_3(SO_4)_2(OH)_6$ compared to $NaFe_3(SO_4)_2(OH)_6$ explains the significance of the size of alkali-ion. $NaFe_3(SO_4)_2(OH)_{5.66}F_{0.34}$ has been synthesized for the first time by the reflux method. The partial fluoro-substitution in $NaFe_3(SO_4)_2(OH)_6$ improves the Li-ion insertion voltage and achievable capacity owing to a synergistic effect of smaller particle size and inductive effect. Variation in synthesis method yielded smaller particles in $NaFe_3(SO_4)_2(OH)_6$ (stoichiometric combination of starting precursors) and showed better

capacity retention compared to non- stoichiometric synthesis reinforcing the effect of particle size in electrochemistry.

A new phase, $NaFe(HPO_4)_2$, has been synthesized through hydrothermal route, and subsequent ion-exchange of sodium and protons produced two different compounds. Aqueous phase ion exchange of Na^+ ion from $NaFe(HPO_4)_2$ with Li^+ ion produces $Li_2Fe(H_{0.5}PO_4)_2$, while solid-state proton exchange from $Li_2Fe(H_{0.5}PO_4)_2$ with Li-ion produces $Li_3Fe(PO_4)_2$, which is a metastable phase. $Li_2Fe(H_{0.5}PO_4)_2$ has been synthesized employing two different routes, hydrothermal (-HT) and via ion exchange (-IEX) and their electrochemical activities were compared. The difference in electrochemistry was attributed to the elongated particle shape in –IEX phase showing the significance of synthesis conditions. $Li_3Fe(PO_4)_2$ was a compositionally predicted phase, which is synthetically realized by our soft-chemical approach. The structure of this compound was solved using *ab initio* method exclusively from synchrotron powder X-ray diffraction data. The compound exhibited good electrochemical activity in Li-ion battery and vanadium analogue would be a two electron candidate for a future target composition.

$Fe_3(PO_4)_2(OH)_2$, barbosalite, a lipscombite structure type was studied for the first time with respect to its lithium insertion electrochemistry. The capacity of Li-ion battery was increased on successive cycling due to structural transformation from a poorly electrochemically active phase to a phase with facile electrochemical activity. Charge-discharge profile, CV and PXRD of the cycled cell indicated structural re-arrangement due to lithium insertion in the compound.

$LiV(HPO_3)_2$, isostructural to $LiFe(HPO_3)_2$ has been synthesized using low-melting flux. Vanadium compounds are known to exhibit multi electron process and thereby high

theoretical capacity can be achieved. $LiV(HPO_3)_2$ can be cycled between $V(HPO_3)_2$ and $Li_2V(HPO_3)_2$. The synthesized vanadium phosphite displayed facile electrochemical properties with an average voltage of 4.0 V vs Li^+/Li and 3.8 V vs Na^+/Na in Li- and Na–ion batteries, respectively, when cycled between 4.5 and 1.2 V. Slight Fe doping in the compound showed better capacity in the lower redox couple compared to the pristine compound.

$Na_3(VO)_2(PO_4)_2F$ has been touted as promising cathode material for Na-ion battery and studied extensively in the recent times. The compound has delivered a constant achievable capacity of 114 $mAh.g^{-1}$ in Li-ion battery (hybrid ion) with an average voltage of 4 V and the possibility of second electron was also tested by discharging the battery till 1 V, and the achievable capacity increased to 187 $mAh.g^{-1}$. Similarly, Na-ion battery of the same materials can achieve 111 $mAh.g^{-1}$ owing to one electron process with an average voltage of 3.78 V, and a capacity of 162 $mAh.g^{-1}$ was achieved upon discharging the battery to 1 V to access the 2^{nd} electron.

2.2. RECOMMENDATIONS

All the Fe compounds discussed were two electron candidates but limited by the electrolyte stability window of the average Fe^{3+}/Fe^{4+} potential with respect Li^+/Li is greater than 4.5V. If new electrolytes which are stable beyond the commercially available ones are prepared, the theoretical capacity could be easily doubled. Vanadium analogues of iron compounds, where multi electron processes are achieved, the overall average voltage is diminished when the batteries are discharge to a low voltage for achieving the lower oxidation couple. In these cases, doping with other transition metals like Fe can help

bringing the average voltage of the lower redox couple to a higher value. Concurrently, all these compounds can be used as hosts for other alkali ions such as, K or alkaline earth ion such as Mg-ion batteries, which are also being considered as alternatives to the Li-ion battery technology.

BIBLIOGRAPHY

1. J. M. Tarascon, M. Armand. *Nature,* **2001**, *414***,** 359 – 367.

2. J. M. Tarascon, *Philos. Trans. R. Soc. London, Ser. A*, **2010**, *368,* 3227 – 3241.

3. M. Armand, J. M. Tarascon. *Nature,* **2008**, *451***,** 652–657.

4. J. B. Goodenough, K. S. Park, *J. Am. Chem. Soc.* 2013, *135*(4), 1167-1176.

5. P. Rozier, J. M. Tarascon. *J. Electrochem. Soc.*, **2015**, *162*(14), A2490 - A2499.

6. W. Li, B. Song, B.; A. Manthiram. *Chem. Soc. Rev.*, **2017,** *46*(10), 3006 – 3059.

7. F. Schipper, E. M. Erickson, C. Erk, J. Y. Shin, F. F. Chesneau, D. Aurbach. *J. Electrochem. Soc.*, **2017**, *164*(1), A6220 - A6228.

8. E. M. Erickson, F. Schipper, T. R. Penki, J. Y. Shin, C. Erk, F. F. Chesneau, B. Markovsky, D. Aurbach. *J. Electrochem. Soc.* **2017**, *164*(1), A6341 - A6348.

9. J. Zheng, S. Myeong, W. Cho, P. Yan, J. Xiao, C. Wang, J. Cho, J. G. Zhang. *Adv. Energy Mater.* **2017**, *7*(6), 1601284 (1-25).

10. A. K. Padhi, K. S. Nanjundaswamy, J. B. Goodenough. *J. Electrochem. Soc.*, **1997**, *144*, 1188–1194.

11. J. B. Goodenough, Y. Kim. *Chem. Mater.* **2010**, *22*, 587–603.

12. A. Wang, S. Kadam, H. Li, *et al. npj Comput Mater* **2018,** *4,* 15.

13. N. Yabuuchi, K. Kubota, M. Dahbi, S. Komaba. *Chem. Rev.* 2014, *114*, 11636-11682.

14. D. Kundu, E. Talaie, V. Duffort, L. F. Nazar. *Angew. Chem. Int. Ed*. **2015**, *54*, 3431-3448.

15. G. Rousse and J. M. Tarascon**,** *Chem. Mater.*, **2014**, *26* (1), 394–406.

16. A. S. Andersson, J. O. Thomas, B. Kalska, L. Haggstrom. *Electrochem. Solid-State Lett.*, **1999**, *3*, 66–68.

17. G. H. Li, H. Azuma, M. Tohda. *Electrochem. Solid-State Lett.*, **2002**, *5*, A135–A137.

18. G. Y. Chen and T. J. Richardson, *J. Power Sources*, **2010**, *195*, 1221– 1224.

19. S. M. Oh, S. W. Oh, C. S. Yoon, B. Scrosati, K. Amine and Y. K. Sun, *Adv. Funct. Mater.*, **2010**, *20*, 3260–3265.

20. A. Nyten, A. Abouimrane, M. Armand, T. Gustafsson and J. O. Thomas, *Electrochem. Commun.*, **2005**, *7*, 156–160.

21. M. E. Arroyo-de Dompablo, M. Armand, J. M. Tarascon and U. Amador, *Electrochem. Commun.*, **2006**, *8*, 1292–1298.

22. Z. L. Gong, Y. X. Li, G. N. He, J. Li and Y. Yang, *Electrochem. Solid-State Lett.*, **2008**, *11*, A60–A63.

23. T. Muraliganth, K. R. Stroukoff and A. Manthiram, *Chem. Mater.*, **2010**, *22*, 5754–5761.

24. R. Dominko, M. Bele, M. Gaberscek, A. Meden, M. Remskar and J. Jamnik, *Electrochem. Commun.*, **2006**, *8*, 217–222.

25. Y. X. Li, Z. L. Gong and Y. Yang, *J. Power Sources*, **2007**, *174*, 528– 532.

26. R. Dominko, I. Arcon, A. Kodre, D. Hanzel and M. Gaberscek, *J. Power Sources*, **2009**, *189*, 51–58.

27. Z. L. Gong, Y. X. Li and Y. Yang, *J. Power Sources*, **2007**, *174*, 524– 527.

28. C. Lyness, B. Delobel, A. R. Armstrong and P. G. Bruce, *Chem. Commun.*, **2007**, 4890–4892.

29. A. R. West and F. P. Glasser, *J. Solid State Chem.*, **1972**, *4*, 20–28.

30. J. Barker, M. Y. Saidi and J. L. Swoyer, *J. Electrochem. Soc.*, **2003**, *150*, A1394–A1398.

31. J. Barker, M. Y. Saidi and J. L. Swoyer, *J. Electrochem. Soc.*, **2004**, *151*, A1670–A1677.

32. M. V. Reddy, G. V. S. Rao and B. V. R. Chowdari, *J. Power Sources*, **2010**, *195*, 5768–5774.

33. F. Zhou, X. M. Zhao and J. R. Dahn, *Electrochem. Commun.*, **2009**, *11*, 589–591.

34. J. Barker, R. K. B. Gover, P. Burns and A. J. Bryan, *Electrochem. Solid-State Lett.*, **2006**, *9*, A190–A192.

35. R. K. B. Gover, A. Bryan, P. Burns and J. Barker, *Solid State Ionics*, **2006**, *177*, 1495–1500.

36. Y. Makimura, L. S. Cahill, Y. Iriyama, G. R. Goward and L. F. Nazar, *Chem. Mater.*, **2008**, *20*, 4240–4248.

37. S. C. Yin, P. S. Herle, A. Higgins, N. J. Taylor, Y. Makimura and L. F. Nazar, *Chem. Mater*., **2006**, *18*, 1745–1752.

38. B. L. Ellis, W. R. M. Makahnouk, Y. Makimura, K. Toghill and L. F. Nazar, *Nat. Mater.*, **2007**, *6*, 749–753.

39. N. Recham, J. N. Chotard, J. C. Jumas, L. Laffont, M. Armand and J. M. Tarascon, *Chem. Mater.*, **2010,** *22*, 1142–1148.

40. T. N. Ramesh, K. T. Lee, B. L. Ellis and L. F. Nazar, *Electrochem. Solid-State Lett.*, **2010**, *13*, A43–A47.

41. N. Recham, J. N. Chotard, L. Dupont, C. Delacourt, W. Walker, M. Armand and J. M. Tarascon, *Nat. Mater.*, **2009**, *9*, 68–74.

42. P. Barpanda, N. Recham, J. N. Chotard, K. Djellab, W. Walker, M. Armand and J. M. Tarascon, *J. Mater. Chem.*, **2010**, *20*, 1659– 1668.

43. P. Barpanda, J. N. Chotard, N. Recham, C. Delacourt, M. Ati, L. Dupont, M. Armand and J. M. Tarascon, *Inorg. Chem.*, **2010**, *49*, 7401–7413.

44. A. Yamada, N. Iwane, Y. Harada, S. Nishimura, Y. Koyama and I. Tanaka, *Adv. Mater*., **2010,** *22*, 3583.

45. V. Legagneur, Y. An, A. Mosbah, R. Portal, A. L. La Salle, A. Verbaere, D. Guyomard and Y. Piffard, *Solid State Ionics*, **2001**, *139*, 37–46.

46. P. Barpanda, L. Lander, S.Nishimura, A. Yamada. *Adv. Energy Mater*. **2018**, *8*, 1703055.

47. Z. Gong, Y. Yang. *Energy Environ. Sci.***, 2011**,*4*, 3223-3242.

48. M. Takahashi , S. Tobishima , K. Takei, Y. Sakurai , *J. Power Sources*, **2001**, *97-98* , 508 -511.

49. S. Franger , F. Le Cras , C. Bourbon, H. Rouault , *J. Power Sources*, **2003**, *119–121*, 252 -257.

50. N. Iltchev , Y. K. Chen , S. Okada, J. Yamaki , *J. Power Sources*, **2003**, *119–121*, 749 – 754.

51. K. F. Hsu , S. Y. Tsay, B. J. Hwang , *J. Mater. Chem.*, **2004**, *14*, 2690 - 2695.

52. J. S. Yang, J. J. Xu , *Electrochem. Solid-State Lett.*, **2004**, *7* , A515 - A518.

53. K. S. Park , J. T. Son , H. T. Chung , S. J. Kim , C. H. Lee, H. G. Kim , *Electrochem. Commun.*, **2003**, *5* , 839 – 842.

54. K. Shiraishi , K. Dokko and K. Kanamura , *J. Power Sources*, **2005**, *146* , 555 - 558.

55. M. H. Lee , J. Y. Kim, H. K. Song , *Chem. Commun.*, **2010**, *46* , 6795 - 6797.

56. R. Yang , X. P. Song , M. S. Zhao and F. Wang , *J. Alloys Compd.*, **2009**, *468* , 365 – 369.

57. D. H. Kim and J. Kim , *Electrochem. Solid-State Lett.*, **2006**, *9* , A439 —A442 .

58. K. T. Lee , W. H. Kan and L. F. Nazar , *J. Am. Chem. Soc.*, **2009**, *131* , 6044 .

59. S. K. Martha , B. Markovsky , J. Grinblat , Y. Gofer , O. Haik , E. Zinigrad , D. Aurbach , T. Drezen , D. Wang , G. Deghenghi and I. Exnar , *J. Electrochem. Soc.*, **2009**, *156* , A541 —A552.

60. D. Y. Wang , H. Buqa , M. Crouzet , G. Deghenghi , T. Drezen , I. Exnar , N. H. Kwon , J. H. Miners , L. Poletto and M. Graetzel , *J. Power Sources*, **2009**, *189* , 624 —628.

61. S. F. Yang , P. Y. Zavalij and M. S. Whittingham , *Electrochem. Commun.*, **2001**, *3* , 505 —508.

62. S. F. Yang , Y. N. Song , P. Y. Zavalij and M. S. Whittingham , *Electrochem. Commun.*, **2002**, *4* , 239 —244.

63. S. Ferrari , R. L. Lavall , D. Capsoni , E. Quartarone , A. Magistris , P. Mustarelli and P. Canton , *J. Phys. Chem. C*, **2010**, *114* , 12598 —12603.

64. J. M. Tarascon , N. Recham , M. Armand , J. N. Chotard , P. Barpanda , W. Walker and L. Dupont , *Chem. Mater.*, **2010**, *22* , 724 —739.

65. N. Recham , M. Armand and J. M. Tarascon , *C. R. Chim.*, **2010**, *13* , 106 —116.

VITA

Prashanth Sandineni was born in Medapelly, India. In December 2011, he received his Integrated Masters in Chemistry from Kakatiya University, Warangal, India. During his masters, he gained knowledge on laboratory work in synthesis with two summer research internships at Indian Institute of Chemical Technology (IICT), Hyderabad and Central University of Hyderabad. Later from July 2012 to December 2014, he worked in Mylan Pharmaceutical Pvt. Ltd., Hyderabad as a Senior Chemist and to further accomplish his goals came to United States in 2015. In May 2020, he received his Ph.D. in Chemistry from Missouri University of Science and Technology, Rolla, Missouri, USA for his work on "Structurally and Electronically diverse polyanion-Based Cathode Materials for Alkali-ion batteries".